1-1-2019

Effects Of Halogen Bonding And Nir Tuning Of Dyes For Dye-Sensitized Solar Cells

Alexandra Baumann

Recommended Citation

Baumann, Alexandra, "Effects Of Halogen Bonding And Nir Tuning Of Dyes For Dye-Sensitized Solar Cells" (2019). *Electronic Theses and Dissertations*. 1916.
https://egrove.olemiss.edu/etd/1916

EFFECTS OF HALOGEN BONDING AND NIR TUNING OF DYES FOR DYE-SENSITIZED SOLAR CELLS

A Dissertation

presented in partial fulfillment of requirements

for the degree of Doctor of Philosophy

in the Department of Chemistry and Biochemistry

The University of Mississippi

ALEXANDRA BAUMANN

DECEMBER 2019

ABSTRACT

With current energy demands being met through the utilization of energy sources such as petroleum, natural gas, and coal, the non-renewable nature of these sources will eventually approach depletion as world wide energy consumption increases yearly. As a result the need for a renewable energy alternative has become imminent. One appealing alternative that has gained considerable attention since its development due to a low cost and a high solar to electric conversion efficiency are dye-sensitized solar cells (DSCs). This dissertation describes efforts to design and synthesize improved organic dyes utilizing three analogous methods: first, through decreasing non-productive pathways such as electron recombination, second, by promoting productive pathways such as dye regeneration and lastly, by expanding the UV-vis absorption of organic dyes to the near-infrared region (800 nm-1000 nm) of the absorption spectrum in order to utilize lower energy photons.

DEDICATION

This dissertation is dedicated to family, friends, and mentors that have provided me with the opportunity, support, and guidance that has helped me to achieve my doctorate. I want to especially thank to my parents for their constant love, my sister Kristin for pushing me to never give up, and my cats, Havok and Fury, for keeping me company on the long nights and being my alarm clocks in the early mornings.

ACKNOWLEDGMENTS

This work would not have been possible without the financial support from the University of Mississippi and the US National Science Foundation (Awards: NSF-1757888, NSF-1539035 & NSF-1757220).

I would especially like the thank my advisor Dr. Jared Delcamp, who not only took a chance and provided me with an incredible opportunity, but spent innumerable hours teaching me to be a better scientist both in and out of the lab. Without his constant dedication and help none of this would have been possible.

I would also like to thank Dr. Gregory Tschumper, for providing me with guidance for three years, and my committee members Dr. Davita Watkins, Dr. Walter Cleland, Dr. Jason Ritchie, and Dr. John Rimoldi for all their time, advice, and collaboration.

Finally, I would like to thank my friends and colleagues, especially Samantha Davila and Hunter Shirley, for all their constant support and help over the past six years.

TABLE OF CONTENTS

LIST OF FIGURES

LIST OF TABLES

LIST OF SCHEMES

CHAPTER 1

INTRODUCTION

1.1 INTRODUCTION TO HALOGEN BONDING AND NEAR-INFRARED TUNING OF DYES FOR DYE-SENSITIZED SOLAR CELLS AND RESEARCH PROGRESS

Since their original development in 1991 by Grätzel and O'Regan, dye-sensitized solar cells (DSCs) have attracted considerable attention due to their low manufacturing cost and flexible dye design.[1] With three classes of sensitizers, Ru-based,[2] porphyrin-based,[3] and metal-free,[4-7] DSCs demonstrated early on that devices could not only achieve decent efficiencies, starting out at 7.1%, but could be systematically improved to achieve efficiencies as high as 12% in 2010, and over 14% most recently.[1, 3, 8]

DSCs operate through a series of electron transfers that take place as follows: (1) a dye or sensitizer bound to a semiconductor surface absorbs light and photoexcites an electron from the ground to excited state, (2) the transfer, or injection, of the excited electron to the semiconductor, (3) the completion of an external circuit ending at the counter electrode, where the injected electron is collected by an oxidized redox shuttle and (4) the return of the injected electron to the oxidized dye by the reduced redox shuttle, regenerating both the dye and oxidized redox shuttle (Figure 1).[9]

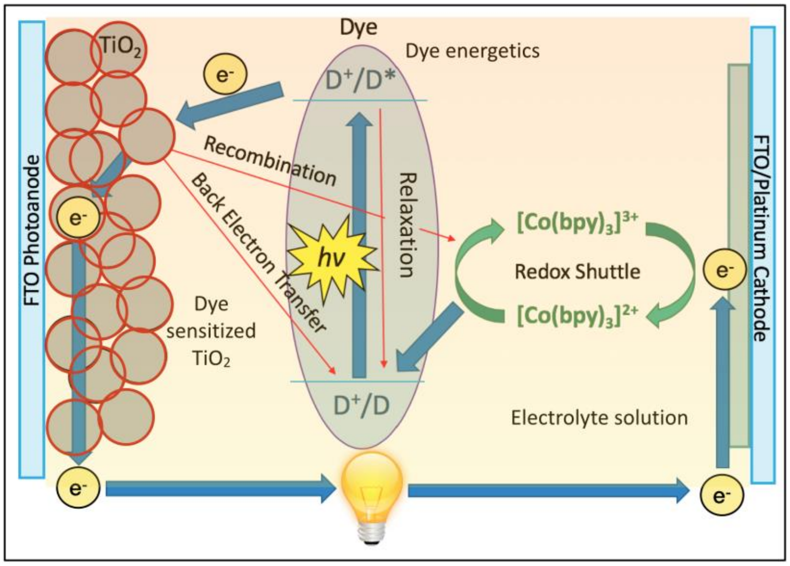

Figure 1. DSC device schematic

The overall performance of a DSC device can be analyzed by the following equation (1) below:

$$\mathrm{PCE} = (V_{oc} \text{ x } J_{sc} \text{ x FF})/I_0 \qquad (1)$$

Where PCE represents the photon conversion efficiency, V_{oc} represents the open-circuit voltage in V, J_{sc} represents the short-circuit current density in mA*cm^{-2}, FF is the fill factor, and I_0 represents the intensity of sunlight, normally set equal to 1 sun. While the V_{oc} is determined by the difference in energy between the reduction potential of the redox shuttle, most commonly I^-/I_3^- or $Co^{3+/2+}$, and the conduction band of the semiconductor (TiO_2), the J_{sc} is controlled by the dye's ability to absorb photons, or the difference between its ground and excited states.

Recent literature has demonstrated not only DSCs ability to achieve reasonable power conversion efficiencies, with the **SM315**[3] single dye cell attaining an efficiency as high as 13.0% while multi-dye systems such as **SGT-137/SGT-021**[8] achieving up to 14.6%, but also the capacity for the dyes to be systematically improved. The tunable nature of DSCs coupled with the wide range of structures available has created a need for smart design that decreases unfavorable interactions, such as recombination, within devices while promoting more favorable pathways, like regeneration.

Unfavorable interactions, such as recombination of the injected electron with an oxidized shuttle, has proven to have considerable detrimental effects on device performance, but the effect can be increased and decreased substantially in dyes containing certain motifs.[10-12] Past studies have shown that coverage of the semiconductor surface through insulation with large alkyl chains can help to decrease recombination events in DSC devices, leading to an overall increase in device efficiency.[4-5, 13] Later studies adapted the idea of surface blockage through the addition of bulky building blocks containing long alkyl chains to a dye motif itself, increasing the efficiency of devices even further (Figure 2).[3, 12, 14]

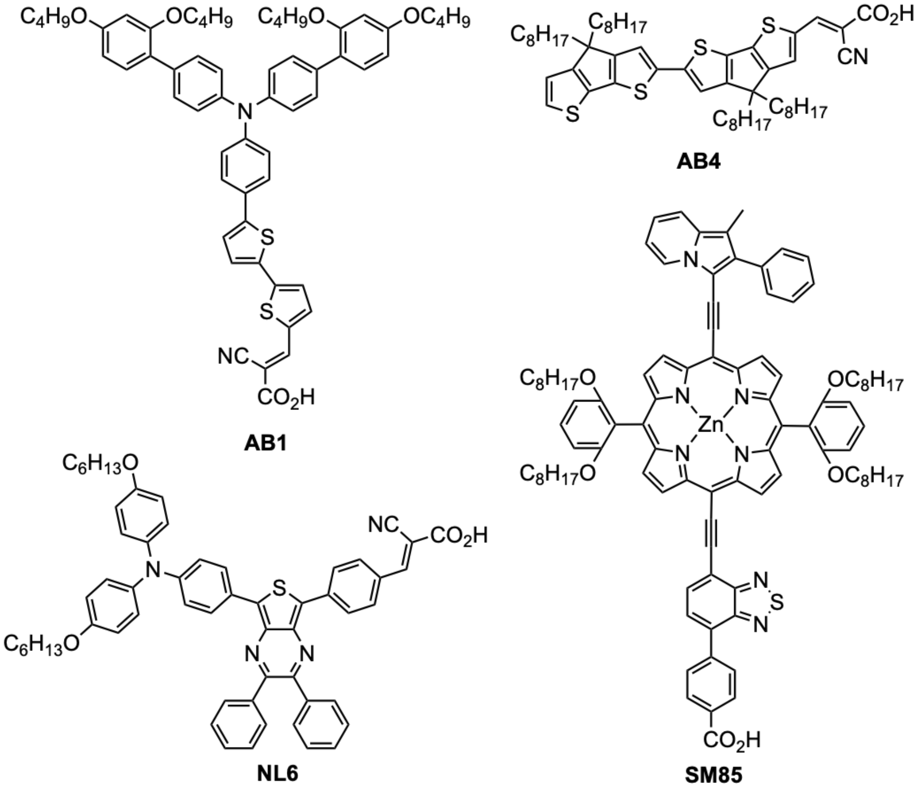

Figure 2. Structures of **AB1**, **AB4**, **NL6** and **SM85**.

While increased surface coverage proved to help decrease recombination, the functionality within the dye proved to be another important variable to device performance. Studies showed that analogous dyes could have significantly different device performance when a single atom switch, such as a nitrogen or sulfur to a carbon or oxygen, was made.[10-12, 15-17] The functionality within the dye has also been shown to help increase beneficial pathways such as dye regeneration.[11, 18-20] In these instances, the creation of a charge transfer event allows for an increased interaction between the reduced redox and oxidized dye. These studies showed that dyes with larger electropositive regions on the donor following photoexcitation exhibited higher device performance attributed to an increase in regeneration.

Dye motifs can be utilized to control dye-redox shuttle interactions within devices, as well as the light harvesting abilities of the dye itself. Studies have shown DSCs ability to efficiently convert the low-energy photons found in the near-infrared region (NIR), increasing the overall PCE of devices. [3, 9, 21-22] By extending conjugation across the π-bridge and promoting intramolecular charge transfer, there is an observed red shift in the absorption spectrum.[8, 23-26] Previous studies have shown that expanding the light absorption capabilities of a dye through red shifting of the absorption spectrum successfully enhances device performance.

A number of dyes have been designed and synthesized during my Ph.D. progress in order to examined the different effects that certain structural motifs have on the performance of a dye.

CHAPTER 2

2.1 CURRENT APPROACHES TO AND A NOVEL ROBUST, SCALABLE SYNTHESIS OF THE BULKY HAGFELDT DONOR FOR DYE-SENSITIZED APPLICATIONS

Adapted with the permission from **Alexandra Baumann**, Jonathon Watson and Jared H. Delcamp.

This project is a collaborative project between Dr. Delcamp's group. Alexandra Baumann contributed to this work by investigating synthetic strategies, synthesizing the intermediates and final product, and scaling up the reaction. Jonathon Watson contributed to the work by characterizing the intermediates and final product.

ABSTRACT

A bulky triarylamine donor commonly referred to as 'the Hagfeldt donor' is a key building block used with a large number of organic dyes for dye-sensitized applications such as dye-sensitized solar cells (DSCs). The popularity of this building block is in part due to a large portion of the highest performing DSC devices in the literature using a dye based on this donor group. The Hagfeldt donor has 4 alkyl chains positioned in a desirable 3-dimensional structure which provides surface protection for electrons injected into a semiconductor from oxidants in the electrolyte. This donor has largely fueled the rise of record setting cobalt and copper redox shuttles that require exquisite surface protection; however, this molecule has proven to be difficult to synthesize reliably. This work describes the 5 common synthetic strategies found in

literature using the Hagfeldt donor in over 140 publications and challenges each of these strategies encounter. Additionally, a novel and reliable synthesis of the Hagfeldt donor is presented which is 72% overall yielding over 5-steps and has been completed on up to a 2 gram scale.

INTRODUCTION

Dye-sensitized solar cells (DSCs) have shown continuous improvement since the modern form was presented in 1991 by Gratzel and O'Regan.[27-28] DSCs provide a cost-effective alternative to current renewable energy sources that are aesthetically appealing due to their wide range of colors, with power conversion efficiencies (PCEs) of >14% in high light and >28% in low light.[5, 8, 29] A key reason for the intense research efforts surrounding dye-sensitized renewable energy applications including dye-sensitized photoelectrochemical cells, solar batteries, and DSCs is the tunable nature of the sensitizers used.[30-43] The donor-π bridge-acceptor (D-π-A) structure has found ubiquitous use in these applications and allows for a wide range of synthetic flexibility in tailoring dyes for specific absorption profiles. Critically these structures can be molecularly engineered to be compatible with new transition metal-based redox shuttles used almost exclusively in devices with >12% PCE with the DSC field.[1, 27]

N-(2',4'-bis(hexyloxy)-[1,1'-biphenyl]-4-yl)-2',4'-bis(hexyloxy)-[1,1'-biphenyl]-4-amine is a triarylamine (TAA) donor building block used within the D-π-A architecture that is commonly referred to as the Hagfeldt (HF) donor (Figure 3). The HF donor has shown exceptional surface insulation of electron

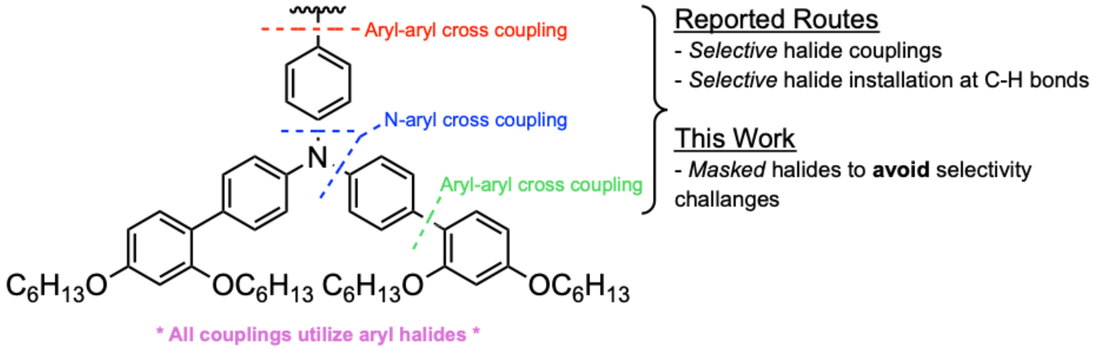

Figure 3. HF donor structure and synthetic analysis.

in a metal oxide semiconductor such as TiO_2 from oxidants in the electrolyte solution to reduce this electron transfer process referred to as recombination. This results in extended charge separation lifetimes, which is exceptionally important when using materials in the electrolyte which typically undergo fast electron transfers at the TiO_2 surface such as Co^{3+} and Cu^{2+} transition metal-based complexes.[9] The unique performance of the HF donor has resulted in the successful incorporation of this group into a large number of DSC dyes seen in literature today with more than 140 unique manuscripts reporting use of this group in a recent literature search. Currently, the four of the five highest performing DSC devices under full sun condition employ dyes based on the HF donor including: **XY1/Y123**, **SM315**, **SGT-137/SGT-021** and **LEG4/ADEKA-1** (Figure 4).[3, 5, 29, 41, 44]

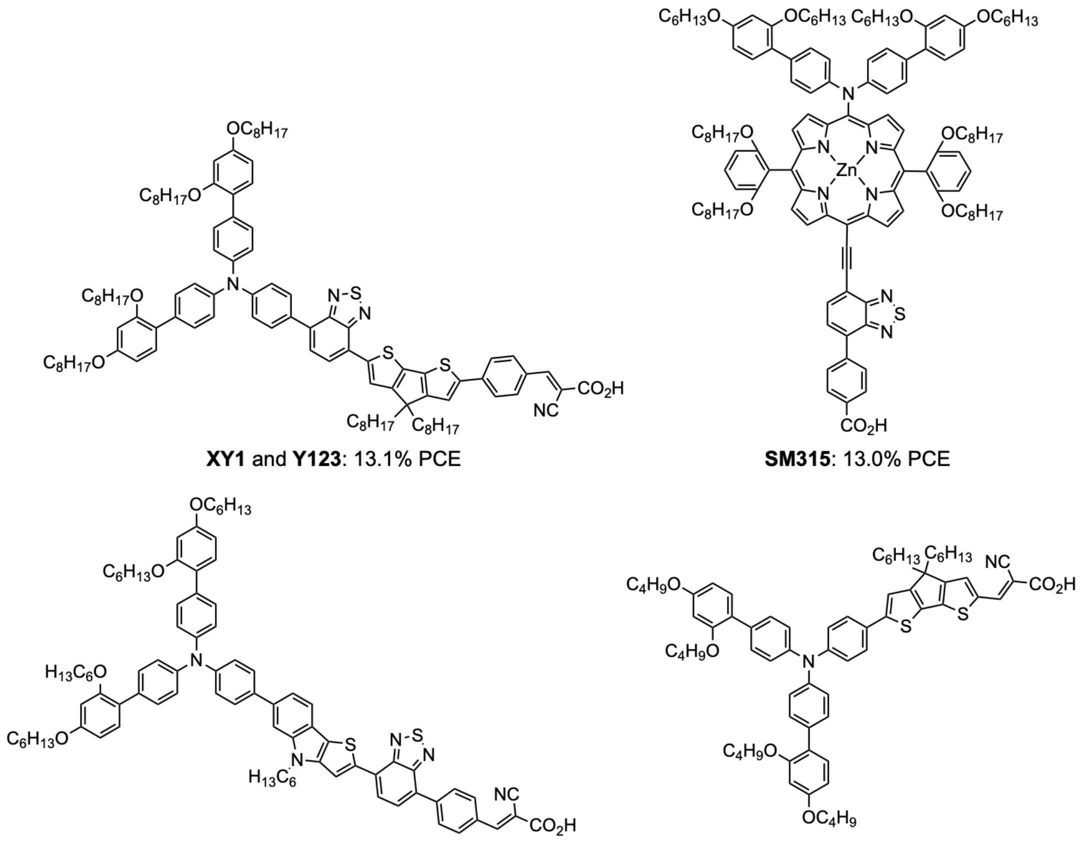

XY1 and **Y123**: 13.1% PCE

SM315: 13.0% PCE

SGT-137 and **SGT-021**: 14.6%

LEG4 and **ADEKA-1**: 14.3% PCE

Figure 4. Example high performing dyes in DSC devices using the Hagfeldt donor or an analogue.

Dyes **XY1/Y123** are used a co-sensitized device with a copper-based redox shuttle, $[Cu(tmby)_2]^{2+/1+}$, showing impressive performance values with a V_{OC} of 1.05 V, a JSC of 15.7 mA/cm^2, and a PCE of 13.1%.[45] This same system gives a record setting 31.8% PCE under artificial indoor light conditions. Specifically, the V_{OC} parameter is heavily influenced by the ability of the dye donor region to slow recombination for higher values. **SM315**,[3] **LEG4/ADEKA-1**,[5] and **SGT-127/SGT-021**[8] based devices represent high performance systems based on a single dye DSC device, a co-sensitized DSC device, and a two-dye tandem DSC device architecture for overall PCEs of 13.0%, 14.3%, and 14.6%, respectively. All of these devices employ either $[Co(bpy)_3]^{3+/2+}$ or $[Co(phen)_3]^{3+/2+}$ redox shuttles which requires the exceptional surface protection from recombination provided by the HF donor.

SYNTHESIS DISCUSSION

As expected given such notable reports, the HF donor has found widespread use in the literature with more than 140 manuscripts using this building block. However, it is somewhat surprisingly that at least 5 distinct synthetic strategies have emerged for installation of the HF donor largely focused on either selective halide couplings or selective halide installations at C-H bonds (Table 1). The need for such a large number of routes to one building block suggests challenges are frequently encountered with these synthetic routes resulting from new approaches being pursued. Commercialization of the boronic ester derivative of the HF donor has provided a convenient method which is gaining popularity for rapid installation of HF donor onto dye π-bridges; however, this approach requires that the halide of the π-bridge be accessible and it limits the alkyl chain lengths available to butyl chains. Clearly, a synthetic route to the HF donor where alkyl groups can be readily selected and the aryl halide is available is desirable. An analysis for each of these routes is described in this manuscript along with a discussion on a novel, scalable, and, in our hands, reliable route to the HF donor in 5 steps from commercial reagents with an overall yield of 72% using a masked halide approach to avoid selectivity issues encountered with other routes.

Table 1. Frequency with which each route is used in literature.

Route	Figure Represented In	Number of Unique Dye Instances Used
TMS- protection route	8	1 (this work)
Sandmeyer route	3	26
Bottom-up non-divergent approach	4	22
Late stage halide installation	5	12
Buchwalk-Hartwig halide differentiation route	6	2
Suzuki halide differentiation route	7	1
Commercial installation of the Hagfeldt donor with C_4H_9 chains only[3, 12, 46-51]	N/A	9

Sandmeyer Reaction Route: The most commonly used route (26 unique dyes follow this route) to obtain the HF donor in the literature is based on a Sandmeyer sequence used to convert a nitro group into an aryl iodide (Figure 5). This route commonly begins with a Williamson ether synthesis to install two n-hexyl groups on 4- bromoresorcinol (**1**) to give compound **2**. A lithium halogen exchange is then used to borylate compound **2** to give boronic ester **3** in moderate yield. Suzuki coupling of compound 3 with 1-bromo-4-nitrobenzene gives nitrodiaryl compound **4**. A Sandmeyer reaction is then used in order to transform the nitro group of compound **3** into an iodine in low yield (20%). Aryl iodide **5** then undergoes a copper catalyzed reaction with 4-bromoaniline to produce compound **6**, the desired brominated HF donor building block. This route is an example of a masked halide route with the nitro group preinstalled that is later converted to an aldehyde which avoids selectivity challenges. However, for this particular case

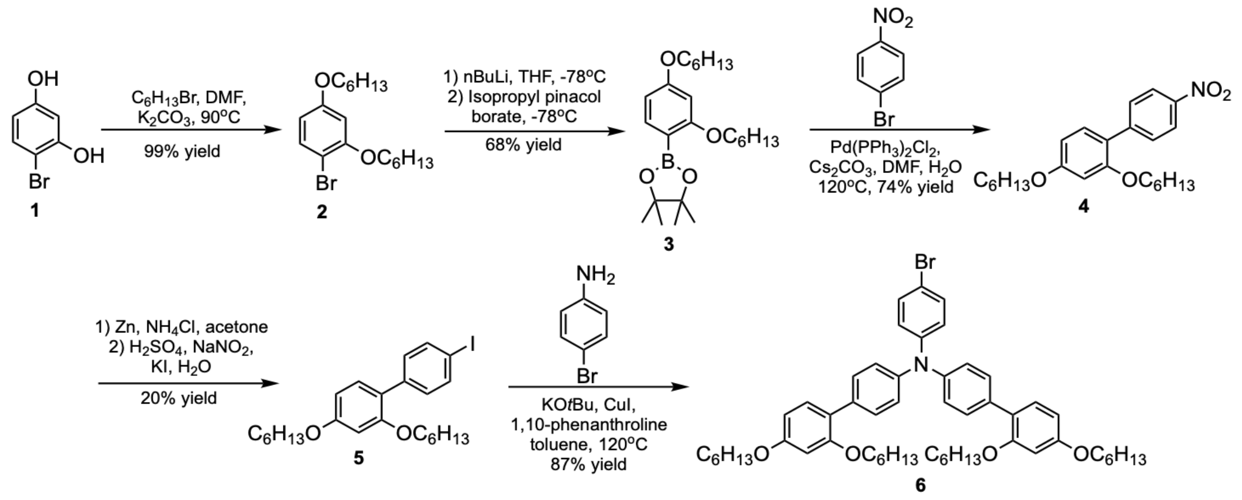

Figure 5. A Sandmeyer reaction-based synthetic route to the brominated HF donor.[41,45-48, 52-54]

the yield for the nitro to iodo group conversion is often reported to be very low at 20% yield. The reagents used in this transformation are solubilized with aqueous solvents while the starting nitro compound (**4**) has two hexyl chains and two benzene rings which limit water solubility of the starting material in water which complicates this reaction. The Sandmeyer, due to its radical nature, can be highly variable in the yield obtained with single digit yields often obtained in our hands. This low yielding reaction leads to a scalability issue, which requires large amounts of material in order to obtain a substantial amount of product. Additionally, the copper catalyzed amination reaction following the Sandmeyer reaction also has variable yields especially with heavily alkylated intermediates although a number of conditions for this reaction are reported. A number of products are observed for this reaction which could potentially arise due to multiple halides being present in the reaction leading to selectivity concerns.

Bottom-Up Approach: The second most frequently used route (22 unique dyes use this route) to dyes with the HF donor group is a bottom-up synthetic strategy where the π-bridge and acceptor groups are first installed followed by a Suzuki coupling to give the HF donor group (Figure 6). An example synthesis starts with a Suzuki reaction to couple brominated TAA **7** with 5-formyl-2-thiopheneboronic acid to give compound **8**. Selective bromination of **8** gives dibromo coupling partner **9** in high yield. Double Suzuki coupling of **9** with (2,4-dibutoxyphenyl)boronic acid gives the HF donor group in modest yield for this example. Notably, a plethora of Suzuki conditions are available in literature which could be used to increase benzene-benzene bond forming reaction yield, if desired. However, the primary drawback of this approach is inherent to linear, bottom-up synthetic approaches in that the desirable convenient modularity of a building block approach is foregone. Since the donor molecule is built around the π-bridge and acceptor motif, rapid divergent structural syntheses are not possible which limits the rate at which dye series can be accessed. Additionally, the bromination of compound **8** relies on good C-H bond site selectivity to give compound **9**. Additional C-H bonds, especially at the ortho positions relative to the amine are active toward bromination.[55] Due to the possibility of multiple undesirable bromination sights on the TAA motif, over bromination may occur, which can lead to lower yields later or challenging to separate side products differing structurally in only a single atom from the desired product.

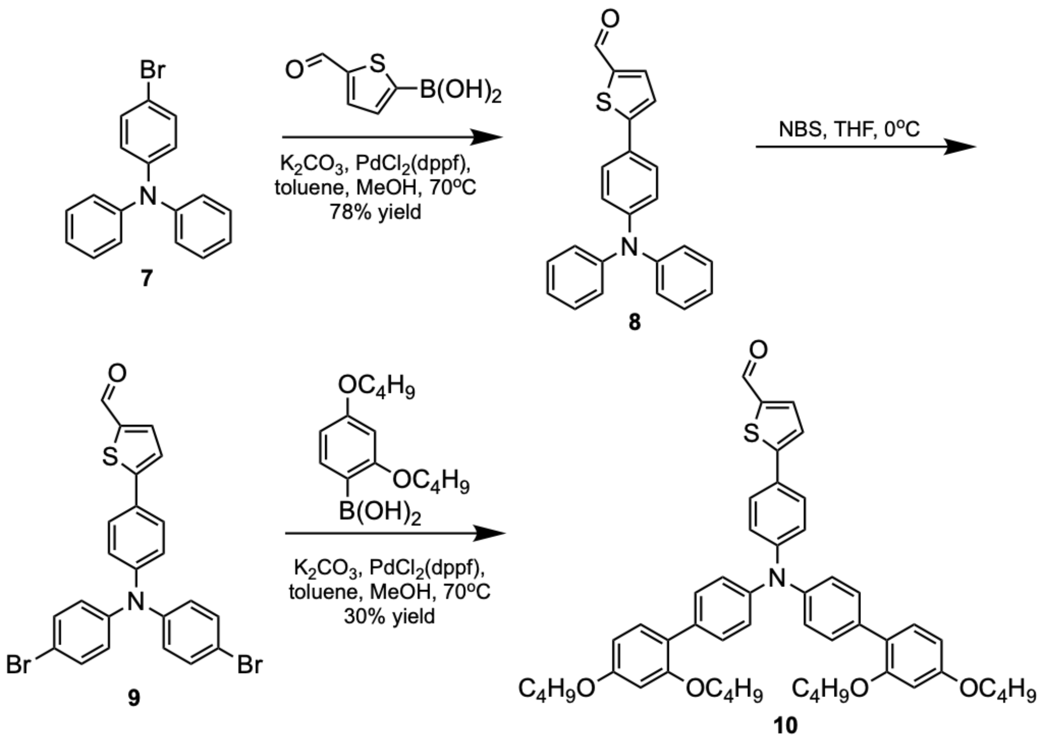

Figure 6. Bottom-up synthetic strategy where the HF donor is built onto the π-bridge.[49, 56-62]

Late Stage Halogenation: A late state halogenation route has found moderate use in literature with 12 unique dyes being synthesized via this method (Figure 7). This route is the least number of steps to a halogenated HF donor building block. An example synthesis begins with dibromo TAA **11** which undergoes a double Suzuki coupling with (2,4-dibutoxyphenyl)boronic acid in order to obtain non-halogenated TAA **12** (the parent HF structure) in high yield. The NBS bromination of compound **12** produces the brominated HF donor building block **13**. In our hands, the exclusive bromination of the para position relative to the nitrogen of compound **12** is challenging, and many of the C-H bond sites are active during the bromination reaction as has been previously noted.[55] Presumably, precise temperature control may aid in a more selective halogenation given the specific values reported for this reaction. Exception selectivity for the desired brominated product is compulsory due to the negligible difference in polarity between the desired compound **13** and other brominated isomers/multiple brominated side products limiting column chromatography options.

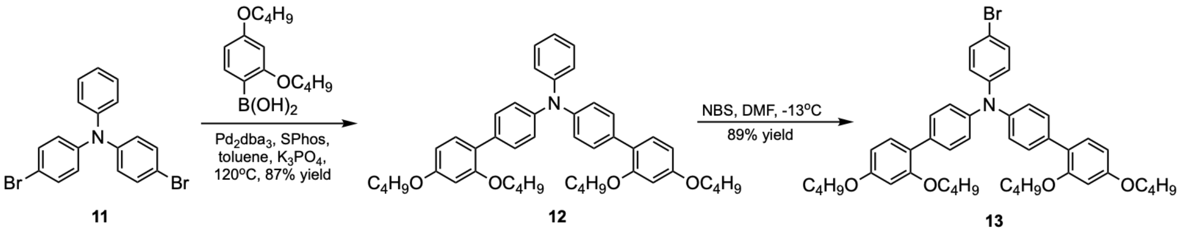

Figure 7. Late stage halogenation route to the HF donor.[36, 44, 63-71]

Selective Aryl Halide Amination: The selective aryl halide amination route is one of the least frequently used routes to the brominated HF donor **6**. In the example case below, the reaction route begins the alkylation of 4-chlororesorcinol (**14**). Next, a Miyaura borylation reaction is used to give aryl boronic ester **3** in good yield. Suzuki coupling of **3** and bis(4-bromophenyl)amine (**16**) leads to diarylamine **17** in 90% yield. The key step in this synthetic pathway is the copper catalyzed coupling of **17** with 1-bromo-4-iodobenzene to give the brominated HF donor **6**. This synthetic route aims to bring the halide on building block **6** pre-installed onto to aryl ring to avoid the selectivity challenges highlighted in the above routes. To do this, a selective coupling of an aryl iodide over an aryl bromide is necessary. While copper based couplings are certainly selective for aryl iodides these reaction are not exclusively selective leading to a mixture of halide products, and the potential of double coupling diarylamine **17** to both halide groups. Additionally, while the selected example of this reaction is reported to be high yielding, this reaction is typically in the 50-70% yield range with an unidentified mixture of side products being formed in our experience with some being challenging to separate via silica chromatography. As noted above for compound **6**, the yields in this aryl amination reaction can be highly variable, seemingly more so with heavily alkylated reagents.

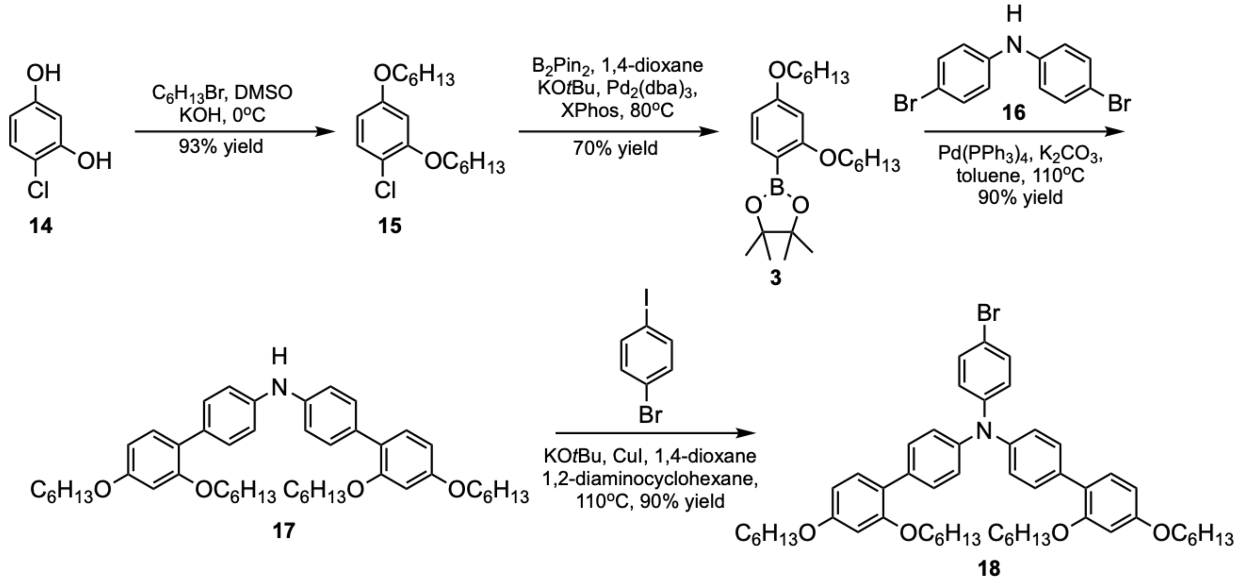

Figure 8. Selective aryl halide amination route using a copper catalyst.[13,72]

Suzuki Halide Differentiation: A final notable synthetic route to the HF donor group has been put forward based on the differentiation of halides during a Suzuki coupling (Figure 9). The synthesis begins with selective bisiodination of TAA bromide **7** to give diiodo monobromo TAA **18**. Then a Suzuki coupling is use differentiate the halides on **18** when coupling with aryl boronic ester **3** to give the brominated HF donor **6**. While this route is very direct, concerns about how selective the halogenation is and how selective the Suzuki coupling is are inherently concerning as described above for other similar key step approaches. These selectivity issues are concerning given that little polarity difference exist between the desired products and side products which limits opportunities for traditional silica gel chromatography approaches for separations. As with many of the separations discussed for the other routes, recrystallization is problematic in that alkylated products such as **6** are oils.

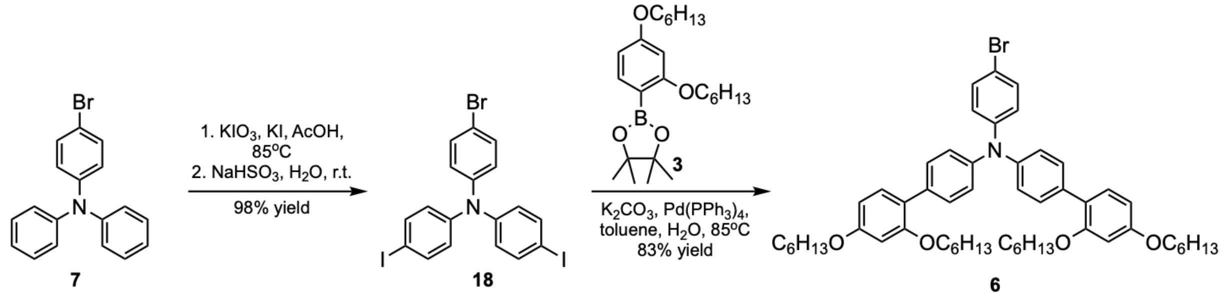

Figure 9. Suzuki halide differentiation route to the HF donor.[73]

Masked Halide Approach: Having attempted many of the above synthetic routes with varying levels of desired product purity arrived at, the selectivity challenges mentioned above became the focus point in designing a robust route to the halogenated HF donor building block. The key transformation put forward in this novel route is the conversion of an aryl-trimethylsilane (TMS) group to an aryl-iodide. In this approach the TMS group serves to mask the halide coupling partner as an inert group with no selectivity challenges associated with the common cross couplings used to make the HF donor building block. This route begins with the alkylation of 4-bromoresorcinol (**1**) with 1-bromohexane on >10 g scale for an 89% yield of arylbromide **2**. Compound **2** then undergoes lithium halogen exchange with n-BuLi, addition to trimethoxyborate, and hydrolysis of the boronic ester to aryl boronic acid **19** in high yield with a 5 gram scale as the largest amount demonstrated in our laboratories. Bis(4-bromophenyl)amine (**16**) is then double Suzuki coupled to **19** to give diarylamine **17** in high yield (94%) with up to a 3 gram scale demonstrated. Compound **17** behaves unusually by ^{1}H NMR as described below and care must be taken in interpreting the NMR spectrum of this compound (see discussion below). Diarylamine **17** is then coupled to 1-bromo-(4-trimethysilyl)benzene via a palladium catalyzed Buchwald-Hartwig reaction to give **20** in high yield (95%) on a 2 gram scale. Finally, iodine monochloride is then used to transform the trimethylsilyl group into an iodine, yielding the iodinated HF donor building block **21**. During this synthetic route, no selective halogenations or selective halide couplings were required whereas the route is carefully chosen to use orthogonal reactivies with the substitution sites having key functionality in place before the route is initiated. We have found this reaction route to be scalable to multigram quantities and to be highly reliable in reactivity after more than 4 times completing this route.

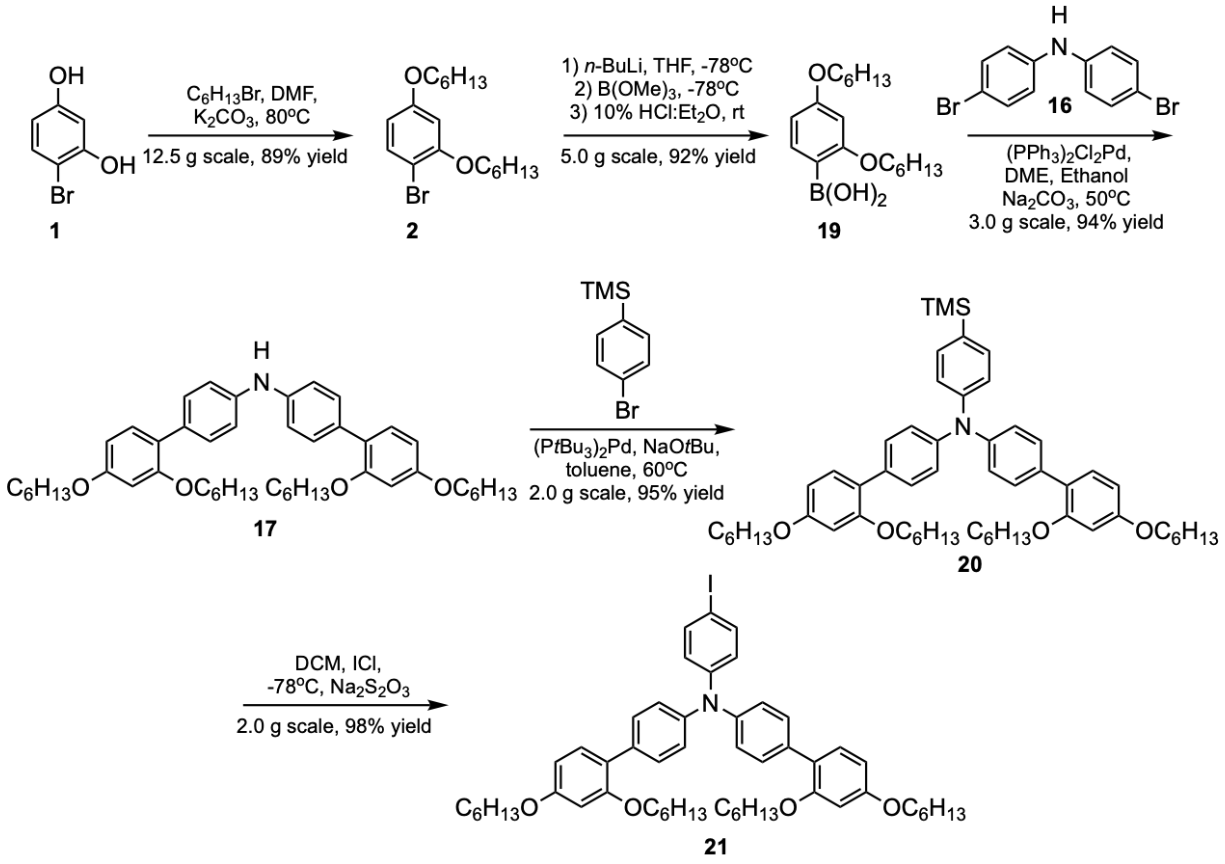

Figure 10. A robust, high yielding, and scalable route to the iodinated HF donor **21**.

As mentioned above, the ^{1}H NMR of diarylamine **17** is unusual once a high purity is reached (Figure 11). Prior to purification, sharp, distinguishable peaks belonging to the compound can be easily identified when an NMR is taken on a sample directly from the reaction mixture (black line labeled “crude"). However, upon purification the signals in the aromatic region take on an extremely broad appearance, causing previously sharp doublet peaks to be unidentifiable (red line). We hypothesized this could be due to some form of intermolecular interactions with strong enough non-covalent interactions to slow the averaging of different proton environments to a single signal as is observed when strong aggregates are made in solution. In order to confirm the presence of compound **17** in the purified sample several ^{1}H NMR experiments were performed in an effort to give well-resolved peaks within the aromatic region. First, variable temperature (VT) NMR was used to heat the sample to 60^{o}C, however the broad signals remained (green line). Dilutions are often used to reduce aggregative effects, and while dilution of the sample did not yield well resolved peaks, the signal was sharpened relative to the other pure NMR spectrum of **17** (blue line). The broadening of the peaks could result from self-hydrogen bonding interactions, thus small amounts of acid (acetic acid) and base (pyridine) were added to the ^{1}H NMR samples. In both cases, the acid or base addition, the signals become well resolved into clearly identifiable peaks with distinguishable coupling constants within the ^{1}H NMR spectrum. We suspect this unusual behavior that is presumably due to hydrogen bonding interactions has been problematic for numerous synthetic groups since this key intermediate is used in at least 12 other manuscripts and is a key building block to **SM315** which is used in the first 13% PCE single dye DSC device. In our experience, the purity of **17** is critical to observing this unique behavior by ^{1}H NMR. In cases where the compound is not a high purity due to solvents or other remaining unidentified side products, the aryl ^{1}H NMR signals can often be identified clearly.

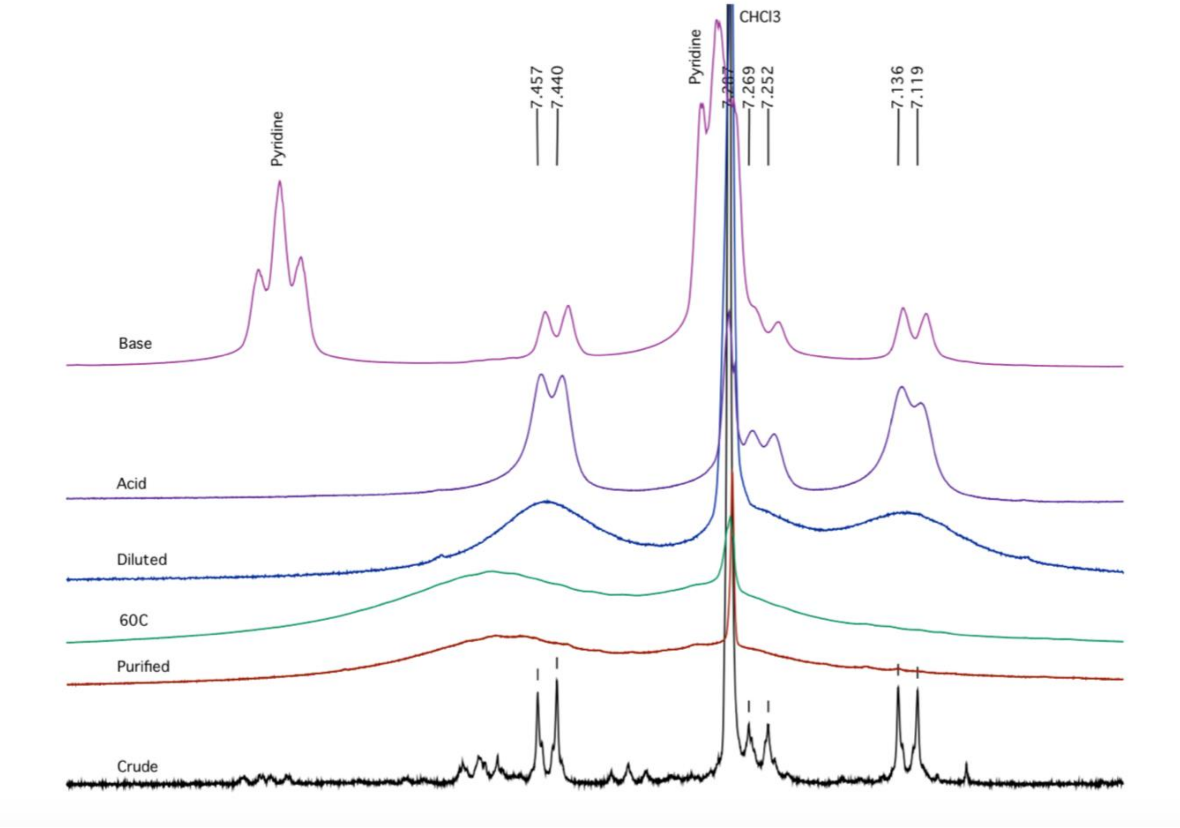

Figure 11. ^{1}H NMR experiments with **17**.

EXPERIMENTAL

The HF donor is a widely used and important building block within the dye-sensitized community, which is seen in a large number of DSC dye motifs due to the addition of 3-dimensional elements that increase solubility, often lower aggregation, and efficiently protect the TiO_2 surface from oxidizing redox shuttles. The importance of the HF donor as a building block can be seen from its presence in many of the highest performing DSC dyes currently found in literature. While a number of syntheses currently exist, the difficultly of synthesizing this molecule can be seen not only through the number of synthetic routes available but also the pitfalls of the routes used which rely on either selective halogenations or selective halide couplings. Low yields, problematic selectivity, and difficulty in the purification process have limited the scalability of this reaction in many cases. A robust, scalable, and high yielding synthetic route to the HF donor is presented that circumvents the selectivity challenges faced in the prior routes. Specifically, the use of a masked halide group, TMS, has allowed for the introduction of functionality at the desired positions from the start of the synthesis. Additionally, a key building block common to two routes to the HF donor is

General experimental details. All commercially obtained regents were used as received. Bis(4-bromophenyl)amine was purchased from Sigma Aldrich, and 1-bromo-4-(trimethylsilyl)benzene was purchased from TCI. Thin-layer chromatography (TLC) was conducted with Sorbtech silica XHL TLC plates and visualized with a UV lamp. Flash column chromatography was performed with Sorbent Tech P60, 40–63 mm (230–400 mesh). ^{1}H and ^{13}C NMR spectra were recorded on a Bruker Avance-400 (400 MHz) spectrometer or a Bruker Avance-500 (500 MHz) spectrometer and are reported in ppm using solvent as an internal standard ($CDCl_3$ at 7.26 ppm). Data reported as s = singlet, d = doublet, t = triplet, q = quartet, p = pentet, m = multiplet, br = broad, ap = apparent, dd = doublet of doublets; coupling constant(s) in Hz. 1-bromo-2,4-bis(hexyloxy)benzene (**2**)[62], (2,4-bis(hexyloxy)phenyl)boronic acid (**19**)[74], and bis(2',4'-bis(hexyloxy)-[1,1'-biphenyl]-4-yl)amine (**17**)[13] were synthesized according to prior literature procedures.

Synthetic protocols. N-(2',4'-bis(ethylhexyloxy)-[1,1'-biphenyl]-4-yl)-2',4'-bis(ethylhexyloxy)-N-(4-(trimethylsilyl)phenyl)-[1,1'-biphenyl]-4-amine (**20**): Bis(2',4'-bis(hexyloxy)-[1,1'-biphenyl]-4-yl)amine (17) (1.79 g, 2.14 mmol), 1-bromo-4-(trimethylsilyl)benzene (1.25 mL, 6.42 mmol) and sodium *tert*-butoxide (617 mg, 6.42 mmol) were dissolved in 8.60 mL of toluene in a 25.0 mL round bottom flask. The solution was then degassed for about 10 minutes with nitrogen. $Pd(P\textit{t}Bu_3)_2$ (110 mg, 0.214 mmol) was then added.

The reaction was sealed, and brought to 55°C for 16 hours. The reaction was removed from heat and cooled to room temperature. The mixture was then extracted with diethyl ether and water and dried with sodium sulfate. The crude product was purified with silica gel chromatography with a gradient from 20% dichloromethane/hexanes to 50% dichloromethane/hexanes (2.0 g, 95% yield). ^{1}H NMR (500 MHz, $CDCl_3$) δ 7.40 (d, *J* = 8.5 Hz, 4H), 7.37 (d, *J* = 7.5 Hz, 2H), 7.24 (m, 2H), 7.16-7.13 (m, 6H), 6.55-6.52 (m, 4H), 4.00-3.90 (m, 8H), 1.75-1.65 (m, 4H), 1.55-1.25 (m, 20H), 0.93-0.85 (m, 20H), 0.26 (s, 9H) ppm. ^{13}C NMR (100 MHz, CDCl3) δ 160.7, 158.1, 149.4, 146.6, 135.0, 134.1, 133.6, 131.6, 131.2, 124.8, 124.2, 123.2, 106.1, 101.2, 71.7, 71.5, 40.4, 40.3, 31.5, 31.5, 30.1, 25.0, 24.8, 24.0, 24.0, 16.2, 15.0, 12.1 ppm. IR (neat) ν = 3205, 3030, 2955, 2922, 2857, 2358, 2089, 1731, 1604 cm^{-1}. ESI HRMS m/z calc'd $C_{65}H_{95}NO_4SiCs$ [M + Cs]$^+$: calculated 1114.6085, found 1114.6112.

N-(2',4'-bis(ethylhexyloxy)-[1,1'-biphenyl]-4-yl)-2',4'-bis(ethylhexyloxy)-N-(4-iodophenyl)-[1,1'-biphenyl]-4-amine (**21**): In a 50.0 mL round bottom flask, 20 (1.92 g, 1.95 mmol) was dissolved in 14.0 mL of dichloromethane and cooled to -78°C. In a separate flask, a solution of iodine monochloride (640 mg, 3.93 mmol) and 2.40 mL of dichloromethane was made. The iodine monochloride solution was then added to the solution of 22 via cannula and stirred for about 30 minutes while monitored by TLC. A saturated solution of $Na_2S_2O_3$ (1.70 mL) was then added to the mixture, and the solution was allowed to warm to room temperature. The mixture was then extracted with dichloromethane and water and dried with sodium sulfate. The crude product was purified with silica gel chromatography with a gradient from 10% dichloromethane/hexanes to 30% dichloromethane/hexanes (2.0 g, 98% yield). ^{1}H NMR (400 MHz, $CDCl_3$) δ 7.50 (d, *J* = 7.6 Hz, 2H), 7.40 (d, *J* = 8.4 Hz, 4H), 7.23 (m, 2H), 7.10 (d, *J* = 8.4 Hz, 4H), 6.91 (d, *J* = 8.4 Hz, 2H), 6.60-6.50 (m, 4H), 3.90-3.80 (m, 8H), 1.80-1.60 (m, 4H), 1.55-1.15 (m, 20H), 1.00-0.80 (m, 20H) ppm. ^{13}C NMR (100 MHz, $CDCl_3$) δ 159.9, 157.2, 147.9, 145.3, 137.9, 133.6, 130.7, 130.4, 125.1, 123.8, 123.1, 105.2, 100.26, 84.2, 70.7, 70.5, 39.5, 39.4, 30.6, 30.6, 29.1, 29.0, 24.0, 23.9, 23.1, 23.0, 14.1, 11.2 ppm. IR (neat) ν = 3200, 3031, 2955, 2921, 2856, 2353, 2091, 1765, 1604 cm^{-1}. ESI HRMS m/z calc'd $C_{62}H_{86}INO_4$ $[M]^+$: calculated 1035.5607, found 1035.5602.

CHAPTER 3

3.1 EFFECT OF DONOR STRENGTH AND BULK ON THIENO[3,4-B]-PYRAZINE-BASED PANCHROMATIC DYES IN DYE-SENSITIZED SOLAR CELLS

Adapted with the permission from Nalaka P. Liyanage,; Hammad Cheema,; **Alexandra Baumann**,; Alexa R. Zylstra,; Jared H. Delcamp *ChemSusChem* **2017**, *10*, 2635. Copyright (2019) The Royal Society of Chemistry.

(See appendix for permission license).

This project is a collaborative project between Dr. Delcamp's group. Nalaka P. Liyange contributed to this work by synthesizing and characterizing the dyes used in the study. Hammad Cheema contributed to the work by fabricating, testing and analyzing all the devices. Alexandra Baumann contributed to the work by synthesizing the donor molecule used on the final dyes. Alexa R. Zylstra contributed by synthesizing parts of the donor molecule used for the dye.

ABSTRACT

Near-infrared-absorbing organic dyes are critically needed in dye-sensitized solar cells (DSCs). Thieno[3,4-b]pyrazine (TPz) based dyes can access the NIR spectral region and show power conversion efficiencies (PCEs) of up to 8.1% with sunlight being converted at wavelengths up to 800 nm for 17.6 mA cm^{-2} of photocurrent in a co-sensitized DSC device. Precisely controlling dye excited-state energies is critical for good performances in NIR DSCs.

Strategies to control TPz dye energetics with stronger donor groups and TPz substituent choice are evaluated here. Additionally, donor size influence versus dye loading on TPz dyes is analyzed with respect to the TiO_2 surface protection designed to prevent recombination of electrons in TiO_2 with the redox shuttle. Importantly, the dyes evaluated were demonstrated to work well with low Li^+ concentration electrolytes, with iodine and cobalt redox shuttle systems, and efficiently as part of co-sensitized devices.

INTRODUCTION

Developing sustainable and renewable energy technologies for future energy needs is an urgent research direction. Dye-sensitized solar cells (DSCs) have shown great improvement in the past two decades since the introduction of the modern form and they may play a prominent role in addressing future energy needs.[1, 27] DSCs operate by: i) a dye absorbing photons to promote an electron to an excited state, ii) transfer of this electron to a semiconductor such as TiO_2, iii) collection of this electron by a redox shuttle at a counter electrode after traversing an external circuit, and iv) return of this electron to the oxidized dye. DSCs critically need to access lower-energy photon wavelengths to further improve power conversion efficiencies (PCEs).[75] The dye component of DSC devices determines the maximum light-absorption breadth.[76-78] However, most efficient metal-free sensitizers do not absorb photons beyond 750 nm wavelengths. Here, we evaluate sensitizer-structure device performance relationships with sensitizers producing electricity beyond 750 nm.

Some of the broadest absorbing organic sensitizers are designed based on the donor–π-bridge–acceptor (D–π–A) configuration. D–π–A dyes absorb light efficiently by separating charges across the molecule.[1] Lower-energy wavelength can be accessed and converted to electricity in DSC devices through the use of an auxiliary acceptor to tune dye energy levels in

D–A–π–A motifs.[1, 77, 79-89] Proaromatic building blocks within the D–A–π–A dye structure can access NIR photons from simple structures to synthesize as is desirable for rapidly gaining understanding of dye performances through structure–property relationships. Proaromaticity leads to the generation of a local aromatic ring, which stabilizes dye excited-state energies for enhanced light absorption at lower-energy wavelengths.[3, 26, 86, 90-95] However, controlling the stabilized excited-state energy levels in proaromatic dyes is crucial for using low-energy light to rapidly transfer electrons from the dye to TiO_2.

In a prior study, we evaluated the structure–function relationship of a proaromatic (3,4-b)thienopyrazine (TPz)-based D–A–π–A dye series in which TPz is the auxiliary acceptor with varied substituents, triphenylamine (TPA) is the donor, cyanoacrylic acid (CAA) is the terminal acceptor, and the π-spacer is varied.[86] The excited-state energies in the studied series was positioned with little driving force for electron injection (ΔG_{inj}) into the conduction band (CB) of TiO_2, which resulted in a required high Li^+ loading in the electrolyte to lower the TiO_2 CB and increase ΔG_{inj} (Figure 12). Among the prior dye series, we found that the highest energy excited-state dyes were based on structures with alkyl substituents on the pyrazine ring of the TPz (**NL2**) and with a phenyl π-spacer (**NL6**, Figure 12). To improve on the highest performing dye in the prior series (**NL6**), we selected target dyes based on combining both modifications in addition to varying donor group strength and size. A second generation of dyes were designed to tune the excited-state and ground-state oxidation potentials through the incorporation of both structural features (**NL11**–**NL13**, Scheme 1). **NL11** keeps the TPA donor constant for direct com- parison to **NL2** and **NL6**, which should lead to the highest energy excited-state between these three dyes. **NL13** incorporates the indoline donor (Ind) in place of TPA for **NL11**. Indoline is a stronger electron-donating group that should raise both the ground-state oxidation potential and increase photon-absorption breadth relative to **NL11**. Additionally, the open-circuit voltage for the prior **NL** series was found to be low (500–600 mV), which we attributed in part to fast recombination rates of injected electrons in the TiO_2 with the redox shuttle. We reasoned either a concise low-surface footprint dye with increased packing density (**NL13**) or a bulky alkylated donor-based dye (**NL12**) could better protect the TiO_2 surface from an oxidizing redox shuttle (Scheme 1).[1, 88, 96-97]

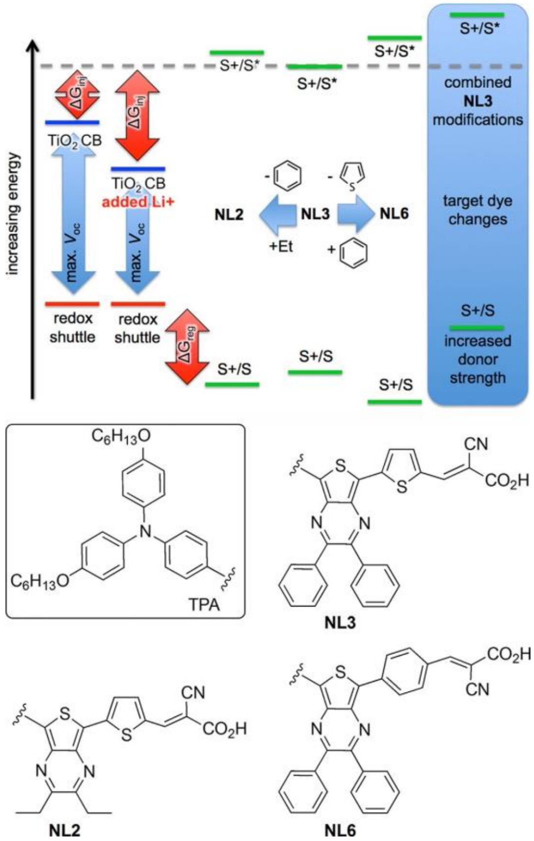

Figure 12: Top: Diagram showing the effects of dye modifications to **NL3** energetics, lithium addition to the electrolyte, and desired dye energetics on the right. Bottom: structures of **NL2**, **NL3**, and **NL6**.

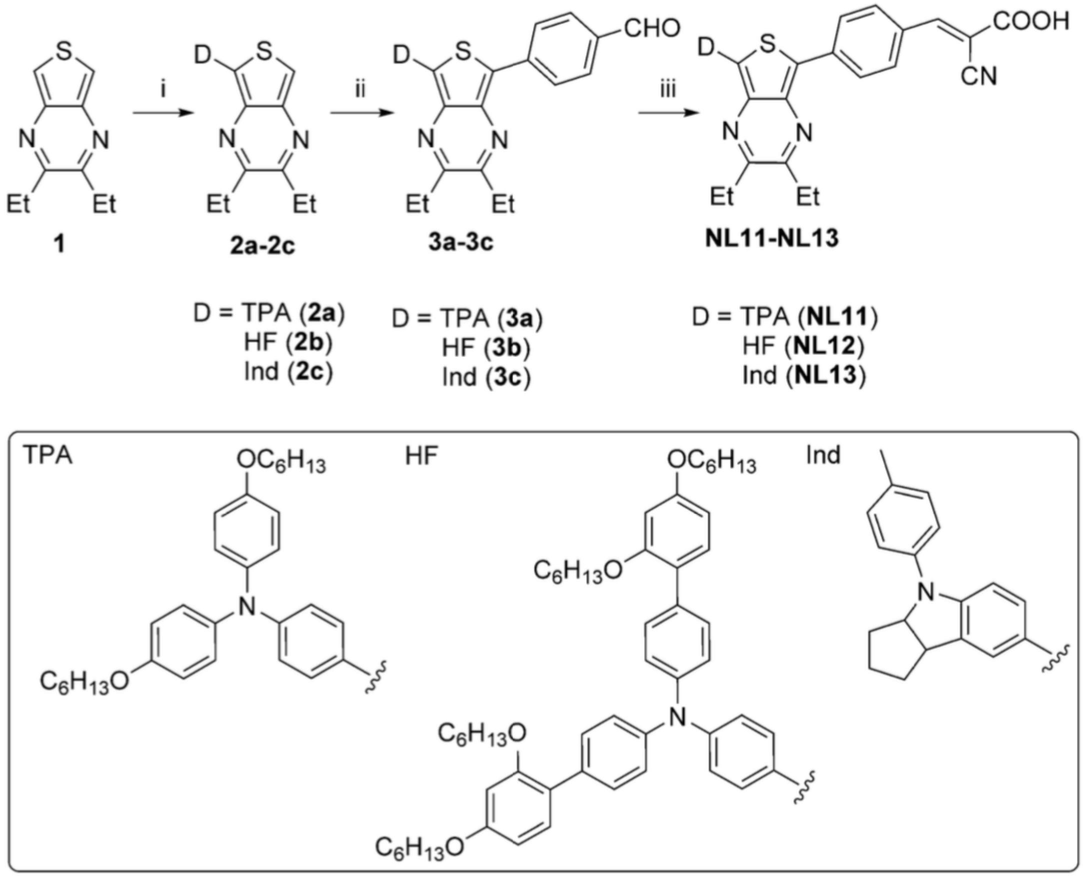

Scheme 1. Synthesis of dyes **NL11**-**NL13**. i) 4-Bromo-N,N-bis(4-hexyloxyphenyl)aniline (TPA-Br, 0.5 equiv., for 2a) or 7-bromo-4-(*p*-tolyl)-1,2,3,3*a*,4,8*b*-hexahydrocyclopenta[*b*]indole (Ind-Br, 0.5 equiv., for 2b) or N-(2’,4’-bis(hexyloxy)-[1,1’-biphenyl]-4-yl)-2’,4’-bis(hexyloxy)-N-(4-iodophenyl)-[1,1’-biphenyl]-4-amine (HF-I, 0.5 equiv., for 2c), X-phos (0.1 equiv.), Cs_2CO_3 (2 equiv.), $Pd(OAc)_2$ (5%), toluene (0.5 M), 120^{O}C, overnight; 61% (2a), 35% (2b), 39% (2c); ii) 4-bromobenzaldehyde (1.2 equiv.), X-phos (0.1 equiv.), Cs_2CO_3 (2 equiv.), $Pd(OAc)_2$ (5%), toluene (0.5 M), 120^{O}C, overnight; 41% (3a), 76% (3b), 50% (3c); iii) cyanoacetic acid (3 equiv.), piperidine (7 equiv.), $CHCl_3$ (0.06 M), 90^{O}C, 1–2 hours ; 85 % (**NL11**), 55 % (**NL12**), 74 % (**NL13**).

RESULTS AND DISCUSSION

The synthesis of **NL11**–**NL13** requires 3 synthetic steps starting from known 2,3-diethyl[3,4-b]thienopyrazine (**1**).[86, 98-99] A Pd-catalyzed C-H activation reaction was performed to couple known halogenated donor building blocks of TPA, Ind, and Hagfedlt's donor (HF) to make compounds 2a–2c in good to moderate yields.[84, 97, 100] Next, a second Pd-catalyzed C-H activation reaction is employed to couple the 4-bromobenzaldehyde to give compounds 3a–3c. Finally, a Knoevenagal condensation reaction furnished the desired dyes **NL11**–**NL13** (Scheme 1).

The electronic properties of the newly synthesized dyes were probed by UV/Vis spectroscopy and cyclic voltammetry to evaluate the effects of dye-substituent tuning. UV/Vis absorption spectra were measured for **NL11**–**NL13** in dichloromethane to find the absorption breadth and optical band gap of the TPz dyes (Figure 13). The **NL11**–**NL13** series shows a broad low-energy charge-transfer band with a significant higher energy band contributing to a panchromatic absorption. The dyes have absorption maxima (λ_{max}) of 565–590 nm and λ_{onset} of 675–715 nm (Figure 13, Table 2).

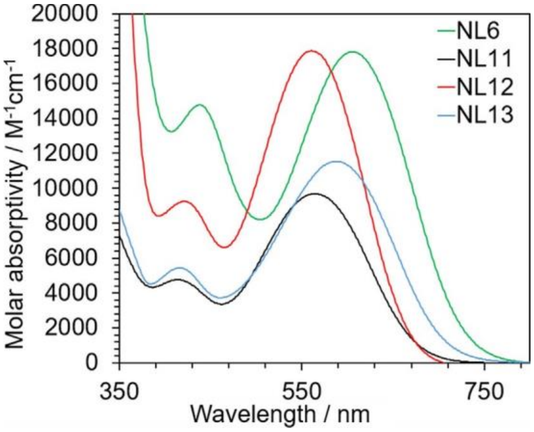

Figure 13. UV/Vis absorption spectra collected for **NL6** and **NL11**–**NL13** dyes in dichloromethane.

This 40 nm shift in absorption spectrum between the dyes highlights the tunability of the TPz-Ph-CAA motif based on increasing donor strength.

The **NL11**–**NL13** dye-absorption properties were compared with the previously examined dye **NL6** (Figure 12). Ideally, the modified dyes should maintain a similar absorption breadth and raise both the ground-state oxidation potential and excited-state oxidation potential in energy. **NL6** differs from **NL11** at the TPz ring substituents (aryl versus alkyl, respectively). **NL11** shows a λ_{max} hypsochromic shift of approximately 40 nm and a decrease in molar absorptivity. The shift in absorption spectrum is likely the result of a decrease in the number of conjugated p-orbitals when the phenyl groups on TPz are removed. This shift in absorption was also apparent at λ_{onset} (**NL6** 730 nm and **NL11** 690 nm). The decrease in molar absorptivity can be addressed through increasing the number of alkyl substituents. Thus, the donor group was changed to a more heavily alkylated donor motif originally set forward by Hagfeldt and co-workers.[97] As desired, **NL12** recovered the lost molar absorptivity of **NL11**, and matches that of **NL6**. No significant change in λ_{max} or λ_{onset} is observed when **NL11** and **NL12** are compared (Figure 13 and Table 2). Since increasing donor strength allows for lower-energy absorption, an indoline donor was evaluated with **NL13** in place of the triphenyl amine donors of **NL11** and **NL12**.[82, 100] **NL13** was the most red shifted dye among the series being evaluated with a bathochromic shift of about 25 nm of both λ_{max} or λ_{onset} when compared with the TPA-based dyes **NL11** and **NL12**.

Table 2. Optical and electrochemical data for **NL11-NL13**.

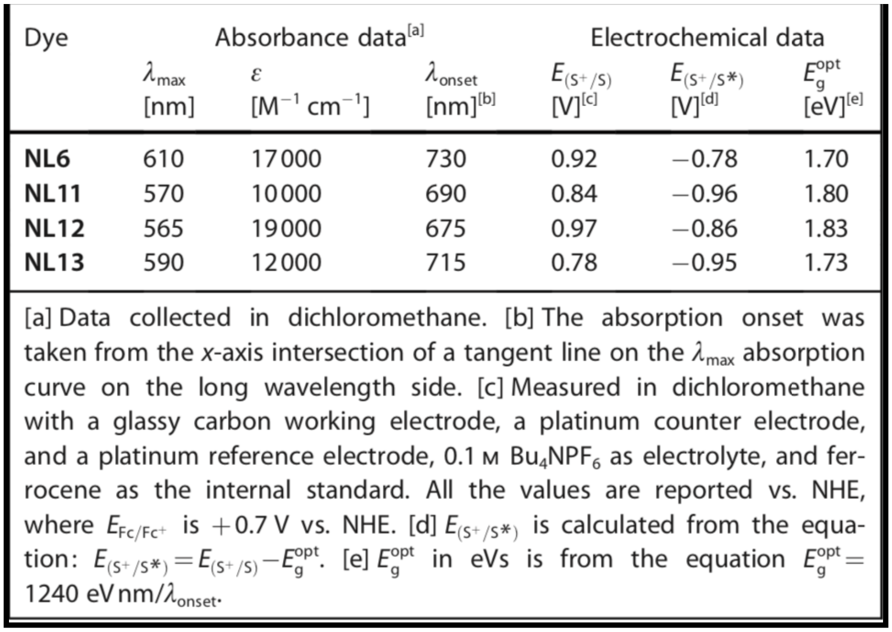

Dye	Absorbance data[a]			Electrochemical data		
	λ_{max} [nm]	ε [M^{-1} cm^{-1}]	λ_{onset} [nm][b]	$E_{(S^+/S)}$ [V][c]	$E_{(S^+/S*)}$ [V][d]	E_g^{opt} [eV][e]
NL6	610	17000	730	0.92	−0.78	1.70
NL11	570	10000	690	0.84	−0.96	1.80
NL12	565	19000	675	0.97	−0.86	1.83
NL13	590	12000	715	0.78	−0.95	1.73

[a] Data collected in dichloromethane. [b] The absorption onset was taken from the *x*-axis intersection of a tangent line on the λ_{max} absorption curve on the long wavelength side. [c] Measured in dichloromethane with a glassy carbon working electrode, a platinum counter electrode, and a platinum reference electrode, 0.1 M Bu_4NPF_6 as electrolyte, and ferrocene as the internal standard. All the values are reported vs. NHE, where E_{Fc/Fc^+} is +0.7 V vs. NHE. [d] $E_{(S^+/S*)}$ is calculated from the equation: $E_{(S^+/S*)} = E_{(S^+/S)} - E_g^{opt}$. [e] E_g^{opt} in eVs is from the equation $E_g^{opt} =$ 1240 eV nm/λ_{onset}.

The electrochemical properties of the dyes **NL11–NL13** were probed with cyclic voltammetry to estimate the ground-state oxidation potential and to derive an estimated excited-state oxidation potential (Table 2, Figure 14). The ground-state oxidation potentials ($E_{(S^+/S^*)}$) were all found to have an energetically favorable driving force for reduction of the dye radical cation after photoinduced electron transfer (ΔG from 430 to reg 620 mV) with the iodide/triiodide redox shuttle (taken as 0.35 V vs. normal hydrogen electrode, NHE). Interestingly, the measured $E_{(S^+/S^*)}$ values were found to vary significantly over a range of nearly 200 mV (0.78–0.97 V vs. NHE, Table 2 and Figure 14) according to the following order from lowest-energy oxidation potential to highest energy : **NL12** (HF) < **NL11** (TPA) < **NL13** (Ind). **NL6** and **NL11** are directly comparable as the only change to dye structure is at the TPz building block, in which the phenyl groups of **NL6** are replaced with alkyl groups on **NL11**. This change resulted in a significant upshift in energy of the ground-state oxidation potential for **NL11** by 80 mV.

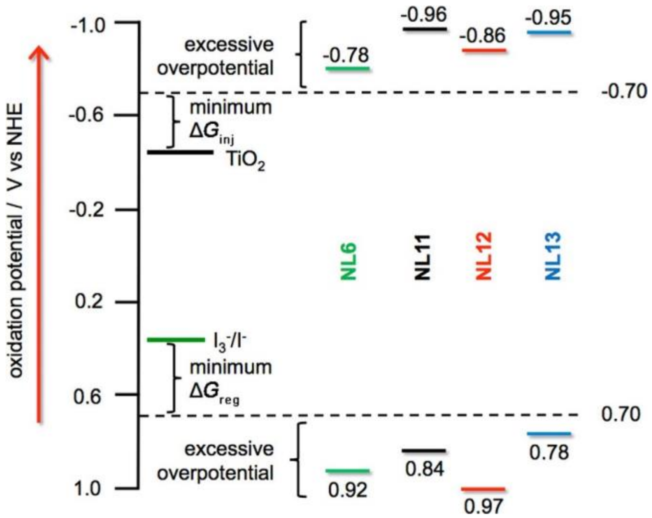

Figure 14. Energy level diagram illustrating the relation of ground-state and excited-state oxidation.

potentials of **NL6**, **NL11**–**NL13** to the TiO_2 CB (-0.50 V) and I^-/I_3^- redox shuttle (0.35 V) potentials. The dotted line represents the ground state (0.70 V) and the excited state (-0.70 V) of an ideal dye with fast, productive electron transfers. All values are indicated vs. NHE.

In addition to a significant driving force for dye regeneration, the excited-state oxidation potential ($E_{(S^+/S^*)}$) of the dye should be positioned favorably for electron injection into the CB of TiO_2. The $E_{(S^+/S^*)}$ values were calculated from the equation: $E_{(S^+/S^*)} = E_{(S^+/S^*)} - E_g^{opt}$, in which $E_{(S^+/S^*)}$ is measured by cyclic voltammetry and E_g^{opt} is measured by UV/Vis absorption spectroscopy. The $E_{(S^+/S^*)}$ values were less strongly affected by the donor group selection (a range of 100 mV versus 200 mV for the ground-state), but the donor group was still found to have a significant influence on the excited-state energy and thus the driving force for electron injection (ΔG_{inj}). ΔG_{inj} was found to range from 360 to 460 mV (Figure 14).[1, 75] Previously, we found **NL6** to have the highest energy excited-state oxidation potential; however, significant Li^+ was still necessary to lower the TiO_2 CB for good current generation. The current series (**NL11**–**NL13**) has taken advantage of careful molecular engineering to raise the excited-state energy level for a larger ΔG_{inj} (-0.78 V versus < -0.86 V). Ideally, this added driving force for electron transfer could lower the amount of Li^+ needed for high photocurrents with these dyes when compared with **NL6**, and allow for higher-voltage devices.

PHOTOVOLTAIC PERFORMANCES

DSC devices were fabricated and measured under AM 1.5G solar simulation after having established **NL11**–**NL13** dyes, TiO_2 semiconductor and I^-/I_3^- or $Co^{+\,3}/Co^{+\,2}$ redox shuttles would have thermodynamically favorable electron transfers. The power conversion efficiency (PCE) was calculated according to the equation : PCE = $J_{SC}V_{OC}FF/I_0$ where, J_{SC} is the short-circuit current, V_{OC} is the open-circuit voltage, FF is the fill factor and I_0 is the intensity of incident light. Devices were prepared containing electrolytes based on I^-/I_3^- with both high (E2, 1.0 M LiI) and low lithium (E1, 0.05 M LiI) loadings (Table 3, Figure 15). Devices with the **NL11**–**NL13** dye series were found to have V_{OC} ranging from 588 to 647 mV, which was a dramatic improvement over the previously studied **NL2**, **NL3**, and **NL6** with V_{OC} of 497–553 mV.[86] For **NL11** and **NL12** the V_{OC}

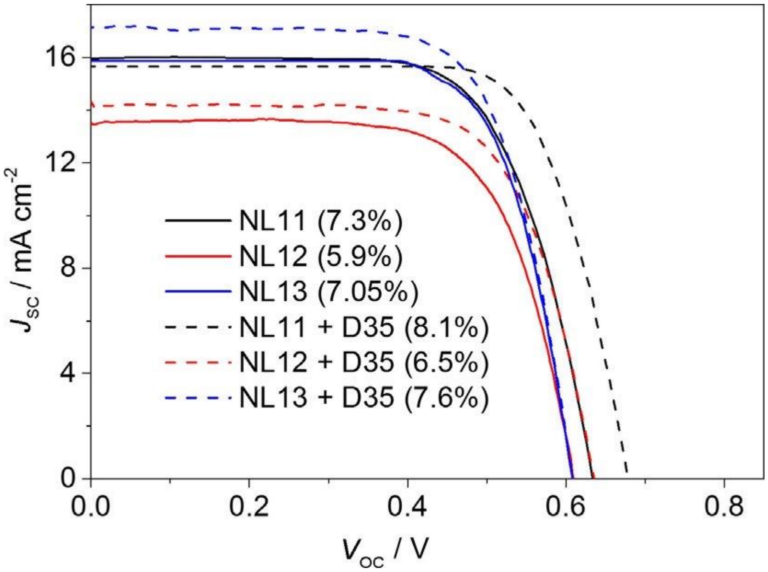

Figure 15. J–V curves for the best iodide devices from Table 3. Solid lines (**NL** dyes). Dashed lines (**NL** dyes+**D35**).

was found to differ only slightly with the high and low lithium content (3 and 20 mV difference, respectively). However, **NL13** was found to differ substantially with a 46 mV higher V_{OC} with lower lithium loading. The former low-energy excited-state series (**NL2**, **NL3**, and **NL6**) were found to give essentially non-functional devices with low lithium loadings. This significant improvement in devices performance is the result of the fine molecular engineering employed in this series design to raise the excited state-energy level. The weaker effect of Li^+ addition to **NL11**- and **NL12**-based cells suggests better surface coverage of the dyes to reduce the amount of Li^+ at the TiO_2 surface. Through dye desorption studies to find the dye loading we found **NL11** > **NL13** > **NL12** with approximately twice the dye loading for **NL11** versus **NL13** and 5x the dye loading for **NL11** versus **NL12** (Table 2 and 16). It should be noted that surface coverage does not depend on dye loading only, but also on the dye-surface footprint.[56, 101]

Table 3. Device parameters for **NL11-NL13**.

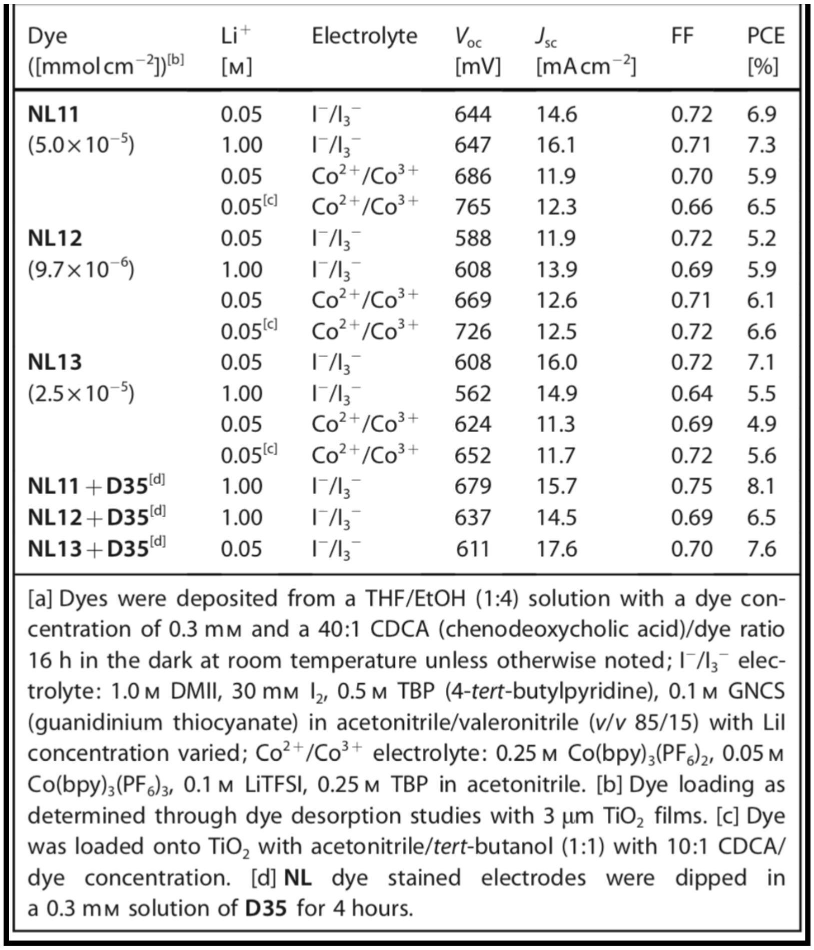

Dye ([mmol cm^{-2}])[b]	Li^{+} [M]	Electrolyte	V_{oc} [mV]	J_{sc} [mA cm^{-2}]	FF	PCE [%]
NL11	0.05	I^-/I_3^-	644	14.6	0.72	6.9
(5.0×10^{-5})	1.00	I^-/I_3^-	647	16.1	0.71	7.3
	0.05	Co^{2+}/Co^{3+}	686	11.9	0.70	5.9
	0.05[c]	Co^{2+}/Co^{3+}	765	12.3	0.66	6.5
NL12	0.05	I^-/I_3^-	588	11.9	0.72	5.2
(9.7×10^{-6})	1.00	I^-/I_3^-	608	13.9	0.69	5.9
	0.05	Co^{2+}/Co^{3+}	669	12.6	0.71	6.1
	0.05[c]	Co^{2+}/Co^{3+}	726	12.5	0.72	6.6
NL13	0.05	I^-/I_3^-	608	16.0	0.72	7.1
(2.5×10^{-5})	1.00	I^-/I_3^-	562	14.9	0.64	5.5
	0.05	Co^{2+}/Co^{3+}	624	11.3	0.69	4.9
	0.05[c]	Co^{2+}/Co^{3+}	652	11.7	0.72	5.6
NL11 + **D35**[d]	1.00	I^-/I_3^-	679	15.7	0.75	8.1
NL12 + **D35**[d]	1.00	I^-/I_3^-	637	14.5	0.69	6.5
NL13 + **D35**[d]	0.05	I^-/I_3^-	611	17.6	0.70	7.6

[a] Dyes were deposited from a THF/EtOH (1:4) solution with a dye concentration of 0.3 mM and a 40:1 CDCA (chenodeoxycholic acid)/dye ratio 16 h in the dark at room temperature unless otherwise noted; I^-/I_3^- electrolyte: 1.0 M DMII, 30 mM I_2, 0.5 M TBP (4-*tert*-butylpyridine), 0.1 M GNCS (guanidinium thiocyanate) in acetonitrile/valeronitrile (*v*/*v* 85/15) with LiI concentration varied; Co^{2+}/Co^{3+} electrolyte: 0.25 M $Co(bpy)_3(PF_6)_2$, 0.05 M $Co(bpy)_3(PF_6)_3$, 0.1 M LiTFSI, 0.25 M TBP in acetonitrile. [b] Dye loading as determined through dye desorption studies with 3 μm TiO_2 films. [c] Dye was loaded onto TiO_2 with acetonitrile/*tert*-butanol (1:1) with 10:1 CDCA/dye concentration. [d] **NL** dye stained electrodes were dipped in a 0.3 mM solution of **D35** for 4 hours.

Specifically, **NL12** is the dye with the lowest loading but the donor group is roughly 2 times larger than that of **NL13** assuming a vertical dye orientation (Figure 59). Taking this into account, the surface foot- print order (**NL11** > **NL12** > **NL13**) is correlated to Li^{+} additive effects with **NL13** devices being the most affected. Small modulation photovoltage transient studies for monitoring electron lifetime in TiO_2 were undertaken to further analyze the degree of surface protection from each dye with variable Li^{+} amounts (Figure 16). The ordering of dye surface protection is confirmed at 1.0 M Li^{+} loadings in which electron lifetime has the following order from longest to shortest: **NL11** > **NL12** > **NL13**. At lower Li^{+} loadings the dyes show **NL11** >>

NL12 ≈ **NL13** with a slightly longer lifetime for **NL13** observed than **NL12**. Device V_{OC} analysis with variable lithium loadings, dye loading studies, and electron lifetime studies agree with **NL11** providing better TiO_2 surface protection than the other dyes in this series and with **NL13** providing the least surface protection.

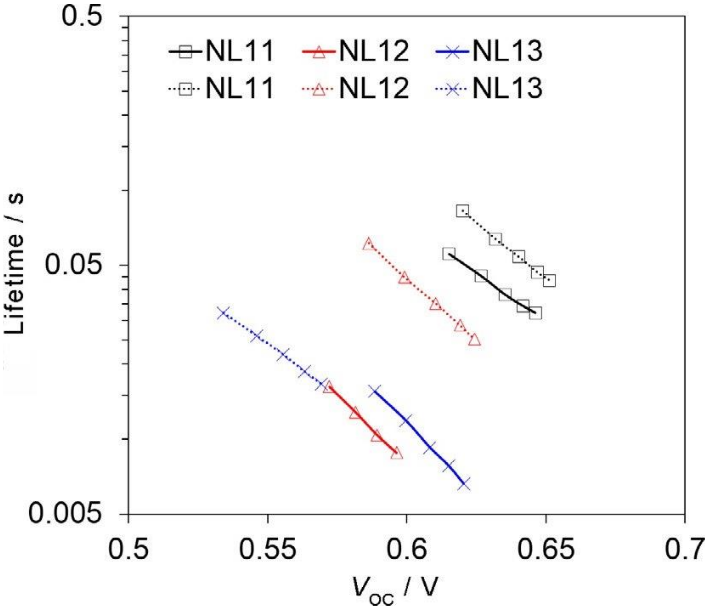

Figure 16. Electron lifetime data measured for devices based on **NL11**–**NL13** with 0.05 M LiI (solid) and 1.00 M LiI (dotted) electrolyte.

Concerning J_{SC} values, the effect of Li^+ loading was most apparent for **NL11** and **NL12** devices based on the observed short-circuit currents increasing by 1.5 and 2.0 mA cm^{-2}, with added Li^+ to 16.1 and 13.9 mA cm^{-2}, respectively. This increase in current is commonly observed with added Li^+ as it lowers the TiO_2 conduction band and increases the driving force for electron transfer, ΔG_{inj} (Figure 12).[102-103] However, this TiO_2 CB shift must be modest as V_{OC} values for these dyes did not change dramatically, and surface protection studies show reasonable surface coverage by these dyes, which limits sites for Li^+ binding (see prior discussion). Added Li^+ had a significantly detrimental effect for both J_{SC} and FF on **NL13** and this has been observed in prior studies in which Li^+ was found to promote dye dissociation from the TiO_2 surface.[104-105] The J_{SC} values were lower for the best devices of each dye than that of the prior published **NL6** (13.9–16.1 mA cm^{-2} versus 17.6 mA cm^{-2}). Incident photon-to-current conversion efficiency (IPCE) measurements were performed on each of these devices to better understand this current loss (Figure 17). Absorption measurements for **NL11**–**NL13** show a blue-shifted absorption onset compared to **NL6**, which is also observed for the IPCE spectrum. The IPCE curve onsets extend toward lower energy light use according to the following series: **NL12** < **NL11** < **NL13** < **NL6** with onset of **NL13** approaching 800 nm, in which **NL6** was observed to onset. This trend is consistent with that observations made by UV/Vis absorption spectroscopy. This shift in IPCE toward higher-energy onsets for the present series was necessary to assure sufficient driving forces for electron transfer for the excited-state of the dye to TiO_2, and thus led to lower-current

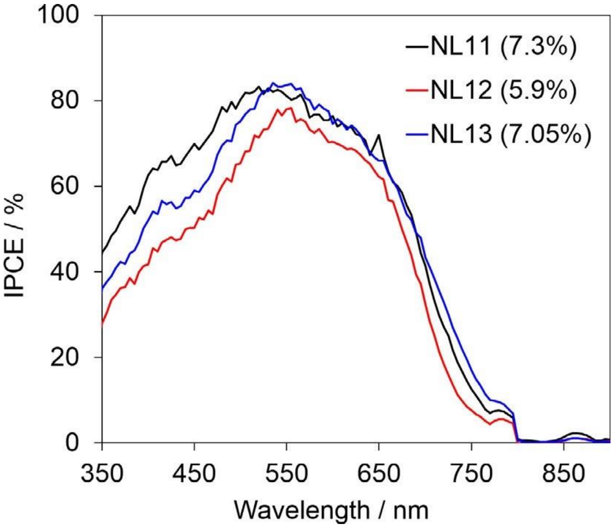

Figure 17. IPCE spectrum for devices made based on the best I^-/I_3^--based devices for **NL11**–**NL13**.

devices. The peak IPCE is similar for **NL11**–**NL13** and **NL6** at approximately 80% for all the dyes indicating the primary source of J_{SC} loss occurs due to a dye blue shifting.

NL11 was found to have the highest PCE of the **NL** series at 7.3 % with performances of 5.9 % for **NL12** and 7.1 % for **NL13**. Increased lithium loadings led to the best performances for **NL11** and **NL13** owing to an enhanced J_{SC} with minimal effect on V_{OC}, whereas **NL13** had the highest performance at low Li^+ concentrations. The PCE values for **NL11** and **NL13** compare favorably to that of **NL6** previously reported at 7.1%. Importantly, **NL11** and **NL13** have PCE values of 6.9 and 7.1% with a low lithium electrolyte, whereas the performance of **NL6** is negligible with low lithium. This retained performance at decreased lithium loadings suggests the dye structure modifications designed to tune the excited-state dye energy level were successful and provided an opportunity for use in cobalt-based electrolyte systems that typically employ lower lithium loadings as the cobalt systems are designed to maximize voltages. Additionally, **NL11** and **NL13** dramatically improved the V_{OC} value over the original dye series reported, and strategically tuned cobalt-electrolyte systems could further enhance these performances.

$Co(bpy)_3(PF_6)_2/Co(bpy)_3(PF_6)_3$ redox-shuttle-based electrolytes were used to evaluate the utility of **NL11**–**NL13** with cobalt redox systems (Table 3, Figures 60, 63, and 64). In each case, the Co^{2+}/Co^{3+} redox shuttles gave higher voltages than the I^-/I_3^--based devices by 20–80 mV when TiO_2 films were prepared from the same solvent. The device V_{OC} dramatically in- creased when films were prepared from MeCN:*t*BuOH dye solutions rather than THF:EtOH with voltages reaching 765 mV for **NL12** (50–140 mV increase compared to I^-/I_3^-).[106] For Co^{3+}/Co^{2+}-based devices, **NL11** showed the longest electron lifetime of the series, which proceeded from longest to shortest electron lifetime according to this order: **NL11** > N**L12** > **NL13** (Figure 63). Bulky donor groups commonly lead to higher device V_{OC} values owing to decreased recombination of electrons in TiO_2 with the redox shuttle through a more complete covering of the surface. However, surface coverage is a balance of dye loading and dye size. Dye loading was found to be much lower for **NL12** compared to **NL11** owing to its bulky size (Table 3). Although a larger donor group with **NL12** is expected to cover a larger surface area per dye, the number of dye molecules has been significantly decreased compared to **NL11**, which shows the highest V_{OC}. **NL11** had comparable PCEs in the optimized Co^{3+}/Co^{2+} -based devices to the I^{-}/I_3^{-} based devices (6.9 versus 6.5%). The gain in voltage for the cobalt-electrolyte devices corresponded with a decrease in current for **NL11** devices. The decrease in current is evident when comparing the IPCE spectrum, in which the diminished IPCE peak height can clearly be observed (80 versus 70%, Figures 17 and 64). We attribute this change to a significantly thinner TiO_2 film being used in the cobalt-based devices, which leads to incomplete light absorption (10 versus 4.5 mm). The current loss was most dramatic for **NL13** and the cobalt-based IPCE reveals significant loss in the high-energy region leading to a PCE of 5.6 versus 7.1% with iodine-based electrolytes. Interestingly, the performance of **NL12** was enhanced with the cobalt redox-shuttle system to 6.6% (a gain of 0.7%) due to a relatively low loss of photocurrent. We attribute this effect to the substantially higher molar absorptivity of **NL12** (19,000 M^{-1} cm^{-2}), which is roughly double that of **NL11** and **NL13**. Molar absorptivities are a very important factor when using thinner film devices.

Devices were prepared with **D35** as a co-sensitizing dye to evaluate the utility of the **NL11**–**NL13** dyes in co-sensitized systems.[22, 56, 107-108] **D35** was chosen because the **NL** series dyes showed diminished IPCE spectrum values in the high-energy region (450 to 550 nm), in which **D35** has a peaking IPCE (Figure 65). The highest preforming iodine-based electrolyte conditions respective to the **NL** dye were used for the co-sensitized devices. In all cases examined the efficiency of the co-sensitized cell exceeded that of the single **NL**-dye device. The increase in performance for **NL12** and **NL13** was owed to increased photocurrent as expected and an increase in photovoltages with PCEs of 6.5 and 7.6%. The PCE of **NL11** co-sensitized with **D35** gave the highest reported efficiency of 8.1% (from 7.3% with **NL11** alone) due to a gain in photovoltage and fill factor. The gain in photovoltage is likely the result of enhanced surface protection by **D35**, which is known to have exceptional surface protection. Electron lifetime studies confirm that in all cases, the electron lifetime is significantly enhanced when **D35** is employed relative to the **NL**-dye only devices (Figure 62).

CONCLUSIONS

Here, we synthesized three thienopyrazine-based dyes with varying donor size and electron donating strengths as well as with tuned π-bridge functionality with respect to prior thienopyrazine-bridged dyes. Through these modifications, enhanced electron-injection efficiencies could be obtained by strategically increasing the excited-state energy of the dyes in this series. Consequently, the increased excited-state oxidation potential energy of **NL11**–**NL13** allowed for the use of the thienopyrazine group for the first time in devices with low Li^+ concentrations, while maintaining electricity production until approximately 800 nm. The use of these dyes in near-infrared (NIR) dye-sensitized solar cell systems is promising based on these results. Dye surface protection was probed through dye desorption studies, computational modeling, device performance metrics, and electron-lifetime studies revealing the medium sized **NL11** dye with a triphenylamine donor had the best surface protection of the series. Combining the high performing **NL11** dye with **D35** into a co-sensitized system gave a 17.6 mA cm^{-1}

photocurrent and a power conversion efficiency (PCE) of 8.1%. Given the demonstrated performance of these dyes with iodine and cobalt redox shuttles, the cooperative devices performance in co-sensitized systems, and one of the highest PCEs for an all-organic NIR dye with an incident photon-to-current conversion efficiency extending to about 800 nm, this series warrants further evaluation in systems designed to minimize the energy loss from excess overpotential for dye regeneration from the redox shuttle.

EXPERIMENTAL SECTION

General information: All commercially obtained reagents were used as received. Thin-layer chromatography (TLC) was conducted with Sorbtech silica XHL TLC plates and visualized with UV light. Flash-column chromatography was performed using Sorbent Tech P60, 40–63 mm (230–400 mesh). ^{1}H NMR spectra were recorded on a Bruker Avance-300 (300 MHz) spectrometer and a Bruker Avance- 500 (500 MHz) spectrometer and are reported in ppm using solvent as an internal standard ($CDCl_3$ at 7.26 ppm). Data reported as s=singlet, d=doublet, t=triplet, q=quartet, p=pentet, m=multiplet, br=broad, ap=apparent, dd=doublet of doublets; coupling constant(s) in Hz; integration. HPLC measurements were taken using an Agilent 1100A HPLC instrument, equipped with an Agilent Eclipse Plus C18 column and UV/Vis detector. 95% isopropanol:5% water was used as the mobile phase for all the measurements. UV spectra were measured with a Cary 5000 UV/Vis-NIR spectrometer with either dichloromethane or a Bu_4NOH/DMF solution (Figures 58). Cyclic voltammetry curves were measured with a C-H Instruments electrochemical analyzer. Measurements were taken using platinum counter electrode, Ag/AgCl reference electrode, and a glassy carbon working electrode. The electrolytic solvent used was 0.1 M Bu_4NPF_6 in dichloromethane. Ferrocene was used as a reference standard, taken as 0.70 V vs. NHE in DCM and oxidation potentials are reported versus normal hydrogen electrode (NHE, Table 2). 2,3-Diethylthieno[3,4-*b*]pyrazine, and 4-bromo-N,N-bis(4-hexyloxyphenyl)aniline (TPA-Br) were prepared according to literature precedent.[98, 109] 7-Bromo-4-(p-tolyl)-1,2,3,3*a*,4,8*b*-hexahydrocyclopenta[*b*]indole (Ind-Br) was prepared according to literature precedent.[110] N-(2',4'-bis(hexyloxy)-[1,1'-bi-phenyl]-4-yl)-2',4'-bis(hexyloxy)-N-(4-iodophenyl)-[1,1'-biphenyl]-4-amine (HF-I) were prepared according to the literature precedent.[13, 111-113] In general, to avoid any potential degradation of intermediates, donor-TPz-H intermediates and donor-TPz-aldehyde intermediates were carried forward immediately after isolation from column chromatography and ^{1}H NMR to verify composition. These intermediates decomposed on silica within a few hours presumably due to oxidation. The decomposition in solution was slower than on silica 5 to 10% per day for donor-TPz-H intermediates. The rate of donor-TPz-aldehyde intermediate decomposition seems slower, however 2D TLC reveals some decomposition. As such, these intermediates were rapidly characterized by ^{1}H NMR after purification and immediately taken forward as a precautionary measure.

4-(2,3-diethylthieno[3,4-b]pyrazin-5-yl)-N,N-bis(4- (hexyloxy)phenyl)aniline (2a)[86]: To a vacuum dried, N_2 filled vial was added **1** (100 mg, 0.52 mmol), 4-bromo-N,N-bis(4-hexyloxyphenyl)aniline (TPA-Br) (136 mg, 0.26 mmol), XPhos (25 mg, 0.052 mmol), Cs_2CO_3 (338 mg, 1.04 mmol), $Pd(OAc)_2$ (6 mg, 0.026 mmol), and anhydrous toluene (1.5 mL). Then the vial was sealed and reaction mixture was stirred at 120^{o}C for 4 hours. Then the reaction mixture was filtered through thin pad of Celite with dichloromethane. The filtrate was concentrated and purified by silica gel chromatography using dichloromethane—>5% ethyl acetate:dichloromethane to give a red colored oil (100 mg, 61%). ^{1}H NMR (300 MHz, $CDCl_3$) δ 8.06 (d, *J* = 8.8 Hz, 2H), 7.57 (s, 1H), 7.09 (d, *J* = 8.9 Hz, 4H), 6.98 (d, *J* = 8.8 Hz, 2H), 6.84 (d, *J* = 8.9 Hz, 4H), 3.94 (t, *J* = 6.6 Hz, 4H), 2.95-2.90 (m, 4H), 1.81-1.77 (m, 4H), 1.48-1.35 (m, 14H), 0.93-0.90 (m, 6H) ppm.

N-(2',4'-bis(hexyloxy)-[1,1'-biphenyl]-4-yl)-N-(4-(2,3- diethylthieno[3,4-b]pyrazin-5-yl)phenyl)-2',4'-bis(hexyloxy)- [1,1'-biphenyl]-4-amine (2b): To a vacuum dried, N_2 filled vial was added **1** (50 mg, 0.26 mmol), N-(2',4'-bis(hexyloxy)-[1,1'-biphenyl]-4-yl)-2',4'-bis(hexyloxy)-N-(4-iodophenyl)-[1,1'-biphenyl]-4-amine (**HF-I**) (120 mg, 0.13 mmol), XPhos (12 mg, 0.026 mmol), Cs_2CO_3 (169 mg, 0.52 mmol), $Pd(OAc)_2$ (3 mg, 0.013 mmol), and anhydrous toluene (1 mL). Then the vial was sealed and reaction mixture was stirred at 120^{o}C 4 hours. Then the reaction mixture was filtered through thin pad of Celite with dichloromethane. The filtrate was concentrated and purified by silica gel chromatography using dichloromethane to give an orange colored oil (47 mg, 35%). ^{1}H NMR (300 MHz, $CDCl_3$) δ 8.16 (d, *J* = 8.6 Hz, 2H), 7.62 (s, 1H), 7.47 (d, *J* = 8.4 Hz, 4H), 7.62-7.19 (m, 8H), 6.55 (d, *J* = 5.9 Hz, 4H), 3.98 (q, *J* = 6.6 Hz, 8H), 2.98-2.90 (m, 4H), 1.83-1.74 (m, 8H), 1.48-1.26 (m, 30H), 0.94- 0.85 (m, 12H) ppm. ^{13}C NMR (125 MHz, $CDCl_3$) δ 159.6, 157.0, 156.9, 155.7, 147.4, 145.6, 143.1, 137.2, 133.3, 133.2, 130.9, 130.2, 128.2, 127.6, 124.0, 123.4, 123.0, 111.7, 105.3, 100.4, 68.4, 68.1, 31.6, 31.5, 29.7, 29.3, 29.1, 28.5, 28.4, 25.9, 25.8, 22.6, 22.6, 14.1, 11.9, 11.4 ppm. IR (neat, cm^{-1}) 2940, 2928, 2862, 1602, 1493, 1467, 1286, 1180, 1134, 8345. HRMS (ESI) m/z calculated for $C_{64}H_{82}N_3O_4S$ ([M+H]$^{+}$) 988.6026, found 988.5945.

2,3-diethyl-5-(4-(p-tolyl)-1,2,3,3a,4,8b-hexahydrocyclopenta[b]indol-7-yl)thieno[3,4-b]pyrazine (2c): To a vacuum dried, N_2 filled vial was added **1** (100 mg, 0.52 mmol), 7-bromo-4-(p-tolyl)-1,2,3,3a,4,8b- hexahydrocyclopenta[b]indole (**Ind-Br)** (85 mg, 0.26 mmol), XPhos (25 mg, 0.052 mmol), Cs_2CO_3 (338 mg, 1.04 mmol), $Pd(OAc)_2$ (6 mg, 0.026 mmol), and anhydrous toluene (1 mL). Then the vial was sealed and reaction mixture was stirred at 120^{o}C 4 hours. Then the reaction mixture was filtered through thin pad of Celite with dichloromethane. The filtrate was concentrated and purified by silica gel chromatography using dichloromethane to give a red colored oil (38 mg, 39%). ^{1}H NMR (500 MHz, $CDCl_3$) δ 8.02 (s, 1H), 7.91 (dd, *J* = 6.8 & 1.5 Hz, 1H), 7.52 (s, 1H), 7.22 (d, *J* = 8.5 Hz, 2H), 7.17 (d, *J* = 9.8 Hz, 2H), 6.97 (d, *J* = 8.4 Hz, 1H), 4.82 (ap t, *J* = 5.8, 1H), 3.90 (ap t, *J* = 7.6 Hz, 1H), 2.98-2.89 (m, 4H), 2.34 (s, 3H), 2.09-2.00 (m, 1H), 1.98-1.93 (m, 1H), 1.84-1.79 (m, 1H), 1.69-1.66 (m, 1H), 1.61-1.57 (m, 2H), 1.44 (t, *J* = 7.3 Hz, 3H), 1.37 (t, *J* = 7.5 Hz, 3H) ppm. ^{13}C NMR (75 MHz, $CDCl_3$) δ 156.8, 155.1, 147.3, 142.9, 140.6, 136.9, 135.3, 134.7, 131.5, 129.8, 127.4, 124.7, 124.2, 120.1, 109.9, 107.6, 69.3, 45.5, 35.0, 33.8, 28.6, 28.3, 24.5, 20.8, 12.0, 11.3 ppm. IR (neat, cm^{-1}) 2959, 2931, 2864, 1603, 1511, 1500, 1453, 1376, 1326, 1267, 1218, 805. HRMS (ESI) m/z calculated for $C_{28}H_{30}N_3S$ ($[M+H]^+$) 440.2160, found 440.2142.

4-(7-(4-(bis(4-(hexyloxy)phenyl)amino)phenyl)-2,3-diethylthieno[3,4-b]pyrazin-5-yl)benzaldehyde (3a): To a vacuum dried, N_2 filled vial was added **2a** (100 mg, 0.16 mmol), 4-bromobenzaldehyde (29 mg, 0.16 mmol), XPhos (8 mg, 0.016 mmol), Cs_2CO_3 (102 mg, 0.31 mmol), $Pd(OAc)_2$ (2 mg, 0.08 mmol), and anhydrous toluene (1 mL). Then the vial was sealed and reaction mixture was stirred at 120°C 4-8 hrs.

Then the reaction mixture was filtered through thin pad of Celite with dichloromethane. The filtrate was concentrated and purified by silica gel chromatography using dichloromethane to give a purple colored oil (30mg, 30%). ^{1}H NMR (300 MHz, $CDCl_3$) δ 9.98 (s, 1H), 8.50 (d, *J* = 8.3 Hz, 2H), 8.12 (d, *J* = 8.9 Hz, 2H), 7.91 (d, *J* = 8.5 Hz, 2H), 7.09 (d, *J* = 8.8 Hz, 4H), 6.97 (d, *J* = 8.2 Hz, 2H), 6.84 (d, *J* = 8.9 Hz, 4H), 2.97-2.92 (m, 4H) ppm. Due to heavy aggregation $NaHCO_3$ (aq) solution was added to the NMR sample to break up the aggregates. The addition of high amounts of $NaHCO_3$ caused some regions of the spectrum to be not clear. ^{13}C NMR was not obtainable. IR (neat, cm^{-1}) 2946, 2926, 2859, 1694, 1595, 1502, 1438, 1317, 1239, 1167, 1023, 827. HRMS (ESI) m/z calculated for $C_{47}H_{53}N_3O_3SCs$ ($[M+Cs]^+$) 872.2862, found 872.2869. Note mass spec ionization is performed in the presence of Cs^+ salts which often allows a Cs^+ adduct to be observed.

4-(7-(4-(bis(2',4'-bis(hexyloxy)-[1,1'-biphenyl]-4-yl)amino)phenyl)-2,3-diethylthieno[3,4-b]pyrazin-5- yl)benzaldehyde (3b): Synthesis is similar to **3a.** The crude product was purified with silica gel column using 10% ethyl acetate:hexane as the eluent to give purple color oil (33 mg, 76%). ^{1}H NMR (300 MHz, $CDCl_3$) δ 10.01 (s, 1H), 8.52 (d, *J* = 8.3 Hz, 2H), 8.23 (d, *J* = 8.8 Hz, 2H), 7.94 (d, *J* = 8.4 Hz, 2H), 7.49 (d, *J* = 8.5 Hz, 4H), 7.29-7.20 (m, 8H), 6.56-6.53 (m, 4H), 4.02-3.95 (m, 8H), 3.00-2.95 (m, 4H), 1.83-1.74 (m, 8H), 1.50-1.26 (m, 30H), 0.93-0.94 (m, 12H). ^{13}C NMR (75 MHz, $CDCl_3$) δ 191.6, 159.7, 157.2, 157.1, 156.0, 148.1, 145.5, 140.8, 140.1, 138.8, 134.2, 133.8, 133,6, 130.9, 130.3, 130.2, 128.5, 127.2, 126.7, 125.7, 124.3, 122.9, 122.8, 105.4, 100.4, 68.4, 68.2, 31.6, 31.5, 29.3, 29.1, 28.4, 28.3, 25.8, 22.6, 22.5, 14.0, 11.2, 11.1 ppm. IR (neat, cm^{-1}) 2955, 2944, 2868, 1733, 1606, 1496, 1463, 1302, 1276, 1175, 1054. HRMS (ESI) m/z calculated for $C_{75}H_{85}N_3O_5SCs$ ($[M+Cs]^+$) 1224.5264, found 1224.5369. Note mass spec ionization is performed in the presence of Cs^+ salts which often allows a Cs^+ adduct to be observed.

4-(2,3-diethyl-7-(4-(p-tolyl)-1,2,3,3a,4,8b-hexahydrocyclopenta[b]indol-7-yl)thieno[3,4-b]pyrazin-5- yl)benzaldehyde (3c): Synthesis is similar to **3a.** The crude product was purified with silica gel column using 10% ethyl acetate: hexane as the eluent to give purple color oil (20 mg, 50%). ^{1}H NMR (300 MHz, $CDCl_3$) δ 10.00 (s, 1H), 8.51 (d, *J* = 8.2 Hz, 2H), 8.11 (s, 1H), 8.02 (d, *J* = 8.1 Hz, 1H), 7.92 (d, *J* = 8.3 Hz, 2H), 7.21 (d, *J* = 6.1 Hz, 2H), 7.17 (d, *J* = 6.0 Hz, 1H), 6.95 (d, *J* = 7.8 Hz, 2H), 4.85 (ap t, *J* = 2.1 Hz, 1H), 3.89 (ap t, *J* = 9.4 Hz, 1H), 2.97-2.95

(m, 4H), 2.35 (s, 3H), 2.11-2.07 (m, 1H), 2.00-1.93 (m, 2H), 1.84-1.78 (m, 1H), 1.71-1.69 (m, 1H), 1.68-1.61 (m, 1H), 1.49-1.44(m, 6H) ppm. ^{13}C NMR (125 MHz, $CDCl_3$) δ 191.6, 157.1, 155.3, 148.4, 140.9, 140.3, 139.9, 138.2, 135.6, 135.5, 133.9, 131.9, 130.2, 129.9, 127.8, 126.9, 124.5, 123.9, 123.6, 120.5, 107.5, 69.3, 45.4, 35.1, 33.7, 28.4, 28.1, 24.4, 20.8, 11.2, 11.0 ppm. IR (neat, cm^{-1}) 2960, 2924, 2855, 1692, 1595, 1513, 1486, 1445, 1377, 1305, 1215, 1168, 811. HRMS (ESI) m/z calculated for $C_{35}H_{33}N_3OS$ (M^+) 543.2344, found 543.2437.

(E)-3-(4-(7-(4-(bis(4-(hexyloxy)phenyl)amino)phenyl)-2,3-diethylthieno[3,4-b]pyrazin-5-yl)phenyl)-2-cyanoacrylic acid (NL11): To a round bottom flask was added **3a** (25 mg, 0.034 mmol) and $CHCl_3$ (4 ml) and the mixture was degassed with N_2 for 30 min. Then cyanoacetic acid (9 mg, 0.10 mmol) and piperidine (0.02 mL, 0.24 mmol) were added into the flask. The flask was sealed and stirred at 90°C for 2 hours. Then acetic acid was added and mixture was extracted with dichloromethane and water. The organic layer was dried over anhydrous Na_2SO_4 and purified through a silica gel plug using 100% dichloromethane —>90% dichloromethane:10% methanol—> 88% dichloromethane:10% methanol:2% acetic acid. Then the dye was again extracted with hexane and water to remove acetic acid and trace silica gel particles. Then the organic layer was dried over anhydrous Na_2SO_4 and concentrated under reduced pressure to give dark blue solid (23 mg, 85%). ^{1}H NMR (300 MHz) δ 8.20 (br), 6.98 (br), 6.86 (br), 3.95 (br), 2.07 (br), 2.04 (br), 1.71 (br), 1.48 (br), 1.41 (br). IR (neat, cm^{-1}) 3373, 2960, 2923, 2855, 1727, 1589, 1503, 1460, 1374, 1240, 1028, 832. UV-Vis (in CH_2Cl_2): λ_{max} = 570 nm (ε = 10,000 $M^{-1}cm^{-1}$), λ_{onset} = 690 nm. HRMS (ESI) m/z calculated for $C_{58}H_{54}N_4O_4S$ [$(M\text{-}H)^-$] 805.3787, found 805.3903. CV (0.1M Bu_4NPF_6 in CH_2Cl_2, sweep width 1.1- (- 0.6), 0.1 Vs^{-1} scan rate) versus NHE: $E_{(S^+/S)}$ = 0.84 V, E_g^{opt} = 1.80 eV, $E_{(S^+/S^*)}$ = -0.96 V [calculated from $E_{(S^+/S^*)} = (E_{(S^+/S)} – E_g^{opt})$]. Note final dye **NL11** is many times heavily alkylated and due to having nitrogen containing functionality and carboxylic acids give peak broadened NMR spectrum in a host of solvents at a host of temperatures, with and without base or acid. As a measure of purity, HPLC analysis for final dyes and copies of HPLC data and ^{1}H NMR files are included below to illustrate the line broadening issue. While we cannot confirm the dye purity definitively by NMR due to the broadening, only the dye related peaks broadens in these spectrum which allows us to see clearly resolved peaks for any non-dye impurities. The purpose of the NMRs in these cases is to observe any impurities, and the HPLC is then used to confirm only one dye is present. **NL11** purity: 98.7 %.

(E)-3-(4-(7-(4-(bis(2',4'-bis(hexyloxy)-[1,1'-biphenyl]-4-yl)amino)phenyl)-2,3-diethylthieno[3,4-b]pyrazin-5- yl)phenyl)-2-cyanoacrylic acid (NL12): Synthesis is similar to **NL11**. Final product is a purple color solid (33 mg, 76%). ^{1}H NMR (300 MHz) δ 8.15 (br), 7.94 (br), 7.44 (br), 7.17 (br), 6.52 (br), 3.94 (br), 1.75 (br), 1.34 (br). IR (neat, cm^{-1}) 2960, 2924, 2855, 1733, 1599, 1492, 1464, 1385, 1287, 1182. UV-Vis (in CH_2Cl_2): λ_{max} = 565 nm (ε = 19,000 $M^{-1}cm^{-1}$), λ_{onset} = 675 nm. HRMS (ESI) m/z calculated for $C_{74}H_{85}N_4O_6S$ ($[M-H]^-$) 1157.6190, found 1157.6637. CV (0.1M Bu_4NPF_6 in CH_2Cl_2, sweep width 1.1- (-0.6), 0.1 Vs^{-1} scan rate) versus NHE: $E_{(s^+/s)}$ = 0.97 V, E_g^{opt} = 1.83 eV, $E_{(s^+/s^*)}$ = -0.86 V [calculated from $E_{(s^+/s^*)} = (E_{(s^+/s)} - E_g^{opt})$]. Note final dye **NL12** is many times heavily alkylated and due to having nitrogen containing functionality and carboxylic acids give peak broadened NMR spectrum in a host of solvents at a host of temperatures, with and without base or acid. As a measure of purity, HPLC analysis for final dyes and copies of HPLC data and ^{1}H NMR files are included below to illustrate the line broadening issue. While we cannot confirm the dye purity definitively by NMR due to the broadening, only the dye related peaks broadens in these spectrum which allows us to see clearly resolved peaks for any non-dye impurities. The purpose of the NMRs in these cases is to observe any impurities, and the HPLC is then used to confirm only one dye is present. **NL12** purity: 98.1 %.

(E)-2-cyano-3-(4-(2,3-diethyl-7-(4-(p-tolyl)-1,2,3,3a,4,8b-hexahydrocyclopenta[b]indol-7-yl)thieno[3,4-b]pyrazin-5-yl)phenyl)acrylic acid (NL13): Synthesis is similar to **NL11**. Final product is a purple color solid (12 mg, 55%). IR (neat, cm^{-1}) 3427, 2956, 2923, 2854, 1733, 1589, 1513, 1486, 1455, 1376, 1261, 1094, 1023, 802. UV-Vis (in CH_2Cl_2): λ_{max} = 590 nm (ε = 12,000 $M^{-1}cm^{-1}$), λ_{onset} = 715 nm. HRMS (ESI) m/z calculated for $C_{38}H_{33}N_4O_2S$ ($[M-H]^-$) 609.2324, found 609.2240. CV (0.1M Bu_4NPF_6 in CH_2Cl_2, sweep width 1.1- (-0.6), 0.1 Vs^{-1} scan rate) versus NHE: $E_{(S^+/S)}$ = 0.78 V, E_g^{opt} = 1.73 eV, $E_{(S^+/S^*)}$ = -0.95 V [calculated from $E_{(S^+/S^*)} = (E_{(S^+/S)} - E_g^{opt})$]. Note final dye **NL13** have nitrogen containing functionality and carboxylic acids give peak broadened NMR spectrum in a host of solvents at a host of temperatures, with and without base or acid. As a measure of purity, HPLC analysis for final dyes and copies of HPLC data and ^1H NMR files are included below to illustrate the line broadening issue. While we cannot confirm the dye purity definitively by NMR due to the broadening, only the dye related peaks broadens in these spectrum which allows us to see clearly resolved peaks for any non-dye impurities. The purpose of the NMRs in these cases is to observe any impurities, and the HPLC is then used to confirm only one dye is present. **NL13** purity: 99.7 %

CHAPTER 4

4.1 NEAR-INFRARED-ABSORBING INDOLIZINE-PORPHYRIN PUSH-PULL DYE FOR DYE-SENSITIZED SOLAR CELLS

Hammad Cheema; **Alexandra Baumann**; E. Kirkbride Loya; Phillip Brogdon; Louis E. McNamara; Casey A. Carpenter; Nathan I. Hammer; Simon Mathew; Chad Risko; Jared H. Delcamp; *ACS Appl. Mater. Interfaces* **2019**, *11*, 16474. Reproduced by permission of The American Chemical Society.

(See appendix for permission license).

This project is a collaborative project between Dr. Delcamp, Dr. Hammer, Dr. Mathew and Dr. Risko's group. Hammad Cheema contributed to this work by fabricating devices and measuring device data for the dyes. Alexandra Baumann contributed to the work by running NMR studies on the dye. E. Kirkbride Loya contributed to the work by performing computational studies of the dyes. Simon Mathew contributed to the work by synthesizing the porphyrin backbone and final porphyrin dyes. Phillip Brogdon and Casey Carpenter contributed to the work by synthesizing the indolizines for the dyes. Louise McNamara contributed to this work by measuring the excited-state lifetime data.

ABSTRACT

Porphyrins are attractive chromophores for application in dye-sensitized solar cells (DSCs), as judicious tuning of donor−acceptor properties can enable excellent near-infrared (NIR) absorption and exceptional device performance. Here, we report a porphyrin-based dye (**SM85**) conjugated to the planar strong electron donor, indolizine, designed to extend absorption further into the NIR region by inducing π−π interactions such as head-to-tail dye aggregation. The optoelectronic consequences of indolizine incorporation in SM85 include raising the ground-state oxidation potential and broadening and red-shifting ultraviolet−visible−NIR absorptions, along with increased molar absorptivity when compared to the dye **SM315**. Density functional theory (DFT) and time-dependent DFT (TD-DFT) calculations confirm the push−pull character of **SM85**, which features an overlap of frontier occupied and unoccupied orbitals. Steady-state spectrophotometric analyses reveal the presence of solution aggregates via absorption and emission spectroscopies. Aggregate modes were probed by DFT and TD-DFT analyses, and plausible models are presented. **SM85**-based DSC devices demonstrate a 5.7% power conversion efficiency (PCE) at full sun (7.4% PCE at 10% sun) with an exceptional improvement to the incident photon-to-current conversion onset at ~850 nm. Current dynamics measurements, time-correlated single photon counting, and computational analyses are used to better understand device performances. This study puts forward a novel intramolecular charge-transfer porphyrin system with a dramatic shift into the NIR region, as is needed for nonprecious metal-based sensitizers, and provides an example of controlled, donor−acceptor-mediated aggregation as a complementary strategy to traditional donor−acceptor modifications to single-molecule π-systems in accessing enhancements in long wavelength light harvesting in molecular-based optoelectronic devices.

INTRODUCTION

Dye-sensitized solar cells (DSCs) have shown dramatic improvements in low-energy photon use with nonprecious metal-based sensitizers since their modern inception.[1, 27, 75, 114-116] n-Type DSCs most commonly operate by (1) photoexcitation of a sensitizer to induce electron injection into TiO_2, (2) regeneration to the neutral dye by reduction of the photogenerated dye cation with a redox shuttle, and (3) collection of the injected electron by the oxidized redox shuttle at the counter electrode after the electron has traversed an external circuit. The sensitizer plays a key role in governing the amount of light that is absorbed by the solar cell device. Further improvements to low-energy photon harvesting can be made by designing sensitizers absorbing light further into the near-infrared (NIR) spectral region.[8, 53, 75, 117] A common strategy to broaden spectral use into the NIR region is through the introduction of strong electron-donating and -withdrawing building blocks to increasingly large π-bridges with extended conjugation to promote stronger low-energy intramolecular charge transfer (ICT) events. This strategy can be synthetically demanding as molecule complexity increases dramatically as the π-system is extended. Alternatively, controlling dye−dye interactions to promote red-shifting through intermolecular interactions within devices can allow for deeper NIR absorption from more readily synthesized dyes.

Porphyrin dyes are some of the deepest NIR-absorbing sensitizers used in DSCs.[21-22, 95, 118-122] Broadening the absorption spectrum of dyes such as **SM315** with a donor functionality is an attractive research direction. For example, porphyrin dyes with solar-to-electric conversion near and beyond 800 nm have been shown using donor groups such as ullazine, N-annulated perylene, and phenothiazine.[123-126] As recognized by these investigations, an exceptionally strongly donating functionality can reduce the optical gap of porphyrin-based sensitizers to absorb further into the NIR region. We envisage that the use of strongly electron donating, planar donor motifs without sterically encumbering alkyl chains will facilitate a π–π stacking interaction with planar, strong electron acceptors such as benzothiadiazole. Thus, we anticipate **SM85** will experience donor–acceptor-mediated aggregation that yields enhancements to NIR light harvesting by a complementary strategy to traditionally investigated increase of donor strength in a D–π–A ensemble (Figure 18).

Indolizine-based donors investigated by our group have shown outstanding properties in reducing the optical energy gap of charge-transfer dyes relative to arylamines.[26, 92-93] This is partially due to the proaromatic nature of indolizine.[92] Proaromatic molecules generate aromatic excited-state structures upon light absorption, which stabilizes the excited state and allows for lower energy photoexcitations. Indolizine is a fully conjugated, fused heterocycle that generates a locally aromatic pyridinium in the excited state after ICT. Excited- state aromaticity reduces the energy needed to access excited states, red-shifting ICT dye absorption curves. Additionally, planarization of a nitrogen atom with a lone pair of electrons and a fully-conjugated donor contribute to significant changes in the ground-state oxidation potential.[92] This exceptionally strong electron donor results in significant red-shifting of ICT absorption curves relative to the commonly employed arylamine donor.[92] Thus, we anticipated that the porphyrin-based sensitizer (**SM85**) featuring a planar, strongly donating indolizine would shift the absorption spectrum further into the NIR region relative to **SM315** because of both the proaromatic nature of indolizine-building blocks and the introduction of π–π interactions of the indolizine-building block with benzothiadiazole (Figure 18). We previously found that the aryl group on the indolizine donor is needed to increase the oxidative stability of the heterocycle during synthesis, and the methyl group on **1** is positioned to block this site from competitive electrophilic aromatic substitution reactions.[92] An alkyne spacer was selected between the porphyrin and the indolizine

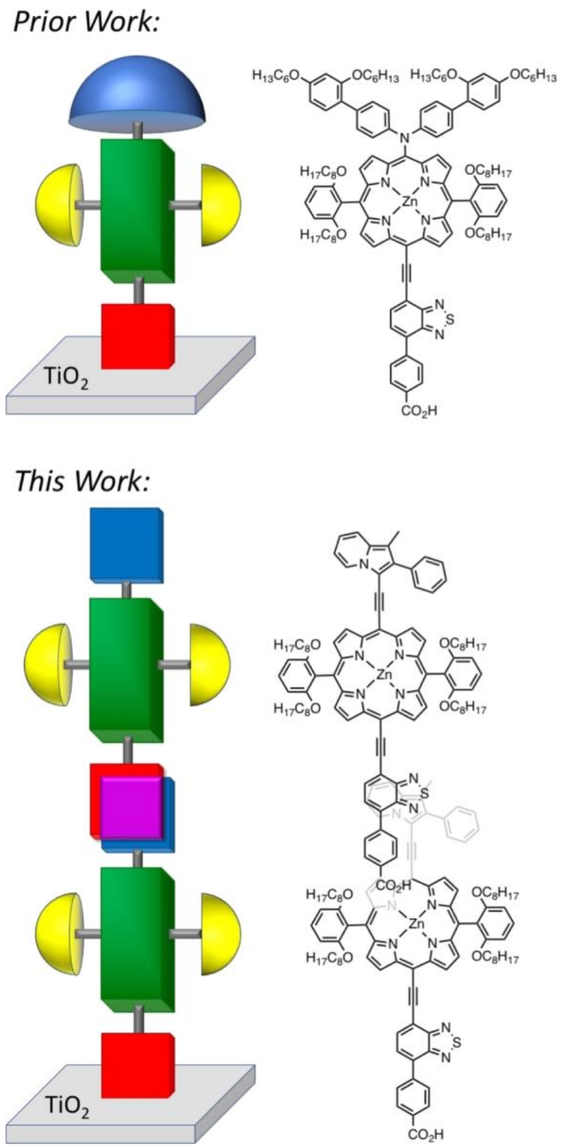

Figure 18. Structures for **SM85** and **SM315** shown as line notation structures and as a cartoon depiction. Typical strategies aim to reduce dye–dye interactions by the use of aggregate diminishing alkylated donors (top). Tailored intermolecular donor–acceptor π–π inter- actions as a method to red shift dye absorption (bottom).

donor to promote greater planarity in the final structure, as the indolizine donor is significantly more sterically encumbered at the desired substitution position compared to aryl amines. All other structural elements were kept constant to allow for a direct comparison of optical and electrochemical properties between **SM85** and **SM315**.

EXPERIMENTAL SECTION

General Synthesis and Characterization Information. All commercially obtained reagents were used as received. Indolizine **1** was synthesized according to the literature (Scheme 2).[92] Porphyrin intermediates **Br-ZnP(OC$_8$)-TIPSA**[22] and **Br-BTD-Ph-CO$_2$Me**[3] were synthesized as previously described. All reactions were carried out under a nitrogen atmosphere, unless otherwise noted. Thin-layer silica gel chromatography (TLC) was conducted with either Sorbent Technologies, Inc. glass-backed 250 μm Silica Gel XHL TLC plates or with Merck KGaA precoated TLC silica gel 60 F_{254} aluminium sheets. Both the TLC plates utilized a UV254 indicator and were visualized with ultraviolet (UV) light. TLC for intermediate **3** was conducted with Uniplate glass-backed 250 μm Alumina GF plates with a UV254 indicator and visualized with UV light. Silica gel flash column chromatography for intermediates **2**, **4**, and **5** was performed with either Sorbent Technologies, Inc. silica gel, porosity 60 Å, 40−63 μm or with SiliaFlash P60 silica gel (Silicycle, 40−63 μm). Purification of intermediate **3** was performed with Agela Technologies neutral alumina gel, porosity 60 Å, 40−60 μm. Nuclear magnetic resonance (NMR) spectra (Figures 104−112) were recorded on a Bruker AMX 400, a Bruker AVANCE-500 (500 MHz), or a Bruker AVANCE-300 (300 MHz) spectrometer and reported in ppm using a solvent as an internal standard ($CDCl_3$ at 7.26 ppm). Peaks are reported as follows: s = singlet, d = doublet, t = triplet, q = quartet, p = pentet/quintet, m = multiplet, and br s = broad-singlet; coupling constant (Hz); integration. Absorbance spectra were measured with a Cary 5000 ultraviolet−visible (UV−vis)−NIR spectrometer or with a Hewlett- Packard 8453 UV−vis spectrophotometer. Cyclic voltammetry (CV) curves were measured with a CH Instruments electrochemical analyzer. Measurements were taken using a platinum counter electrode, an Ag/AgCl or platinum reference electrode with ferrocene as an internal standard, and a glassy carbon working electrode. The electrolytic solvent used was 0.1 M Bu_4NPF_6 in N,N-dimethylformamide (DMF) or tetrahydrofuran (THF). Ferrocene was used as a reference standard, taken as 0.69 V versus normal hydrogen electrode (NHE) in DMF (0.80 V vs NHE in THF), and oxidation potentials are reported versus NHE. Fluorescence emission spectra were recorded on a SPEX Fluorolog 3 fluorometer. Fluorescence lifetime curves were obtained using the 485 nm line of an LDH series 485B pulsed diode laser (pulse width approx. 100 ps) as the excitation source, and emission was detected using a PicoQuant PDM series single photon avalanche diode (time resolution approx. 50 ps) and a TimeHarp 260 time-correlated single photon counter (25 ps resolution). Field desorption mass spectrometry (FD-MS) was performed with an AccuTOF GC v4g, JMS-T100GCV mass spectrometer equipped with an FD Emitter (10 kV, Figures 114 and 115). Attenuated total reflection Fourier transform infrared (ATR−FTIR) spectra of samples were recorded on a Bruker Alpha FTIR spectrometer (Figure 113).

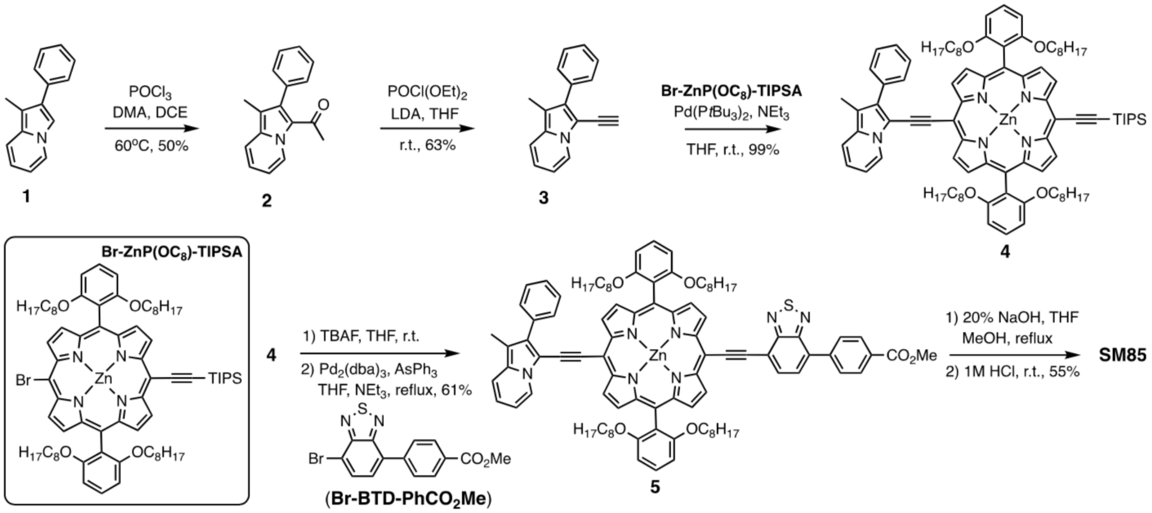

Scheme 2. Synthetic route to SM85

Synthetic Protocols. 2.2.1. 1-(1-Methyl-2-phenylindolizin-3-yl)ethan-1-one (**2**). In a flame-dried flask, $POCl_3$ (3.89 g, 25.4 mmol) and dimethylacetamide (DMA, 2.21 g, 25.4 mmol) were stirred under nitrogen at room temperature in dry dichloroethane (DCE) (30 mL) for 21 h. In a separate flame-dried flask was dissolved **1** (5 g, 24.2 mmol) in dry DCE (30 mL). The indolizine solution was transferred under nitrogen via cannula to the reaction flask containing the $POCl_3$/DMA mixture and heated to 60°C for 27 h. The reaction was cooled to room temperature, and $KOAc_{(aq)}$ (2 M, 60 mL) was added to the mixture. The resulting biphasic mixture was stirred vigorously for 4 h at room temperature. The reaction was then diluted with dichloromethane (DCM) (200 mL), washed with H_2O (2 × 200 mL), and dried with Na_2SO_4. The crude product was then purified via flash chromatography on SiO_2 (solvent gradient 5−50% ethyl acetate in hexanes) to afford a dark colored solid product (3.0 g, 50%) and an unreacted starting material (1.7 g, 34% recovery). ^{1}H NMR (500 MHz, $CDCl_3$): δ 10.02 (d, J = 7.2 Hz, 1H), 7.47 (ap t, J = 1.2 Hz, 3H),7.43(d,J=10.5Hz,1H),7.31(d,J=6.8Hz,2H),7.14(t,J= 6.9 Hz, 1H), 6.85 (t, J = 6.0 Hz, 1H), 2.09 (s, 3H), 1.95 (s, 3H); ^{13}C NMR (125 MHz, $CDCl_3$): δ 187.7, 137.8, 136.6, 135.8, 130.1, 128.8, 128.4, 127.7, 123.4, 120.8, 116.5, 113.6, 111.3, 30.1, 8.9; IR (neat, cm^{-1}): 3124, 3081, 2975, 2919, 2668, 1774, 1626, 1594, 1448, 1389; HRMS m/z: calcd for $C_{62}H_{73}NO_7S_2$ [M + Cs]$^+$, 1140.3883; found, 1140.3894.

2.2.2. 3-Ethynyl-1-methyl-2-phenylindolizine (**3**). In a flame-dried flask, with a stir bar, under nitrogen, diisopropylamine (DIPA, 0.43 g, 0.60 mL, 4.2 mmol, 1.05 equiv) was dissolved in THF (4 mL) and cooled to 0°C. To this solution was added n-butyllithium (2.5 M in hexanes, 1.7 mL, 1.05 equiv) dropwise and stirred for 30 min at 0°C before being cooled to −78°C. 2 (1 g, 4.0 mmol) was dissolved in 1− 2 mL of THF under nitrogen and slowly added via cannula to the lithium diisopropylamide (LDA) solution and stirred for 1 h at −78°C. Diethyl chlorophosphate (0.73 g, 0.77 mL, 4.2 mmol, 1.05 equiv) was added dropwise to the reaction mixture and was allowed to warm to room temperature over 2 h before being cooled back to −78°C. In a separate flame-dried flask, a second portion of LDA was prepared as described above using THF (10 mL) and DIPA (9.0 mmol, 0.91 g, 1.3 mL, 2.25 equiv) followed by n-butyllithium (2.5 M in hexanes, 9.0 mmol, 3.6 mL, 2.25 equiv). This is then cannulated into the reaction mixture at −78°C slowly under a positive nitrogen pressure. The resulting mixture is allowed to warm to room temperature overnight under nitrogen. The reaction was quenched with H_2O and extracted with DCM and H_2O. The crude mixture was flushed through an alumina plug with diethyl ether to yield a dark colored oil (0.58 g, 63%). The product decomposes rapidly on silica and slowly on alumina. ^{1}H NMR (300 MHz, $CDCl_3$): δ 8.24 (d, J = 7.0 Hz, 1H), 7.65 (d, J = 6.9 Hz, 2H), 7.49 (d, J = 7.5, 2H), 7.42−7.34 (m, 2H), 6.81 (t, J = 6.7 Hz, 1H), 6.64 (t, J = 6.9 Hz, 1H), 3.79 (s, 1H), 2.39 (s, 1H); ^{13}C NMR (125 MHz, $CDCl_3$): δ 134.5, 133.4, 132.2, 129.9, 128.3, 127.1, 124.7, 118.4, 117.4, 111.3, 106.7, 103.5, 86.6, 75.4, 9.6; IR cm^{-1}: 3290, 3060, 2920, 2090, 1600, 1520, 1460, 1390, 1250, 1150, 1070, 740, 540; HRMS m/z: calcd for $C_{17}H_{13}N$ $[M + H]^+$, 232.1126; found, 232.1124.

2.2.3. Porphyrin **4**. A solution of alkyne **3** (118 mg, 0.51 mmol, 4.95 equiv) in Et_3N (5.2 mL) was added to a solution of **Br- ZnP(OC_8)-TIPSA** (134 mg, 0.103 mmol) and Pd(t-$Bu_3P)_2$ (0.25 mg, 0.49 μmol, 0.5 mol %) in THF (5.2 mL) at an ambient temperature. The solution was stirred at room temperature for 4 h, and then water (50 mL) and EtOAc (100 mL) were added. The organics were separated, dried (Na_2SO_4), filtered, and evaporated. The reaction mixture was subjected to column chromatography (silica, THF/ hexane, 1:9) to afford the desired product (148 mg, 99%) as a green solid. ^{1}H NMR (400 MHz, $CDCl_3$ + 1 drop C_5D_5N): δ 9.50 (d, J = 4.5 Hz, 2H), 9.41 (d, J = 4.5 Hz, 2H), 8.86 (d, J = 6.8 Hz, 1H), 8.73 (d,J=4.5Hz,2H),8.72(d,J=4.5Hz,2H),8.01(d,J=7.1Hz,2H), 7.71−7.61 (m, 2H), 7.52−7.46 (m, 2H), 6.99 (d, J = 8.5 Hz, 4H), 6.89(t,J=7.6Hz,1H),6.79(t,J=6.4Hz,1H),3.82(t,J=6.6Hz, 8H), 2.51 (s, 3H), 1.41−1.36 (m, 22 H), 0.97−0.88 (m, 8H), 0.86− 0.78 (m, 8H), 0.69−0.60 (m, 8H), 0.57−0.48 (m, 28 H), 0.47−0.39 (m, 8H). ^{13}C NMR (100 MHz $CDCl_3$ + 1 drop C_5D_5N): δ 160.0, 152.3, 150.4, 150.3, 150.1, 135.8, 132.7, 132.6, 131.5, 131.1, 130.4, 130.3, 130.0, 129.4, 128.4, 127.0, 125.5, 125.3, 121.7, 118.0, 117.5, 114.6, 111.4, 111.0, 107.4, 106.5, 105.3, 103.5, 101.0, 98.2, 95.1, 86.9, 68.7, 67.9, 31.1, 28.7, 28.6, 25.2, 22.2, 19.0, 13.8, 11.2, 9.6. FT-IR (neat, ATR, cm^{-1}): 2924, 2857, 2155, 1588, 1454, 1246, 1205, 1097, 1060, 995, 711. HRMS (FD-MS, m/z): $[M]^+$ calcd for $C_{92}H_{115}N_5O_4SiZn$, 1445.8010; observed, 1445.8048.

2.2.4. Porphyrin **5**. Tetra-n-butylammonium fluoride (TBAF) (1 M in THF, 0.293 mL, 0.93 mmol, 2.5 equiv) was added to a solution of porphyrin **4** (170 mg, 0.117 mmol) in THF (11.7

mL), and the resulting solution was stirred at room temperature for 1 h. Water (50 mL) and CH_2Cl_2 (50 mL) were added to the flask, and the organics were extracted further with aliquots of CH_2Cl_2 (2 × 20 mL). The combined organics were dried (Na_2SO_4), filtered, and evaporated. The porphyrinic residue was combined with **Br-BTD-Ph-CO_2Me** (82 mg, 0.235 mmol, 2 equiv), $AsPh_3$ (72 mg, 0.235 mmol, 2 equiv), $Pd_2(dba)_3$ (21.4 mg, 0.0235 mmol, 20 mol %), THF (11.7 mL), and Et_3N (2.3 mL), and the solution was held at reflux for 15 h. The solvents were evaporated, and the reaction mixture was purified by column chromatography (silica, DCM/hexane, 2:1) affording the product (112 mg, 61%) as a brown solid. ^{1}H NMR (400 MHz, $CDCl_3$ + 1 drop C_5D_5N): δ9.86(d,J=4.5Hz,2H),9.42(d,J=4.5Hz, 2H), 8.88, (d, J = 6.8 Hz, 1H), 8.84 (d, J = 4.5 Hz, 2H), 8.73 (d, J = 4.5 Hz, 2H), 8.23 (d, 8.5 Hz, 2H), 8.20 (d, J = 7.4 Hz, 1H), 8.14 (d, J =8.5Hz,2H),8.02(d,J=7.0Hz,2H),7.89(d,J=7.4Hz,1H),7.70 (t, J = 8.5 Hz, 2H), 7.67 (t, J = 7.6 Hz, 2H), 7.54−7.48 (m, 2H, 2 signals), 7.02, (d, J = 8.5 Hz, 4H), 6.88 (t, J = 7.22 Hz, 1H), 6.81 (t, J = 5.9 Hz, 1H), 3.98 (s, 3H), 3.86 (t, J = 6.6 Hz, 8H), 2.51 (s, 3H), 0.99−0.91 (m, 8H), 0.89−0.79 (m, 8H), 0.73−0.65 (m, 8H), 0.61− 0.55 (m, 16H), 0.52−0.43 (m, 8H), 0.50 (t, J = 7.3 Hz, 12H). ^{13}C NMR (100 MHz $CDCl_3$ + 1 drop C_5D_5N): δ 166.9, 159.9, 156.1, 153.2, 152.3, 150.42, 150.41, 150.38, 141.7, 135.6, 135.3, 135.2, 135.1, 132.9, 132.7, 132.0, 131.7, 131.1, 130.6, 130.4, 130.3, 130.2, 129.9, 129.7, 129.5, 129.1, 128.6, 128.5, 127.1, 125.3, 121.5, 118.8, 118.2, 117.5, 115.3, 111.5, 107.5, 106.4, 105.2, 103.6, 103.2, 102.1, 97.5, 91.7, 87.5, 68.7, 52.2, 31.4, 28.72, 28.68, 25.3, 22.3, 13.8, 9.6. FT-IR (neat, ATR, cm^{-1}): 2925, 2854, 2178, 1722, 1588, 1456, 1281, 1246, 1099, 995, 770. HRMS (FD-MS, m/z): $[M]^+$ calcd for $C_{97}H_{103}N_7O_6SZn$, 1557.6982; observed, 1557.7031.

2.2.5. **SM85**. Porphyrin **5** (100 mg, 0.0641 mmol) was dissolved in THF (30 mL), MeOH (30 mL), and $NaOH_{(aq)}$ (20% w/w, 8 mL) and the resulting solution was heated at 40°C for 2 h. After cooling to room temperature, the solution was diluted with Et_2O (100 mL), washed with HCl (1 M, 50 mL) and water (50 mL), dried (Na_2SO_4), filtered, and evaporated. The residue was subjected to column chromatography (silica, CH_2Cl_2 then MeOH/CH_2Cl_2, 1:9) to afford **SM85** (55 mg, 55%) as a brown solid. ^{1}H NMR (400 MHz, $CDCl_3$ + 1 drop C_5D_5N): δ 9.86 (d, J = 4.4 Hz, 2H), 9.41 (d, J = 4.4 Hz, 2H), 8.87(d,J=6.9Hz,1H),8.83(d,J=4.4Hz,2H),8.72(d,J=4.4Hz, 2H),8.33(d,J=7.4Hz,2H),8.20(d,J=7.1Hz,1H),8.15(d,J= 7.4 Hz, 2H), 8.01 (d, J = 8.0 Hz, 2H), 7.90 (d, J = 7.1 Hz, 1H), 7.69 (t, J = 8.4 Hz, 2H), 7.68−7.60 (m, 2H), 7.50 (t, J = 8.6 Hz, 2H), 7.01 (d, J = 8.4 Hz, 4H), 6.87 (t, J = 7.58 Hz, 1H), 6.80 (t, J = 6.9 Hz, 1H), 3.85 (t, J = 6.3 Hz, 8H), 2.50 (s, 3H), 0.98−0.89 (m, 8H), 0.88−0.79 (m, 8H), 0.72−0.63 (m, 8H), 0.60−0.53 (m, 16H), 0.52−0.41 (m, 8H), 0.49 (t, J = 7.3 Hz, 12H). ^{13}C NMR (100 MHz $CDCl_3$ + 1 drop C_5D_5N): 169.0, 160.0, 156.1, 153.3, 152.3, 150.41, 150.39, 150.34, 141.1, 132.9, 132.7, 132.2, 132.1, 131.9, 131.4, 131.1, 130.7, 130.4, 130.3, 130.1, 129.7, 129.5, 129.3, 128.9, 128.5, 128.4, 127.1, 125.3, 121.5, 118.5, 118.1, 117.6, 115.3, 111.4, 107.5, 106.4, 105.2, 103.6, 102.9, 101.9, 97.7, 97.1, 91.7, 87.4, 68.6, 31.4, 28.7, 28.6, 25.2, 22.2, 13.7, 9.6. FT-IR (neat, ATR, cm^{-1}): 2926, 2854, 2360, 2170, 1724, 1692, 1587, 1456, 1244, 1096, 996, 795, 769. HRMS (FD-MS, m/z): $[M]^+$ calcd for $C_{96}H_{101}N_7O_6SZn$ calculated 1543.6825, observed 1543.6987.

2.3. DSC Device Fabrication Procedure. For the photoanode, TEC 10 glass was purchased from Hartford Glass. Once cut into squares of dimensions 2 × 2 cm^2, the substrate was submerged in a 0.2% deconex 21 aqueous solution and sonicated for 15 min at room temperature. The electrodes were rinsed with water and sonicated in acetone for 10 min, followed by sonication in ethanol for

10 min. Finally, the electrodes were placed under UV/ozone for 15 min (UV− Ozone Cleaning System, Model ProCleaner by UVFAB Systems). A compact TiO_2 underlayer is then applied by pretreatment of the substrate submerged in a 40 mM $TiCl_4$ solution in water (prepared from 99.9% $TiCl_4$ between 0 and 5°C). The submerged substrates (conductive side up) were heated for 30 min at 70°C. After heating, the substrates were rinsed first with water and then with ethanol. The photoanode consists of thin TiO_2 electrodes comprised of a 10 μm mesoporous TiO_2 layer (particle size, 20 nm, Dyesol, DSL 18NR-T). All photoanodes had a 5.0 μm TiO_2 scattering layer (particle size, >100 nm, Solaronix R/SP). All layers were screen printed from a Sefar screen (54/137-64W). Between each print, the substrate was heated for 7 min at 125°C, and the thickness was measured with a profilometer (Alpha-Step D-500 KLA Tencor). After all layers were deposited, the substrate was then sintered with progressive heating from 125°C (5 min ramp from room temperature, 5 min hold) to 325°C (15 min ramp from 125°C, 5 min hold) to 375°C (5 min ramp from 325°C, 5 min hold) to 450°C (5 min ramp from 375°C, 15 min hold) to 500°C (5 min ramp from 450°C, 15 min hold) using a programmable furnace (Vulcan 3-Series model 3-550). The cooled sintered photoanode was soaked for 30 min at 70°C in 40 mM $TiCl_4$ in water solution. The photoanode was rinsed sequentially with water and then ethanol and heated again at 500°C for 30 min prior to sensitization. The complete working electrode was prepared by immersing the TiO_2 film into the dye solution. The solution was 0.15 mM of dye in different solvent mixtures (Table 7). The dye/chenodeoxycholic acid (CDCA) molar ratio was changed accordingly as given in Table 7. For preparing counter electrodes, squares of dimensions 2 × 2 cm^2 of TEC 7 FTO glasses were drilled using Dremel-4000 with Dremel 7134 Diamond Taper Point Bit from the taped fluorine-doped tin oxide (FTO) side. The electrodes were washed with water, followed by 0.1 M HCl in EtOH wash and sonication in acetone bath for 10 min. The

washed FTO electrodes were then dried at 400°C for 15 min. A thin layer of Pt paste (Solaronix, Platisol T/SP) was slot printed on the FTO, and the printed electrodes were then cured at 450°C for 10 min. After allowing them to cool to room temperature, the working electrodes were then sealed with a 25 μm-thick hot melt film (Surlyn, Solaronix, “Meltonix 1170-25”) by heating the system at 130°C under 0.2 psi pressure for 1 min. Devices were completed by filling the electrolyte by predrilled holes in the counter electrodes, and finally, the holes were sealed with a Surlyn precut circle and a thin glass cover by heating at 130°C under pressure 0.1 psi for 25 s. Finally, the soldered contacts were added to a MBR Ultrasonic soldering machine (model USS-9210) with a solder alloy (Cerasolzer wire diameter 1.6 mm item # CS186-150). A circular black mask (active area 0.15 cm^2) punched from a black tape was used in the subsequent photovoltaic studies.

2.4. Photovoltaic Measurements. 2.4.1. Current−Voltage Curves. Photovoltaic characteristics were measured using a 150 W Xenon lamp (model SF150B, Sciencetech Inc. Class ABA) solar simulator equipped with an AM 1.5G filter for less than 2% spectral mismatch. Prior to each measurement, the solar simulator output was calibrated with a KG5 filtered monocrystalline silicon NREL- calibrated reference cell from ABET Technologies (model 15150- KG5). The photocurrent density−voltage characteristic of each cell was obtained with a Keithley digital source meter (model 2400).

2.4.2. Incident Photon-to-Current Conversion Efficiency Curves. The incident photon-to-current conversion efficiency (IPCE) was measured with an IPCE instrument manufactured by Dyenamo comprised of a 175 W Xenon lamp (CERMAX, model LX175F), a monochromator (Spectral Products, model CM110, Czerny-Turner, dual-grating), a filter wheel [Spectral Products, model

AB301T, fitted with filter AB3044 (440 nm high pass), filter AB3051 (510 nm high pass)], a calibrated UV-enhanced silicon photodiode reference, and Dyenamo issued software.

2.4.3. Current Dynamic Measurements. Photocurrent transient measurements made at varying light intensities were performed with the same current−voltage curve-generating light source and source meter in combination with an electronically controlled shutter (UNIBLITZ model# VMM-D1), an electronically controlled filter wheel (Thorlabs FW102C), and custom-written LabView Software to simultaneously control all components. The 6-position filter wheel was loaded with neutral density filters from Thorlabs allowing 100, 79, 50, 32, and 10% intensities of light to pass.

2.4.4. Electrochemical Impedance Spectroscopy. Electrochemical impedance spectroscopy (EIS) was measured in the dark with a bias at open-circuit voltages measured during illumination using an impedance analyzer CHI6054E potentiostat (CH Instruments). The spectra were scanned in a frequency range of 10^{-1} to 10^{5} Hz at room temperature. The alternating current amplitude was set at 10 mV.

RESULTS AND DISCUSSION

The synthesis of **SM85** began with the Vilsmeier−Haack reaction of indolizine (**1**) with N,N-dimethylacetamide to give ketone **2** in 50% yield (Scheme 2). Alkyne **3** was formed in a single step from **2** via a phosphonate ester intermediate, which undergoes a Wittig-type elimination to give **3** in 63% yield. Sonogashira coupling of indolizine **3** and **Br-ZnP(OC$_8$)-TIPSA**[22] gave the triisopropylsilyl (TIPS)-protected donor-π bridge **4** in a quantitative yield. The porphyrin alkyne **4** was deprotected with TBAF, and the terminal porphyrin alkyne was carried forward directly after extraction. Sonogashira coupling of the

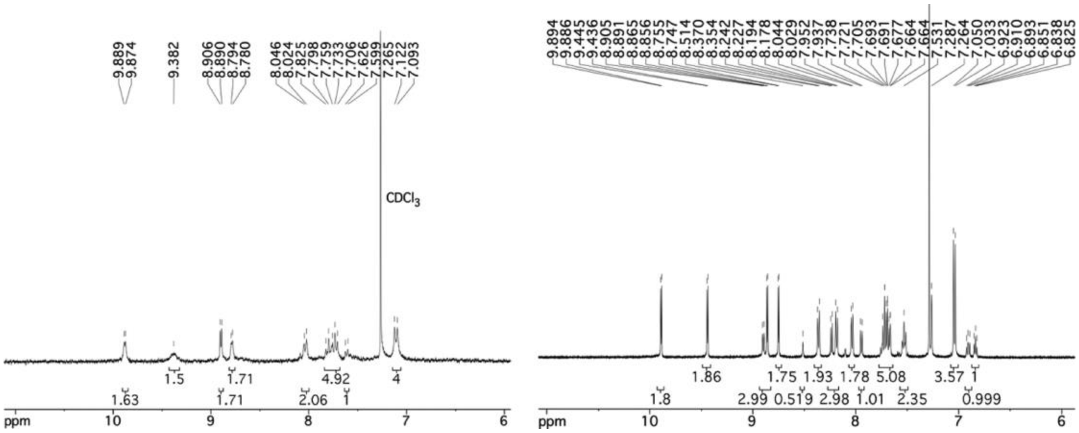

Figure 19. ^{1}H NMR spectrum of **SM85** in CDCl$_3$ (left) and in CDCl$_3$ + 1 drop of d_5-pyridine added (right), zoomed in on the aromatic region.

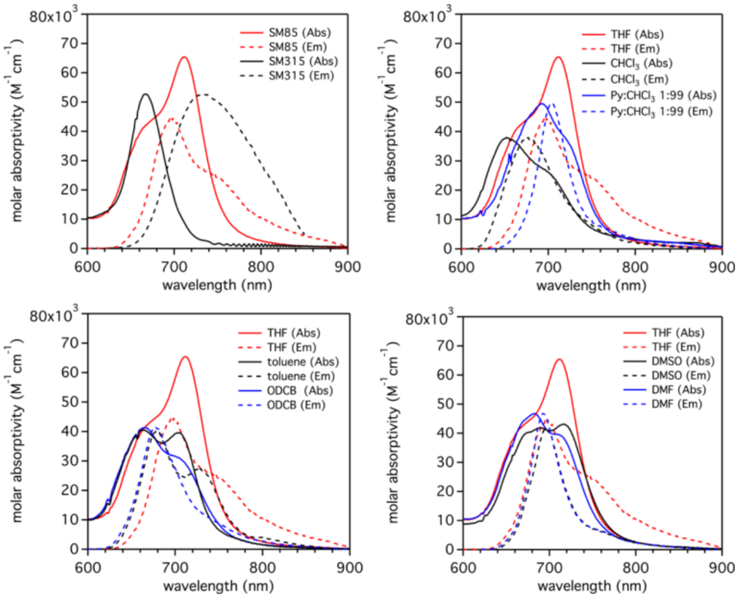

Figure 20. UV−vis absorption and emission of **SM315** and **SM85** in THF (top left), **SM85** in CHCl$_3$ with and without pyridine (top right), where coordinated pyridine to the zinc porphyrin affords a red shift in absorbance, **SM85** in toluene, ODCB, and THF (bottom left), and **SM85** in THF, DMF, and DMSO (bottom right), all at 2.6 × 10^{-6} M. See the Supporting Information for the full spectral range and a varying concentration study.

deprotected porphyrin alkyne and **Br-BTD-PhCO$_2$Me**[3] gave ester **5**, which was hydrolyzed to give the final dye, **SM85**, in 75% yield.

The ^{1}H NMR spectrum of **SM85** shows substantial aggregation in pure CDCl$_3$ (Figure 19), with significantly fewer signals observed than proton resonances expected for SM85. Although β-pyrrolic resonances from the porphyrin core are evident, those pertaining to benzothiadiazole and indolizine (two resonances at <7 ppm) are obscured or unobserved with approximately 20 of the 29 aromatic hydrogens accounted for in the ^{1}H NMR spectrum of **SM85**. Several resonances are notably broadened in the aromatic region, with signals such as δ = 9.38 ppm showing substantial broadening. Interestingly, addition of a single drop of *d*$_5$-pyridine to the NMR sample instantly afforded a well-resolved spectrum, and all 29 hydrogens were accounted. The diagnostic indolizine peaks at approximately 6.91 and 6.84 ppm are clearly resolved, along with the benzothiadiazole peaks assigned as 7.94 and as a part of the group of signals at 7.70 ppm. The missing resonances in the spectrum without *d*$_5$-pyridine are likely due to a significant aggregation phenomenon. This aggregation is unlikely to involve aromatic stacking

Table 4. Summary of Optical and Electrochemical Data for **SM85**[a]

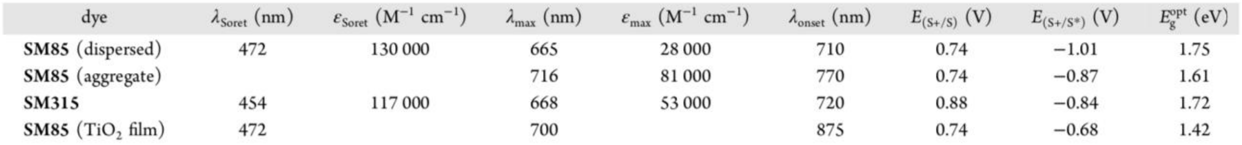

dye	λ_{Soret} (nm)	$\varepsilon_{\text{Soret}}$ (M^{-1} cm^{-1})	$\lambda_{\max}$ (nm)	$\varepsilon_{\max}$ (M^{-1} cm^{-1})	λ_{onset} (nm)	$E_{(S+/S)}$ (V)	$E_{(S+/S*)}$ (V)	E_g^{opt} (eV)
SM85 (dispersed)	472	130 000	665	28 000	710	0.74	−1.01	1.75
SM85 (aggregate)			716	81 000	770	0.74	−0.87	1.61
SM315	454	117 000	668	53 000	720	0.88	−0.84	1.72
SM85 (TiO$_2$ film)	472		700		875	0.74	−0.68	1.42

[a] Optical data is measured in THF or on TiO$_2$ films; electrochemical data above is reported in DMF for comparison to literature. E_g^{opt} was estimated from the onset of the absorption curve. Conversion from nanometers to eV was calculated by $E_g^{opt} = 1240/\lambda_{\text{onset}}$. **SM315** data is from a prior report.[3] The $E_{(S^+/S^*)}$ value for **SM315** is estimated from the absorption spectrum tangent line on the lower energy slide similar to **SM85**. We note that this value differs from the reduction potential value obtained by CV previously reported.

interactions between porphyrin cores as H-aggregates because the porphyrin core is sterically shielded from the porphyrin−porphyrin interaction by the *meso*-(2,6-dioctyloxy)phenyl groups, which is well-described and utilized ubiquitously in the porphyrin dye design.[127-128] Acid−base interaction between the nitrogen lone pair of the donor and the proton of the carboxylic anchor is a likely cause of the poorly resolved spectrum in $CDCl_3$, given the issue is resolved upon the addition of the pyridine base. The acid−base interaction may also preorganize dyes to facilitate aromatic stacking inter- actions between the indolizine donor and the benzothiadiazole acceptor leading to a head-to-tail-oriented linear aggregate. This type of aggregation in $CDCl_3$ solution is consistent with the observation of resolved porphyrin resonances with poorly resolved signals from the donor and acceptor moieties. Therefore, determination of the aggregation modes of **SM85** warranted a spectrophotometric investigation with a complementary computational study to probe possible aggregation modes (vide infra).

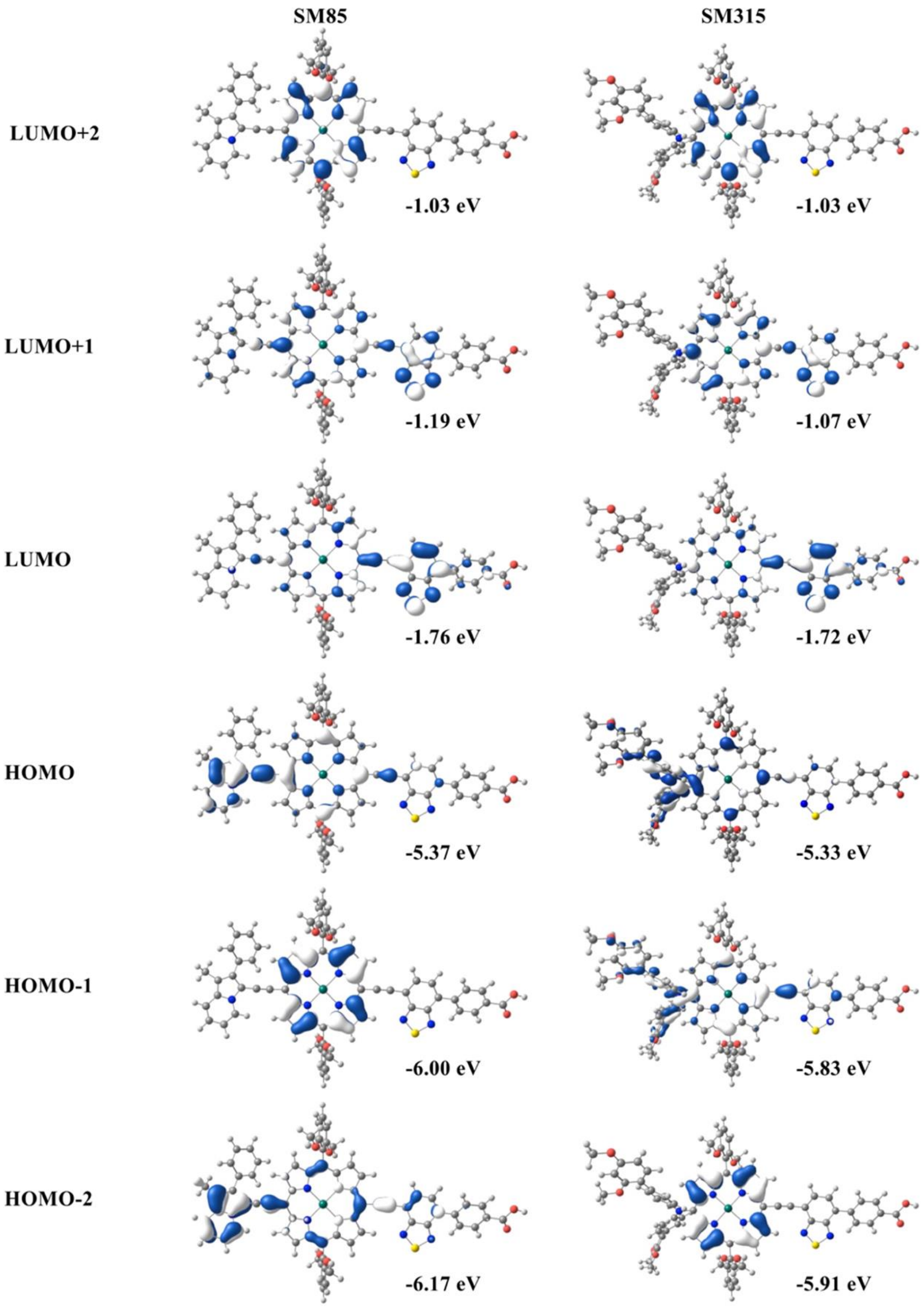

Figure 21. Pictorial representations of select frontier molecular orbitals of SM85 (left) and SM315 (right) as determined at the OT-LC-ωPBE/6- 31G(d,p) level of theory. Extended alkoxy chains are truncated to methoxy groups. Isovalues are set to 0.03 Å^{-3}.

Table 5. Select One-Electron Vertical Transition Energies (E), Wavelengths (λ), Oscillator Strengths (f), and Electronic Configurations for **SM85** and **SM315** as Determined via TD-DFT Calculations at the OT-LC-ωPBE/6-31G(d,p) Level Of Theory[a]

dye	transition	*E* (eV)	*λ* (nm)	*f*	electronic configuration
SM85	$S_0 \rightarrow S_1$	1.80	688	1.21	HOMO − 2 → LUMO (5%) HOMO − 1 → LUMO + 2 (6%) HOMO → LUMO (75%) HOMO → LUMO + 1 (10%)
	$S_0 \rightarrow S_5$	2.62	474	0.28	HOMO − 2 → LUMO (41%) HOMO − 2 → LUMO + 1 (19%) HOMO − 1 → LUMO + 2 (22%) HOMO → LUMO (6%)
SM315	$S_0 \rightarrow S_1$	1.80	686	0.76	HOMO − 2 → LUMO + 2 (6%) HOMO − 1 → LUMO (8%) HOMO → LUMO (63%) HOMO → LUMO + 1 (18%)
	$S_0 \rightarrow S_3$	2.21	562	0.15	HOMO − 5 → LUMO (4%) HOMO − 1 → LUMO (49%) HOMO → LUMO + 1 (35%) HOMO → LUMO + 4 (2%)

[a] Transitions with oscillator strengths greater than 0.1 are reported.

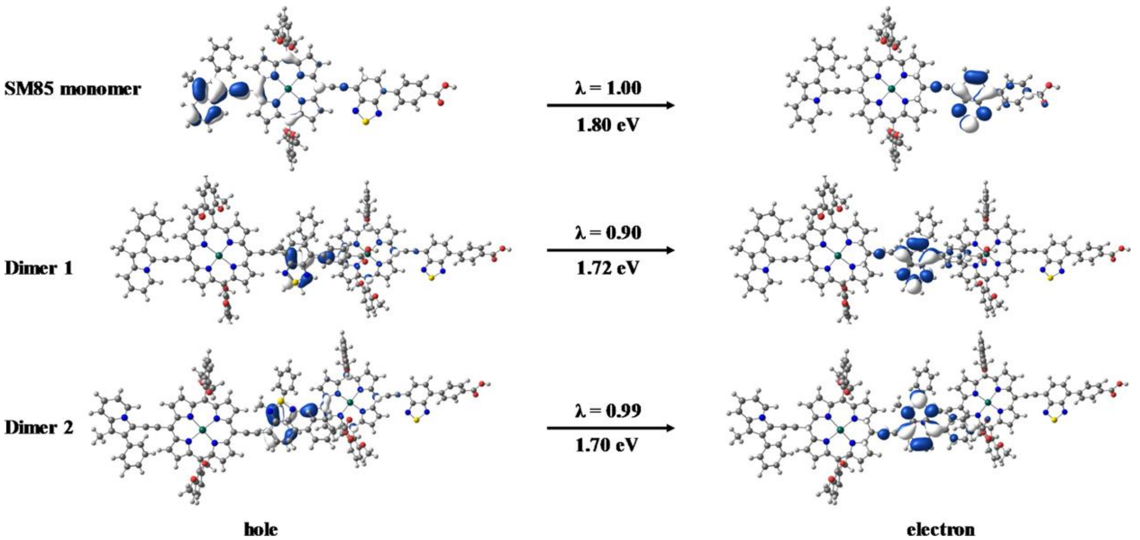

Figure 22. $S_0 \rightarrow S_1$ NTO for the **SM85** monomer and two dimers as determined via TD-DFT calculations at the OT-LC-ωPBE/6-31G(d,p) level of theory. In each instance, the lowest energy transition is primarily a transition from the indolizine donor to the benzothiadiazole acceptor and is intermolecular in the case of the dimers.

With **SM85** in hand, optical and electrochemical properties were analyzed through UV−vis−NIR absorption spectroscopy and CV measurements to quantify the effect of indolizine as a donor on the ground-state oxidation potential ($E_{(S^+/S)}$), excited-state oxidation potential ($E_{(S^+/S^*)}$), and the optical gap (E_g^{opt}) values. Initially, optical data was acquired in THF to allow for comparison to prior literature.[3] The absorption maximum (λ_{max}, Q-band) of **SM85** in THF reveals a significant red shift of 48 nm (0.12 eV) further into the NIR region relative to **SM315** (716 nm versus 668 nm, respectively, Figure 20, Table 4). The red shift is in part attributed to the stronger electron-donating strength of indolizine, relative to the arylamine of **SM315**. In line with the red-shifted absorption, the molar absorptivity (ε) at λ_{max} is substantially higher for **SM85** relative to **SM315** (81,000 M^{-1} cm^{-1} vs 53,000 M^{-1} cm^{-1}, respectively). The increased molar absorptivity demonstrates the utility of the indolizine group in promoting ICT. However, this lowest energy Q-band of **SM85** features a shoulder at 650 nm. The shoulder is unexpected as this absorption is known to originate from light-induced polarization along the donor−acceptor axis in the same manner as **SM315** yielding a single absorption. In a similar manner, the emission spectrum of **SM85** in THF affords a maximum with a shoulder and extensive charge-transfer tailing.

Standard normalization of absorption and emission spectra affords the lowest energy absorption maximum occurring after the highest energy emission. Anti-Stokes behavior is very unlikely. More likely, the presence of different emissive species arising from aggregation can explain the absorption and emission curve behaviors of **SM85**. The evolution of lower energy absorption than the first emission feature can be rationalized via the formation of head-to-tail J-aggregates along with emission from the monodispersed dye.

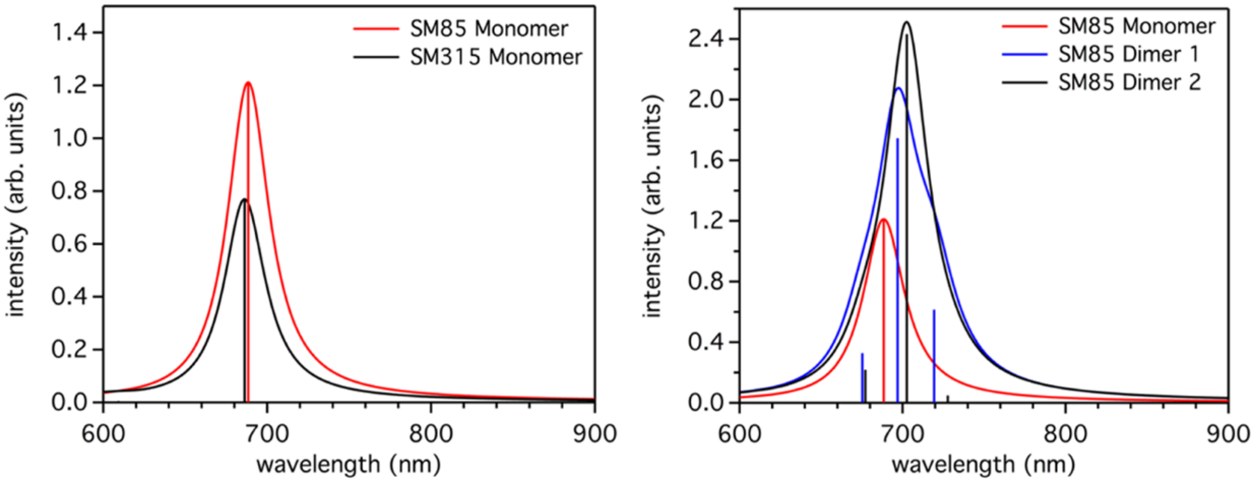

Figure 23. Simulated spectra of **SM85** and **SM315** (left) and simulated spectra of **SM85** and two dimers (right) as determined via TD-DFT calculations at the OT-LC-ωPBE/6-31G(d,p) level of theory (see Figure S6 for the full simulated spectrum from 350 to 900 nm). The bars indicate the vertical transitions from which the simulated spectra are generated by application of Lorentzian broadening with full-width at half-maximum (FWHM) of 0.0807 eV.

Table 6. Select One-Electron Vertical Transition Energies (E), Wavelengths (λ), Oscillator Strengths (f), and NTO Electronic Configurations for SM85 Dimers as Determined via TD-DFT Calculations at the OT-LC-ωPBE/6-31G(d,p) Level Of Theory[a]

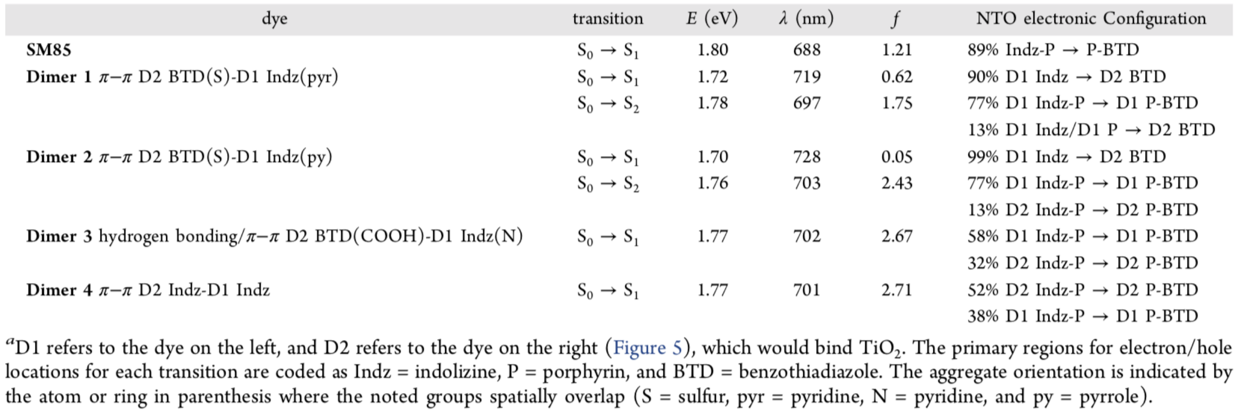

dye	transition	*E* (eV)	*λ* (nm)	*f*	NTO electronic Configuration
SM85	$S_0 \rightarrow S_1$	1.80	688	1.21	89% Indz-P → P-BTD
Dimer 1 *π*–*π* D2 BTD(S)-D1 Indz(pyr)	$S_0 \rightarrow S_1$	1.72	719	0.62	90% D1 Indz → D2 BTD
	$S_0 \rightarrow S_2$	1.78	697	1.75	77% D1 Indz-P → D1 P-BTD 13% D1 Indz/D1 P → D2 BTD
Dimer 2 *π*–*π* D2 BTD(S)-D1 Indz(py)	$S_0 \rightarrow S_1$	1.70	728	0.05	99% D1 Indz → D2 BTD
	$S_0 \rightarrow S_2$	1.76	703	2.43	77% D1 Indz-P → D1 P-BTD 13% D2 Indz-P → D2 P-BTD
Dimer 3 hydrogen bonding/*π*–*π* D2 BTD(COOH)-D1 Indz(N)	$S_0 \rightarrow S_1$	1.77	702	2.67	58% D1 Indz-P → D1 P-BTD 32% D2 Indz-P → D2 P-BTD
Dimer 4 *π*–*π* D2 Indz-D1 Indz	$S_0 \rightarrow S_1$	1.77	701	2.71	52% D2 Indz-P → D2 P-BTD 38% D1 Indz-P → D1 P-BTD

[a] D1 refers to the dye on the left, and D2 refers to the dye on the right (Figure 5), which would bind TiO_2. The primary regions for electron/hole locations for each transition are coded as Indz = indolizine, P = porphyrin, and BTD = benzothiadiazole. The aggregate orientation is indicated by the atom or ring in parenthesis where the noted groups spatially overlap (S = sulfur, pyr = pyridine, N = pyridine, and py = pyrrole).

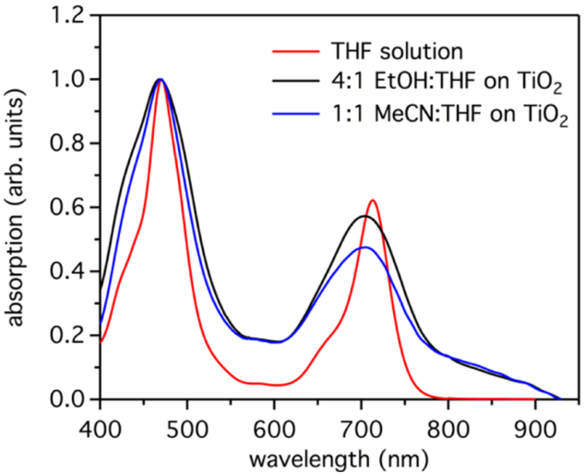

Figure 24. UV−vis absorption comparison of **SM85** as a THF solution and on TiO_2 films (3 μm) sensitized with EtOH/THF (4:1) and MeCN/THF (1:1).

As this interpretation is supported by the aggregation phenomena observed in ^{1}H NMR, we further probed the absorption and emission of **SM85** in various solvents (Figures 31 and 96−100) to ascertain if one of the maxima in the absorption/emission spectra originates from the J-aggregate. Although a slight, solvent-dependent shifting of the Q-band maxima by 20 nm (0.05 eV) is seen, the relative ratio of the two distinct absorptions within the Q-band was found to alter dramatically with varying solvents, giving further credence to the prevalence of the solvent-dependent aggregation of **SM85** in solution.

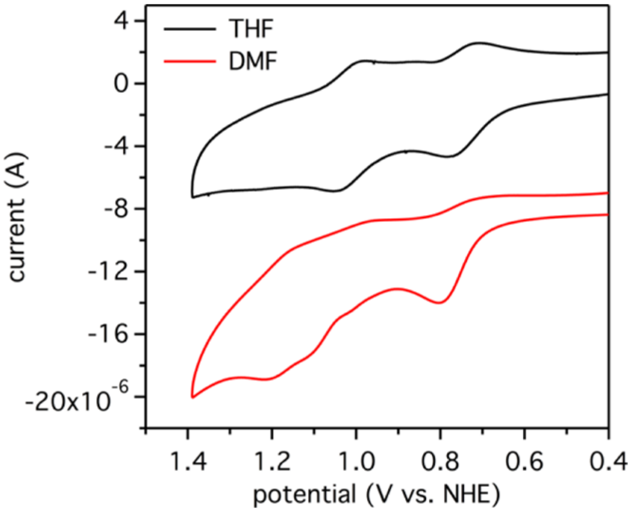

Figure 25. CV curves of SM85 in THF and DMF vs NHE.

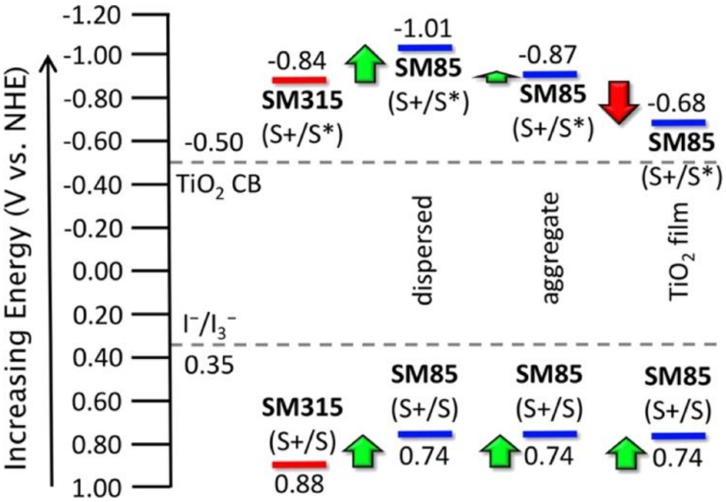

Figure 26. Comparison of SM85 and SM315 energy levels relative to TiO_2 and I^-/I_3^-.

Table 7. Summary of Photovoltaic Parameters for DSC Devices Prepared with **SM85**[a]

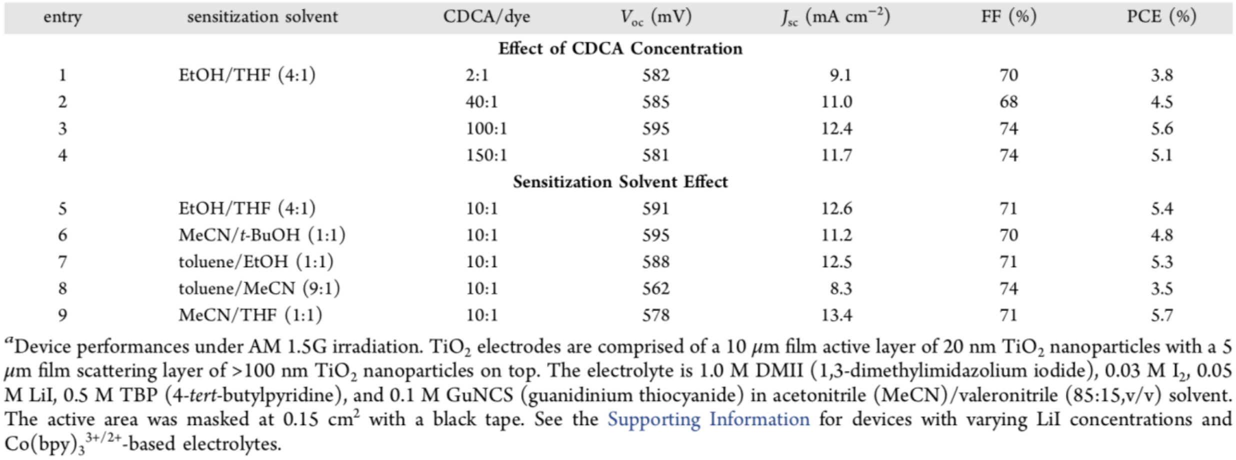

entry	sensitization solvent	CDCA/dye	V_{oc} (mV)	J_{sc} (mA cm^{-2})	FF (%)	PCE (%)
Effect of CDCA Concentration						
1	EtOH/THF (4:1)	2:1	582	9.1	70	3.8
2		40:1	585	11.0	68	4.5
3		100:1	595	12.4	74	5.6
4		150:1	581	11.7	74	5.1
Sensitization Solvent Effect						
5	EtOH/THF (4:1)	10:1	591	12.6	71	5.4
6	MeCN/*t*-BuOH (1:1)	10:1	595	11.2	70	4.8
7	toluene/EtOH (1:1)	10:1	588	12.5	71	5.3
8	toluene/MeCN (9:1)	10:1	562	8.3	74	3.5
9	MeCN/THF (1:1)	10:1	578	13.4	71	5.7

[a] Device performances under AM 1.5G irradiation. TiO_2 electrodes are comprised of a 10 μm film active layer of 20 nm TiO_2 nanoparticles with a 5 μm film scattering layer of >100 nm TiO_2 nanoparticles on top. The electrolyte is 1.0 M DMII (1,3-dimethylimidazolium iodide), 0.03 M I_2, 0.05 M LiI, 0.5 M TBP (4-*tert*-butylpyridine), and 0.1 M GuNCS (guanidinium thiocyanide) in acetonitrile (MeCN)/valeronitrile (85:15,v/v) solvent. The active area was masked at 0.15 cm^2 with a black tape. See the Supporting Information for devices with varying LiI concentrations and $Co(bpy)_3^{3+/2+}$-based electrolytes.

The significant aggregation of **SM85** observed in ^1H NMR using $CDCl_3$ prompted the acquisition of absorption and emission spectra in $CHCl_3$ (Figure 20) where the relative peak heights and position of the Q-band and the shoulder changed compared to those in THF. The introduction of pyridine to the $CHCl_3$ solution of **SM85** resulted in a red shift of absorbance maxima instead of the expected blue shift coincident with the deprotonation of the carboxylic acid moiety in **SM85** and the suppression of acid−base interactions, in line with ^1H NMR observations. This red shift in absorption in the $CHCl_3$/pyridine solution is ascribed to the chelation of pyridine to the zinc atom of the metalloporphyrin, obscuring the expected blue shift upon deprotonation. Despite this red-shifting of the absorption spectrum, the relative heights of Q-bands and shoulder remain intact, and the new energy of the absorption correlates well with the Q-bands observed in THF, suggesting that the aggregation phenomenon is mediated by the donor−acceptor interaction of indolizine and benzothiadiazole π-systems. Additionally, the change from two emission peaks in THF to one emission peak in $CHCl_3$ or $CHCl_3$/pyridine suggests that the dominant species in THF solution is an aggregate. The emission curve behavior when changing from THF to $CHCl_3$/pyridine can be rationalized as improved dye dispersion resulting in a significantly reduced emission from the aggregate, yielding a clear, single emission maximum. Simple deprotonation of the carboxylic acid acceptor in **SM85** by pyridine and prevention of an acid−base mediated aggregation would cause blue-shifting of charge transfer absorption as the carboxylate anion reduces the electron- accepting strength within the donor−acceptor dye. The persistence of the red-shifted aggregate absorption suggests that interactions between the π-systems of the respective donor and acceptor of neighboring dyes provide the impetus aggregate formation. In further support of the solvent- dependent behavior of SM85, ^{1}H NMR studies in d_6-DMF, d_8-toluene, and d_8-THF were undertaken with and without d_5-pyridine (Figures 110-112). Within these solvents, aggregation can also be observed with a significant influence of d_5-pyridine on the resolution of the d_8-toluene sample.

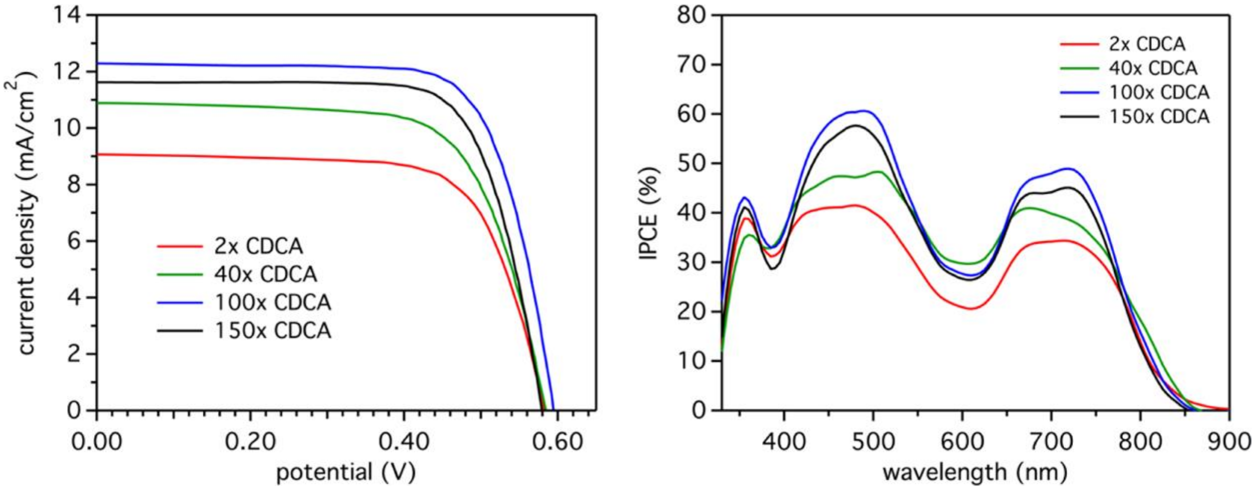

Figure 27. J−V curves (left) and IPCE spectrum (right) with variable CDCA ratios relative to dye concentration in the loading solvent (EtOH/ THF 4:1). The curves correspond to Table 7, entries 1−4.

Comparison of the UV−vis−NIR and emission spectra of **SM85** in aromatic solvents, toluene and *o*-dichlorobenzene (ODCB) (employed to overcome solution aggregation in organic polymers)[129] reveals similar aggregation phenomena. The absorption of **SM85** in toluene shows a significant amount of aggregate compared to the dispersed dye in both absorption and emission spectra. Although ODCB has a significantly higher dielectric constant, the spectra overlap perfectly (i.e., no solvatochromism), with an increase in the amount of dispersed dye to aggregate in solution observable in both absorption and emission spectra. Presumably, the greater polarity of ODCB combined with its aromatic nature imparts a unique ability in effectively interacting with the similar polar aromatic donor–acceptor components of **SM85**. In a similar manner, the very polar solvents DMF and dimethyl sulfoxide (DMSO) yielded little solvatochromic effects compared to THF; however, a decrease in the amount of aggregate is observed in both absorption and emission spectra.

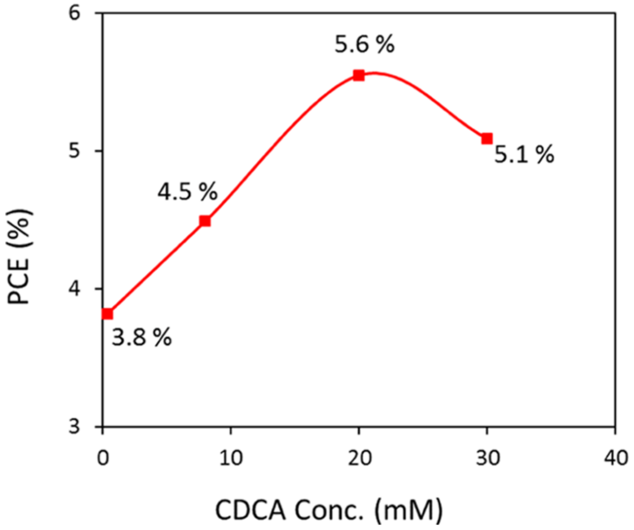

Figure 28. Effect of CDCA concentration on the PCE values for the EtOH/THF sensitization solvent.

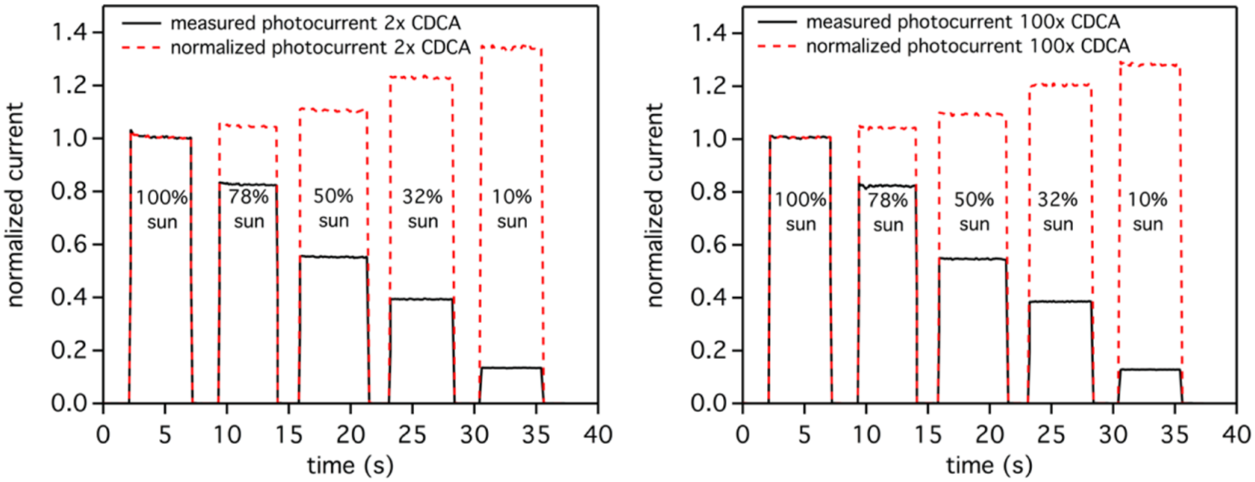

Figure 29. Current dynamics comparing the effect of CDCA concentration for 2 equiv CDCA (left) and 100 equiv CDCA (right). From these graphs, it is apparent that CDCA has only a modest effect on extrapolated current values from low light intensities.

On the basis of the observed optical properties, **SM85** is a good candidate for use in NIR DSC devices. To function efficiently in DSC devices, the dye orbitals should be spatially positioned with the lowest unoccupied molecular orbital (LUMO) near the TiO_2 surface to promote desirable electron injection, and the highest occupied molecular orbital (HOMO) should be positioned far from the TiO_2 surface to slow back-electron transfer. To explore these aspects and the intriguing optical characteristics in more detail, density functional theory (DFT) and time-dependent DFT (TD- DFT) calculations were carried out on **SM85** and, for comparison, on **SM315**, using the Gaussian 16 (Rev. A.03) software suite[130] at the optimally tuned (OT)-LC-Perdew−Burke−Ernzerhof (ωPBE)[131-135]/6-31G(d,p)[136-137] level of theory; the (OT)-LC-ωPBE functional was selected to avoid substantial multielectron self-interaction errors observed with many commonly used functionals. Omega tuning[138] was performed via the iterative, nonempirical gap tuning procedure for both **SM85** and **SM315** after initial geometry optimizations at the LC-ωPBE/6-31G(d,p) level of theory; the optimized omega values are 0.128

bohr^{-1} for **SM85** and 0.125 bohr^{-1} for **SM315**. The D3 version of Grimme's dispersion,[139] with the Becke−Johnson damping factor,[140] was used for all calculations.

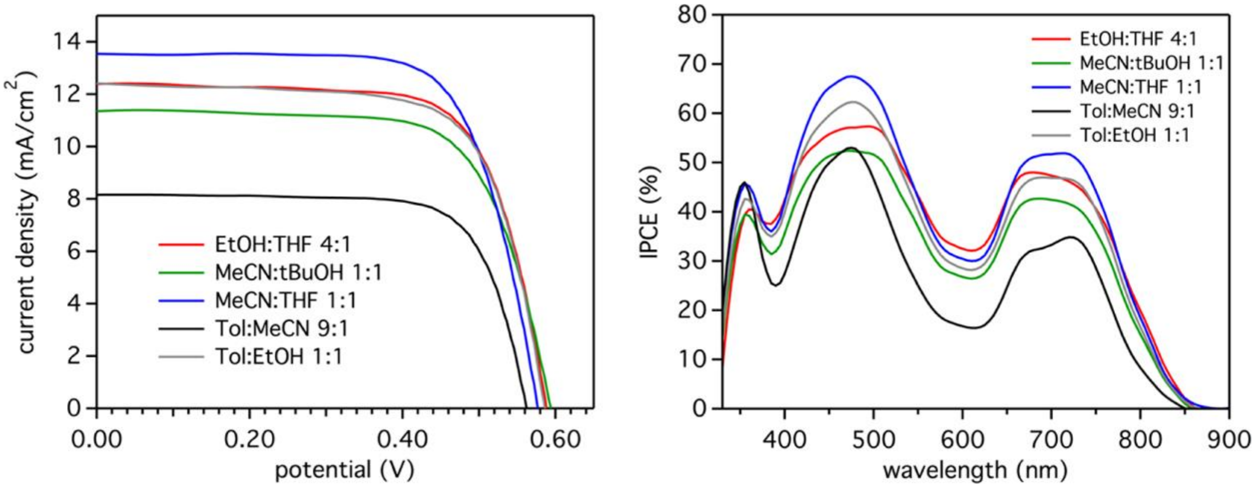

Figure 30. J−V curves (left) and IPCE spectrum (right) with variable loading solvents. The curves correspond to Table 7, entries 5−9.

Normal mode analyses were carried out for all optimized structures to ensure that the geometries were located in minima on the potential energy surface.

For both **SM85** and **SM315**, the HOMO is primarily localized on the donor and porphyrin moieties far from the carboxylic anchoring group (Figure 21). These features ensure that the HOMO is positioned desirably far from the TiO_2 surface to slow back-electron transfers after the photoexcited dye injects an electron. It is noteworthy that slightly higher delocalization of the HOMO onto the porphyrin core is observed with **SM85**. This extended delocalization in **SM85** is likely due in part to the more planar configuration of the indolizine π-system relative to the porphyrin π-system, whereas the diarylamine group of **SM315** is substantially twisted. For both dyes, the LUMO is primarily localized on the benzothiadiazole group with some delocalization on the porphyrin bridge and the phenylcarboxylic acid anchoring group. The positioning of the LUMO is well-suited for electron transfer to TiO_2 after photoexcitation. **SM85** is expected to demonstrate ICT upon photoexcitation, given the spatial separation of the HOMO and LUMO with some overlap at the porphyrin bridge as is needed for ICT.

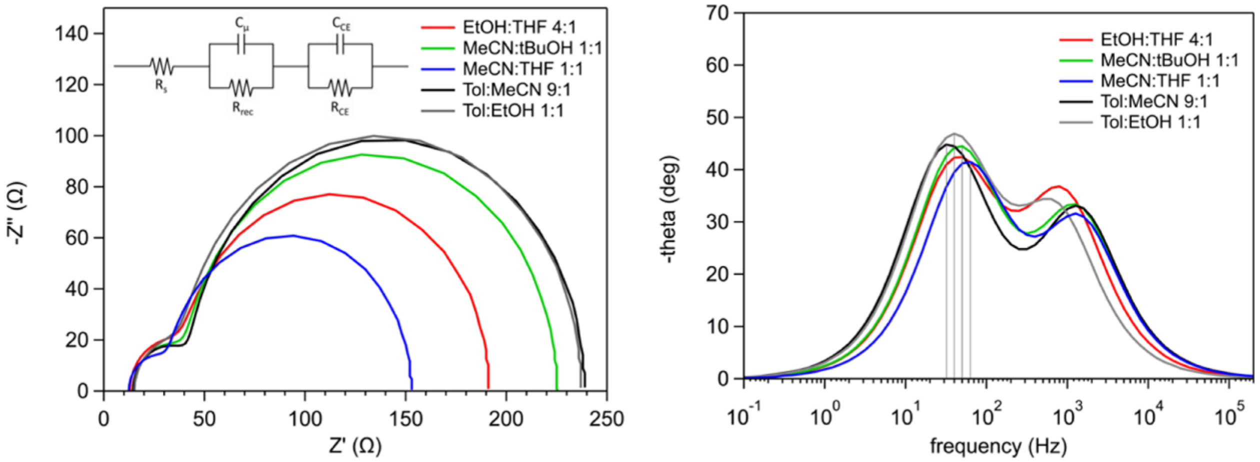

Figure 31. Nyquist (left) and Bode (right) plots resulting from EIS. The fitting circuit is shown as the inset on the left.

To probe the photoexcitation processes in more detail, TD- DFT calculations at the OT-LC-ωPBE/6-31G(d,p) level of theory were carried out (Table 5). Validation for stronger electronic coupling between the donor and the acceptor in **SM85** is supported by a larger oscillator strength for **SM85** (1.21) when compared to **SM315** (0.76) for the predominately HOMO → LUMO based $S_0 \rightarrow S_1$ transition, in agreement with the experimental molar absorptivities (Table 5, Figure 20). The next bright (nonzero oscillator strength) excitations are $S_0 \rightarrow S_5$ for **SM85** and $S_0 \rightarrow S_3$ for **SM315** (Table 5). We note that these transitions are highly mixed, with contributions coming from a number of one-electron excitations. Simulated UV−vis spectra based on the TD-DFT calculations for **SM85** and **SM315** at the OT-LC-ωPBE/6-31G(d,p) level of theory, created by Lorentzian broadening of the vertical transitions, show a reasonable agreement with the experiment (Figures 35 and 101), providing credence for the detailed analyses of the transitions on this level of theory.

Table 8. EIS Data[a]

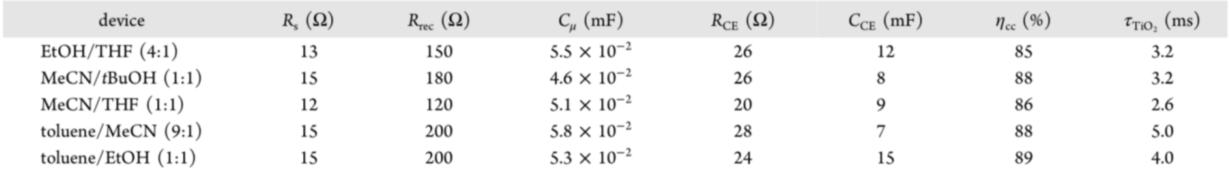

device	R_s (Ω)	R_{rec} (Ω)	C_μ (mF)	R_{CE} (Ω)	C_{CE} (mF)	η_{cc} (%)	τ_{TiO_2} (ms)
EtOH/THF (4:1)	13	150	5.5×10^{-2}	26	12	85	3.2
MeCN/*t*BuOH (1:1)	15	180	4.6×10^{-2}	26	8	88	3.2
MeCN/THF (1:1)	12	120	5.1×10^{-2}	20	9	86	2.6
toluene/MeCN (9:1)	15	200	5.8×10^{-2}	28	7	88	5.0
toluene/EtOH (1:1)	15	200	5.3×10^{-2}	24	15	89	4.0

[a] R_s is the series resistance, R_{rec} is the recombination resistance of electrons in TiO_2 across the TiO_2−dye interface to an oxidized redox shuttle, C_μ is the chemical capacitance for charge accumulation in TiO_2, R_{CE} is the electron-transfer resistance at the counter electrode to an oxidized redox shuttle, and C_{CE} is the capacitance at the electrolyte-counter electrode interface. $\eta_{CC} = 1/(1 + (R_{CE}/R_{rec}))$, where η_{CC} is the charge collection efficiency. $\tau_{TiO2} = 1/(2\pi f)$, where τ τ_{TiO2} is the lifetime of injected electrons in TiO_2 and f is the peak frequency from the Bode plot for the lower frequency peak between 10 and 100 Hz (illustrated as gray lines in Figure 31).

To gain insight into the effects of aggregation in **SM85** observed by absorption spectroscopy and NMR, additional calculations were performed on a series of dimers. These dimers were created by using the optimized (isolated) **SM85** geometries, with the closest atom contacts at no closer than ≈3 Å. No further geometry optimizations were carried out. Here, we report the results for two dimers: For **Dimer 1**, the indolizine portion of one monomer is aligned with the benzothiadiazole of the other monomer, with the first monomer's benzothiadiazole sulfur oriented toward the pyridine in the other monomer's indolizine. **Dimer 2** resembles **Dimer 1**, but the first monomer is rotated 180° so that the sulfur of the benzothiadiazole is toward the pyrrole in the other monomer's indolizine, as seen in Figure 23.

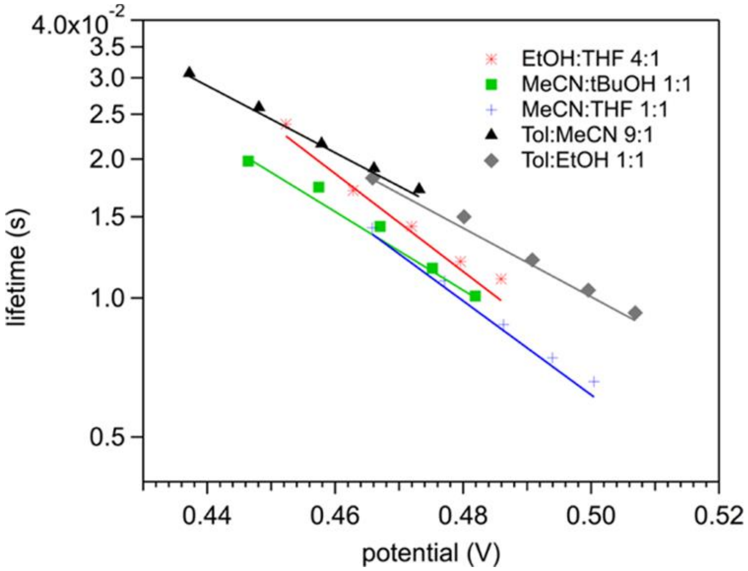

Figure 32. Small modulated photovoltage transient measurements of electron lifetimes in TiO_2.

Relative to the monomer, simulated absorption profiles for these two aggregates (**Dimer 1** and **Dimer 2**) present bathochromically shifted vertical transitions (Figure 24) with an intermolecular charge transfer between the aggregated dyes, as shown by the natural transition orbitals (NTO) in Figure 23. Both aggregation modes arise from stacking between the electron-rich indolizine and the electron-deficient benzothiadiazole groups (Figure 23). For **Dimer 1**, the oscillator strength is substantially larger than that of **Dimer 2** (0.62 vs 0.05, respectively, Table 6). The strong absorption in THF of the aggregate is consistent with a significantly strong transition and may be attributed to the aggregate with the sulfur-pyridine ring overlap. For both aggregate states, the ICT ($S_0 \rightarrow S_2$) for a single dye is apparent at high oscillator strength (≥1.75 eV) and is slightly blue-shifted relative to the intermolecular charge-transfer state ($S_0 \rightarrow S_1$) (~0.06 eV shift, Table 6). With regard to implications on device performance, selective aggregation of dyes can have profoundly strong positive effects.[141] However, desirable orbital positioning is needed such that the intermolecular charge-transfer event leads to movement of an electron into close proximity to the TiO_2 surface. In the aggregation modes here, both would move the electron away from the TiO_2 surface undesirably. Because of this, disruption of aggregation for **SM85** is critical for efficient devices. Interestingly, this finding suggests that a nonintuitive dye design in principle may lead to high performances, where a π-acceptor is placed far from the surface to π-stack with a donor group. Traditionally, acceptors are placed as close to the TiO_2 surface as possible. However, through targeted intermolecular engineering designs, a weak acceptor on the "donor side" of a charge-transfer dye should lead to a beneficial interaction with the strong donor of a second dye for the self- assembled red-shifting of the absorption spectrum, which would have electron flow in the desired direction. Investigation into the merits of such a design is ongoing.

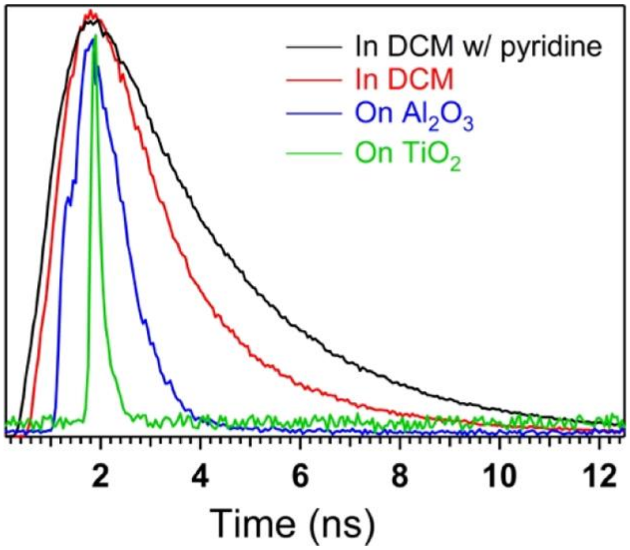

Figure 33. Excited-state fluorescence decay of **SM85** in DCM, in DCM with added pyridine, on a 3 μm thick Al_2O_3 film, and on a 3 μm thick TiO_2 film

Two additional potential aggregation states were also examined, formed via either a hydrogen-bonding type event from the carboxylic acid group to the indolizine (**Dimer 3**) or by a π–π overlap of the indolizine groups (**Dimer 4**). For these aggregation modes, the ICT is the lowest energy vertical transition. Because intermolecular charge transfer is not the lowest energy-excited state for these aggregation modes, it is less likely that these modes are leading to the red-shifted aggregates observed in solution and TiO_2 film measurements.

Ultimately, the optical data that is most pertinent to the performance of **SM85** in DSC devices is based on the dye behavior on the surface of TiO_2. Thus, films of TiO_2 and **SM85** were prepared by sensitization in either EtOH/THF or MeCN/THF mixtures (Figure 25). EtOH and MeCN cosolvents are classic DSC dye loading solvents due in part to favorable dielectric constants in addition to several other features.[142-143] The dye-sensitized TiO_2 films from either solvent system gave near-identical curve profiles with a notable broadening of the Soret and the Q-bands relative to THF solution. The absorption curve onset of **SM85** shifts to near 875 nm because of a low energy shoulder from the Q-band. This is a dramatically longer wavelength absorption than is observed in solution (770 nm onset), which suggests that aggregation modes are present as a film that shift the absorption onset >100 nm into the NIR region. Given that few dyes produce photocurrent beyond 800 nm, this aggregate- induced NIR absorption has allowed access to a spectral region that is often underutilized.[114]

Controlling the aggregation state of dyes within DSCs is critical to understanding the actual dye energetics within the device, which is imperative in the rational and iterative design of next-generation dyes. Estimation of the solution absorption onset of the dispersed dye in THF, aggregate in THF, and on a TiO_2 film gives a change in optical gap energies of over 165 nm (0.33 eV, Table 4, Figure 25). The changes from solution-state measurements alone show a 90 nm shift (0.19 eV) between the dispersed dye and the aggregate. Changes of this magnitude can have significant effects on the dye energy levels in the NIR region and, in turn, on NIR performance in DSC devices.

Table 9. TCSPC Excited-State Lifetime Measurements

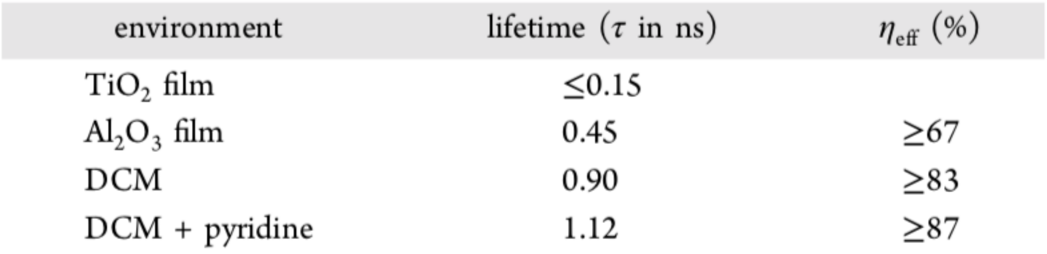

environment	lifetime (τ in ns)	η_{eff} (%)
TiO_2 film	≤0.15	
Al_2O_3 film	0.45	≥67
DCM	0.90	≥83
DCM + pyridine	1.12	≥87

Having found that the indolizine donor imparts a desirable red shift of the absorption spectrum for **SM85**, electrochemical measurements were undertaken to evaluate the thermodynamic suitability of **SM85** for DSC devices using TiO_2 as a semiconductor and iodide/triiodide as a redox shuttle (Figure 26). $E_{(S^+/S)}$ of **SM85** is measured at 0.74 V versus NHE in both THF and DMF, which is ~140 mV higher in energy than **SM315** (Table 4, Figure 27). In THF, two oxidations are observed, both of which are reversible. In DMF, the first oxidation wave was irreversible, and several waves can be seen after this event, which could be due to decomposition or aggregates in solution. A regenerative driving force (ΔG_{reg}) is estimated at 390 mV for the regeneration of **SM85** with the I^-/ I_3^- redox shuttle. This is a significantly lower ΔG_{reg} for **SM85** than for **SM315** at 530 mV, which is attributed to the stronger donation strength of indolizine relative to a diarylamine. For higher performing dyes, ΔG_{reg} (and electron injection driving force ΔG_{inj}) must be minimized for optimal performance.[75] In this regard, the molecular design of **SM85** shows significant improvement thermodynamically relative to **SM315** in minimizing regenerative energy losses. To approximate $E_{(S^+/S^*)}$ values, the equation $E_{(S^+/S^*)} = E_{(S^+/S)} - E_g^{opt}$ is used, where E_g^{opt} is taken as the onset of the absorption spectrum on the low-energy side of the Q-band features (λ_{max}). As the solution features both dispersed dye monomer and aggregate species in the absorption spectrum, each with different energetic considerations, we evaluated the energetic implications of each by estimating the onset for each species. We estimate the dispersed dye and aggregate species as having solution onsets at 710 nm (1.74 eV) and 770 nm (1.61 eV), respectively (Figure 21). This leads to respective $E_{(S^+/S^*)}$ values of −1.01 and −0.87 V. On TiO_2, we estimate the absorption curve onset at 875 nm (1.42 eV) for an $E_{(S^+/S^*)}$ of −0.68 V. For the solution measurements of dispersed and aggregated **SM85**, the $E_{(S^+/S^*)}$ values are higher than those of **SM315** by 170−30 mV. An increase in the excited-state oxidation potential energy is commonly observed when strong donor groups are used, which again indicates a stronger donation strength of indolizine relative to the diarylamine used with **SM315**.[125] On the basis of solution measurements, both dyes have favorable ΔG_{inj} values of ≥340 mV for electron transfer to TiO_2, assuming the ground-state oxidation potential is held constant for aggregates of **SM85** (Figure 27). Interestingly, control of the aggregation state by solvent selection could be used to tune the dye energetics substantially without requiring a completely new synthesis if the aggregation state could be controlled within a DSC device. On the basis of optical film measurements, the $E_{(S^+/S^*)}$ value lowers significantly to −0.68 V for only a 180 mV ΔG_{inj} value. This suggests that efficient electron injection may be an issue for SM85 as this driving force for electron transfer is small.

Having found suitable dye energetics for electron transfers from **SM85** to TiO_2 and from I^- to the **SM85** cation, **SM85** was evaluated in DSC devices with aggregation disrupted to varying degrees under AM 1.5G solar simulation. Table 7 summarizes the device parameters obtained for **SM85** with different CDCA concentrations as an aggregation suppressant in ethanol/THF (EtOH/THF, 4:1) as the sensitizing solvent (Table 7, Figure 28). The power conversion efficiency [PCE, calculated according to the equation PCE = (J_{sc} × V_{OC} × FF)/ I_0, where J_{sc} is the short-circuit current density, V_{OC} is the open- circuit voltage, FF is the fill factor, and I_0 is the intensity of incident light] was found to increase as CDCA concentration increased from 2 equiv relative to the dye concentration to 100 equiv relative to the dye concentration (3.8−5.6%, respectively). This indicates that aggregation is reduced in the presence of CDCA, and the primary gain in device performance arises from a significant increase in J_{sc}. Addition of larger quantities of CDCA (150 equiv) leads to a diminished PCE and a visually lower dye loading as the TiO_2 electrode shows less coloration. CDCA is known to compete for adsorption sites on TiO_2 with dye molecules, which explains the lower device performance and observed lighter staining of the electrodes at very high loading ratios.[144-145] These results show that for peak performance, a balance between high dye loading with low CDCA concentrations and reduced degree of aggregation with high CDCA concentrations must be reached for the highest performing devices (Figure 29). IPCE measurements also confirm the rise in current as the area under the curve responds appropriate to that measured via the J−V curve. Interestingly, the IPCE extends significantly further into the NIR region than the solution absorption values in any solvent analyzed (onset of ~850 nm vs 800 nm, respectively). This extended absorption spectrum is likely due to productive aggregation events on the surface, culminating in a ~50 nm red shift in the IPCE spectrum onset of **SM85** relative to **SM315**. This is a significant extension of electricity production into the NIR region through a tailored π−π interaction. Notably, this interaction is strong enough to not be disrupted by a large amount of CDCA because the IPCE onset remains at ~850 nm across all concentrations of CDCA examined. Since the **SM85** molecular design has likely resulted in charge transfer across noncovalently bound π-systems, effects such as external electric field influences could play a role in the device IPCE and overall performance.[146-148]

Some modes of surface aggregation (such as multilayer aggregation) can be observed through photocurrent dynamic studies at a variable light intensity.[149] This measurement can be conducted by shuttering light on/off with a filter wheel and changing filters to vary sun intensity during the off cycles while current flow is monitored. The current output is then normalized to 1 sun intensity as controlled by the filter to give a profile of how efficiently light is converted to current at variable sun intensities. This measurement is also diagnostic for electrolyte diffusion issues and in identifying severe dye regeneration issues, neither of which are observed in our case.[150] Aggregation is clearly apparent when this measurement is performed with **SM85** at both low and high loadings of CDCA (Figure 30). The normalized-to-sun-intensity current (dotted line) shows substantially higher current outputs at low light than under full sun conditions at both high and low CDCA loadings. Employing two molar equivalents of CDCA in the dipping solution results in a 25% loss in photocurrent upon comparison of the 10% sun and 100% sun normalized measurements. The photocurrent loss is further reduced to 20% upon addition of 100 molar equivalents of CDCA in the dipping solution. These results suggest that the head-to-tail aggregation event targeted with the design of **SM85** is present and is disrupted to varying degrees with CDCA, which is substantiated by the device performance metrics above.

The sensitizing solution solvent can also play a huge role in controlling the device performance and changing the aggregation modes. During our solution studies, we observed significant changes in absorption curve shapes by using different solvents. For these studies, we focus first on two of the widely employed dye sensitization solvent combinations: EtOH/THF (4:1) and MeCN/t-BuOH (1:1). Additionally, we analyzed several other solvent combinations employing either THF (aggregate inducing) or toluene (aggregate reducing relative to THF) with MeCN and EtOH. MeCN and EtOH have been kept in each loading solvent as these have been empirically shown to give some of the highest performing cells in the DSC literature due seemingly to a balance between maintaining a high dielectric solution constant and reducing dye aggregation relative to many other solvents.[142-143] Also, the sensitization time was shortened to 3 h instead of overnight, which has also been shown to have a significant effect on device performances.[151] The CDCA loading was reduced to 10 equiv to retain effective dye loadings and to allow for comparative probing of less polar solvents in which CDCA is less soluble. The lower dielectric constant ($\varepsilon = 6$) system using 90% toluene and 10% acetonitrile gave the lowest J_{sc} value of 8.3 mA cm^{-2} with the lowest dye loading of 2.0×10^{-6} mol cm^{-2} (Figure 31, Table 27). Toluene was shown to diminish aggregation in solution relative to solvents such as THF; however, the IPCE onset did not change relative to the other solvents tested, such as THF, which was shown to promote aggregation. This suggests that the loading solvent has a lesser effect on surface aggregation, and the effects of dielectric strength play a larger role in the device performance differences observed from different loading solvents.

Changing to a 50% toluene and 50% ethanol solution ($\varepsilon = 14$) improved the J_{sc} value to 12.5 mA cm^{-2} with an increase in dye loading to 3.3×10^{-6} mol cm^{-2}. Removal of toluene and replacement with THF/ethanol (1:4) as a sensitization mixture ($\varepsilon = 20$) results in a very similar photocurrent of 12.6 mA cm^{-2} despite a higher dye loading of 7.1×10^{-6}. Since many DSC devices perform best when sensitized out of MeCN mixtures, due in part to a very high dielectric constant ($\varepsilon = 37$), the next experiments focused on increasing the amount of MeCN while maintaining high dye solubility. In a 1:1 MeCN/t-BuOH mixture ($\varepsilon = 26$), the photocurrent diminished to 11.2 mA cm^{-2}. Because the highest dye loading was achieved with this mixture (1.2×10^{-5} mol cm^{-2}), the decrease in current is likely due to an increase in nonproductive aggregation states. However, replacing *t*-BuOH with THF in the same ratio ($\varepsilon = 23$) led to the highest performing device of the series with 13.4 mA cm^{-2} and a peak IPCE value of 70% from the Soret band region. Under these optimal conditions, substantial differences in photocurrent dynamic measurements at reduced versus full sun intensities are observed, indicating that a multilayered dye aggregation system is still present in these devices (Figure 102).

EIS was conducted with each of the different loading solvents at an open-circuit potential (Figure 32, Table 8). Interestingly, charge recombination resistance (R_{rec}) was the lowest with the highest performing loading solvent system in DSC devices (MeCN/THF) upon analyzing the Nyquist plot. R_{rec} was the highest for the worst performing devices made from toluene/EtOH. This observation can be explained in that while aggregation is needed to red shift the dye absorption, excessive aggregation exists in low dielectric constant mixtures, which lowers device performances but more effectively blocks the TiO_2 surface from recombination events. Notably, the overall effect of varying R_{rec} is low in these devices, which is apparent when analyzing the charge collection efficiency (η_{CC}) via the equation, $\eta_{CC} = 1/(1 + (R_{CE}/R_{rec}))$, where R_{CE} is the resistance at the counter electrode. Accordingly, all solvent systems have good η_{CC} within the range of 85−89%. Analysis of the electron lifetime in TiO_2 was undertaken via EIS with a Bode plot. In this plot, the TiO_2−dye interfacial electron transfer to the electrolyte is seen at frequencies between 10 and 100 Hz (Figure 32). The peak frequency value in this measurement can be used to calculate the electron lifetime in TiO_2 (τ_{TiO2}) via the equation $\tau_{TiO2} = 1/(2\pi f)$, where f is the frequency. This analysis reveals a trend similar to that observed when analyzing R_{rec} with electron lifetimes the longest in the toluene/EtOH-based system (5.0 ms) and the shortest in the MeCN/THF system (2.6 ms). Small modulated photovoltage transient measurements were also undertaken to further probe electron lifetimes (Figure 33). These measurements are in agreement with the EIS lifetime analysis, with identical trends being observed. Thus, electron lifetime analyses support the conclusion that a balance of aggregation extent is needed for higher performances because longer lifetimes are correlated with poorer device performances, which is consistent with a more extensive nonproductive surface aggregation with toluene/EtOH-based devices.

Time-correlated single photon counting (TCSPC) studies were performed to better understand the electron-transfer process to TiO_2. Excited-state lifetimes in solution, on an insulator (Al_2O_3), and on TiO_2 films were measured, and the electron injection efficiency (η_{eff}) was calculated according to the equation $\eta_{eff} = 1 - (\tau_{TiO2}/\tau_{env})$, where τ_{TiO2} is the excited-state fluorescence lifetime on TiO_2 and τ_{env} is the excited-state fluorescence lifetime in another environment such as on an insulator or in solution (Figure 33 and Table 9).[9, 92, 152-153] The excited-state lifetime was found to be 0.90 ns in DCM solution. Upon addition of pyridine, the lifetime increased to 1.12 ns presumably due to disruption of aggregation, as was observed by the NMR and UV−vis absorption studies. On TiO_2, the lifetime is shorter than the response function of the instrument at ≤0.15 ns. This corresponds to an electron injection efficiency of ≥83% if DCM is used as the τ_{env} component of the η_{eff} equation and ≥87% if DCM with added pyridine is used as the τ_{env} component. This difference in efficiency highlights the fact that aggregation may be shrinking the excited-state lifetimes. It is important to note that only the emissive components (aggregates or monomer) can be observed with this technique, but if nonemissive aggregates are present in solution, they will not be observed. Dark aggregates would then have unknown excited-state lifetimes and could potentially diminish the reported electron injection efficiencies estimated above. Solution measurements are more biased toward dispersed single molecules than condensed solid-state measurements. Thus, the excited-state lifetimes of **SM85** were also measured on Al_2O_3 films. τ_{env} is considerably shorter on Al_2O_3 than in solution at 0.45 ns, which is likely due to increased aggregation, lowering the excited-state lifetimes. The τ_{env} value for the Al_2O_3 film corresponds to a η_{eff} of ≥67%. Whereas this measurement is limited by the response function of our instrument, it is noteworthy that the excited-state lifetime is very short, which likely means η_{eff} is not quantitative. This is consistent with the estimated low-energy excited state of **SM85** aggregates on TiO_2 surfaces (Figures 36 and 38). Additionally, the possibility of dark aggregates nonmeasurable by this technique further suggests that electron injection into TiO_2 may not be quantitative, which could play a role in the diminishment of peak IPCE values below a theoretical ~90%.

CONCLUSIONS

A porphyrin dye (**SM85**) with NIR absorbance based on the proaromatic indolizine donor was synthesized and characterized in solution and on films. Solution absorption and emission spectroscopies reveal a substantial red shift of the absorption spectrum relative to record setting **SM315** and the presence of significant aggregation in solution. Dye energetic analysis through CV measurements shows that DSC devices can be made from all aggregates, with energetically favorable driving forces for electron transfers to TiO_2 and from I^-. DFT calculations reveal that the frontier orbitals are well-positioned spatially for efficient device performance. TD-DFT analyses of dimer aggregates reveal specific modes of aggregation involving the donor and the acceptor and present excited-state characteristics that are consistent with solution absorption measurements. A series of devices with varying CDCA concentrations show performance enhancements as aggregation extent is reduced; however, aggregation is not completely diminished before CDCA concentrations became high enough to visibly lower the dye sensitization of TiO_2. Dye loading solvent selection significantly affects device performances, with the highest PCE of 5.7% observed in this study. Current dynamic studies reveal that substantial aggregation is present in all devices. EIS and photovoltage transient studies show effects of loading solvent on electron lifetimes with the longer electron lifetimes presumably coming from solvent systems with more extensive aggregation. The combined strategy of increasing the donor strength in the D−π−A system of **SM85** by utilizing the proaromatic indolizine donor coupled with the deliberate inducement of aggregation by donor−acceptor-mediated π−π stacking yields significant enhancements in long wavelength light harvesting, with **SM85** exhibiting an IPCE onset of ~850 nm, a substantial (~50 nm) red shift upon comparison to **SM315**. Future work will seek to impart greater control over aggregation phenomena to minimize performance diminishments with this bifaceted approach to enhanced NIR absorption through supramolecular design.

CHAPTER 5

5.1 IODINE BINDING WITH THIOPHENE AND FURAN BASED DYES FOR DSCS

Alexandra Baumann; Hammad Cheema; Md Abdus Sabuj; Louis E. McNamara; Yanbing Zhang**;** Adithya Peddapuram; Suong T. Nguyen; Davita L. Watkins; Nathan I Hammer; Neeraj Rai; Jared. H. Delcamp; *Phys. Chem. Chem.Phys.* **2018**, *20*, 17895. Reproduced by permission of The Royal Chemistry Society.

(See appendix for permission license).

This project is a collaborative project with Dr. Delcamp, Dr. Watkins, Dr. Hammer and Dr. Rai's group. Alexandra Baumann contributed to this work by synthesizing and characterizing the **AB1**-**AB3** dyes, and performing studies on all dyes. Hammad Cheema and Yanbing Zhang contributed to the work by fabricating and measuring the data of the devices. Adithya Peddapuram contributed to the work by synthesizing the **LD03** and **LD04** dyes. Louise McNamara contributed to this work by performing Raman spectroscopy experiments. Md Abdus Sabuj contribute to this work by performing computational studies on the **AB1**-**AB3** and **D35** dyes. Suong T. Nguyen contributed to this work by synthesizing the Br-TF-COH and Br-TT-COH intermediates.

ABSTRACT

Iodine binding to thiophene rings in dyes for dye-sensitized solar cells (DSCs) has been hypothesized to be performance degrading in a number of literature cases. Binding of iodine to dyes near the semiconductor surface can promote undesirable electron transfers and lower the overall efficiency of devices. Six thiophene or furan containing dye analogs were synthesized to analyze iodine binding to the dyes via Raman spectroscopy, UV-Vis studies, device performance metrics and density functional theory (DFT) based computations. Evidence suggests I_2 binds thiophene-based dyes stronger than furan-based dyes. This leads to higher DSC device currents and voltages from furan analogues, and longer electron lifetimes in DSC devices using furan based dyes. Raman spectra of the TiO_2 surface-bound dyes reveals additional and more instense peaks for thiophene dyes in the presence of I_2 relative to no I_2. Additionally, broader and shifted UV-Vis peaks are observed for thiophene dyes in the presence of I_2 on TiO_2 films suggesting significant interaction between the dye molecules and I_2. These observations are also supported by DFT and TD-DFT calculations which indicate the absence of a key geometric energy minimum in the dye-I_2 ground state for furan dyes which are readily observed for the thiophene based analogues.

INTRODUCTION

The need for an energy source that is both sustainable and renewable is apparent. One viable option that is cost-effective and potentially aesthetically appealing are dye-sensitized solar cells (DSCs).[1, 27] DSC devices operate by: (1) photoexcitation of a dye molecule, (2) injection of excited electrons into a semiconductor conduction band (e.g. TiO_2 CB), (3) an electron traversing an external circuit to the counter electrode, (4) collection of the electron at the counter electrode by a redox shuttle, and finally (5) transfer of the electron from the redox shuttle to the oxidized dye molecule.[28] Organic dye based DSCs have been able to reach power conversion efficiencies (PCEs) for this process in excess of 14%, but there is still room for improvement by minimizing non-productive electron transfers such as from TiO_2 to the dye (back electron transfer) or from TiO_2 to the redox shuttle (recombination).[5, 154-155] Undesirable charge recombinations are thought to increase when the iodine (I_2) redox shuttle binds with a dye near the TiO_2 surface (Figure 34).[15-17, 156] Minimizing recombination events which prevent electrons from completing an external circuit is critical to developing higher efficiency DSC devices.

Isothiocyanates (NCS) bound to transition metals, amine, cyano, halide and thioether groups have been demonstrated to bind iodine and iodide through prior spectroscopic, computational and device studies.[17-18, 156-166] Despite good evidence of sulfur-based NCS groups and aromatic 5-member heterocycle selenophenes[16] interacting with iodine, experimental evidence of thiophenes binding I_2 is lacking. However, thiophene is commonly implicated in promoting recombination by binding I_2 near the semiconductor surface.[10-11] Several computational reports suggest thiophene-based dyes binding I_2 may be favorable and likely has device performance implications.[163, 167-170] The possibility of thiophene binding I_2 is concerning since thiophenes have become ubiquitous in DSC organic-dye design. To probe the ongoing hypothesis that I_2 in DCSs is binding to the sulfur atom present in thiophene stronger than the oxygen atom present in furan rings, we have systematically studied a series of six thiophene or furan based-dye analogs experimentally via Raman spectroscopy, UV-Vis absorption, and DSC device performance properties, as well as computationally via geometry analysis, binding strength comparisons, and analysis of vertical transition events. The results put forward in this manuscript offer strong evidence of thiophenes binding I_2 which leads to lower DSC device performances.

We hypothesized sulfur would bind I_2 stronger than oxygen due to the higher polarizability of sulfur which is more similar to iodine.[171] Additionally, the widened C-S-C angle of thiophene relative to the C-O-C angle of furan could play an important role in accessibility of the S atom to I_2. To test this, we employed dyes in our studies which replace a thiophene ring with a furan ring to give a single atom change within the larger dye structure. Donor and π-bridge functionality was examined for three sets of dyes which all employ the ubiquitous cyanoacrylic acid acceptor within the donor-π bridge-acceptor (D-π-A) framework. Specifically, **LD03** (thiophene) and **LD04** (furan) have a simple alkyl ether donor group as part of the D-π-A conjugated system (Figure 35). This limits the heteroatom (non-carbon or hydrogen) binding positions relative to more complex dye systems. Hagfeldt's triarylamine donor was used to compare dyes varying π-bridges from one thiophene (**D35**), one furan (**AB3**), two thiophenes (**AB1**), and one thiophene with one furan (**AB2**) (Figure 35). This donor was selected as **D35** has been extensively studied and allows for a

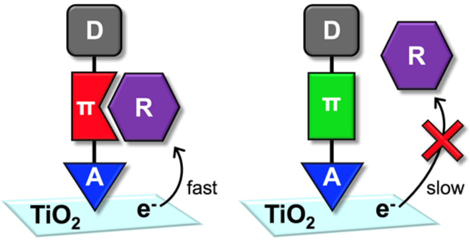

Figure 34. Example of a D-π-A dye binding a redox shuttle "R" near the TiO_2 surface (left) and a dye with no redox shuttle binding (right).

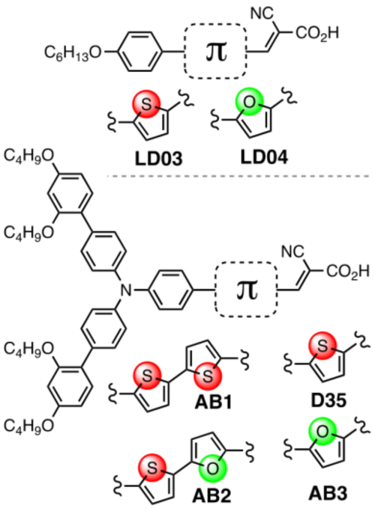

Figure 35. Target structures of **AB1, AB2, AB3, D35, LD03** and **LD04** dyes.

comparison to an established dye. The target dyes were known (**AB1**, **LD03** and **LD04**),[63, 172] commercially available (**D35** via Dyenamo), or prepared through analogous routes to the thiophene analogues[63, 97] for the unknown furan dyes (**AB2** and **AB3**, see Scheme 4 for synthetic route).

RESULTS AND DISCUSSION

Raman Spectroscopy. First, we examined the vibrational spectrum of the dyes with and without I_2 present on TiO_2 films in acetonitrile (MeCN) via Raman spectroscopy. Raman spectroscopy provides a sensitive spectroscopic method for evaluation of dye vibrational modes under conditions similar to those in devices for the neutral ground-state dye at a surface in the presence of MeCN with and without I_2. If iodine binding were to occur to the sulfur atom stronger than oxygen, we reasoned a change in the vibrational spectra of the dye molecules would be expected due to new vibrational peaks resulting from new vibrational modes associated with a S-I_2 binding or a change in the relative intensity of already existing peaks by perturbation of ring breathing/stretching modes of thiophene through introduction of an S-I_2 bond.[173-174] To compare thiophene versus furan dyes binding I_2, TiO_2-dye films were prepared with **D35** (thiophene), **AB3** (furan), **LD03** (thiophene) and **LD04** (furan). **AB1** (thiophene) and **AB2** (furan) were not studied via Raman spectroscopy since they suffer from decomposition on films in the presence of I_2 alone. Notably, **AB1** and **AB2** were stable in operational DSC devices presumably due to the full electrolyte stabilizing the dyes. For the other 4 dyes, Raman spectra were collected on the TiO_2-dye films with and without I_2 in the common DSC device electrolyte solvent MeCN. **D35** (thiophene) and **AB3** (furan) both show an increase in the relative intensity of the peaks seen between 1000-1600 cm^{-1} when compared with the 300-1000 cm^{-1} region; however, the increase is substantially greater for **D35** (thiophene) (Figure 36a and 36b). Initial pure dye peaks and new peaks associated with I_2 addition can be seen around 950 cm^{-1}, 1025 cm^{-1}, 1060 cm^{-1}, and 1400-1600 cm^{-1} for **AB3** (furan) (Figure 36b), but **D35** (thiophene) shows few original dye peaks after I_2 addition with numerous intense signals being added from 1000-1600 cm^{-1} (Figure 36a). This points to the presence of iodine binding in both dyes, however the presence of the sulfur atom in **D35** (thiophene) has resulted in a larger change in the Raman spectrum relative to **AB3** (furan). This larger change in the **D35** (thiophene) Raman spectrum is the result of a single atom change from oxygen in **AB3** (furan) to a sulfur. Given that the experimental conditions were held constant, this single atom is responsible for the large change in the Raman spectrum when I_2 is present. The changes are consistent with a sulfur-halogen bonding event to I_2 as discussed in the computational section below.

To reduce the possible influence of the nitrogen atom of the amine donor during these studies, the simple alkoxy donor-based dyes, **LD03** (thiophene) and **LD04** (furan), were examined in an identical study. Changes in the Raman spectra were subtler for these two derivatives which could be due to the absence of nitrogen-I_2 interactions or due to a less electron rich thiophene binding weaker to I_2 when only a relatively weak ether donor is used. A larger difference in the relative intensity of the peaks between 1000-1600 cm^{-1} with and without I_2 present is observed for **LD03** (thiophene, Figure 36c) when compared with the 300-1000 cm^{-1} region, while the change for **LD04** (furan, Figure 36d) is less dramatic when these regions are compared. These results indicate a difference in the influence of I_2 on the Raman spectrum of **LD03** (thiophene) when compared to **LD04** (furan) which may be attributed to the stronger binding of I_2 by thiophene. This observation is consistent with Raman spectroscopy studies performance on films of **D35** (thiophene) and **AB3** (furan).

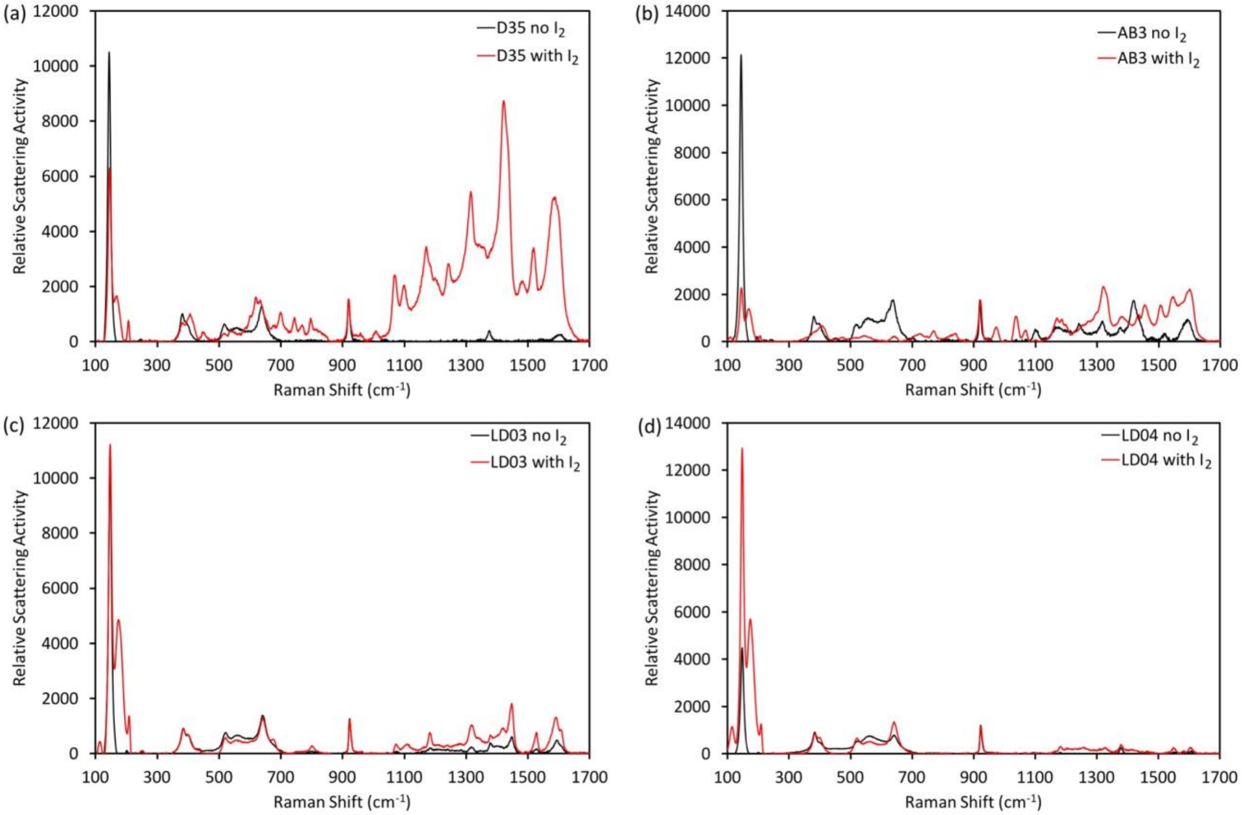

Figure 36. Raman spectra for (a) **D35**, (b) **AB3**, (c) **LD03** and (d) **LD04** on TiO_2 films under acetonitrile with and without I_2 present. Background spectrum were subtracted in each case without the dye present but all other components were present.

Computational Analysis. To gain insight into the changes observed experimentally in the Raman spectra, the interactions of **AB1** (thiophene), **AB2** (furan), **D35** (thiophene) and **AB3** (furan) with I_2 were probed computationally to examine the hypothesis of thiophene interacting non-covalently with I_2 more strongly than furan. **AB1** (thiophene) and **AB2** (furan) were also of interest since spectroscopic film studies in the presence of I_2 could not be conducted. Since **LD03** (thiophene) and **LD04** (furan) displayed similar Raman spectra trends to **D35** (thiophene) and **AB3** (furan), the more common benchmark dye **D35** (thiophene) was chosen for computational studies to compare with analogue **AB3** (furan). First, geometries of the dyes were optimized in two different conformations (referred to as *cis* and *trans* based on the orientation of the CN group of the cyanoacrylic acid relative to the thiophene sulfur or furan oxygen atoms, Figure 37) in isolation without I_2 present at the wB97XD/6-31+G* level of theory. On TiO_2 film surfaces the exact dye geometry is challenging to predict, thus two geometries were analyzed for the four dyes examined. Calculations were conducted in the absence of solvent and the TiO_2 surface to reduce the complexity in trying to evaluate vibrational changes induced by non-covalent bonding with a large number of atoms present.

To examine the dye interactions of I_2 at the thiophene or furan rings, I_2 was positioned near the heterocycles of the geometry optimized dyes in space with a linear orientation of I_2 and the S/O atom all in the same plane as the heterocycle. The geometries were then optimized to the lowest energy conformation. It is noteworthy that a number of binding sites are evident on each dye with stronger binding at the nitrogen atoms of the triarylamine and cyanoacrylic acid; however, these binding events are present in all dyes. We have focused on the heterocycles as these binding events differentiate the thiophene and furan dyes. A close interaction for sulfur and iodine of ~3.45 Å is observed for *cis*- or *trans*-**AB1** (thiophene) with an end-on binding to I_2 at the presumed sigma-hole location (Figure 38, Table 10). When comparing these results to **AB2** (furan) it is interesting that only one conformer (*trans*) binds I_2 to give a linear O-I_2 geometry orientation. The *cis*-**AB2** (furan) conformer does not show an energy minimum with a linear geometry, but instead the I_2 shifts to above the π-face of the system as the nearest energy minimum (Table 10, Figure 38). This result supports our experimental finding that sulfur of thiophene binds I_2 stronger than the oxygen of furan, since one of the potential binding sites for furan is non-active in the *cis* conformation. For the cases where I_2 adopts a linear orientation relative to the sulfur and oxygen atoms, the I_2 molecule adopts a 65° to 81° dihedral angle with the π-system of the heterocycle (Figure 38, Table 10). Similar results are observed when the *trans* and *cis* isomers of **D35** (thiophene) and **AB3** (furan) are compared. For the comparable *trans* isomers, the location of the highest occupied molecular orbital (HOMO) and the lowest unoccupied molecular orbital (LUMO) offer some insight into the nature of this binding event. The HOMO of *trans*-**D35** (thiophene) and *trans*-**AB3** (furan) is delocalized onto the heterocycles

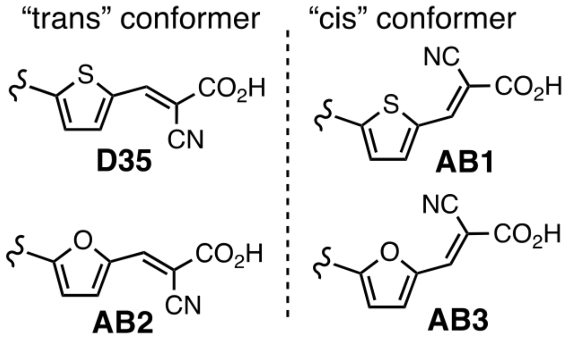

Figure 37. Illustration of the *trans* and *cis* conformer of **D35, AB1, AB2,** and **AB3** assignments.

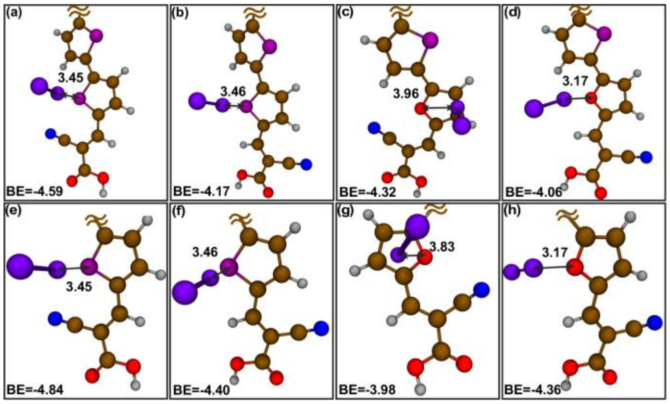

Figure 38. Illustration of the closest I_2 binding energy minima at the heterocycle near that CAA acceptor for *cis*-**AB1**, *trans*-**AB1**, *cis*-**AB2**, *trans*-**AB2**, *cis*-**D35**, *trans*-**D35**, *cis*-**AB3**, and *trans*-**AB3**. Calculations were done at wB97XD/6-31+G* level of theory and basis set. (Figure 39, see Figure 82–85 in Appendix for **AB1** and **AB2** orbitals). In both cases the LUMO is heavily localized on the I_2 molecule suggesting an intermolecular charge transfer event may be possible. This interaction is indicative of a halogen bonding event in a conformation that would be predicted by a first principle approximation.

Binding energies were analyzed for these dyes to I_2 by summing the energies of the dye and I_2 separately optimized in isolation, then comparing with the system energy having both the dye and I_2 present. Again, only the *trans* isomers could be compared as no *cis*-**AB2** (furan)-I_2 optimized geometry could be located which was comparable to thiophene analogue (Table 10). The *trans*-**AB1** (thiophene)-I_2 binding energy was found to be stronger than that of the *trans*-**AB2** (furan)-I_2 binding energy by a 0.11 kcal difference. A very similar analysis can be made comparing **D35** (thiophene) and **AB3** (furan), with **AB3** (furan) again showing no binding in a linear orientation to I_2 for the *cis* conformer and the *trans* conformer showing weaker binding relative to the *trans*-**D35** (thiophene) analogue (Figure 39, Table 10). When the *cis* and *trans* isomers are compared for the thiophene based dyes **AB1** and **D35**, a 0.42-0.44 kcal/mol greater binding energy is present for the *cis* isomers. Thus, not only do thiophene-based dyes have a stronger analogue binding mode than the furans in the *trans* conformation, but they also bind even stronger in the *cis* conformation which is exclusive to thiophene. These results suggest that an I_2 binding event may not be completely absent from furan heterocycles, but thiophene analogues exhibit much stronger halogen bonding interactions in multiple conformations.

Having found optimized geometries for **D35** (thiophene) and **AB3** (furan) with and without I_2, we simulated Raman spectra from DFT calculations at the wB97XD/6-31+G* level of theory to better understand the vibrational modes in the 1400-1800 cm^{-1} range of

Table 10. Computational results of **AB1, AB2, D35** and **AB3** for I_2 binding distance, binding energies and dihedral angles at wB97XD/6-31+G* level.

dye	S/O-I_2 distance (Å)	Binding energy (kcal/mol)	S/O-I_2 dihedral (°)
cis-**AB1** (thiophene)	3.45	-4.59	81
trans-**AB1** (thiophene)	3.46	-4.17	71
cis-**AB2** (furan)	no minimum	no minimum	---
trans-**AB2** (furan)	3.17	-4.06	65
cis-**D35** (thiophene)	3.45	-4.84	81
trans-**D35** (thiophene)	3.46	-4.40	70
cis-**AB3** (furan)	no minimum	no minimum	---
trans-**AB3** (furan)	3.17	-4.36	70

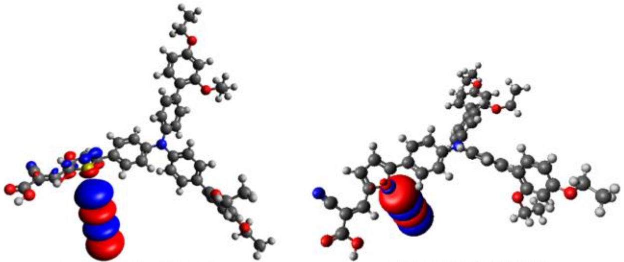

trans-**D35** LUMO *trans*-**AB3** LUMO

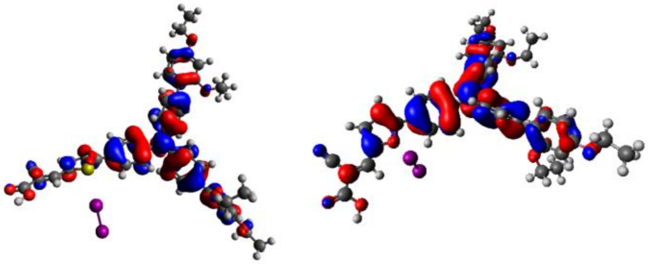

trans-**D35** HOMO *trans*-**AB3** HOMO

Figure 39. HOMO and LUMO orbitals of trans **D35** and **AB3**. Calculations were done at wB97XD/6-31+G* level of theory and basis set. Iso values are set to 0.2.

the experimental Raman spectrum which were changing much more dramatically for **D35** (thiophene) in the presence of I_2 relative to **AB3** (furan, Figures 43 and Figure 81 in Appendix). Two different geometries for each dye were analyzed with and without I_2 present. While the simulated spectra can be used to help understand the experimental spectra, a direct comparison cannot be made since the simulated Raman spectra is obtained in the gas phase with only one I_2 molecule present and under harmonic approximations while the experimental data was collected on the surface with acetonitrile solvent present with a large excess of I_2 molecules. Thus, the comparison of the data is restricted to broad wavenumber ranges rather than to wavenumber peaks. It could be seen that in both the *cis* and *trans* conformations for **AB3** (furan) no shift or emergence of new peaks can be seen when I_2 is present and only a slight change in intensities for 2-3 peaks between 1500-1700 cm^{-1} is observed (Figure 81 in Appendix). However, in terms of **D35** (thiophene), the *cis* conformation shows a slight change in intensity along with a shifting of peaks between 1500-1600 cm^{-1} by 3-5 cm^{-1} toward higher energy, while the *trans* conformation shows intensity changes and some shifting of peaks near 1100 and 1600 cm^{-1} with a new peak at ~1250 cm^{-1} evident (Figure 81 in Appendix). For the DFT Raman spectra, the 1500-1600 cm^{-1} region where the most significant changes are occurring corresponds to ring breathing and stretching modes for both thiophene and furan. Experimentally, the largest changes in the Raman spectrum are occurring near this region as well. Given that the experimental changes when I_2 is present were significantly more pronounced for the thiophene based dyes, this suggests that I_2 is interacting stronger with thiophene resulting in significant changes in ring breathing/stretching modes for this heterocycle but to a lesser extent for furan. It is reasonable that the presence of this interaction for thiophene is due to halogen bonding from the sulfur atom to I_2.

UV-Vis Absorption Spectroscopy. To further evaluate our hypothesis that the sulfur of thiophene binds I_2 more strongly than the oxygen of furan, we measured film UV-Vis absorption spectra for **D35** (thiophene), **AB3** (furan), **LD03** (thiophene) and **LD04** (furan). We reasoned that if I_2 binding were occurring with thiophene effects should also be visible in the UV-Vis spectrum. A S-I_2 halogen bond would be predicted to red-shift the dye absorption spectrum since the I_2 serves as an electron acceptor which would lower the LUMO energy based on first approximations. Therefore, we predict significant observable changes in dye absorption transition energies for the thiophene-based dyes **D35** and **LD03** due to S-I_2 binding and relatively minor changes for the furan-based dyes **AB3** and **LD04** due to a weaker O-I_2 interaction. To probe this prediction, we prepared TiO_2 films of each of the dyes and submerged them in solutions of acetonitrile with and without I_2 present. The UV-Vis spectra were analyzed by comparing the shift in the λ_{max} and shape of the normalized absorption curves. On TiO_2 films submerged in acetonitrile with and without I_2, the λ_{max} of **D35** (thiophene) shifts about 10 nm, while the λ_{max} of **AB3** (furan) shows no shift (Figure 40). For the simple alkoxy donor dyes, **LD03** (thiophene) shows a 7 nm shift in the λ_{max} value, while **LD04** (furan) shows a smaller 3 nm shift (Figure 40). The larger shift in λ_{max} for the thiophene based dyes can be attributed to a halogen bonding event due to the presence of I_2 binding stronger with the sulfur atom in thiophene than the oxygen of furan. Additionally, the shift toward lower energy photon absorption (red-shift) in the presence of I_2 occurs as predicted. This is consistent with the hypothesis that halogen bonding with thiophene and I_2 is occurring by donation of electron density from the sulfur to I_2.

To computationally probe the experimentally observed changes in the UV-Vis spectrum in the presence of I_2, time dependent-density functional theory (TD-DFT) calculations were undertaken to evaluate which orbitals were contributing to the observed red-shift and to identify the position of these orbitals. If I_2 binding is causing the red-shift, a low energy transition of electron density from the dye to I_2 is predicted. To evaluate this prediction, the first 10 states were examined using the previously optimized geometries (both *cis* and *trans* for each dye) for **AB1** (thiophene), **AB2** (furan), **D35** (thiophene), and **AB3** (furan) with TD-DFT calculations at the wB97XD/6-31+G* level of theory. For all of the dyes, in the presence of I_2 the first two states have very low oscillator strengths (*f* of ~0.0005) ranging from 0.3 to 0.5 eV lower in energy than

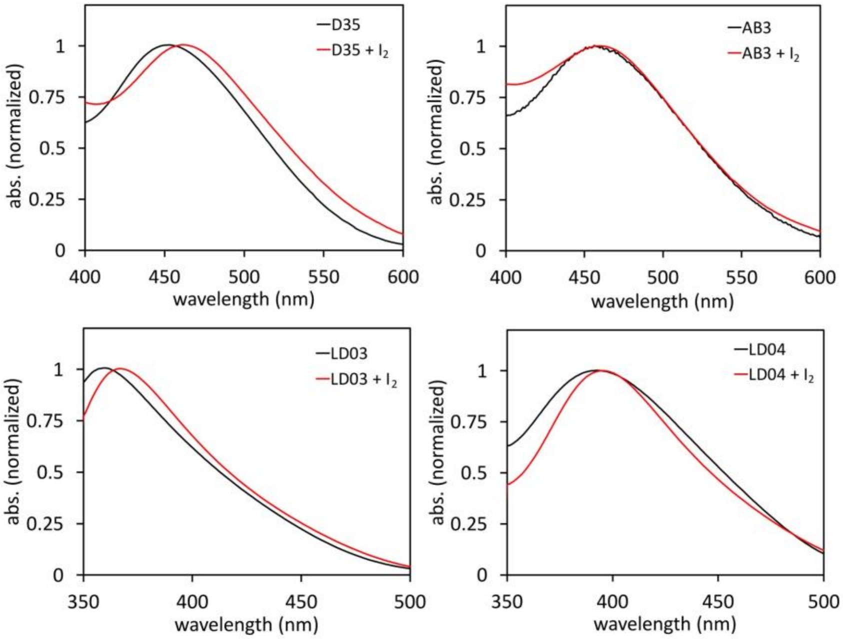

Figure 40. UV-Vis absorption spectra for dyes **D35, AB3**, **LD03,** and **LD04** in acetonitrile with and without I_2 present on films. Background spectrum were subtracted in each case without the dye present but all other components were present.

the first major transition (Table 19-26 in Appendix). The transitions for the first two states also involve a large number of orbitals (up to five occupied to unoccupied transitions). The first strong transition (state 3, *f* of 0.99) for *cis* **AB1** (thiophene) is made up of several transitions from occupied orbitals centered on the dye with no significant concentration on I_2 to unoccupied orbitals localized on I_2. Among the transitions involved in this state, the HOMO-LUMO transition is the strongest contributor at 27% followed by the HOMO-1 to LUMO at 15% with 9 total transitions (Table 11 and Figure 82 in Appendix). Compared to the first state (*f* = 1.7, primarily HOMO to LUMO and HOMO-1 to LUMO) of *cis* **AB1** (thiophene) in the absence of I_2, state 3 of *cis* **AB1** (thiophene) with I_2 is 0.14 eV lower in energy. Analysis of *trans* **AB1**

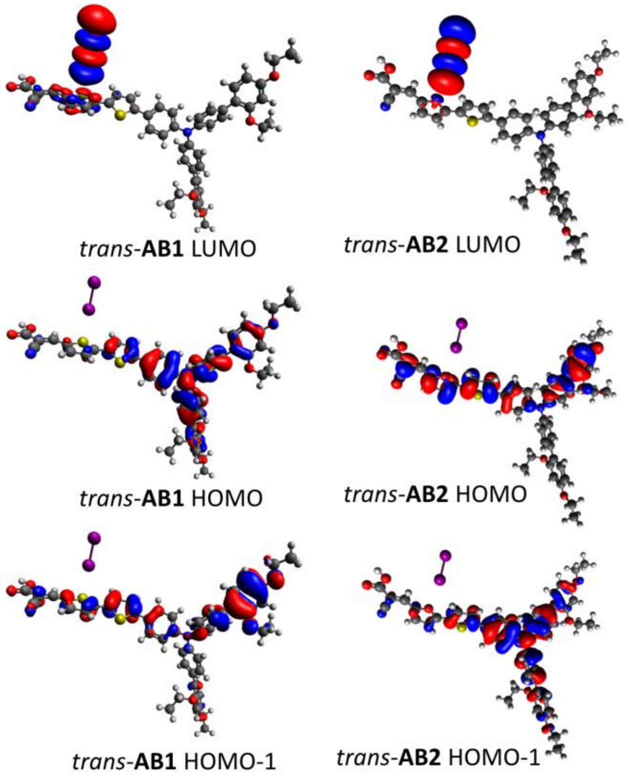

trans-**AB1** LUMO
trans-**AB2** LUMO
trans-**AB1** HOMO
trans-**AB2** HOMO
trans-**AB1** HOMO-1
trans-**AB2** HOMO-1

Figure 41. Orbitals contributing to the first strong oscillator strength state for trans **AB3** and **D35**. Calculations were done at wB97XD/6-31+G* level of theory and basis set.

(thiophene) with and without I_2 reveals a very similar set of observations (Figures 40, Table 10 and Figure 83 in Appendix). As noted previously, the geometry minima for *cis* **AB2** (furan) is significantly different. However, for both *cis* and *trans* isomers of **AB2** (furan), the first two states show very weak oscillator strengths, and the first major oscillator strength observed is for state 3 when I_2 is present. State 3 for *cis* **AB2** (furan) is still comprised of the same dominate orbital transitions as *cis* **AB1** (thiophene) (HOMO to LUMO and HOMO-1 to LUMO, Table 7, Figure 84 in Appendix) and a similar magnitude red-shift, but with fewer transition (5 versus 9). Interestingly, the oscillator strength for this third state is significantly lower in strength for *cis* **AB2** (furan) than for *cis* **AB1** (thiophene) (0.15 versus 0.99). This again suggests a significantly stronger interaction of I_2 with thiophene than furan and supports a S-I_2 halogen bonding hypothesis. *Trans* **AB2** (furan) follows the same analysis as *cis* **AB2** (furan) only with a dramatically lower oscillator strength for state 3 (*f* = 0.02, Table S5, Figure 8 and 84). This data suggests a very weak interaction between the furan heterocycle and I_2 presumably due to the lack of a significant halogen bonding event between O and I_2. These weak red-shifted transition oscillator strengths for **AB2** (furan) in the presence of I_2 are consistent with the relatively minor changes observed by experimental UV-Vis spectroscopy for the furan-based dyes (**AB3** and **LD04**). Computationally, **AB1** (thiophene) shows a much stronger red-shifted transition oscillator strength in the presence of I_2 which is consistent with the experimental data for the thiophene dyes (**D35** and **LD03**) showing a significant red-shift of the UV-Vis spectrum in the presence of I_2. Computationally, both cis and trans isomers of **D35** (thiophene) and **AB3** (furan) follow a similar trend to that described above for **AB1** (thiophene) and **AB2** (furan) (Tables 19-22). The experimental and computational data is again consistent with a stronger S-I_2 halogen bonding event than O-I_2.

Device Data. Given the spectroscopic observations from the surface Raman studies and film UV-Vis studies, several predictions about the performance of the furan-based and thiophene-based dyes in DSC devices can be made based on the cascade of electron transfer events after photoexcitation of the dye. After the injection of an electron from the photoexcited dye into the TiO_2 CB (equation 1), the ground-state dye can be regenerated with iodide (equation 2). Although a number of possible electron transfer pathways exist concerning the iodide redox shuttle,[175] a commonly cited pathway suggests the I_2^- product from equation 2 can then undergo disproportionation to give I_3^- and I^- via equation 3. I_3^- represents the fully oxidized redox shuttle species in DSC devices and is involved with an equilibrium reaction to give I_2 and I^- via equation 4. Thus, I_2 is both continuously being generated within the DSC cell under operational conditions and is explicitly added to the electrolyte to generate a concentration of the triiodide species in solution needed for rapid electron collection at the counter electrode. The electrons injected into the TiO_2 CB can either traverse an external circuit to the counter electrode as desired before following the reverse reactions equation 3 and the reduction of I_2^- via equation 5 to give the original iodide reductant, or these electrons can be transferred to an oxidizing species directly from the TiO_2 CB undesirably (equation 6). Specifically, the recombination rate of electrons in the TiO_2 semiconductor conduction band (CB) with the redox shuttle should be slower for the furan-based dyes compared with the thiophene-based analogues if the sulfur of thiophene is halogen bonding to I_2 near the TiO_2 surface. The rate of this recombination is a function of distance for the through-space electron transfer, and sulfur halogen bonding with I_2 will increase the local concentration of I_2 near the TiO_2 surface to promote the undesirable electron transfer shown in equation 6:

$$\text{dye}^* + TiO_2 \rightarrow \text{dye}^+ + TiO_2(e^-) \qquad (1)$$

$$\text{dye}^+ + 2\,I^- \rightarrow \text{dye} + I_2^- \qquad (2)$$

$$2\,I_2^- \rightarrow I_3^- + I^- \qquad (3)$$

$$I_3^- \rightleftharpoons I_2 + I^- \qquad (4)$$

$$I_2^- + e^- \rightarrow 2\,I^- \qquad (5)$$

$$I_2 + TiO_2(e^-) \rightarrow I_2^- + TiO_2 \qquad (6)$$

Since equation 6 represents a non-productive DSC device electron transfer pathway, it will lower photocurrent because fewer electrons are traveling the external circuit. Additionally, the electron transfer event represented by equation 6 will also lower photovoltage since electrons are being transferred out of TiO_2 more rapidly leading to a depletion of the number of electrons in the TiO_2 CB and lowering the TiO_2 fermi level. These predictions can all be tested through a series of DSC device measurements including current-voltage (*J*-*V*) curve, incident photon-to-current conversion efficiency (IPCE), and small modulation photovoltage transient measurements.

First device performances were analyzed for all of the dyes via *J*-*V* curve measurements (Figure 42, Table 11). In all cases, the furan-based dyes (**AB2**, **AB3**, **LD04**) gave both higher current and voltage than the thiophene analogues (**AB1**, **D35**, **LD03**) as is predicted if a S-I_2 halogen bonding event were occurring. The open-circuit voltage (V_{oc}) values averaged 28 mV higher and the short-circuit current density (J_{sc}) values averaged 0.5 mA/cm^2 higher for the furan derivatives. Via the equation PCE = (V_{oc} x J_{sc} x FF)/I_0, where FF is fill-factor and I_0 is the sun intensity (set to 1 for this study), the furan-based dyes were found to average 0.6% higher in PCE. This equates to a >10% overall gain in performance for the furan-based dyes when compared with the thiophene-based dyes. Upon analysis of the IPCE spectrum, thiophene based dyes **AB1** and **D35** are significantly red-shifted relative to the furan analogues (**AB2** and **AB3**, respectively); however, the peak IPCE value for the furan analogues is significantly higher which explains the observed photocurrents via the *J*-*V* curve measurements (Figure 43). The red-shift of the IPCE spectrum is similar to that observed in the UV-Vis measurements for **D35** (thiophene) when I_2 was added. It is noteworthy, that there is little change in the dye-film absorption spectrum under pure acetonitrile when **D35** (thiophene) and **AB3** (furan) absorption spectrum are

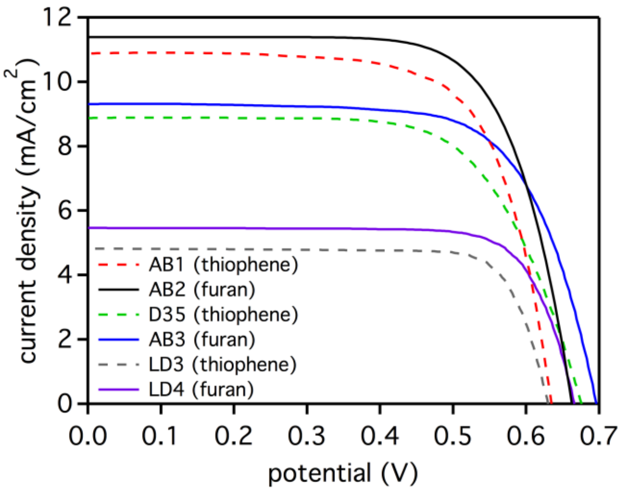

Figure 42. J-V curve comparison for **AB1**, **AB2**, **AB3**, **D35**, **LD03** and **LD04**.

compared (Figure 40). As hypothesized for the UV- Vis data explanation, the IPCE red-shift for the furan dyes can be rationalized as I_2 binding to the thiophene containing dyes to remove electron density from the π-system and lowering the LUMO energy of the system. Having I_2 coordinate to the sulfur in thiophene results in electron density being pulled out of the system, effectively lowering the LUMO of the dye and shrinking the HOMO-LUMO gap as was shown via TD-DFT above. This causes the thiophene-based dyes IPCE's to be selectively red-shifted relative to the film absorption spectrum. For the **LD03** (thiophene)/**LD04** (furan) comparison, the IPCE onset values are similar, but the furan derivative again shows a higher peak performance. The relative increased peak IPCE performance is consistent with the S of thiophene halogen bonding to I_2 to promote unwanted recombination, while a significantly weaker interaction (if any) is present for the O of furan with I_2 which does not promote recombination.

Table 11. Device parameters for **AB1**, **AB2**, **AB3**, **D35**, **LD03** and **LD04**.

dye	V_{oc} (mV)	J_{sc} (mA/cm^2)	*FF*	PCE (%)	dye loading (mol/cm^2)
AB1 (T)	631	11.0	0.65	4.6	2.49×10^{-7}
AB2 (F)	659	11.4	0.71	5.5	2.50×10^{-7}
D35 (T)	675	8.9	0.64	3.9	3.53×10^{-8}
AB3 (F)	696	9.4	0.67	4.5	4.62×10^{-8}
LD03 (T)	630	4.8	0.77	2.4	1.87×10^{-7}
LD04 (F)	664	5.5	0.76	2.8	1.20×10^{-7}

See device fabrication section for TiO_2 thicknesses and compositions. Dyes were deposited from a THF:EtOH (1:4) solution with a dye concentration of 0.3 mM and a 40:1 CDCA:dye ratio overnight in the dark at room temperature. The electrolyte was composed of 0.1 M GuCNS, 1.0 M DMII, 0.03 M I_2, 0.5 M TBP and 0.05 M LiI in 85:15 MeCN:valeronitrile. T = thiophene. F = furan.

To better understand the rate of recombination of electrons in the TiO_2 CB with I_2 (equation 6), electron lifetime measurements were made via small modulated photovoltage transient studies (Figure 44). Given the larger V_{oc} and J_{sc} values for the furan-based dyes, longer electron lifetimes are expected for **AB2** (furan), **AB3** (furan), and **LD04** (furan) than the thiophene analogues. This is indeed the case, with **AB2** (furan) and **LD04** (furan) showing dramatically longer electron lifetimes than **AB1** (thiophene) and **LD03** (thiophene) (Figure 44). Even for the case of the exceptionally long electron lifetime benchmark dye **D35** (thiophene), the furan analogue **AB3**

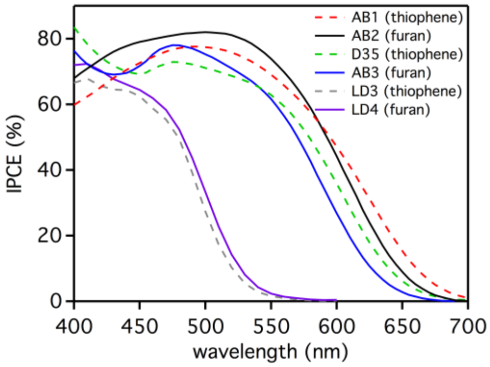

Figure 43. IPCE curves for **AB1**, **AB2**, **D35**, **AB3**, **LD03**, and **LD04**.

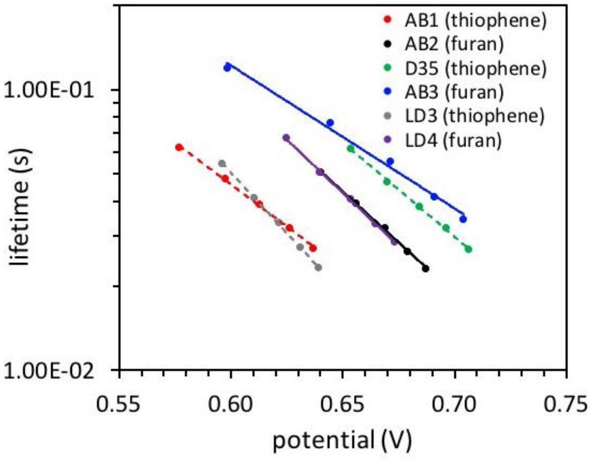

Figure 44. Electron lifetime measurements for dyes **AB1**, **AB2**, **AB3**, **D35**, **LD03** and **LD04** using small modulation photovoltage transient measurements.

shows a longer electron lifetime. These results add further evidence that the sulfur of thiophene is halogen bonding with I_2 near the TiO_2 surface to promote a faster electron recombination event.

Since V_{oc} and J_{sc} device performance metrics are often correlated to dye loadings, dye desorption studies were conducted to probe if dye loading could have had a significant influence in the device data results in addition to the stronger halogen bonding of thiophene relative to furan (Table 11). While the dye analogues only differ by a single atom, the atom used in the heterocycle has a significant influence on the geometry of the substituents at the 2 and 5 positions of furan or thiophene. The O-C bond lengths are shorter for furan which leads to more of a “U” shape, while the S-C bonds are longer in the case of thiophene which leads to more of a linear geometry. The variation in geometry could result in a difference in dye loading despite the seemingly subtle change of a single atom. However, the dye loadings were all found to be similar between the analogues. Specifically, the dye loadings for **AB1** (thiophene) and **AB2** (furan) were found to be near identical at 2.5 x 10^{-7} mol/cm^2, and **D35** (thiophene) was found to have a dye loading within 25% of the value of **AB3** (furan). Interestingly, the dye loading varied the most between **LD03** (thiophene) and **LD04** (furan) with about 55% more **LD03** (thiophene) in the devices, yet despite the higher dye loadings for the thiophene based dye, the furan-based dye still has a higher photocurrent, photovoltage, and electron lifetime within DSC devices. This highlights that the factors controlling the recombination rate for these systems is certainly more than just a simple surface blocking model dominated by dye loadings. These observations further suggest that the halogen bonding of S to I_2 is a primary factor in the uniformly lower V_{oc} and J_{sc} values of thiophene dyes relative to furan.

CONCLUSION

Overall, evidence for stronger binding of I_2 to thiophene containing dyes versus furan containing dyes is observed. Raman spectroscopy on TiO_2 surface bound dyes shows a much more dramatic change in the intensity and shifting of vibrational peaks in the presence of iodine for thiophene-based dyes **LD03** and **D35** relative to the furan-based analogues **LD04** and **AB3**, respectively. UV-Vis analysis again lends evidence of I_2 binding **LD03** (thiophene) and **D35** (thiophene) on TiO_2 showing a red shift in the λ_{max}. Indirect evidence of I_2 binding could be seen for **AB1** (thiophene) and **AB2** (furan) where device V_{oc} and J_{sc} measurements show a higher value for the furan-based dye despite identical dye loadings. This suggests a lower recombination rate which was confirmed via electron lifetime studies through small modulated photovoltage transient measurements for **AB1** and **AB2**. IPCE measurements also showed a red-shift and decrease in IPCE for thiophene based dyes **AB1** and **D35** similar to the addition of an electron withdrawing group, hinting toward the coordination of I_2 to sulfur lowering the LUMO energy. Computational studies lend further evidence to these experimental observations as the thiophene based dyes **AB1** and **D35** were both found to have a stronger influence from an I_2 binding mode at the sulfur atom of thiophene than at the oxygen atom of furan for **AB2** and **AB3**, respectively. TD-DFT results reveal that the thiophene based dyes more readily transfer electron density (have a higher oscillator strength) from the dye to I_2 via the HOMO centered on the dye and LUMO centered on I_2. The oscillator strengths were significantly lower for the analogues charge transfer event with furan-based dyes. This study shows substantial evidence for I_2 binding to the sulfur atoms of thiophene which means dyes should be carefully designed to reduce S and I_2 interactions near the TiO_2 surface for higher device performances.

EXPERIMENTAL

General Experimental Details. All commercially obtained regents were used as received. 2’,4’-dibutoxy-N-(2’,4’-dibutoxy-[1,1’-biphenyl]-4-yl)-N-(4-(4,4,5,5-tetramethyl-1,3,2-dioxaborolan-2-yl)phenyl)-[1,1’-biphenyl]-4-amine and (*E*)-3-(5-(4-(bis(2',4'-dibutoxy-[1,1'-biphenyl]-4-yl)amino)phenyl)thiophen-2-yl)-2-cyanoacrylic acid (D35) were purchased from Dyenamo. 5-bromofuran-2-carbaldehyde was purchased from ArkPharm. Thin-layer chromatography (TLC) was conducted with Sorbtech silica XHL TLC plates and visualized with UV. Flash column chromatography was performed with Sorbent Tech P60, 40-63 um (230-400 mesh). Reverse phase column chromatography was performed with Sorbent Tech C18 P60, 40-63 um (230-400 mesh). ^{1}H and ^{13}C NMR spectra were recorded on a Bruker Avance-300 (300 MHz) spectrometer and a Bruker Avance-500 (500 MHz) spectrometer and are reported in ppm using solvent as an internal standard ($CDCl_3$ at 7.26 and Acetone-d_6 at 2.09). Data reported as s = singlet, d = doublet, t = triplet, q = quartet, p = pentet, m = multiplet, br = broad, ap = apparent, dd = doublet of doublets; coupling constant(s) in Hz. UV spectra were measured with a Cary 5000 UV-Vis-NIR spectrometer with either dichloromethane or 0.1 M Bu_4NOH in DMF solution. Cyclic voltammetry curves were measured with a C-H Instruments electrochemical analyzer CHI600E. (*E*)-3-(5'-(4-(bis(2',4'-dibutoxy-[1,1'-biphenyl]-4-yl)amino)phenyl)-[2,2'-bithiophen]-5-yl)-2-cyanoacrylic acid (AB1), (*E*)-2-cyano-3-(5-(4-(hexyloxy)phenyl)thiophen-2-yl)acrylic acid (LD03) and (*E*)-2-cyano-3-(5-(4-(hexyloxy)phenyl)furan-2-yl)acrylic acid (LD04) were synthesized according to literature procedures.[63-172]

Raman Experimental Details. A Horiba Scientific LabRAM HR Evolution Raman Spectroscopy system was used for the acquisition of Raman spectra. The 633 nm line from a HeNe laser was focused onto solid samples using a 100x objective with a 0.9 NA and a 1800 grooves/mm grating and CCD camera were used for detection.

Computational Details. All geometry optimization and binding energy calculations were completed with Gaussian 16 package.[130] *w*B97XD functional[176] was used to include long-range corrections with D2 dispersion model.[177] Tight optimization criteria were used for both force and density matrix convergence along with ultrafine grid for numerical integration. We used a 6-31+G* basis set for all atoms except for I, where we used LANL2DZdp[178-179] basis set and associated effective core potential. Each dye molecules consists of two different configurations; *cis*- and *trans*-, which are defined as whether the S (for thiophene ring) and O (for furan ring) were on the same or on the different side of N (for nitrile functional group). For the binding energy calculations, 5 (five) different sites were considered for **AB1** and **AB2**; however, in case of **AB3** and **D35**, 4 (four) different sites were considered. In each of these sites, the I_2 molecule was placed at 4 different locations around the considered sites to account for the variations in binding energy. Frequency calculations indicate all geometries are in their corresponding local minima's.

SYNTHETIC PROTOCOLS

5-(5-(4-(bis(2',4'-dibutoxy-[1,1'-biphenyl]-4-yl)amino)phenyl)thiophen-2-yl)furan-3-carbaldehyde: In a 8.0 mL glass vial, 2',4'-dibutoxy-*N*-(2',4'-dibutoxy-[1,1'-biphenyl]-4-yl)-*N*-(4-(4,4,5,5-tetramethyl-1,3,2-dioxaborolan-2-yl)phenyl)-[1,1'-biphenyl]-4-amine (75 mg, 0.092 mmol), 5-(5-bromothiophen-2-yl)furan-2-carbaldehyde[180] (22 mg, 0.084 mmol) and potassium phosphate (53 mg, 0.25 mmol) were dissolved in 1.68 mL of toluene and 0.073 mL of water. The solution was then degassed for about 10 minutes under nitrogen, after which $Pd_2(dba)_3$ (3.0 mg, 0.003 mmol) and XPhos (6.0 mg, 0.013 mmol) were added together. The reaction was then sealed, and brought to 80 ^{o}C for 15 hours. The reaction was then removed from heat and cooled to room temperature. The mixture was then extracted with ethyl acetate and water and dried with magnesium sulfate. The crude product was purified with silica gel chromatography with a gradient from 10% ethyl acetate/hexanes to 20% ethyl acetate/hexanes (0.076 g; 95% yield). ^{1}H NMR (500 MHz, Acetone-d_6) δ 9.66 (s, 1H), 7.71 (d, *J* = 8.7 Hz, 2H), 7.66 (d, *J* = 3.9 Hz, 1H), 7.60-7.55 (m, 5H), 7.51 (d, *J* = 3.9 Hz, 1H), 7.32 (d, *J* = 8.4 Hz, 2H), 7.21 (d, *J* = 8.6 Hz, 4H), 7.18 (d, *J* = 8.7 Hz, 2H), 7.03 (d, *J* = 3.8 Hz, 1H), 6.68 (d, *J* = 2.3 Hz, 2H), 6.64 (dd, *J* = 2.4, 2.4 Hz, 2H), 4.13-4.04 (m, 8H), 1.85-1.73 (m, 8H), 1.62-1.46 (m, 8H), and 1.05-0.95 (m, 12H) ppm. ^{13}C NMR (500 MHz, $CDCl_3$) δ 176.9, 159.7, 157.1, 155.2, 151.5, 148.4, 147.1, 145.5, 133.7, 131.0, 130.4, 129.4, 127.5 (appears broad, assumed 2 signals), 126.9, 126.7, 124.3, 123.3, 123.1, 123.0, 107.3, 105.4, 100.6, 68.3, 67.9, 31.5, 31.3, 19.5, 19.4, 14.0, and 14.0 ppm. IR (neat) ν = 3190, 3073, 3030, 2955, 2926, 2868, 2330, 2117, 1730, 1670, 1599 cm^{-1}. HRMS *m/z* calc'd for $C_{55}H_{59}NO_6SCs$ [M + Cs]$^+$: calculated 994.3118, found 994.3125.

(E)-3-(5-(5-(4-(bis(2',4'-dibutoxy-[1,1'-biphenyl]-4 yl)amino)phenyl)thiophen-2-yl)furan-3-yl)-2-cyanoacrylic acid (AB2): In a 8 mL vial, compound 5-(5-(4-(bis(2',4'-dibutoxy-[1,1'-biphenyl]-4-yl)amino)phenyl)thiophen-2-yl)furan-3-carbaldehyde (0.040 g, 0.047 mmol) was dissolved in 0.94 mL chloroform. The mixture was then degassed with N_2 for approximately 30 minutes. Cyanoacetic acid (0.012 g, 0.14 mmol) and piperidine (0.032 mL, 0.33 mmol) were added to vial, which was then sealed, heated to 90 °C and allowed to stir for 16 hours. The reaction mixture was diluted with dichloromethane and purified through a plug of silica gel with 100% dichloromethane to 10% methanol/dichloromethane to 12% methanol/3% acetic acid/dichloromethane. The solvent of the third fraction was evaporated under reduced pressure. The dye was then extracted with hexanes and water to give the final dye (**AB2**, 0.040 g, 91% yield). ^{1}H NMR (500 MHz, Acetone-*d$_6$*) δ 8.07 (s, 1H), 7.73-7.69 (m, 4H), 7.57 (d, *J* = 8.6 Hz, 4H), 7.55 (d, *J* = 3.9 Hz, 1H), 7.32 (d, *J* = 8.4 Hz, 2H), 7.22-7.17 (m, 6H), 7.11 (d, *J* = 3.7 Hz, 1H), 6.69 (d, *J* = 2.3 Hz, 2H), 6.64 (dd, *J* = 2.4, 2.4 Hz, 2H), 4.11-4.00 (m, 8H), 1.85-1.70 (m, 8H), 1.60-1.46 (m, 8H), and 1.05-0.95 (m, 12H) ppm. IR (neat) ν = 3050, 2952, 2924, 2854, 2360, 2340, 1699, 1602 cm^{-1}. ESI HRMS *m/z* calc'd for $C_{58}H_{59}N_2O_7S$ [M - H]$^-$: calculated 927.4043, found 927.4072.

5-(4-(bis(2',4'-dibutoxy-[1,1'-biphenyl]-4-yl)amino)phenyl)furan-2-carbaldehyde: In a 8.0 mL glass vial, 2',4'-dibutoxy-*N*-(2',4'-dibutoxy-[1,1'-biphenyl]-4-yl)-*N*-(4-(4,4,5,5-tetramethyl-1,3,2-dioxaborolan-2-yl)phenyl)-[1,1'-biphenyl]-4-amine (100 mg, 0.12 mmol), 5-bromofuran-2-

carbaldehyde (20 mg, 0.11 mmol) and potassium phosphate (71 mg, 0.34 mmol) were dissolved in 2.24 mL of toluene and 0.097 mL of water. The solution was then degassed for about 10 minutes under nitrogen, after which $Pd_2(dba)_3$ (4.0 mg, 0.005 mmol) and XPhos (8.5 mg, 0.018 mmol) were added together. The reaction was then sealed, and brought to 80°C for 15 hours. The reaction was then removed from heat and cooled to room temperature. The mixture was then extracted with ethyl acetate and water and dried with magnesium sulfate. The crude product was purified with silica gel chromatography with 10% ethyl acetate/hexanes (0.092 g; 96% yield). ^1H NMR (500 MHz, $CDCl_3$) δ 9.59 (s, 1H), 7.67 (d, *J* = 8.9 Hz, 2H), 7.47 (d, *J* = 8.6 Hz, 4H), 7.30 (d, *J* = 3.8 Hz, 1H), 7.28 (s, 2H), 7.20-7.10 (m, 6H), 6.71 (d, *J* = 3.7 Hz, 1H), 6.65-6,45 (m, 4H), 4.05-3.85 (m, 8H), 1.85-1.70 (m, 8H), 1.50-1.45 (m, 8H), 1.05-0.90 (m, 12H) ppm.^{13}C NMR (500 MHz, $CDCl_3$) δ 177.1, 160.4, 160.0, 157.3, 151.9, 149.8, 145.3, 134.4, 131.2 (signal appears larger than expected, assumed 2 signals), 130.7, 126.7, 124.9, 123.1, 122.4, 122.1, 106.6, 105.7, 100.8, 68.5, 68.1, 31.7, 31.5, 19.7, 19.6, 14.2, 14.2 ppm. IR (neat) ν = 3200, 3037, 2957, 2931, 2870, 2360, 2333, 2115, 1672, 1602, 1600 cm^{-1}. ESI HRMS *m/z* calc'd for $C_{51}H_{57}NO_6Cs$ $[M + Cs]^+$: calculated 912.3240, found 912.3235.

(E)-3-(5-(4-(bis(2',4'-dibutoxy-[1,1'-biphenyl]-4-yl)amino)phenyl)furan-2-yl)-2-cyanoacrylic acid (AB3): In a 8.0 mL vial, 5-(4-(bis(2',4'-dibutoxy-[1,1'-biphenyl]-4-yl)amino)phenyl)furan-2-carbaldehyde (0.056 g, 0.072 mmol) was dissolved in 1.50 mL chloroform. The mixture was then degassed with N_2 for approximately 30 minutes. Cyanoacetic acid (0.018 g, 0.217 mmol) and piperidine (0.050 mL, 0.507 mmol) were added to vial, which was then sealed, heated to 90°C and allowed to stir for 16 hours. The reaction mixture was diluted with dichloromethane and purified through a plug of silica gel with 100% dichloromethane to 10% methanol/dichloromethane to 12% methanol/3% acetic acid/dichloromethane. The solvent of the third fraction was evaporated under reduced pressure. The dye was then extracted with hexanes and water to give **AB3** with trace impurities. The product was then purified using reverse phase column chromatography with a gradient from 10% methanol/acetonitrile to 50% methanol/acetonitrile, then with a CombiFlash R_f^+ chromatography system (RediSep R_f Gold high performance silica gel, 0% methanol/dichloromethane —> 10% methanol/dichloromethane) to give the final pure dye (0.014 g, 23%). ^{1}H NMR (500 MHz, $CDCl_3$) δ7.94 (s, 1H), 7.72 (d, *J* = 8.8 Hz, 2H), 7.47 (d, *J* = 8.7 Hz, 4H), 7.28-7.25 (m, 3H), 7.21-7.16 (m, 6H), 6.81 (d, *J* = 3.8 Hz, 1H), 6.60-6.52 (m, 4H), 4.05-3.95 (m, 8H), 1.85-1.70 (m, 8H), 1.50-1.45 (m, 8H), 1.05-0.90 (m, 12H) ppm. IR (neat) ν = 3340, 2944, 2923, 2854, 2333, 2114, 1602, 1593 cm^{-1}. ESI HRMS *m/z* calc'd for $C_{54}H_{59}N_2O_7$ $[M + H]^+$: calculated 847.4323, found 847.4347.

Photovoltaic Device Characterization. Photovoltaic characteristics were measured using a 150 W xenon lamp (Model SF150B, SCIENCETECH Inc. Class ABA) solar simulator equipped with an AM 1.5 G filter for a less than 2% spectral mismatch. Prior to each measurement, the solar simulator output was calibrated with a KG5 filtered mono-crystalline silicon NREL calibrated reference cell from ABET Technologies (Model 15150-KG5). The current density-voltage characteristic of each cell was obtained with a Keithley digital source-meter (Model 2400). The incident photon-to-current conversion efficiency was measured with an IPCE instrument manufactured by Dyenamo comprised of a 175 W xenon lamp (CERMAX, Model LX175F), monochromator (Spectral Products, Model CM110, Czerny-Turner, dual-grating), filter wheel (Spectral Products, Model AB301T, fitted with filter AB3044 [440 nm high pass] and filter AB3051 [510 nm high pass]), a calibrated UV-enhanced silicon photodiode reference and Dyenamo issued software.

Photovoltaic Device Fabrication. For the photoanode, TEC 10 glass was purchased from Hartford Glass. Once cut into 2x2 cm squares, the substrate was submerged in a 0.2% Deconex 21 aqueous solution and sonicated for 15 minutes at room temperature. The electrodes were rinsed with water and sonicated in acetone 10 minutes followed by sonication in ethanol for 10 minutes. Finally, the electrodes were placed under UV/ozone for 15 minutes (UV-Ozone Cleaning System, Model ProCleaner by UVFAB Systems). A compact TiO_2 underlayer is then applied by treatment of the substrate submerged in a 40 mM $TiCl_4$ solution in water (prepared from 99.9% $TiCl_4$ between 0-5^{o}C). The submerged substrates (conductive side up) were heated for 30 minutes at 70^{o}C. After heating, the substrates were rinsed first with water then with ethanol. The photoanode consists of thin TiO_2 electrodes comprised of a 10 μm mesoporous TiO_2 layer (particle size: 20 nm, Dyesol, DSL 18NR-T) for iodine cells with a 5 μm TiO_2 scattering layer (particle size: >100 nm, Solaronix R/SP). Both layers were screen printed from a Sefar screen (54/137–64W) resulting in 5 μm thickness for each print. Between each print, the substrate was heated for 7 minutes at 125^{o}C and the thickness was measured with a profilometer (Alpha-Step D-500 KLA Tencor). The substrate was then sintered with progressive heating from 125^{o}C (5 minute ramp from r.t., 5 minute hold) to 325^{o}C (15 minute ramp from 125^{o}C, 5 minute hold) to 375^{o}C (5 minute ramp from 325^{o}C, 5 minute hold) to 450^{o}C (5 minute ramp from 375^{o}C, 15 minute hold) to 500^{o}C (5 minute ramp from 450^{o}C, 15 minute hold) using a programmable furnace (Vulcan® 3-Series Model 3-550). The cooled, sintered photoanode was soaked 30 minutes at 70^{o}C in a 40 mM $TiCl_4$ water solution and heated again at 500^{o}C for 30 minutes prior to sensitization. The complete working electrode was prepared by immersing the TiO_2 film into the dye solution for 16 hours. The solution for all the dyes consists of 0.3 mM dye, with 40x of CDCA (chenodeoxycholic acid) (i.e. 40:1, CDCA:dye ratio) in (4:1)

EtOH:THF. For preparing the counter electrode, 2x2 cm squares of TEC 7 FTO glass were drilled using Dremel-4000 with a Dremel 7134 Diamond Taper Point Bit from the back side to a taped FTO side. After the tape was removed, the electrodes were washed with water followed by a 0.1 M HCl in EtOH wash and sonication in acetone bath for 10 minutes. The washed electrodes were then dried at 400^{o}C for 15 minutes. A thin layer of Pt-paste (Solaronix, Platisol T/SP) on TCO was slot printed though a punched tape and the printed electrodes were then cured at 450^{o}C for 10 minutes. After allowing them to cool to room temperature, the working electrodes were then sealed with a 25 μm thick hot melt film (Meltonix 1170-25, Solaronix) by heating the system at 130^{o}C under 0.2 psi pressure for 1 minute. Devices were completed by filling the electrolyte through the pre-drilled holes in the counter electrodes and finally the holes were sealed with a Meltonix 1170-25 circle and a thin glass cover slip by heating at 130^{o}C under pressure 0.1psi for 25 seconds. Finally, soldered contacts were added with a MBR Ultrasonic soldering machine (model USS-9210) with solder alloy (Cerasolzer wire dia 1.6mm item # CS186-150). A circular black mask (active area 0.15 cm^{2}) punched from black tape was used in the subsequent photovoltaic studies.

Electron Lifetime Measurements. Electron lifetime measurements *via* small modulated photovoltage transient measurements, were carried out with a Dyenamo Toolbox (DN-AE01) instrument and software. The intensity of the LED light source (Seoul Semiconductors, Natural White, S42182H, 450 to 750 nm emission) is varied to modulate the device open-circuit voltage. The biased light intensity was modulated by applied voltages of 2.80, 2.85, 2.90, 2.95, and 3.00 V applied to the LED with the 3.0 V bias approaching 1 sun intensity (97%). The direction of illumination was from the photoanode to the counter electrode, and the device was positioned 5 cm from the LED light source. The voltage rise and decay times are fitted with a Levenberg-

Marquardt fitting algorithm via LabView, and the electron lifetime was obtained from the averaging of rise and decay time.

CHAPTER 6

6.1 ACCELERATED ELECTRON TRANSFER VIA SELF-ASSEMBLED HALOGENATED ORGANIC DYES AND PERIPHERAL LEWIS BASE DECORATED REDOX SHUTTLES IN DYE-SENSITIZED SOLAR CELLS

Alexandra Baumann; Leigh Anna Hunt; Md. Abdus Sabuj; Hammad Cheema; Yanbing Zhang; Neeraj Rai; Nathan I. Hammer; Jared H. Delcamp

This project is a collaborative project between Dr. Delcamp, Dr. Hammer, and Dr. Rai's groups. Alexandra Baumann contributed to this work by synthesizing the AB4-AB7 dyes and cobalt redox shuttles. Hammad Cheema and Yanbing Zhang contributed to this work by fabricating and testing devices. Md Abdus Sabuj contributed to this work by running computational studies on the AB4-AB7 dyes. Leigh Anna Hunt contributed to this work by running transient absorption spectroscopy studies on the dyes.

ABSTRACT

A metal-free CPDT-based molecular framework with varying halogens installed within the conjugated path of the motif has been introduced to study the effects of halogen bonding on dye regeneration. Four sensitizers (**AB4**, **AB5**, **AB6**, and **AB7**) have been synthesized and fully characterized via UV–Vis absorption, cyclic voltammetry, density functional theory (DFT)

calculations, and in dye-sensitized solar cell (DSC) devices. Modifications to attached halogen and redox shuttles structure and availability to partake in halogen bonding were evaluated via device efficiency to examine if a trend was seen. Ground- and excited-state oxidation potentials were measured to show energetically favorable charge transfer events with little to no change in the potentials between dyes. Importantly, the placement of the halogen within the path of the conjugated system of the dye structure was found to have a strong influence on trends seen from device data. The DSC device electrolyte was also found to little influence on the performance trend seen with the dyes. Electron transfer events were probed for each dye with DSC device measurements and TAS studies.

INTRODUCTION

Dye-sensitized solar cells (DSCs) are a viable renewable energy source for sustainable solar-to-electric energy conversion due to a relatively low cost compared to many other photovoltaic technologies, ease of fabrication, and design flexibility of the molecular components.[1,75,114,116,117,201-204] DSCs operate through a series of electron transfers as follows: (1) photoexcitation of a dye molecule to drive electron injection into the TiO_2 conduction band (CB), (2) movement of the injected electron through an external circuit to the counter electrode, (3) collection of the injected electron at the counter electrode by the oxidized redox shuttle, and (4) transfer of the injected electron to the dye cation by the redox shuttle to regenerate the neutral dye. One of the key steps in this cycle is the regeneration of the neutral dye by a reduced redox shuttle. In order for a DSC device to efficiently operate the regeneration step should be orders of magnitude faster than the non-desirable electron transfer pathway from the TiO_2 CB to the oxidized dye. Molecular component designs capable of speeding up the regeneration step with organic dyes and transition metal complexes are particularly intriguing since organic dyes and transition metal complexes have been dominate with respect to recent DSC record setting devices.[3,5,8,29,41,44,205] Recently, halogen bonding between halogenated organic dyes and the iodide/triiodide redox shuttle has shown exceptional promise for increasing the rate of dye regeneration.[18,160,185]

Halogen bonds typically refer to non-covalent interactions involving a halogen atom,[206] which can have a negative influence on DSCs by holding an oxidized redox shuttle at dye site near the TiO_2 surface[11,12,16] or a positive influence on DSCs by association to the reduced redox shuttle to a dye site far from the TiO_2 surface.[18,160,185] Within DSCs, this effect has commonly been observed with the I^-/I_3^- redox shuttle, and to the best of our knowledge halogen bonding has not been observed with transition metal-based redox shuttles to a halogen on a dye molecule. Given the importance of Co and Cu based redox shuttles and compatible dyes on progressing the DSC field to higher efficiencies,[207] designing systems with faster regeneration events using transition metal based redox shuttles via self-assembly or non-covalent interactions is an important direction to further progress the field.[19,186,208] Literature has shown significant precedent for the use of Lewis Basic functionality coordinating to halogens. Thus, a redox shuttle with an accessible peripheral Lewis Basic site ($Co(N\text{-tpy})_2^{2+}$) was targeted for analysis via computational analysis, DSC performances, and transient absorption spectroscopy (TAS) with a series of dyes having a single atom change (H, Cl, Br, and I) at the position furthest from the TiO_2 surface (Figure 45). This series allows for probing of potential halogen bonding events expected to increase in strength as the halogen size increases, which could result in faster dye regeneration with Co(*N*-tpy)$_2^{2+}$ as halide size increases relative to a non-halogen bonding redox shuttle Co(tpy)$_2^{2+}$.

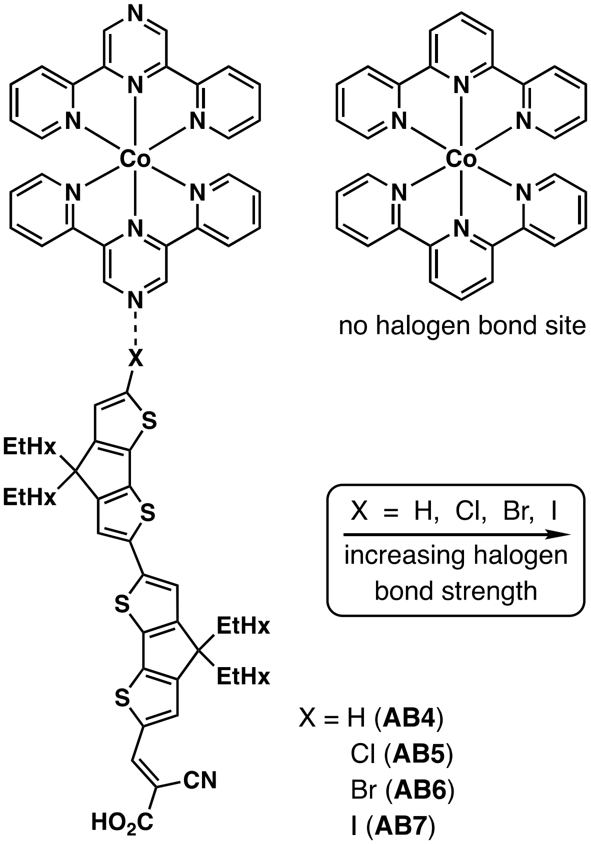

Figure 45. Non-covalent interaction between a cobalt-based redox shuttle (Co(*N*-tpy)$_2$) and a halogen atom on a dye.

A series of analogous dyes were synthesized that differed only by the identity of a single atom substituent attached to a cyclopentadithiophene (CPDT) group (Scheme 3). The use of a CPDT group to attach halogen atoms provides an opportunity to examine the effects of having a halogen in conjugation with the intramolecular charge transfer (ICT) π-system which can allow for migration of a positive charge toward the halide on the donor region after photoinduced electron transfer from the dye to the TiO_2 CB.[209] Additional of positive charge near the halide has been shown to increase halogen bond donor strength and could result in stronger binding of the redox shuttle to the cationic dye for fast regeneration after charge injection. Two CPDT groups were used to extend the conjugation of the system to allow for both broader and increased visible light absorption.[23] The synthesis of the target dyes **AB4** (H derivative), **AB5** (Cl derivative), **AB6** (Br derivative), and **AB7** (I derivative) began with the Stille coupling of known stannylated CPDT compound **1**[210] and known brominated CPDT **2**[211] to give bis-CPDT **3** in 68% yield. **3** can then be halogenated with the appropriate succinimde-halide to give the chlorinated (**4**), brominated (**5**), and iodinated (**6**) intermediates in 75-94% yield. Finally, a Knoevenagel reaction with cyanoacetic acid yielded the target dyes in 85-89% yield. [Co(tpy)$_2$][TFSI]$_2$, [Co(tpy)$_2$][TFSI]$_3$, [Co(*N*-tpy)$_2$][TFSI]$_2$, [Co(*N*-tpy)$_2$][TFSI]$_3$ were prepared according to literature precident.[212]

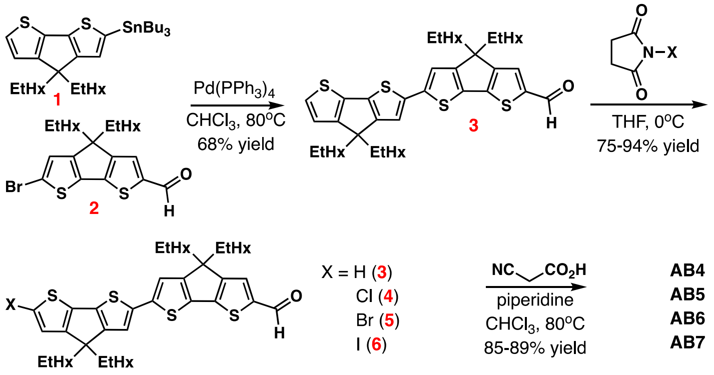

Scheme 3: Synthetic route for target dyes **AB4**, **AB5**, **AB6** and **AB7**.

RESULTS AND DISCUSSION

Computational studies were undertaken on all four dyes to evaluate the orbital positions and predicted optical properties of the neutral and charged dyes at the 6-31G(d,p)/ωB97XD level to account for long-range interactions[177] with a D2 dispersion correction.[178] The LANL2DZdp basis set with effective core potential was used for all halides.[137,179] Geometry optimization reveals that the highest occupied molecular orbital (HOMO) is distributed across the two CPDT groups for all of the neutral dyes with some HOMO orbital contribution on the halides (when present). No significant change in HOMO orbital position is noted based on halide choice (Figure 46). The lowest unoccupied molecular orbital (LUMO) is primarily located on the CPDT group attached to the cyanoacrylic acid (CAA) group and on the CAA. No significant change based on halide is observed for the LUMO, and no LUMO contribution is observed on the halide group. Based on the orbital positions and analysis of charge transfer amounts and distances (Table 12), these dyes are clearly behaving as ICT dyes. Upon photoinduced electron transfer a cationic dye is generated, and to examine this the singly occupied molecular orbitals (SOMO) and singly unoccupied molecular orbitals (SUMO) were examined. The SOMO and HOMO orbitals are very similar in positioning on the dyes; however, unlike the LUMO, the SUMO shows considerable involvement on both CPDT groups with the beta-SUMO showing significant contribution on the halide groups. This suggests that a redox shuttle with Lewis basic

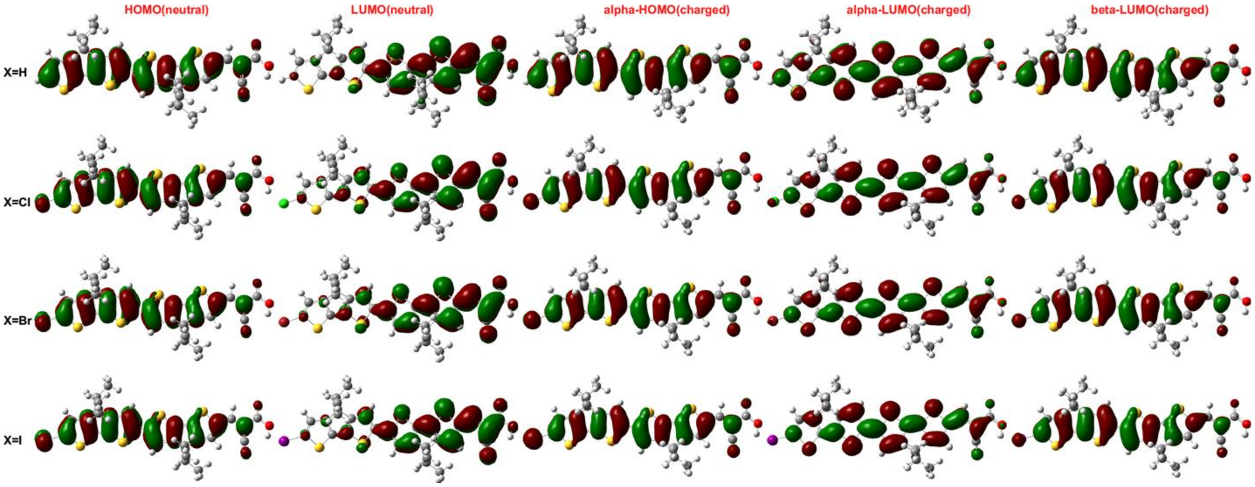

Figure 46. HOMO and LUMO orbitals of the neutral and charged dyes.

functionality on the periphery could coordinate the halide with a close interaction of the SUMO to increase regeneration rates. Notably, the halides have almost no effect on the orbital energies (Table 13) thus no changes in free energy for electron transfers are expected for each dye which allows of a more direct evaluation of halogen bonding effects.

Table 12: Calculated charge transfer distance due to excitation from ground to first excited states, the total amount of charge transfer between ground to excited states, transition energies due to the excitation from the ground to the first singlet excited state (S_0-S_1) with oscillator strengths for the neutral and positively charged dyes.

Substituents (*X*)	D_{CT} (Å)		q_{CT} ($\|e^-\|$)		λ (nm)		*f*	
	Neutral	Charged	Neutral	Charged	Neutral	Charged	Neutral	Charged
H	2.96	1.79	0.484	0.374	423.08	782.26	2.08	0.40
Cl	2.86	1.46	0.472	0.378	422.20	797.11	2.16	0.44
Br	2.87	1.36	0.473	0.387	423.00	800.92	2.20	0.46
I	2.88	1.23	0.477	0.401	424.50	805.66	2.24	0.49

Table 13: Computed frontier molecular orbital energies, energy gap, optical gap and partial charges on the substituents for neutral and positively charged dyes.

Substituents (*X*)	HOMO (eV)		LUMO (eV)		HOMO-LUMO gap (eV)		Optical gap (eV) (S_0-S_1)		CM5 charges (e^-)	
	Neutral	Charged	Neutral	Charged	Neutral	Charged	Neutral	Charged	Neutral	Charged
H	-6.82	-7.45	-1.27	-1.84	5.55	5.61	2.93	1.58	0.122	0.141
Cl	-6.87	-7.47	-1.28	-1.89	5.58	5.57	2.94	1.55	-0.069	-0.017
Br	-6.86	-7.47	-1.28	-1.90	5.58	5.57	2.93	1.55	-0.018	0.039
I	-6.85	-7.46	-1.28	-1.89	5.57	5.57	2.92	1.54	-0.0007	0.063

The optical properties of the dyes were evaluated with absorption spectroscopy in dichloromethane. The dyes have absorption maxima (λ_{max}) narrowly ranging from 536-547 nm with absorption curve onsets (λ_{onset}) also closely grouped at 660-675 nm (Table 14). These values differ by 0.04 eV or less with no obvious trend based on halide. Interestingly, a clear trend is observed for the dye molar absorptivities (ε) with a modest increase in molar absorptivity from 25,000 $M^{-1}cm^{-1}$ to 31,000 $M^{-1}cm^{-1}$ according to the following order: H < Cl < Br < I. TD-DFT analysis shows a similar data set with no clear trend based on halide for the vertical transitions, but an increasing oscillator strength is observed as the halide increases size (Table 15).

Table 14. Optical and electrochemical properties of **AB4-AB7**.[a]

Dye	λ_{max}	ε_{max}	λ_{onset}	$E_{(S+/S)}$ (V)	$E_{(S+/S*)}$	E_g^{opt} (eV)
AB4	536	25000	660	0.96	-0.92	1.88
AB5	545	27000	675	0.99	-0.85	1.84
AB6	541	28000	665	0.99	-0.89	1.87
AB7	547	31000	660	0.99	-0.89	1.88

[a]Optical data is measure in dichloromethane, electrochemical data above is reported in acetonitrile from solution measurements. E_g^{opt} was estimated from the onset of the absorption curve. Conversion from nanometers to eV was calculated by $E_g^{opt} = 1240/\lambda_{onset.}$

Table 15: Calculated charge transfer distance due to excitation from ground to first excited states, the total amount of charge transfer between ground to excited states, transition energies due to the excitation from the ground to the first singlet excited state (S_0-S_1) with oscillator strengths for the neutral and positively charged dyes.

Substituents (*X*)	Orbital Contribution (%)		λ (nm)		*f*	
	Neutral	Charged	Neutral	Charged	Neutral	Charged
H	H -> L 98%	H -> L 98%	423.08	782.26	2.08	0.40
Cl	H -> L 98%	H -> L 98%	422.20	797.11	2.16	0.44
Br	H -> L 98%	H -> L 98%	423.00	800.92	2.20	0.46
I	H -> L 98%	H -> L 98%	424.50	805.66	2.24	0.49

Cyclic voltammographs (CVs) were obtained for each of the dyes in dichloromethane showing a closely group set of ground state oxidation potentials ($E_{(S+/S)}$) from 0.96 V to 0.99 V versus normal hydrogen electrode (NHE) (Table 14). The excited state oxidation potentials ($E_{(S+/S*)}$) of the dyes were found via the equation $E_{(S+/S*)} = E_{(S+/S)} - E_g^{opt}$ with another close grouping of potentials at –0.85 V to –0.92 V with no halide trend observed. The $E_{(S+/S*)}$ and $E_{(S+/S)}$ value differences among the dyes agrees with the computational data showing little change in orbital energies. All of the dyes can adequately inject electrons into TiO_2 based on orbital position and the favorable free energy for electron transfer from the excited state dye to the TiO_2 CB by at least 350 mV when the TiO_2 CB is taken at –0.5 V versus NHE. To prove the generation favorability with these dyes and the two cobalt redox shuttles, CV data was collected with $Co(N\text{-tpy})_2^{2+}$ and $Co(tpy)_2^{2+}$ redox shuttles.

The molecular electrostatic potential (MEP) surfaces were analyzed for each of the dyes to assess the possibility of halogen bonding with each dye to the $Co(N\text{-tpy})_2^{2+}$ redox shuttle (Figure 47). In both the neutral and cationic states of the dyes, the halide group shows a

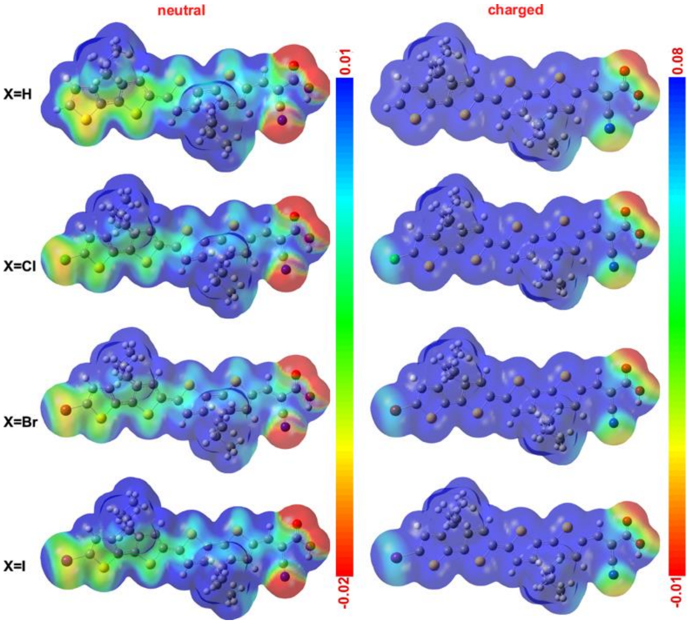

Figure 47: Molecular electrostatic potential (MEP) surface for the neutral and positively charged

dyes. The Isosurface value for the total electron density is 0.001 au with the potential value shown in the scale. The blue and red surface represents the highest (less electrons) and lowest (more electrons) electrostatic potential, respectively.

significantly positive region at the end of the halide as a σ-hole. The size and charge of the σ-hole increases as the halides increase in size suggesting $Co(N\text{-tpy})_2^{2+}$ should bind **AB7** the strongest followed by **AB6**, and **AB5**. When the Lewis basic functionality of $Co(N\text{-tpy})_2^{2+}$ is placed near the halogen atom σ-hole a favorable interaction and geometry could be observed computationally. The binding energy obtained from this interaction gave the following halide trend from low to high binding strength: Cl < H < Br < I with a range of –6.37 kcal/mole for **AB5** to –9.44 kcal/mole for **AB7** (Tables 16). A similar biding energy is observed in the cationic state as well with bonding distances of 2.34 Å to 3.14 Å observed which is a common halogen bonding distance. Interestingly, when $Co(tpy)_2^{2+}$ was evaluated in place of $Co(N\text{-tpy})_2^{2+}$ no binding of the redox shuttle to any of the neutral dyes was observed computationally. For the cationic dyes, $Co(tpy)_2^{2+}$ was observed to bind to the dyes with a lower binding energy of –5.01 kcal/mole or less for each dye. These results suggest a significant halogen bonding event can take place with these dyes for $Co(N\text{-tpy})_2^{2+}$ which can lead to increase regeneration rates for the dyes based on halide choice.

DSC devices were constructed with each dye with both $Co(N\text{-tpy})_2^{3+/2+}$ and $Co(tpy)_2^{3+/2+}$ after having established suitable dye and redox shuttle energetics, good orbital positioning on the dyes, and favorable predicted binding of the $Co(N\text{-tpy})_2^{2+}$ redox shuttle to the halogenated dyes. The device performance efficiencies were evaluated via current density-voltage (*J*-*V*) curves according to the equation PCE = $(J_{SC} \times V_{OC} \times FF)/I_0$, where PCE is the power conversion efficiency, J_{SC} is the short-circuit current density, V_{OC} is the open circuit voltage, FF is the fill factor, and I_0 is the incident sun intensity (Table 17). This allowed for any differences in device data to be attributed to the effects of non-covalent interactions between the redox shuttles and the dyes in devices. Based on initial spectroscopic data, it can be predicted that in the absence of non-covalent interactions performance of all the dyes within DSC devices should vary minimally. However, if non-covalent interactions between the halogenated dye and redox shuttles are present, a difference in device performance would be seen.

Table 16: Calculated binding energy between the redox-shuttles and different dyes and the distance between the dye substituents (*X*) and redox-shuttles.

Redox-shuttle	Substituents (*X*)	Binding Energy (kcal/mole)		Distance (Å)	
		Neutral	Charged	Neutral	Charged
Co(N-tpy)$_3$	H	-7.17	-7.27	2.34	2.28
	Cl	-6.37	-6.22	3.14	3.07
	Br	-7.69	-7.39	3.07	3.00
	I	-9.44	-9.30	3.07	3.00
Co(tpy)$_3$	H	-	-4.62	-	3.08
	Cl	-	-4.81	-	3.63
	Br	-	-4.86	-	3.76
	I	-	-5.01	-	3.96

Table 17. Summary of photovoltaic parameters for DSC devices prepared with dyes **AB4**, **AB5**, **AB6** and **AB7**.

Dye	V_{oc} (mV)	J_{sc} (mA*cm^{-2})	FF (%)	PCE (%)	dye-loading (mol/cm^2)
$Co(N\text{-}tpy)_2^{3+/2+}$					
AB4	700	2.2	66	1.00	
AB5	713	3.0	65	1.40	
AB6	732	3.0	69	1.50	
AB7	760	5.3	68	2.80	
$Co(tpy)_2^{3+/2+}$					
AB4	523	4.1	65	1.43	
AB5	558	4.7	71	1.90	
AB6	559	4.9	65	1.83	
AB7	573	6.3	67	2.45	

Device performances were initially analyzed for all dyes in the presence of each redox shuttle *via J-V* curve measurements (Figure 113, Table 18). In the case of all three redox shuttles it was seen that the absence of a halogen (**AB4**) produced the lowest current and voltage in comparison to the halogen analogues (**AB5**, **AB6**, **AB7**) as is predicted if a halogen bonding event were occurring. For the halogen-based dyes it was seen that the device performance for Cl- and Br-based dyes (**AB5**, **AB6**) in the presence of all redox shuttles varied minimally, while I-based dye (**AB7**) always produced the highest performing devices. The open-circuit voltage (Voc) values averaged 6-79 mV lower and short-circuit current density (Jsc) and 0.6-4.3 mA/cm-2 lower for H-based **AB4** in comparison to halogen-based **AB5**, **AB6**, **AB7**, with the biggest difference being seen between **AB4** and **AB7**. The PCE, from the equation PCE = (Voc x Jsc x FF)/Io, of H-based **AB4** averaged 0.4-0.8% and 1.0-2.4% lower when compared to Cl- and Br-based **AB5** and **AB6** and I-based **AB7**, respectively.

Table 18. Summary of photovoltaic parameters for DSC devices prepared with dyes **AB4**, **AB5**, **AB6** and **AB7**.

Dye	V_{oc} (mV)	J_{sc} (mA cm^{-2})	FF (%)	PCE (%)
Iodine				
AB4	510	6.9	69	2.43
AB5	517	8.7	71	3.33
AB6	524	8.5	72	3.22
AB7	589	11.2	73	4.82
Co(terpy)$_2^{2+/3+}$				
AB4	523	4.1	65	1.43
AB5	558	4.7	71	1.90
AB6	559	4.9	65	1.83
AB7	573	6.3	67	2.45
Co(N-terpy)$_2^{2+/3+}$				
AB4	700	2.2	66	1.00
AB5	713	3.0	65	1.40
AB6	732	3.0	69	1.50
AB7	760	5.3	68	2.80

Analysis of the IPCE spectrum for the dyes in the case of all redox shuttles showed while there was no shift in the IPCE between any of the dyes, the peak IPCE values were always significantly lower for H-based **AB4** in comparison to the halogen-based **AB5**, **AB6**, and **AB7** (Figure 114). However, while the peak IPCE for Cl- and Br-based **AB5** and **AB6** remained extremely close, I-based **AB7** appeared significantly higher than all dyes.

In order to better understand how the non-covalent interactions between the dyes and redox shuttles in devices were effecting the recombination and regeneration rates, electron lifetime measurements and electrochemical impedance spectroscopy (EIS) were conducted with each of the different redox shuttles for each dye. Small modulated photovoltage transient measurements probed the electron lifetimes (Figure S10). With I-based **AB7** having larger Voc and Jsc values for all three redox shuttles, it was expected that it would also exhibit the longest electron lifetime. This was seen to be the case for the I^-/I_3^- and $Co(terpy)_2^{2+/3+}$ based redox shuttles. While the $Co(N\text{-}terpy)_2^{2+/3+}$ redox shuttle showed **AB7** having a shorter lifetime than Br-based **AB6**, the difference between the two is extremely small and can be considered a negligible difference. These results provide evidence that halogen effects have the ability to influence the rate of recombination. EIS was also conducted with each of the different redox shuttles at an open circuit potential in order to further probe how electron collection was influenced by any halogen effects (Figure 48, Table 34). The charge recombination resistance was seen to be the lowest for the dye with the largest halogen (**AB7**) regardless of the redox shuttle used upon analyzing the Nyquist plots. With this observation it would be expected that the dye exhibiting the smallest charge recombination resistance, **AB7**, should also exhibit a smaller charge collection efficiency (η_{cc}) based on the equation: $\eta_{cc} = 1/(1+(R_{CE}/R_{rec}))$, where R_{CE} is the resistance at the counter electrode. However there is little difference in the collection efficiency between dyes, varying between 3-12%, indicating that the effect of R_{rec} is low.

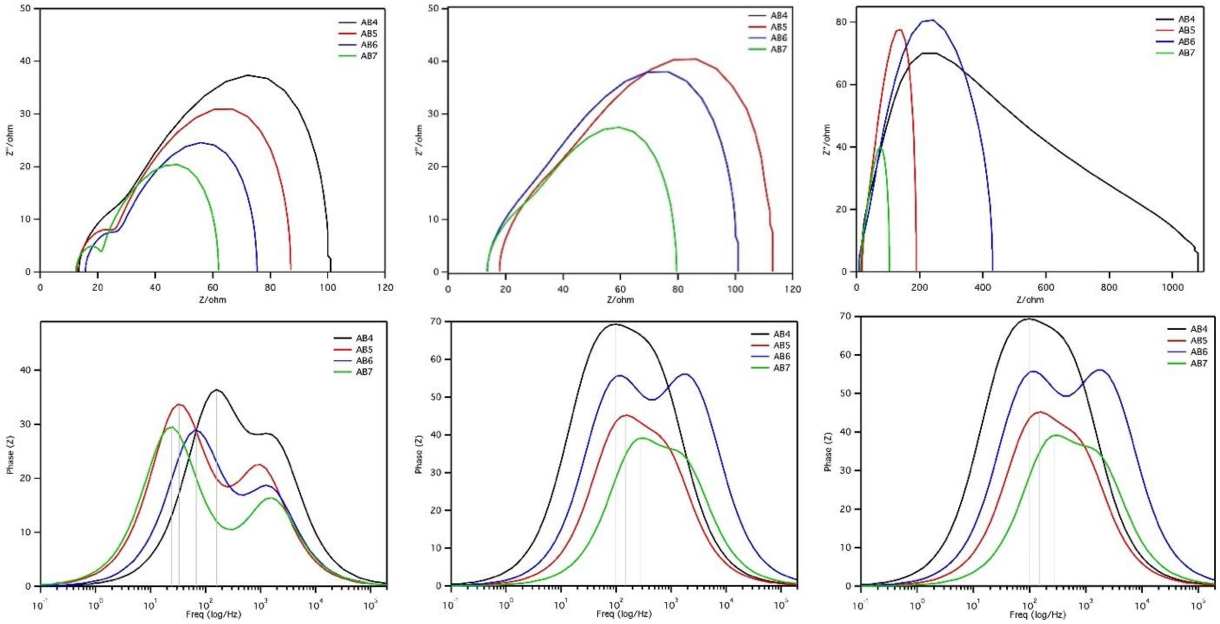

Figure 48: Nyquist (top) and Bode (bottom) plots resulting from electrochemical impedance spectroscopy for dyes with left) iodine middle) Co(terpy)$_2^{2+/3+}$ and right) Co(N-terpy)$_2^{2+/3+}$ redox shuttles.

By analyzing the electron lifetime in TiO_2 via EIS with the Bode plot varying trends to that seen with R_{rec} was observed depending on the redox shuttle being looked at. In the case of I^-/I_3^-, the inverse trend was seen, with **AB7** exhibiting the longest lifetime (6.6 ms) and the shortest being seen in **AB4** (1.0 ms). For the cobalt-based redox shuttles, Co(terpy)$_2^{2+/3+}$ showed no real trend with all four dyes exhibiting short lifetimes (< 1.0 ms), while the lifetimes for Co(N-terpy)$_2^{2+/3+}$ were in agreement with R_{rec} data, with **AB7** exhibiting the shortest lifetime (0.50 ms) and **AB4** exhibiting the longest (2.0 ms). The discrepancy between the R_{rec} and electron lifetime from EIS data may be attributed to the η_{cc} cancelling the effects that high recombination rates may have on the electron lifetimes. For the differences in electron lifetimes between the EIS measurements and small modulated photovoltage transient measurements may come from the difference in how the measurements are taken and whether a dye cation is present. For EIS, the electron placed in titania is obtained from the redox shuttle with no dye cation present on the surface allowing for the differences seen in the electron lifetimes to be due to how closely the different redox shuttles are held to the titania surface. If the redox shuttle is not held near the surface, like is commonly seen with I^-/I_3^-, lifetimes would be expected to be longer than with a cobalt-based redox shuttle, like $Co(terpy)_2^{2+/3+}$, which is normally held near the surface resulting in shorter lifetimes. For electron lifetimes using small modulated photovoltage transient measurements, the formation of the dye cation in the presence of the redox shuttle may allow for non-covalent interactions to play a role in lifetime of an injected electron in the titania surface. This can be seen in the lifetime data where halogen based dyes **AB5**, **AB6** and **AB7** exhibited longer lifetimes in the presence of redox shuttles capable of forming non-covalent interactions (I^-/I_3^- and $Co(N\text{-}terpy)_2^{2+/3+}$) however electron lifetimes showed small to negligible variance when non-non-covalent interaction could not be form ($Co(terpy)_2^{2+/3+}$).

To better understand the possible interactions occurring within the devices between the dye and redox shuttles, transient absorption spectroscopy measurements were performed. In order to do this, the regeneration efficiency of the dyes was calculated using equations 1-4 by observing the regeneration rate of the dyes both with and without redox shuttle present in devices.

(1) $\Delta OD(t) = \Delta OD(0)\, e^{-\left(\frac{t}{\tau_{WW}}\right)^{\beta}}$

(2) $\tau_{obs} = \frac{\tau_{WW}}{\beta}\Gamma\left(\frac{1}{\beta}\right)$

(3) $k_{obs} = \frac{1}{\tau_{obs}} \qquad k_{rec} = k_{obs}^{mock}$

(4) $\Phi = \frac{k_{rec}}{k_{obs}} * 100$

Utilizing a KWW fit, τ_{obs} values could be calculated and then used to obtain the rates of regeneration and recombination with the redox shuttle and mock electrolyte solutions, with the ratio of the rates being equal to the regeneration efficiency of the dyes (Table 19). For iodine-based devices, the increase in halogen size led to a small increase in regeneration efficiency, however the change was so slight it could be considered to have a negligible effect on the rates. In contrast, the cobalt-based devices showed a more appreciable trend could be seen. For the $Co(terpy)_2^{2+/3+}$ redox shuttle, which was expected to be unable to halogen bond, a small change in the regeneration efficiency could be seen, with no regeneration increase being observed going from H to Cl, a 3% increase when a Cl was swapped for an Br and finally a 7% increase when the halogen was increased from a Br to an I. Interesting, the cobalt redox shuttle capable of halogen bonding, $Co(N\text{-}terpy)_2^{2+/3+}$, showed a consistent trend in regeneration efficiency as halogen size increased. When a H was employed regeneration efficiency was seen to be extremely low, at only 34% (Table 19). However once an atom capable of halogen bonding, starting with Cl, was used the regeneration rate increased to 73% efficiency. As larger halogens

Table 19: Summary of transient absorption spectroscopy data for target dyes **AB4**, **AB5**, **AB6** and **AB7**[a].

Dye	k_{reg} (s^{-1})	k_{rec} (s^{-1})	Φ (%)
$\mathrm{Co}(N\text{-tpy})_2^{3+/2+}$			
AB4	460	300	34
AB5	1800	500	73
AB6	3900	400	90
AB7	7800	130	98
$\mathrm{Co(tpy)}_2^{3+/2+}$			
AB4	2300	300	87
AB5	3800	500	87
AB6	4000	400	90
AB7	4000	130	98

[a] All measurements were taken under open-circuit conditions, with the pump power = <3.5 mJ/pulse and the probe wavelength set to 720 nm.

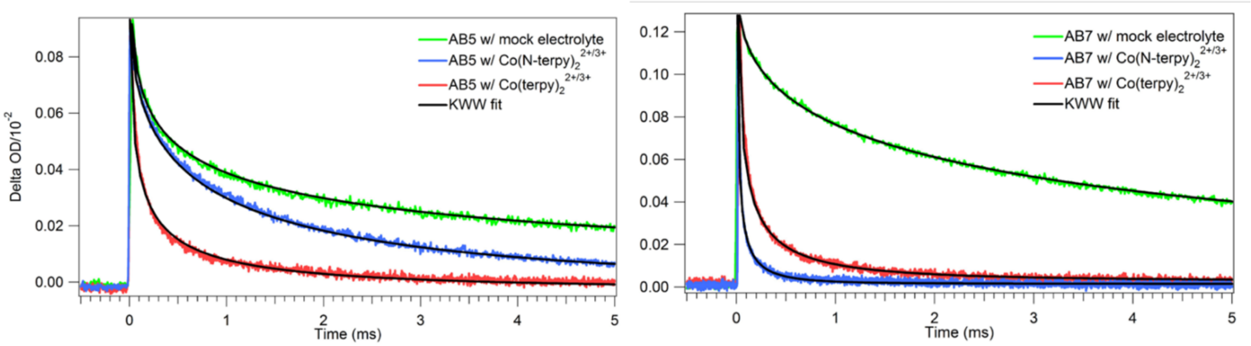

Figure 49: **AB5** (left) and **AB7** (right) decay plots resulting from transeint absorption spectroscopy for dyes with mock, $\mathrm{Co(terpy)}_2^{2+/3+}$ and $\mathrm{Co(N\text{-}terpy)}_2^{2+/3+}$ redox shuttles.

were used, Br and I, regeneration efficiency increased further to 90% and 98%, respectively. The increased regeneration rate of the dyes when halogen bonding is present can be seen more conclusively with the decay spectrum (Figure 49). When comparing dyes **AB5** and **AB7**, a steady decay rate can be observed for dye **AB5** in all the solutions however for **AB7** a drastic increase in the decay rates is seen when the halogen bonding redox shuttle is introduced. This effect could be due to the presence of a stronger halogen bonding partner, I versus Cl, in solution which is allowing for a faster regeneration rate and quicker rate of decay for the cationic dye.

CONCLUSIONS

Four dyes differing only in the identity of a halogen atom were synthesized and tested on films with varying redox shuttles to study the effects of non-covalent interactions. Solution absorption spectroscopy and electrochemical data showed little difference in the energy levels of the dyes, indicating that all four dyes should exhibit similar device performance if non-covalent interactions due to halogen effects were absent. Initial device data showed a trend toward better performing devices as halogen size increased, with I-based **AB7** having significantly better performance than H-based **AB4**, indicating that the presence of a halogen can effect the overall performance of a dye. However, the increased device performance was seen regardless of the ability for the dye to form non-covalent interactions with redox, indicating that while halogen effects may be present, halogen bonding may not. Electron lifetime data using small modulated photovoltage transient measurements showed longer electron lifetimes as halogen size increased with all redox shuttles. However, EIS showed varying lifetimes trends that included increasing lifetimes with increased halogen size for iodine redox shuttle, no change in lifetime between dyes with Co(terpy)$_2^{2+/3+}$ and decreasing lifetimes has halogen size increased for Co(N-terpy)$_2^{2+/3+}$. Overall, data shows that while non-covalent interactions are present, and play a role in the device performance of a dye, halogen effects rather than halogen bonding may be the cause behind differences in device performance.

EXPERIMENTAL DETAILS

Computational details: The geometry optimizations, binding energy and TDDFT calculations were performed with Gaussian 16 program package.[130] To account for the long-range interactions, wB97XD[176] functional was used with D2 dispersion corrections.[177] The residual force and density matrix were converged with tight convergence criteria and ultrafine grid was used for the numerical integration. *LANL2TZ(f)* and *LANL2DZdp* basis sets with effective core potential[178-179] were used for the cobalt (Co) and halogens, respectively. For all other atoms, 6-31G(d,p) basis set was used.[137] The geometry optimizations and binding energy calculations were performed with two different charge states of the dyes: neutral and oxidized state. First, the dyes and the cobalt-complex were optimized separately and the optimized geometries were placed together for the final optimization.

The multiplicity of the cobalt-complex was determined by full geometry optimization at +2 charge with different multiplicities (2,4,6 and 8) followed by stability test of the wavefunction (stable=opt), which gives a lowest energy conformation with multiplicity 4. Therefore, all the geometry optimization, binding energy and excited state calculations were performed with +2 charge on cobalt-complex with a multiplicity of 4. For the charged dyes, the total charge of the system was +3 with multiplicity 5.

For a difficult convergence case where the SCF cycles were not converged within 200 cycles, a quadratically convergence procedure[192] for SCF was utilized [scf =(maxconventionalcycles=200, xqc)].

All calculations were performed in the presence of implicit solvent. Integral Equation Formalism (IEFPCM) of the Polarizable Continuum Model (PCM)[193-195] was used with acetonitrile as the implicit solvent. A fragment guess calculation was used to generate the initial guess for the individual fragments with a full geometry optimization afterwards. To reduce the computational cost, the $-C_6H_{13}$ group was replaced with $-C_2H_5$ and all geometries were considered optimized once the forces on all atoms were converged to zero.[196]

Geometry optimizations were performed without any symmetry constraint. Frequency calculations were performed on each geometry to confirm the local minima. Most of the optimized geometries (where the dyes and cobalt-complex were optimized together), consist of a small negative frequency which was expensive and difficult to remove due to the transition metal present in the system. A highest negative frequency of ~ $-26\ cm^{-1}$ was obtained from H-substituted neutral dye.

Binding energy calculation was done without the consideration of basis set superposition error. The analysis of binding energies involved the energy difference between the dye-cobalt-complex (E_{Total}) with energy of the dye ($E_{Fragment-1}$) and cobalt-complex ($E_{Fragment-2}$). For the $E_{Fragment-1}$ and $E_{Fragment-2}$ energy, a single point energy calculation was performed on the total system (cobalt-complex+dyes) by replacing the other fragments with a ghost-atom.

$$E_{BE} = E_{Total} - E_{Fragment-1} - E_{Fragment-2}$$

For the excited states, time-dependent density functional theory (TDDFT)[197-198] calculation was performed with Tamm-Dancoff approximation.[196] These calculations involved computation of vertical excitation of the lowest 25 singlet excited states. TDDFT calculations were performed at the same level of theory and basis set as DFT calculations using acetonitrile as implicit solvent.

General Experimental Details: All commercially obtained regents were used as received. 4H-cyclopenta[2,1-b:3,4- b']dithiophene and 2-ethylhexyl bromide were purchased from Matrix Scientific. Thin-layer chromatography (TLC) was conducted with Sorbtech silica XHL TLC plates and visualized with UV. Flash column chromatography was performed with Sorbent Tech P60, 40-63 um (230-400 mesh). ^{1}H and ^{13}C NMR spectra were recorded on a Bruker Avance-300 (300 MHz) and Bruker Avance-500 (500 MHz) spectrometer and are reported in ppm using solvent as an internal standard ($CDCl_3$ at 7.26). Data reported as s = singlet, d = doublet, t = triplet, q = quartet, p = pentet, m = multiplet, br = broad, ap = apparent, dd = doublet of doublets; coupling constant(s) in Hz. UV spectra were measured with a Cary 5000 UV-Vis-NIR spectrometer with dichloromethane solution. Cyclic voltammetry curves were measured with a C-H Instruments electrochemical analyzer CHI600E. 4,4-diethylhexyl-4H-cyclopenta[2,1-b:3,4-b']dithiophene-2-carbaldehyde, 6'-bromo-4,4-diethylhexyl-4H-cyclopenta[2,1-b:3,4-b']dithiophene-2-carbaldehyde, Tributyl-(4,4-diethylhexyl-4a,7a-dihydro-4H-cyclopenta[2,1-b;3,4-b']dithiophen-2-yl)- stannane, 4,4,4',4'-Tetraethylhexyl-4a,7a,4',7'b-tetrahydro-4H,3'aH-[2,2']bi[cyclopenta[2,1-b;3,4- b']dithiophenyl]-6-carbaldehyde, 2-Cyano-3-(4,4,4',4'-tetraethylhexyl-4a,7a,4',7'b-tetrahydro-4H,3'aH- [2,2']bi[cyclopenta[2,1-b;3,4-b']dithiophenyl]-6-yl)-acrylic acid and 6'-bromo-4,4,4',4'-tetraethylhexyl-4a,7a,4',7'b-tetrahydro-4H,3'aH-

[2,2']bi[cyclopenta[2,1-b;3,4-b']dithiophenyl]-6-carbaldehyde were synthesized account to literature procedure.[23]

2-Cyano-3-(6'-bromo-4,4,4',4'-tetraethylhexyl-4a,7a,4',7'b-tetrahydro-4H,3'aH-[2,2']bi[cyclopenta[2,1- b;3,4-b']dithiophenyl])-acrylic acid (**AB5**): In a 8.0 mL vial, 6'-bromo-4,4,4',4'-tetraethylhexyl-4a,7a,4',7'b-tetrahydro-4H,3'aH-[2,2']bi[cyclopenta[2,1- b;3,4-b']dithiophenyl])-6-carbaldehyde (0.05 g, 0.055 mmol) was dissolved in 1.10 mL chloroform. The mixture was then degassed with N_2 for approximately 30 minutes. Cyanoacetic acid (0.014 g, 0.165 mmol) and piperidine (0.038 mL, 0.385 mmol) were added to the vial, which was then sealed, heated to 90^{o}C and allowed to stir for 16 hours. The reaction mixture was diluted with dichloromethane and purified through a plug of silica gel with 100% dichloromethane —> 10% methanol/dichloromethane —> 12% methanol/3% acetic acid/dichloromethane. The solvent of the third fraction was evaporated under reduced pressure. The dye was then extracted with hexanes and water and purified further with a CombiFlash R_f^+ chromotography system (RediSep R_f Gold high performance silica gel, 0% methanol/dichloromethane —> 10% methanol/dichloromethane) to give the final pure dye (xx, xx). ^{1}H NMR (300 MHz, $CDCl_3$) δ 7.94 (s, 1H), 7.72 (d, J = 8.8 Hz, 2H), 7.47 (d, J = 8.7 Hz, 4H), 7.28-7.25 (m, 3H), 7.21-7.16 (m, 6H), 6.81 (d, J = 3.8 Hz, 1H), 6.60-6.52 (m, 4H), 4.05-3.95 (m, 8H), 1.85-1.70 (m, 8H), 1.50-1.45 (m, 8H), 1.05-0.90 (m, 12H) ppm. IR (neat) ν = 3340, 2944, 2923, 2854, 2333, 2114, 1602, 1593 cm^{-1}. ESI HRMS m/z calc'd for $C_{54}H_{74}BrNO_2S_4Cs$ [M + Cs]$^+$: calculated 1108.2841, found 1108.2832.

6'-chloro-4,4,4',4'-tetraethylhexyl-4a,7a,4',7'b-tetrahydro-4H,3'aH-[2,2']bi[cyclopenta[2,1-b;3,4-b']dithiophenyl]-6-carbaldehyde: In a 10.0 mL roundbottom flask, 4,4,4',4'-Tetraethylhexyl-4a,7a,4',7'b-tetrahydro-4H,3'aH-[2,2']bi[cyclopenta[2,1-b;3,4- b']dithiophenyl]-6-carbaldehyde (0.100 g, 0.120 mmol) was dissolved in 2.86 mL tetrahydrofuran. The solution was then degassed for about 10 minutes with N_2 and cooled to 0^oC. Recrystallized NCS (0.018 g, 0.132 mmol) was then added. The reaction was sealed and stirred at 0^oC for 1 hour, then allowed to warm to room temperature for 16 hours. The mixture was then extracted with diethyl ether and water, and dried with sodium sulfate. The crude product was purified with silica gel chromotography with 25% dicholormethane/hexanes (xx, xx). ^1H NMR (300 MHz, $CDCl_3$) δ 7.94 (s, 1H), 7.72 (d, J = 8.8 Hz, 2H), 7.47 (d, J = 8.7 Hz, 4H), 7.28-7.25 (m, 3H), 7.21-7.16 (m, 6H), 6.81 (d, J = 3.8 Hz, 1H), 6.60-6.52 (m, 4H), 4.05-3.95 (m, 8H), 1.85-1.70 (m, 8H), 1.50-1.45 (m, 8H), 1.05-0.90 (m, 12H) ppm. IR (neat) ν = 3340, 2944, 2923, 2854, 2333, 2114, 1602, 1593 cm^{-1}. ESI HRMS m/z calc'd for $C_{51}H_{73}ClOS_4Cs$ $[M + Cs]^+$: calculated 997.3287, found 997.3277.

2-Cyano-3-(6'-chloro-4,4,4',4'-tetraethylhexyl-4a,7a,4',7'b-tetrahydro-4H,3'aH-[2,2']bi[cyclopenta[2,1- b;3,4-b']dithiophenyl])-acrylic acid (**AB6**): In a 8.0 mL vial, 6'-chloro-4,4,4',4'-tetraethylhexyl-4a,7a,4',7'b-tetrahydro-4H,3'aH-[2,2']bi[cyclopenta[2,1- b;3,4-b']dithiophenyl])-6-carbaldehyde (0.05 g, 0.058 mmol) was dissolved in 1.20 mL chloroform. The mixture was then degassed with N_2 for approximately 30 minutes. Cyanoacetic acid (0.015 g, 0.173 mmol) and piperidine (0.040 mL, 0.406 mmol) were added to the vial, which was then sealed, heated to 90^oC and allowed to stir for 16 hours. The reaction mixture was diluted with dichloromethane and purified through a plug of silica gel with 100% dichloromethane —> 10%

methanol/dichloromethane —> 12% methanol/3% acetic acid/dichloromethane. The solvent of the third fraction was evaporated under reduced pressure. The dye was then extracted with hexanes and water and purified further with a CombiFlash R_f^+ chromotography system (RediSep R_f Gold high performance silica gel, 0% methanol/dichloromethane —> 10% methanol/dichloromethane) to give the final pure dye (xx, xx). ^{1}H NMR (300 MHz, $CDCl_3$) δ 7.94 (s, 1H), 7.72 (d, J = 8.8 Hz, 2H), 7.47 (d, J = 8.7 Hz, 4H), 7.28-7.25 (m, 3H), 7.21-7.16 (m, 6H), 6.81 (d, J = 3.8 Hz, 1H), 6.60-6.52 (m, 4H), 4.05-3.95 (m, 8H), 1.85-1.70 (m, 8H), 1.50-1.45 (m, 8H), 1.05-0.90 (m, 12H) ppm. IR (neat) ν = 3340, 2944, 2923, 2854, 2333, 2114, 1602, 1593 cm^{-1}. ESI HRMS m/z calc'd for $C_{54}H_{73}ClNO_2S_4$ $[M - H]^-$: calculated 930.4213, found 930.4236.

6'-iodo-4,4,4',4'-tetraethylhexyl-4a,7a,4',7'b-tetrahydro-4H,3'aH-[2,2']bi[cyclopenta[2,1- b;3,4-b']dithiophenyl]-6-carbaldehyde: In a 10.0 mL roundbottom flask, 4,4,4',4'-Tetraethylhexyl-4a,7a,4',7'b-tetrahydro-4H,3'aH-[2,2']bi[cyclopenta[2,1-b;3,4- b']dithiophenyl]-6-carbaldehyde (0.050 g, 0.060 mmol) was dissolved in 1.43 mL tetrahydrofuran. The solution was then degassed for about 10 minutes with N_2 and cooled to 0^oC. Recrystallized NIS (0.015 g, 0.066 mmol) was then added. The reaction was sealed and stirred at 0^oC for 1 hour, then allowed to warm to room temperature for 16 hours. The mixture was then extracted with diethyl ether and water, and dried with sodium sulfate. The crude product was purified with silica gel chromotography with 25% dicholormethane/hexanes (xx, xx). ^{1}H NMR (300 MHz, $CDCl_3$) δ 7.94 (s, 1H), 7.72 (d, J = 8.8 Hz, 2H), 7.47 (d, J = 8.7 Hz, 4H), 7.28-7.25 (m, 3H), 7.21-7.16 (m, 6H), 6.81 (d, J = 3.8 Hz, 1H), 6.60-6.52 (m, 4H), 4.05-3.95 (m, 8H), 1.85-1.70 (m, 8H), 1.50-1.45 (m, 8H), 1.05-0.90 (m, 12H) ppm. IR (neat) ν = 3340, 2944, 2923, 2854, 2333, 2114, 1602, 1593 cm^{-1}. ESI HRMS m/z calc'd for $C_{54}H_{73}IOS_4Cs$ [M + Cs]$^+$: calculated 1089.2643, found 1089.2625.

2-Cyano-3-(6'-iodo-4,4,4',4'-tetraethylhexyl-4a,7a,4',7'b-tetrahydro-4H,3'aH-[2,2']bi[cyclopenta[2,1- b;3,4-b']dithiophenyl])-acrylic acid (**AB7**): In a 8.0 mL vial, 6'-iodo-4,4,4',4'-tetraethylhexyl-4a,7a,4',7'b-tetrahydro-4H,3'aH-[2,2']bi[cyclopenta[2,1- b;3,4-b']dithiophenyl])-6-carbaldehyde (0.0173 g, 0.0181 mmol) was dissolved in 0.362 mL chloroform. The mixture was then degassed with N_2 for approximately 30 minutes. Cyanoacetic acid (0.005 g, 0.0542 mmol) and piperidine (0.013 mL, 0.127 mmol) were added to the vial, which was then sealed, heated to 90^{o}C and allowed to stir for 16 hours. The reaction mixture was diluted with dichloromethane and purified through a plug of silica gel with 100% dichloromethane —> 10% methanol/dichloromethane —> 12% methanol/3% acetic acid/dichloromethane. The solvent of the third fraction was evaporated under reduced pressure. The dye was then extracted with hexanes and water and purified further with a CombiFlash R_f^+ chromotography system (RediSep R_f Gold high performance silica gel, 0% methanol/dichloromethane —> 10% methanol/dichloromethane) to give the final pure dye (xx, xx). ^{1}H NMR (300 MHz, $CDCl_3$) δ 7.94 (s, 1H), 7.72 (d, J = 8.8 Hz, 2H), 7.47 (d, J = 8.7 Hz, 4H), 7.28-7.25 (m, 3H), 7.21-7.16 (m, 6H), 6.81 (d, J = 3.8 Hz, 1H), 6.60-6.52 (m, 4H), 4.05-3.95 (m, 8H), 1.85-1.70 (m, 8H), 1.50-1.45 (m, 8H), 1.05-0.90 (m, 12H) ppm. IR (neat) ν = 3340, 2944, 2923, 2854, 2333, 2114, 1602, 1593 cm^{-1}. ESI HRMS m/z calc'd for $C_{54}H_{74}INO_2S_4Cs$ [M + Cs]$^+$: calculated 1156.2701, found 1156.2683.

CHAPTER 7

7.1 OVERALL CONCLUSION

The development of dye-sensitized solar cells has helped to provide a renewable energy source that can be used as an alternative to the non-renewable sources, such as petroleum and natural gas, that are widely used today. While the low fabrication costs make DSCs an attractive alternative to silicon-based solar cells the true appeal lies in the flexibility of the dye motifs, creating tunable band gaps that allow for optimization of the dye design. The research in this thesis focused on the design and synthesis of organic dyes to gain an understanding of the effects that certain dye motifs have on the performance of DSCs in order to help promote productive pathways while diminishing detrimental ones. Previous studies have shown that alkyl chains could be used to help improve surface coverage by reducing recombination within DSC. The highest performing dyes found in literature use a large aryl amine with multiple alkoxy groups, the Hagfeldt donor, to help reduce recombination by blocking the titania surface. Although the Hagfeldt donor has shown to be an effective tool in reducing recombination, the need for a reliable synthetic route was apparent based on the large number of routes found in literature. A route utilizing a masked halide transformation, free of selective halogen- and aminations, was developed in order to provide a reliable route that could be scaled up. **AB1**, **AB2**, and **AB3** were synthesized based on the known dye **D35**, which contains the Hagfeldt donor in its structure, to probe the effects replacing a thiophene atom with a furan atom has on device performance. Experimental studies, along with computational results, showed that in the presence of thiophene, a decrease in device performance was seen as well as differing spectroscopic signature upon the introduction of iodine to the systems. Results confirmed the presence of halogen bonding between the sulfur atom in thiophene and the oxidized redox shuttle, leading to an increase in recombination as well as decrease in device performance. Although halogen bonding was seen to decrease device performance in some cases through the promotion of recombination pathways, installation of a halogen on the donor end of the dye has been show to increase the favorable regeneration pathway. Dyes **AB4**, **AB5**, **AB6**, and **AB7** were synthesized in order to examine the effects halogen bonding can have on regeneration rates. It was seen that as the size of the halogen atom increased, the voltage, current and overall dye performance was seen to increase as well. This increase in device performance with halogen installation indicates that while poor dye design may decrease the efficiency of a dye by promoting detrimental electron transfer pathways, proper dye design can help to improve device performance through promotion of productive electron transfers. By utilizing the flexibility DSCs allow to the dye structure, while also taking advantage of the functionality provided by certain motifs, proper dye design can lead to the realization of higher efficiencies in DSCs.

The **NL** series and **SM85** were synthesized and tested in order to study the effects that extended conjugation had on the absorption spectrum and overall device performance. In both cases, extending the conjugation of the π-bridge of the dye successfully redshifted the absorption spectrum of the dyes. It was also seen that increasing the conjugation could also lead to increased aggregation, particularly in the case of **SM85**. While this aggregation could be detrimental to the device performance, if aggression could be successfully controlled a previously disadvantageous aspect may be utilized to increase device performance.

LIST OF REFERENCES

REFERENCES

1. Hagfeldt, A. *et al.* Dye-Sensitized Solar Cells. *Chem. Rev.* **110**, 6595–6663 (2010).
2. Chen, C.-Y. *et al.* Highly Efficient Light-Harvesting Ruthenium Sensitizer for Thin-Film Dye-Sensitized Solar Cells. *ACS Nano* **3**, 3103–3109 (2009).
3. Mathew, S. *et al.* Dye-sensitized solar cells with 13% efficiency achieved through the molecular engineering of porphyrin sensitizers. *Nat. Chem.* **6**, 242-247 (2014).
4. Kakiage, K. *et al.* An achievement of over 12 percent efficiency in an organic dye-sensitized solar cell. *Chem. Commun.* **50**, 6379–6381 (2014).
5. Kakiage, K. *et al.* Highly-efficient dye-sensitized solar cells with collaborative sensitization by silyl-anchor and carboxy-anchor dyes. *Chem. Commun.* **51**, 15894–15897 (2015).
6. Yao, Z. *et al.* Donor/Acceptor Indenoperylene Dye for Highly Efficient Organic Dye-Sensitized Solar Cells. *J. Am. Chem. Soc.* **137**, 3799–3802 (2015).
7. Wang, H. *et al.* Kinetics of electron recombination of dye-sensitized solar cells based on TiO_2 nanorod arrays sensitized with different dyes. *Phys. Chem. Chem. Phys.* **13**, 17359–17366 (2011).
8. Eom, Y. K. *et al.* Significant Light Absorption Enhancement by a Single Heterocyclic Unit Change in the π-Bridge Moiety from Thieno[3,2-*b*]benzothiophene to Thieno[3,2-*b*]indole for High Performance Dye-Sensitized and Tandem Solar Cells. *J. Mater. Chem.*

A. **5**, 2297-2308 (2017).

9. Zhang, Y. *et al.* Ullazine Donor–π-bridge-Acceptor Organic Dyes for Dye-Sensitized Solar Cells. *Chem. – A Eur. J.* **24**, 5939–5949 (2018).
10. Cariello, M. *et al.* An investigation of the roles furan *versus* thiophene π-bridges play in donor-π-acceptor porphyrin based DSSCs. *Dalton Trans.* **47**, 6549-6556 (2018).
11. Aghazada, S. *et al.* Unraveling the Dual Character of Sulfur Atoms on Sensitizers in Dye-Sensitized Solar Cells. *ACS Appl. Mater. Interfaces* **8**, 26827-26833 (2016).
12. Baumann, A. *et al.* Iodine binding with thiophene and furan based dyes for DSCs. *Phys. Chem. Chem. Phys.* **20**, 17859-17870 (2018).
13. Gao, P. *et al.* Facile synthesis of a bulky BPTPA donor group suitable for cobalt electrolyte based dye sensitized solar cells. *J. Mater. Chem. A.* **1**, 5535-5544 (2013).
14. Cheema, H. *et al.* Near-Infrared-Absorbing Indolizine-Porphyrin Push-Pull Dye for Dye-Sensitized Solar Cells. *ACS Appl. Mater. Interfaces* **11**, 16474-16489 (2019).
15. Reynal, A. *et al.* Interfacial Charge Recombination Between e^- -TiO_2 and the I^-/I_3^- Electrolyte in Ruthenium Heteroleptic Complexes: Dye Molecular Structure-Open Circuit Voltage Relationship. *J. Am. Chem. Soc.* **130**, 13558-13567 (2008).
16. Hu, K. *et al.* Direct Spectroscopic Evidence for Constituent Heteroatoms Enhancing Charge Recombination at a TiO_2-Ruthenium Dye Interface. *J. Phys. Chem. C* **118**, 17079-17089 (2014).
17. Li, X. *et al.* Measured binding coefficients for iodine and ruthenium dyes; implications for recombination in dye sensitized solar cells. *Phys. Chem. Chem. Phys.* **14**, 15421-15428 (2012).

18. Swords, W. B. *et al.* Evidence of Interfacial Halogen Bonding. *Angew. Chem. Int. Ed.* **55**, 5956-5960 (2016).

19. Nguyen, T. -D. *et al.* Effect of the CF_3 Substituents on the Charge-Transfer Kinetics of High-Efficiency Cyclometalated Ruthenium Sensitizers. *Inorg. Chem.* **56**, 252-260 (2017).

20. Barr, T. J. & Meyer, G. J. Evidence for First-Order Charge Recombination in Dye-Sensitized Solar Cells. *ACS Energy Lett.* **2**, 2335-2340 (2017).

21. Urbani, M. *et al.* Meso-Substituted Porphyrins for Dye-Sensitized Solar Cells. *Chem. Rev.* **114**, 12330-12396 (2014).

22. Yella, A. *et al.* Porphyrin-Sensitized Solar Cells with Cobalt (II/III)–Based Redox Electrolyte Exceed 12 Percent Efficiency. *Science* **334**, 629-634 (2011).

23. Hu, Y. *et al.* High Absorption Coefficient Cyclopentadithiophene Donor-Free Dyes for Liquid and Solid-State Dye-Sensitized Solar Cells. *J. Phys. Chem. C* **120**, 15027-15034 (2016).

24. Li, Y. *et al.* Correlating excited state and charge carrier dynamics with photovoltaic parameters of perylene dye sensitized solar cells: influences of an alkylated carbazole ancillary electron-donor. *Phys. Chem. Chem. Phys.* **19**, 2549-2556 (2017).

25. Zhang, Y. *et al.* Panchromatic cross-conjugated π-bridge NIR dyes for DSCs. *Phys. Chem. Chem. Phys.* **20**, 2438–2443 (2018).

26. Huckaba, A. J. *et al.* Molecular Design Principles for Near-Infrared Absorbing and Emitting Indolizine Dyes. *Chem. – A Eur. J.* **22**, 15536–15542 (2016).

27. O'Regan, B. & Grätzel, M. A low-cost, high-efficiency solar cell based on dye-sensitized

colloidal TiO2 films. *Nature* **353**, 737–740 (1991).

28. Gratzel, M. Dye-sensitized solar cells. *J. Photochem. Photobiol. C* **4**, 145-153 (2003).

29. Cao, Y. L. *et al.* Direct Contact of Selective Charge Extraction Layers Enables High-Efficiency Molecular Photovoltaics. *Joule* **2**, 1108-1117 (2018).

30. Prier, C. K. *et al.* Visible Light Photoredox Catalysis with Transition Metal Complexes: Applications in Organic Synthesis. *Chem. Rev.* **113**, 5322-5363 (2013).

31. Yan, N. F. *et al.* Electroactive Organic Compounds as Anode-Active Materials for Solar Rechargable Redox Flow Battery in Duel-Phase Electrolytes. *J. Electrochem. Soc.* **161**, 736-741 (2014).

32. Pashaei, B. S. *et al.* Transition Metal Complex Redox Shuttles for Dye-Sensitized Solar Cells. *RSC Adv.* **5**, 94814-94848 (2015).

33. Sun, Z. *et al.* Kinetics of Iodine-Free Redox Shuttles in Dye-Sensitized Solar Cells: Interfacial Recombination and Dye Regeneration. *Acc. Chem. Res.* **48**, 1541–1550 (2015).

34. Yu, Z. *et al.* Recent Advances in Dye-Sensitized Photoelectrochemical Cells for Solar Hydrogen Production Based on Molecular Components. *Energy Envir. Sci.* **8**, 760-775 (2015).

35. Kakiage, K. *et al.* Achievement of Over 1.4 V Photovoltage in a Dye-Sensitized Solar Cell by the Application of a Silly-Anchor Coumarin Dye. *Sci. Rep.* **6**, 35888-35893 (2016).

36. Schmidt, I. P. *et al.* Spatially Resolved Analysis of Screen Printed Photoanodes of Dye-Sensitized Solar Cells by Scanning Electrochemical Microscopy. *Electrochimica Acta* **222**, 735-746 (2016).

37. Liang, Y. W. *et al.* Achieving High Open-Circuit Voltages up to 1.57 V in Hole-

Transport-Material-Free $MAPbBr_3$ Solar Cells with Carbon Electrodes. *Adv. Energy Mater.* **8**, 1701159-1702018 (2017).

38. Marzo, L. P. *et al.* Visible-Light Photocatalysis: Does It Make a Difference in Organic Synthesis? *Angew. Chem. Int. Ed.* **57**, 10034-10072 (2018).
39. Rodrigues, R. R. *et al.* A High Voltage Molecular Engineered Organic Sensitizer-Iron Redox Shuttle Pair: 1.4 V DSC and 3.3 V SSM-DSC Devices. *Angew. Chem. Int. Ed.* **57**, 5472-5476 (2018).
40. Sheridan, M. V. *et al.* Light Driven Water Splitting Mediated by Photogenerated Bromine. *Angew. Chem. Int. Ed.* **57**, 3449-3453 (2018).
41. Zhang, W. *et al.* Comprehensive control of voltage loss enables 11.7% efficient solid-state dye-sensitized solar cells. *Energy Envir. Sci.* **11**, 1779-1787 (2018).
42. Lei, B. *et al.* A Quasi-Solid-State Solar Rechargable Battery with Polyethylene Oxide Gel Electrolyte. *ACS Appl. Energy Mater.* **2**, 1000-1005 (2019).
43. Lhermitte, C. R. & Sivula, K. Alternative Oxidation Reactions for Solar-Driven Fuel Production. *ACS Catal.* **9**, 2007-2017 (2019).
44. Freitag, M. *et al.* Dye-sensitized solar cells for efficient power generation under ambient lighting. *Nat. Photonics* **11**, 372-378 (2017).
45. Tsao, H. N. *et al.* Cyclopentadithiophene bridged donor-acceptor dyes achieve high power conversion efficiencies in dye-sensitized solar cells based on the tris-cobalt bipyridine redox couple. *ChemSusChem* **4**, 591-594 (2011).
46. Li, X. *et al.* Stacked graphene platelet nanofibers dispersed in the liquid electrolyte of highly efficient cobalt-mediator-based dye-sensitized solar cells. *Chem. Commun.* **51**,

10349-10352 (2015).

47. Li, X. *et al.* Insight into quinoxaline containing D-π-A dyes for dye-sensitized solar cells with cobalt and iodine based electrolytes: the effect of π-bridge on the HOMO energy level and photovoltaic performance. *J. Mater. Chem. A* **3**, 21733-21743 (2015).

48. Lim, K. *et al.* Organic Sensitizers Featuring a Planar Indeno[1,2-*b*]thiophene for Efficient Dye-Sensitized Solar Cells. *ChemSusChem* **6**, 1425-1431 (2013).

49. Tian, H. *et al.* Development of an organic redox couple and organic dyes for aqueous dye-sensitized solar cells. *Energy Environ. Sci.* **12**, 9752-9755 (2012).

50. Hilal, H. M. *et al.* Large Enhancement of Dye Sensitized Solar Cell Efficiency by Co-sensitizing Pyridyl- and Carboxylic Acid-Based Dyes. *ACS Appl. Energy Mater.* **1**, 2776-2783 (2018).

51. Liu, P. *et al.* Novel and Stable D-A-π-A Dyes for Efficient Solid-State Dye-Sensitized Solar Cells. *ACS Omega* **2**, 1812-1819 (2017).

52. Guo, X. *et al.* Dithieno[2,3-*d*;2',3'-*d*']benzo[1,2-*b*;4,5-*b*']dithiophene based organic sensitizers for dye-sensitized solar cells. *RSC Adv.* **4**, 54130-54133 (2014).

53. Eom, Y. K. *et al.* Thieno[3,2-*b*][1]benzothiophene Derivative as a New π-Bridge Unit in D-π-A Structural Organic Sensitizers with Over 10.47% Efficiency for Dye-Sensitized Solar Cells. *Adv. Energy Mater.* **5**, 1500300 (2015).

54. Ahmad, S. *et al.* Toward flexibility: metal free plastic cathodes for dye sensitized solar cells. *Chem. Commun.* **48**, 9714-9716 (2012).

55. Shen, Z. *et al.* Synthesis and Photovoltaic Properties of Powerful Electron-Donating Indeno[1,2-*b*]thiophene-Based Green D-A-π-A Sensitizers for Dye-Sensitized Solar Cells.

ACS Sustainable Chem. Eng. **4**, 3518-3525 (2016).

56. Hagberg, D. P. *et al.* Symmetric and unsymmetrical donor functionalization: comparing structural and spectral benefits of chromophores for dye-sensitized solar cells. *J. Mater. Chem.* **19**, 7232-7238 (2009).
57. Laskova, B. *et al.* Electron Kinetics in Dye Sensitized Solar Cells Employing Anatase with (101) and (001) Facets. *Electrochimica Acta* **160**, 296-305 (2015).
58. Polander, L. E. *et al.* Unravelling the Potential for Dithienopyrrole Sensitizers in Dye-Sensitized Solar Cells. *Chem. Mater.* **25**, 2642-2648 (2013).
59. Pazoki, M. *et al.* Mesoporous TiO_2 Microbead Electrodes for Cobalt-Mediator-Based Dye-Sensitized Solar Cells. *J. Phys. Chem. C* **118**, 16472-16478 (2014).
60. Yu, Z. *et al.* Tetrathiafulvalene as a one-electron iodine-free organic redox mediator in electrolytes for dye-sensitized solar cells. *RSC Adv.* **2**, 1083-1087 (2012).
61. Jiang, X. *et al.* Highly Efficient Solid-State Dye-Sensitized Solar Cells Based on Triphenylamine Dyes. *Adv. Funct. Mater.* **21**, 2944-2952 (2011).
62. Zhang, X. *et al.* Molecular Engineering of Potent Sensitizers for Very Efficient Light Harvesting in Thin-Film Solid-State Dye-Sensitized Solar Cells. *J. Am. Chem. Soc.* **138**, 10742-10745 (2016).
63. Gabrielsson, E. *et al.* Convergent/Divergent Synthesis of a Linker-Varied Series of Dyes for Dye-Sensitized Solar Cells Based on the D35 Donor. *Adv. Energy Mater.* **3**, 1647–1656 (2013).
64. Ellis, H. *et al.* Influence of Dye Architecture of Triphenylamine Based Organic Dyes on the Kinetics in Dye-Sensitized Solar Cells. *J. Phys. Chem. C* **119**, 21775-21783 (2015).

65. Freitag, M. *et al.* High-efficiency dye-sensitized solar cells with molecular copper phenanthroline as solid hole conductor. *Energy Environ. Sci.* **8**, 2634-2637 (2015).

66. Freitag, M. *et al.* Copper Phenanthroline as a Fast and High-Performance Redox Mediator for Dye-Sensitized Solar Cells. *J. Phys. Chem. C* **120**, 9595-9603 (2016).

67. Park, B. -W. *et al.* Understanding Interfacial Charge Transfer between Metallic PEDOT Counter Electrodes and a Cobalt Redox Shuttle in Dye-Sensitized Solar Cells. *ACS Appl. Mater. Interfaces* **6**, 2074-2079 (2014).

68. Sharmoukh, W. *et al.* Molecular Engineering of D-D-π-A-Based Organic Sensitizers for Enhanced Dye-Sensitized Solar Cell Performance. *ACS Omega* **3**, 3819-3829 (2018).

69. Zhang, X. *et al.* Comparative Study of Pyrido[3,4-*b*]pyrazine-Based Sensitizers by Tuning Bulky Donors for Dye-Sensitized Solar Cells. *ACS Appl. Mater. Interfaces* **7**, 2760-2771 (2015).

70. Zhao, J. *et al.* Highly efficient iso-quinoline cationic organic dyes without vinyl groups for dye-sensitized solar cells. *J. Mater. Chem. A* **1**, 2441-2446 (2013).

71. Ellis, H. *et al.* Linker Unit Modification of Triphenylamine-Based Organic Dyes for Efficient Cobalt Mediated Dye-Sensitized Solar Cells. *J. Phys. Chem. C* **117**, 21029-21036 (2013).

72. Yum, J.-H. *et al.* Towards high-performance DPP-based sensitizers for DSC applications. *Chem. Commun.* **48**, 10727–10729 (2012).

73. Gao, P., Tsao, H. N., Yi, C., Grätzel, M. & Nazeeruddin, M. K. Extended π-Bridge in Organic Dye-Sensitized Solar Cells: the Longer, the Better? *Adv. Energy Mater.* **4**, 1301485 (2014).

74. Eggers, F. *et al.* Concave 1,10-Phenanthrolines as Ligands for Cyclopropanations - Towards a Deeper Understanding of the Stereoselectivity. *Eur. J. Org. Chem.* **2009**, 2328-2341 (2009).

75. Hardin, B. E. *et al.* The renaissance of dye-sensitized solar cells. *Nat. Photonics* **6**, 162-169 (2012).

76. Mishra, A. *et al.* Metal-Free Organic Dyes for Dye-Sensitized Solar Cells: From Structure: Property Relationships to Design Rules. *Angew. Chem. Int. Ed.* **48**, 2474–2499 (2009).

77. Zhang, M. *et al.* Design of high-efficiency organic dyes for titania solar cells based on the chromophoric core of cyclopentadithiophene-benzothiadiazole. *Energy Environ. Sci.* **6**, 2944–2949 (2013).

78. Ardo, S. & Meyer, G. J. Photodriven heterogeneous charge transfer with transition-metal compounds anchored to TiO_2 semiconductor surfaces. *Chem. Soc. Rev.* **38**, 115–164 (2009).

79. Haid, S. *et al.* Significant Improvement of Dye-Sensitized Solar Cell Performance by Small Structural Modification in π-Conjugated Donor-Acceptor Dyes. *Adv. Funct. Mater.* **22**, 1291-1302 (2012).

80. Cai, N. *et al.* Engineering of Push-Pull Thiophene Dyes to Enhance Light Absorption and Modulate Charge Recombination in Mesoscopic Solar Cells. *Adv. Funct. Mater.* **23**, 1846-1854 (2013).

81. Ahmad, S. *et al.* Metal free sensitizer and catalyst for dye sensitized solar cells. *Energy Environ. Sci.* **6**, 3439–3466 (2013).

82. Yang, J. *et al.* Influence of the Donor Size in D-π–A Organic Dyes for Dye-Sensitized Solar Cells. *J. Am. Chem. Soc.* **136**, 5722-5730 (2014).

83. Wu, J. B. *et al.* Monoamine Oxidase A Inhibitor-Near-Infrared Dye Conjugate Reduces Prostate Tumor Growth. *J. Am. Chem. Soc.* **137**, 2366-2374 (2015).

84. Wu, Y. *et al.* High-conversion-efficiency organic dye-sensitized solar cells: molecular engineering on D-A-π–A featured organic indoline dyes. *Energy Environ. Sci.* **5**, 8261-8272 (2012).

85. Zhu, W. *et al.* Organic D-A-π–A Solar Cell Sensitizers with Improved Stability and Spectral Response. *Adv. Funct. Mater.* **21**, 756-763 (2011).

86. Liyanage, N. P. *et al.* Thieno[3,4-b]pyrazine as an Electron Deficient π-Bridge in D–A−π–A DSCs. *ACS Appl. Mater. Interfaces* **8**, 5376–5384 (2016).

87. Ying, W. *et al.* Series of New D–A−π–A Organic Broadly Absorbing Sensitizers Containing Isoindigo Unit for Highly Efficient Dye-Sensitized Solar Cells. *ACS Appl. Mater. Interfaces* **4**, 4215-4224 (2012).

88. Qu, S. *et al.* A novel D-A-π–A organic sensitizer containing a diketopyrrolopyrrole unit with a branched alkyl chain for highly efficient and stable dye-sensitized solar cells. *Chem. Commun.* **48**, 6972-6974 (2012).

89. Holcombe, T. W. *et al.* Diketopyrrolopyrrole-based sensitizers for dye-sensitized solar cell applications: anchor engineering. *J. Mater. Chem. A* **1**, 13978-13983 (2013).

90. Delcamp, J. H. *et al.* The Molecular Engineering of Organic Sensitizers for Solar-Cell Applications. *Angew. Chemie Int. Ed.* **52**, 376–380 (2013).

91. Dualeh, A. *et al.* Solid-State Dye-Sensitized Solar Cells Using a Novel Class of Ullazine

Dyes as Sensitizers. *Adv. Energy Mater.* **3**, 496–504 (2013).

92. Huckaba, A. J. *et al.* Indolizine-Based Donors as Organic Sensitizer Components for Dye-Sensitized Solar Cells. *Adv. Energy Mater.* **5**, 1401629 (2015).

93. Huckaba, A. J. *et al.* A low recombination rate indolizine sensitizer for dye-sensitized solar cells. *Chem. Commun.* **52**, 8424–8427 (2016).

94. Brogdon, P. *et al.* A Computational and Experimental Study of Thieno[3,4-b]thiophene as a Proaromatic π-Bridge in Dye-Sensitized Solar Cells. *Chem. – A Eur. J.* **22**, 694–703 (2016).

95. Kang, S. H. *et al.* Porphyrin Sensitizers with Donor Structural Engineering for Superior Performance Dye-Sensitized Solar Cells and Tandem Solar Cells for Water Splitting Applications. *Adv. Energy Mater.* **7**, 1602117 (2017).

96. Wu, Y. & Zhu, W. Organic sensitizers from D−π–A to D–A−π–A: effect of the internal electron-withdrawing units on molecular absorption, energy levels and photovoltaic performances. *Chem. Soc. Rev.* **42**, 2039-2058 (2013).

97. Feldt, S. M. *et al.* Design of Organic Dyes and Cobalt Polypyridine Redox Mediators for High-Efficiency Dye-Sensitized Solar Cells. *J. Am. Chem. Soc.* **132**, 16714–16724 (2010).

98. McNamara, L. E. *et al.* Donor–Acceptor–Donor Thienopyrazines via Pd-Catalyzed C–H Activation as NIR Fluorescent Materials. *J. Org. Chem.* **81**, 32–42 (2016).

99. Chao, C. -Y. *et al.* Band structure engineering for low band gap polymers containing thienopyrazine. *J. Mater. Chem.* **22**, 7331-7341 (2012).

100. Kwon, O. *et al.* Aromatic Amines: A Comparison of Electron-Donor Strengths. *J. Phys. Chem. A* **109**, 9346-9352 (2005).

101. Pazoki, M. *et al.* The effect of dye coverage on the performance of dye-sensitized solar cells with a cobalt-based electrolyte. *Phys. Chem. Chem. Phys.* **16**, 8503-8508 (2014).

102. Jennings, J. R. & Wang, Q. Influence of Lithium Ion Concentration on Electron Injection, Transport, and Recombination in Dye-Sensitized Solar Cells. *J. Phys. Chem. C* **114**, 1715-1724 (2010).

103. Koops, S. E. *et al.* Parameters Influencing the Efficiency of Electron Injection in Dye-Sensitized Solar Cells. *J. Am. Chem. Soc.* **131**, 4808-4818 (2009).

104. Gao, J. *et al.* Cation-Dependent Photostability of Co(II/III)-Mediated Dye-Sensitized Solar Cells. *J. Phys. Chem. C* **119**, 24704-24713 (2015).

105. Gao, J. *et al.* Long-term stability for cobalt-based dye-sensitized solar cells obtained by electrolyte optimization. *Chem. Commun.* **50**, 6249-6251 (2014).

106. Yum, J. H. *et al.* A cobalt complex redox shuttle for dye-sensitized solar cells with high open-circuit potentials. *Nat. Commun.* **3**, 631 (2012).

107. Pei, K. *et al.* Cosensitization of D-A-π-A Quinoxaline Organic Dye: Efficiently Filling the Absorption Valley with High Photovoltaic Efficiency. *ACS Appl. Mater. Interfaces* **7**, 5296–5304 (2015).

108. Zhang, S. *et al.* Improvement of spectral response by co-sensitizers for high efficiency dye-sensitized solar cells. *J. Mater. Chem. A* **1**, 4812-4819 (2013).

109. Xu, M. *et al.* Energy-Level and Molecular Engineering of Organic D-π–A Sensitizers in Dye-Sensitized Solar Cells. *J. Phys. Chem. C* **112**, 19770-19776 (2008).

110. Akhtaruzzaman, M. *et al.* Donor-acceptor dyes incorporating a stable dibenzosilole π–conjugated spacer for dye-sensitized solar cells. *J. Mater. Chem.* **22**, 10771-10778 (2012).

111. Della Pia, A. *et al.* Two-Dimensional Ketone-Droven Metal-Organic Coordination on Cu(111). *Chem. Eur. J.* **22**, 8105-8112 (2016).

112. Katono, M. *et al.* Effect of Extended π–Conjugation of the Donor Structure of Organic D-A-π–A Dyes on the Photovoltaic Performance of Dye-Sensitized Solar Cells. *J. Phys. Chem. C* **118**, 16486-16493 (2014).

113. Kuss-Petermann, M. & Wenger, O. S. Increasing Electron-Transfer Rates with Increasing Donor-Acceptor Distance. *Angew. Chem. Int. Ed.* **55**, 815-819 (2016).

114. Brogdon, P. *et al.* Near-Infrared-Absorbing Metal-Free Organic, Porphyrin, and Phthalocyanine Sensitizers for Panchromatic Dye-Sensitized Solar Cells. *ChemSusChem* **11**, 86–103 (2018).

115. Polman, A. *et al.* Photovoltaic Materials: Present Efficiencies and Future Challenges. *Science* **352**, aad4424 (2016).

116. Zhang, S. *et al.* Highly efficient dye-sensitized solar cells: progress and future challenges. *Energy Environ. Sci.* **6**, 1443–1464 (2013).

117. Ji, J. -M. *et al.* Rational design criteria for D-π–A structured organic and porphyrin sensitizers for highly efficient dye-sensitized solar cells. *J. Mater. Chem. A* **6**, 14518-14545 (2018).

118. Zeng, K. *et al.* Efficient solar cells sensitized by a promising new type of porphyrin: dye-aggregation suppressed by double strapping. *Chem. Sci.* **10**, 2186-2192 (2019).

119. Cheng, Y. *et al.* Organic Sensitizers with Extended Conjugation Frameworks as Cosensitizers of Porphyrins for Developing Efficient Dye-Sensitized Solar Cells. *ACS Appl. Mater. Interfaces* **10**, 38880-38891 (2018).

120. Song, H. *et al.* Porphyrin-Sensitized Solar Cells: Systematic Molecular Optimization, Coadsorption and Cosensitization. *Chem. Commun.* **54**, 1811−1824 (2018).

121. Yang, G. *et al.* Efficient Solar Cells Based on Porphyrin Dyes with Flexible Chains Attached to the AuxiliaryBenzothiadiazole Acceptor: Suppression of Dye Aggregation and the Effect of Distortion. *ACS Appl. Mater. Interfaces* **9**, 36875-36885 (2017).

122. Wang, Y. *et al.* Efficient Solar Cells Sensitized by Porphyrins with an Extended Conjugation Framework and a Carbazole Donor: From Molecular Deisgn to Cosensitization. *Angew. Chem. Int. Ed.* **53**, 10779-10783 (2014).

123. Luo, J. *et al.* N-Annulated Perylene as an Efficient Electron Donor for Porphyrin-Based Dyes: Enhanced Light-Harvesting Ability and High-Efficiency Co(II/III)-Based Dye-Sensitized Solar Cells. *J. Am. Chem. Soc.* **136**, 265−272 (2014).

124. Mathew, S. *et al.* Synthesis, characterization and ab initio investigation of a panchromatic ullazine–porphyrin photosensitizer for dye-sensitized solar cells. *J. Mater. Chem. A* **4**, 2332–2339 (2016).

125. Xie, Y. *et al.* Porphyrin Cosensitization for a Photovoltaic Efficiency of 11.5%: A Record for Non-Ruthenium Solar Cells Based on Iodine Electrolyte. *J. Am. Chem. Soc.* **137**, 14055−14058 (2015).

126. Krishna, N. V. *et al.* Donor-π-Acceptor Based Stable Porphyrin Sensitizers for Dye-Sensitized Solar Cells: Effect of π- Conjugated Spacers. *J. Phys. Chem. C* **121**, 6464−6477 (2017).

127. Wang, C.-L. *et al.* Enveloping Porphyrins for Efficient Dye-Sensitized Solar Cells. *Energy Environ. Sci.* **5**, 6933−6940 (2012).

128. Liu, Y.-C. *et al.* A Feasible Scalable Porphyrin Dye for Dye-Sensitized Solar Cells under One Sun and Dim Light Environments. *J. Mater. Chem. A* **4**, 11878−11887 (2016).

129. Maś-Montoya, M. & Janssen, R. A. J. The Effect of H- and J- Aggregation on the Photophysical and Photovoltaic Properties of Small Thiophene-Pyridine-DPP Molecules for Bulk-Heterojunction Solar Cells. *Adv. Funct. Mater.* **27**, 1605779 (2017).

130. Frisch, M. J., Trucks, G. W., Schlegel, H. B., Scuseria, G. E, Robb, M. A., Cheeseman, J. R.; Scalmani, G., Barone, V., Petersson, G. A., Nakatsuji, H., Li, X., Caricato, M., Marenich, A. V., Bloino, J., Janesko, B. G., Gomperts, R., Mennucci, B., Hratchian, H. P., Ortiz, J. V., Izmaylov, A. F., Sonnenberg, J. L., Williams-Young, D., Ding, F., Lipparini, F., Egidi, F., Goings, J., Peng, B., Petrone, A., Henderson, T., Ranasinghe, D., Zakrzewski, V. G., Gao, J., Rega, N., Zheng, G., Liang, W., Hada, M., Ehara, M., Toyota, K., Fukuda, R., Hasegawa, J., Ishida, M., Nakajima, T., Honda, Y., Kitao, O., Nakai, H., Vreven, T., Throssell, K., Montgomery, J. A., Jr., Peralta, J. E., Ogliaro, F., Bearpark, M. J., Heyd, J. J., Brothers, E. N., Kudin, K. N., Staroverov, V. N., Keith, T. A, Kobayashi, R., Normand, J., Raghavachari, K., Rendell, A. P., Burant, J. C., Iyengar, S. S., Tomasi, J., Cossi, M., Millam, J. M., Klene, M., Adamo, C., Cammi, R., Ochterski, J. W., Martin, R. L., Morokuma, K., Farkas, O., Foresman, J. B., Fox, D. J. Gaussian 16, Revision A.03; Gaussian, Inc.: Wallingford CT, 2016.

131. Vydrov, O. A. *et al.* Tests of Functionals for Systems with Fractional Electron Number. *J. Chem. Phys.* **126**, 154109 (2007).

132. Vydrov, O. A. & Scuseria, G. E. Assessment of a Long-Range Corrected Hybrid Functional. *J. Chem. Phys.* **125**, 234109 (2006).

133. Vreven, T. *et al.* Geometry Optimization with QM/MM Methods II: Explicit Quadratic Coupling. *Mol. Phys.* **104**, 701−714 (2006).

134. Perdew, J. P. *et al.* Generalized Gradient Approximation Made Simple. *Phys. Rev. Lett.* **78**, 1396 (1997).

135. Perdew, J. P. *et al.* Generalized Gradient Approximation Made Simple. *Phys. Rev. Lett.* **77**, 3865−3868 (1996).

136. Hariharan, P. C. & Pople, J. A. The Influence of Polarization Functions on Molecular Orbital Hydrogenation Energies. *Theor. Chim. Acta* **28**, 213−222 (1973).

137. Francl, M. M. *et al.* Self-consistent molecular orbital methods. XXIII. A polarization-type basis set for second-row elements. *J. Chem. Phys.* **77**, 3654−3665 (1982).

138. Stein, T. *et al.* Reliable Prediction of Charge Transfer Excitations in Molecular Complexes Using Time-Dependent Density Functional Theory. *J. Am. Chem. Soc.* **131**, 2818−2820 (2008).

139. Grimme, S. *et al.* Effect of the Damping Function in Dispersion Corrected Density Functional Theory. *J. Comput. Chem.* **32**, 1456−1465 (2011).

140. Johnson, E. R. & Becke, A. D. A Post-Hartree-Fock Model of Intermolecular Interactions: Inclusion of Higher-Order Corrections. *J. Chem. Phys.* **124**, 174104 (2006).

141. Ito, S. *et al.* High-Conversion-Efficiency Organic Dye-Sensitized Solar Cells with a Novel Indoline Dye. *Chem. Commun.* 5194−5196 (2008).

142. Ozawa, H. *et al.* Effects of Dye- Adsorption Solvent on the Performances of the Dye-Sensitized Solar Cells Based on Black Dye. *Chem. —Asian J.* **7**, 156−162 (2012).

143. Cole, J. M. *et al.* Modulation of N3 and N719 Dye···TiO_2 Interfacial Structures in Dye-

Sensitized Solar Cells as Influenced by Dye Counter Ions, Dye Deprotonation Levels, and Sensitizing Solvent. *ACS Appl. Energy Mater.* **1**, 2821−2831 (2018).

144. Li, W. *et al.* Thiophene-Functionalized Porphyrins: Synthesis, Photophysical Properties, and Photovoltaic Performance in Dye-Sensitized Solar Cells. *J. Phys. Chem. C* **119**, 5265−5273 (2015).

145. Neale, N. R. *et al.* Effect of a Coadsorbent on the Performance of Dye-Sensitized TiO_2 Solar Cells: Shielding Versus Band-Edge Movement. *J. Phys. Chem. B* **109**, 23183−23189 (2005).

146. Song, P. *et al.* Insight into External Electric Field Dependent Photoinduced Intermolecular Charge Transport in Bhj Solar Cell Materials. *J. Mater. Chem. C* **3**, 4810−4819 (2015).

147. Song, P. *et al.* External Electric Field-Dependent Photoinduced Charge Transfer in a Donor-Acceptor System for an Organic Solar Cell. *J. Phys. Chem. C* **117**, 15879− 15889 (2013).

148. Song, P. *et al.* Vibronic Quantized Tunneling Controlled Photoinduced Electron Transfer in an Organic Solar Cell Subjected to an External Electric Field. *Phys. Chem. Chem. Phys.* **19**, 16105−16112 (2017).

149. Peddapuram, A. *et al.* A Stable Panchromatic Green Dual Acceptor, Dual Donor Organic Dye for Dye-Sensitized Solar Cells. *J. Phys. Chem. C* **121**, 8770–8780 (2017).

150. Yella, A. *et al.* Dye-Sensitized Solar Cells Using Cobalt Electrolytes: The Influence of Porosity and Pore Size to Achieve High-Efficiency. *J. Mater. Chem. C* **5**, 2833−2843 (2017).

151. Kim, B.-M. *et al.* Control and Monitoring of Dye Distribution in Mesoporous TiO_2 Film

for Improving Photovoltaic Performance. *ACS Appl. Mater. Interfaces* **9**, 2572−2580 (2017).

152. Brogdon, P. *et al.* Toward Tightly Bound Carboxylic Acid-Based Organic Dyes for DSCs: Relative TiO_2 Binding Strengths of Benzoic Acid, Cyanoacrylic Acid, and Conjugated Double Carboxylic Acid Anchoring Dyes. *Synth. Met.* **222**, 66–75 (2016).
153. Cheema, H. *et al.* Molecular Engineering of Near Infrared Absorbing Thienopyrazine Double Donor Double Acceptor Organic Dyes for Dye-Sensitized Solar Cells. *J. Org. Chem.* **82**, 12038–12049 (2017).
154. Cheema, H. & Delcamp, J. H. Harnessing Photovoltage: Effects of Film Thickness, TiO2 Nanoparticle Size, MgO and Surface Capping with DSCs. *ACS Appl. Mater. Interfaces* **9**, 3050–3059 (2017).
155. Listorti, A. *et al.* Electron Transfer Dynamics in Dye-Sensitized Solar Cells. *Chem. Mater.* **23**, 3381–3399 (2011).
156. Mazloum-Ardakani, M. & Khoshroo, A. Enhanced performance of dye-sensitized solar cells with dual-function coadsorbent: reducing the surface concentration of dye–iodine complexes concomitant with attenuated charge recombination. *Phys. Chem. Chem. Phys.* **17**, 22985–22990 (2015).
157. O'Regan, B. C. *et al.* Structure/Function Relationships in Dyes for Solar Energy Conversion: A Two-Atom Change in Dye Structure and the Mechanism for Its Effect on Cell Voltage. *J. Am. Chem. Soc.* **131**, 3541–3548 (2009).
158. Liu, T. & Troisi, A. Theoretical evidence of multiple dye regeneration mechanisms in dye-sensitized solar cells. *Chem. Phys. Lett.* **570**, 159–162 (2013).

159. Jeanbourquin, X. A. *et al.* Rediscovering a Key Interface in Dye-Sensitized Solar Cells: Guanidinium and Iodine Competition for Binding Sites at the Dye/Electrolyte Surface. *J. Am. Chem. Soc.* **136**, 7286–7294 (2014).

160. Simon, S. J. C. *et al.* Halogen Bonding Promotes Higher Dye-Sensitized Solar Cell Photovoltages. *J. Am. Chem. Soc.* **138**, 10406–10409 (2016).

161. Kusama, H. *et al.* Intermolecular interactions between a Ru complex and organic dyes in cosensitized solar cells: a computational study. *Phys. Chem. Chem. Phys.* **16**, 16166–16175 (2014).

162. Kusama, H. & Sayama, K. A comparative computational study on the interactions of N719 and N749 dyes with iodine in dye-sensitized solar cells. *Phys. Chem. Chem. Phys.* **17**, 4379–4387 (2015).

163. Pastore, M. *et al.* Computational Investigation of Dye–Iodine Interactions in Organic Dye-Sensitized Solar Cells. *J. Phys. Chem. C* **116**, 5965–5973 (2012).

164. Robson, K. C. D. *et al.* Atomic Level Resolution of Dye Regeneration in the Dye-Sensitized Solar Cell. *J. Am. Chem. Soc.* **135**, 1961–1971 (2013).

165. Gu, D.-M. *et al.* Dye regeneration mechanisms of dye sensitized solar cells: Quantum chemical studies on the interaction between iodide and O/S-containing organic dyes. *Dyes Pigm.* **132**, 136–141 (2016).

166. Asghar, M. I. *et al.* Intriguing Photochemistry of the Additives in the Dye-Sensitized Solar Cells. *J. Phys. Chem. C* **120**, 27768–27781 (2016).

167. Xie, M. *et al.* Theoretical description of dye regeneration on the TiO2–dye–electrolyte model. *Comput. Mater. Sci.* **111**, 239–246 (2016).

168. Li, H.-B. *et al.* Theoretical studies on organic D-π-A sensitizers with planar triphenylamine donor and different π-linkers for dyes-sensitized solar cells. *J. Mol. Model.* **20**, 2309 (2014).

169. Zhang, J. *et al.* A promising anchor group for efficient organic dye sensitized solar cells with iodine-free redox shuttles: a theoretical evaluation. *J. Mater. Chem. A* **1**, 14000–14007 (2013).

170. Balanay, M. P. & Kim, D. H. Theoretical study on the correlations between dye–iodine interactions and open-circuit voltages in dyes containing furan and thiophene. *Comput. Theor. Chem.* **1029**, 1–12 (2014).

171. Metrangolo, P., *et al.* Halogen Bonding in Supramolecular Chemistry. *Angew. Chemie Int. Ed.* **47**, 6114–6127 (2008).

172. Luo, J. *et al.* A co-sensitized approach to efficiently fill the absorption valley, avoid dye aggregation and reduce the charge recombination. *Electrochim. Acta* **215**, 506–514 (2016).

173. Deplano, P. *et al.* On the Use of Raman Spectroscopy in the Characterization of Iodine in Charge-Transfer Complexes. *Appl. Spectrosc.* **46**, 1625–1629 (1992).

174. Asseily, G. A. *et al.* A solid-state structural and theoretical study on the 1 : 1 addition compounds of thioethers with dihalogens and interhalogens I–X (X = I, Br, Cl). *New J. Chem.* **29**, 315–319 (2005).

175. Boschloo, G. & Hagfeldt, A. Characteristics of the Iodide/Triiodide Redox Mediator in Dye-Sensitized Solar Cells. *Acc. Chem. Res.* **42**, 1819–1826 (2009).

176. Chai, J.-D. & Head-Gordon, M. Long-range corrected hybrid density functionals with

damped atom–atom dispersion corrections. *Phys. Chem. Chem. Phys.* **10**, 6615–6620 (2008).

177. Grimme, S. Semiempirical GGA-type density functional constructed with a long-range dispersion correction. *J. Comput. Chem.* **27**, 1787–1799 (2006).

178. Feller, D. The role of databases in support of computational chemistry calculations. *J. Comput. Chem.* **17**, 1571–1586 (1996).

179. Schuchardt, K. L. *et al.* Basis Set Exchange: A Community Database for Computational Sciences. *J. Chem. Inf. Model.* **47**, 1045–1052 (2007).

180. Kim, S.-H. & Rieke, R. D. 5-Substituted-2-furaldehydes: A Synthetic Protocol Utilizing an Organozinc Route. *J. Org. Chem.* **78**, 1984–1993 (2013).

181. Vanderkooy, A. & Taylor, M. S. Exploring the construction of multi compartmental micelles by halogen bonding of complementary macromolecules. *Faraday Discuss.* **203**, 285-299 (2017).

182. Cheng, F. *et al.* Halogen bonded supramolecular porous structures with a kgm layer. *Cryst. Eng. Comm.* **18**, 9227-9230 (2016).

183. Vanderkooy, A. *et al.* Self-Assembly of Polymer Nanostructures through Halogen Bonding Interactions of an Iodoperfluoroarene-Functionalized Polystyrene Derivative. *Macromolecules* **50**, 3807-3817 (2017).

184. Simon, S. J. C. *et al.* Halogen Bonding Promotes Higher Dye-Sensitized Solar Cell Photovoltages. *J. Am. Chem. Soc.* **138**, 10406-10409 (2016).

185. Parlane, F. G. L. *et al.* Spectroscopic detection of halogen bonding resolves dye regeneration in the dye-sensitized solar cell. *Nat. Commun.* **8**, 1761 (2017).

186. Casarin, L. *et al.* Rapid Static Sensitizer Regeneration Enabled by Ion Pairing. *Inorgan. Chem.* **56**, 7324-7327 (2017).

187. Chiykowski, V. A. *et al.* On how electron density effects the redox stability of phenothiazine sensitizers on semiconducting surfaces. *Chem. Commun.* **53**, 2547-2550 (2017).

188. Chiykowski, V. A. *et al.* Comparative analysis of triarylamine and phenothiazine sensitizer donor units in dye-sensitized solar cells. *Chem. Commun.* **53**, 2367-2370 (2017).

189. Ogunsolu, O. O. *et al.* Increasing the Open-Circuit Voltage of Sye-Sensitized Solar Cells via Metal-Ion Coordination. *Inorg. Chem.* **56**, 11168-11175 (2017).

190. Chen, K. Y. *et al.* High-Voltage Dye-Sensitized Solar Cells Mediated by [Co(2,2'-pipyrimidine)$_3$]^z . *Inorg. Chem.* **56**, 2382-2386 (2017).

191. Tian, L. *et al.* Ultrafast dye regeneration in a core-shell NiO-dye-TiO_2 mesoporous film. *Phys. Chem. Chem. Phys.* **20**, 36-40 (2018).

192. Bacskay, G. B. A Quadratically Convergent Hatree-Fock (QC-SCF) Method. Application to Closed Systems. *Chem. Phys.* **61**, 385-404 (1981).

193. Tomasi, J. *et al.* Quantum mechanical continuum salvation models. *Chem. Rev.* **105**, 2999-3093 (2005).

194. Miertus, S. *et al.* Electrostatic Interaction of a Solute with a Continuum. A Direct Utilization of ab initio Molecular Potentials for the Prevision of Solvent Effects. *Chem. Phys.* **55**, 117-129 (1981).

195. Cossi, M. *et al.* Ab initio study of solvated molecules: A new implementation of the polarizable continuum model. *Chem Phys. Lett.* **255**, 327-335 (1996).

196. Foresman, J. B. & Frisch, Æ. Exploring chemistry with electronic structure methods. (2013).

197. Bauernschmitt, R. & Ahlrichs, R. Treatment of electronic excitations within the adiabatic approximation of time dependent density functional theory. *Chem. Phys. Lett.* **256** 454-464 (1996).

198. Adamo, C. & Jacquemin, D. The calculations of excited-state properties with Time-Dependent Density Functional Theory. *Chem. Soc. Rev.* **42**, 845 (2013).

199. Le Bahers, T. *et al.* A qualitative index of spatial extent in charge-transfer excitations. *J. Chem. Theor. Comp.* **7**, 2498-2506 (2011).

200. Prakongpan, S. & Nagai, T. Solubility of Acetominophen in Cosolvents. *Chem. Pharm. Bull.* **32**, 340-343 (1984).

201. Saygili, Y. *et al.* Metal Coordination Complexes as Redox Mediators in Regenerative Dye-Sensitized Solar Cells. *Inorganics* **7**, 30 (2019).

202. Cole, J. M. *et al.* Cosensitization in Dye-Sensitized Solar Cells. *Chem. Rev.* **119**, 7279-7327 (2019).

203. Wu, Y. *et al.* Insight into D-A-π-A Structured Sensitizers: A Promising Route To Highly Efficient and Stable Dye-Sensitized Solar Cells. *ACS Appl. Mater. Interfaces* **18**, 9307-9318 (2015).

204. Fakharuddin, A. *et al.* A perspective on the production of dye-sensitized solar modules. *Energy Environ Sci.* **7**, 3952-3981 (2014).

205. Zhang, L. *et al.* 13.6% Efficient Organic Dye-Sensitized Solar Cells by Minimizing Energy Losses of the Excited State. *ACS Energy Lett.* **4**, 943-951 (2019).

206. Cavallo, G. *et al.* The Halogen Bond. *Chem. Rev.* **116**, 2478-2601 (2016).

207. Baumann, A. *et al.* Robust Scalable Synthesis of the Bulky Hagfeldt Donor for Dye-Sensitized Solar Cells. *ChemSusChem.* (2019).

208. Ogunsolu, O. O. *et al.* Influence of Dye-Coordinated Metal Ions on Electron Transfer Dynamics at Dye-Semiconductor Interfaces. *ACS Appl. Energy Mater.* **2**, 29-36 (2018).

209. Delcamp, J. H. *et al.* The Molecular Engineering of Organic Sensitizers for Solar-Cell Applications. *Angew. Chem. Int. Ed.* **52**, 376-380 (2013).

210. Karsten, B. P. *et al.* Electronic structure of small band gap oligomers based on cyclopentadithiophenes and acceptor units. *J. Mater. Chem.* **19**, 5343 (2009).

211. Guo, S. *et al.* Synthesis of star-shaped non-fullerene acceptors and their applications in organic solar cells. *Synt. Met.* **245**, 167-174 (2018).

212. Lazar, M. A. *et al.* Enhanced thermal energy harvesting performance of a cobalt redox couple in ionic liquid-solvent mixtures. *Phys. Chem. Chem. Phys.* **18**, 1404-1410 (2016).

APPENDIX

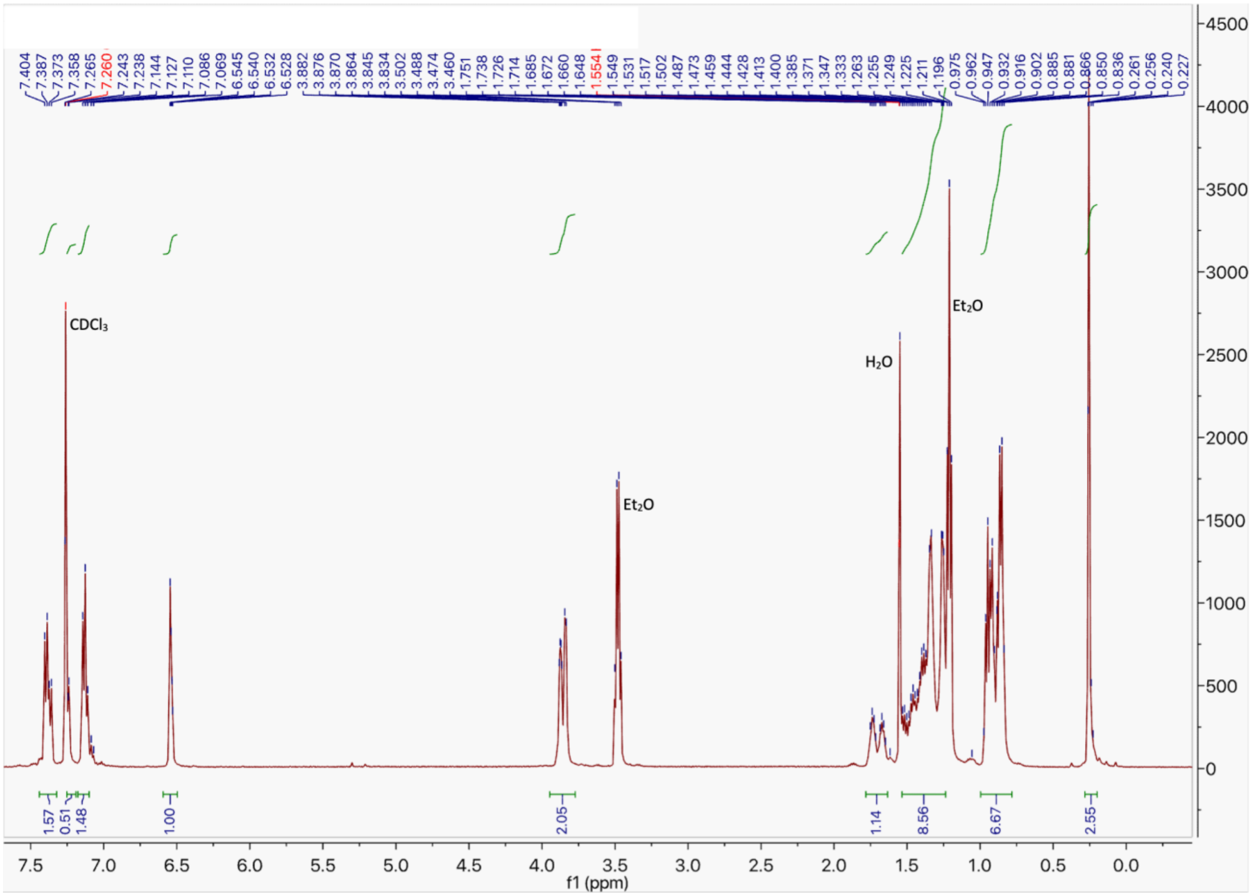

Figure 50. Proton NMR of compound **20** for 500 MHz in $CDCl_3$ at room temp.

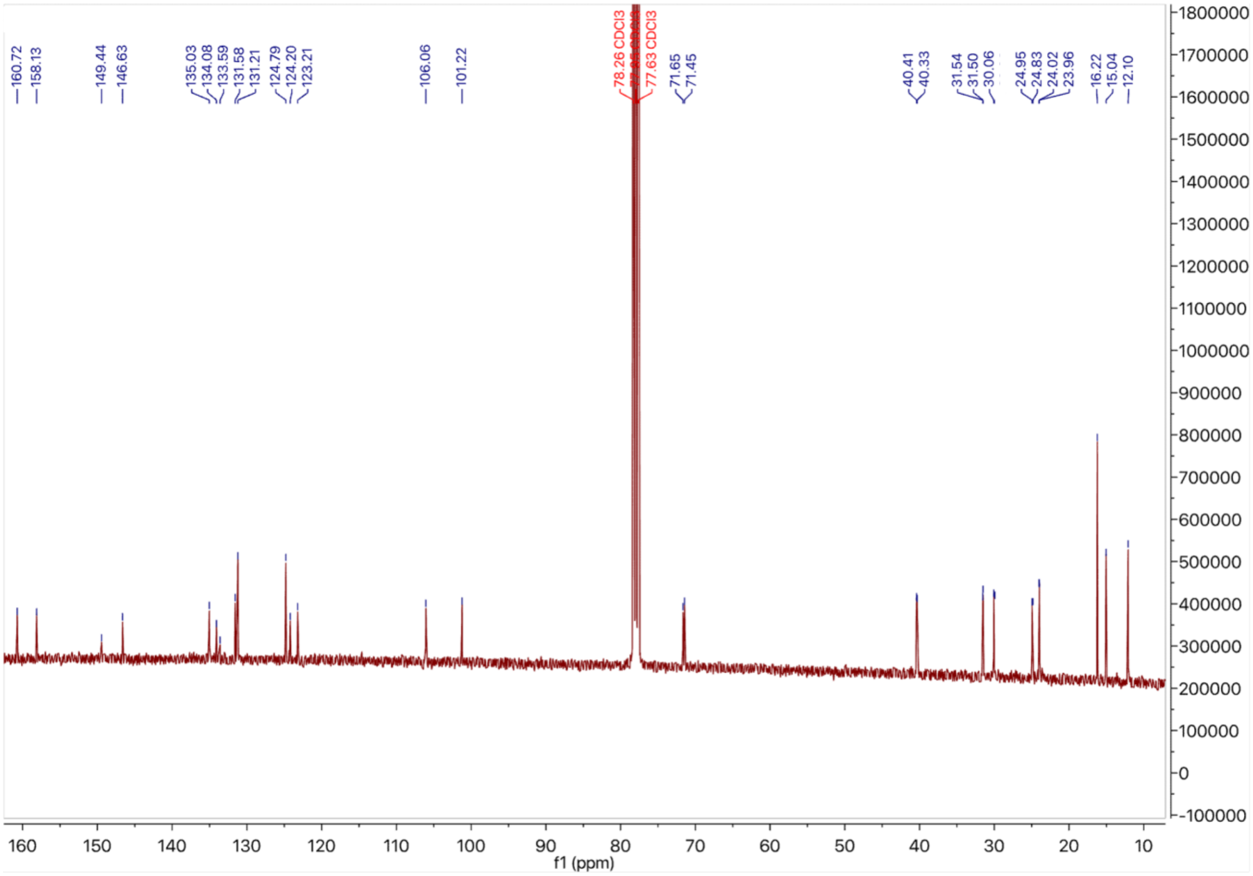

Figure 51. Carbon NMR of compound **20** for 100 MHz in $CDCl_3$ at room temp.

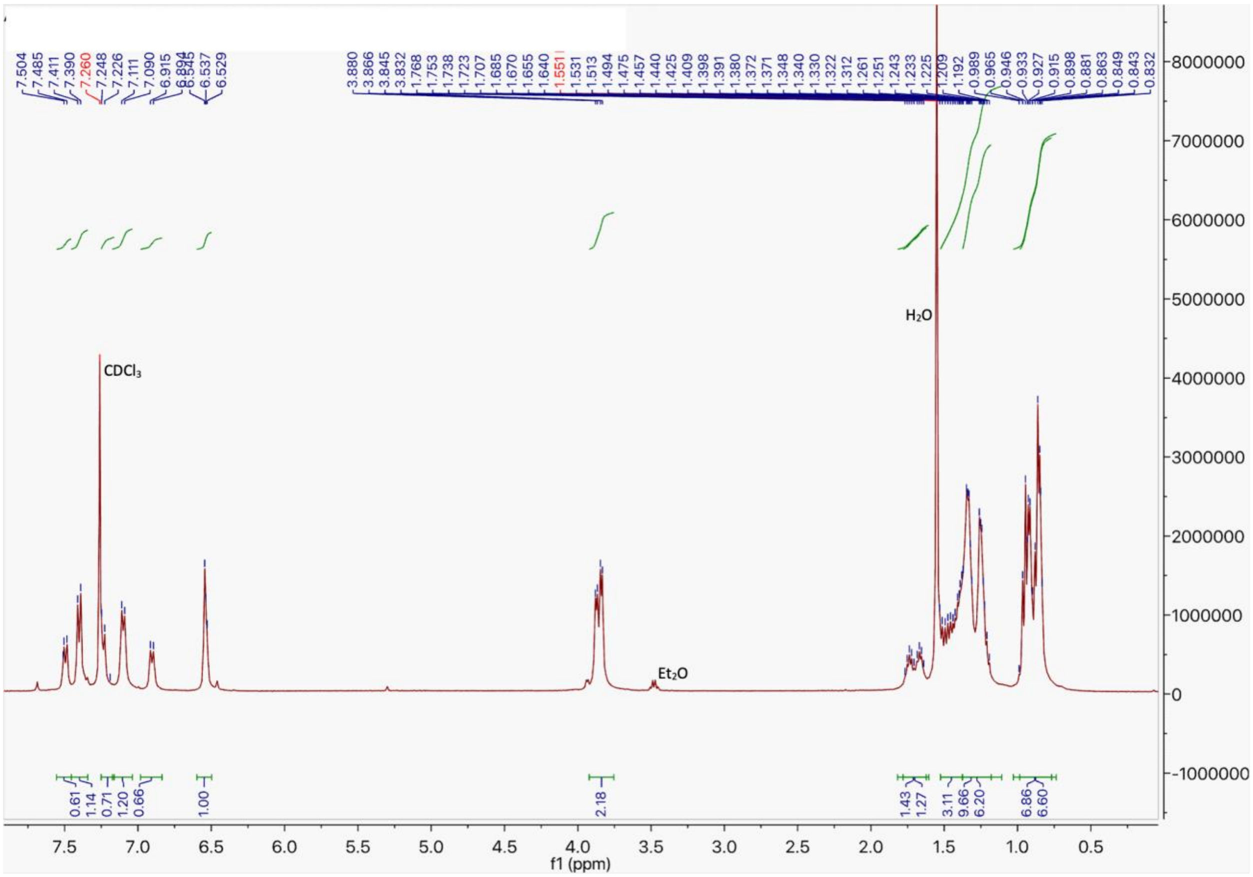

Figure 52. Proton NMR of compound **21** for 500 MHz in CDCl$_3$ at room temp.

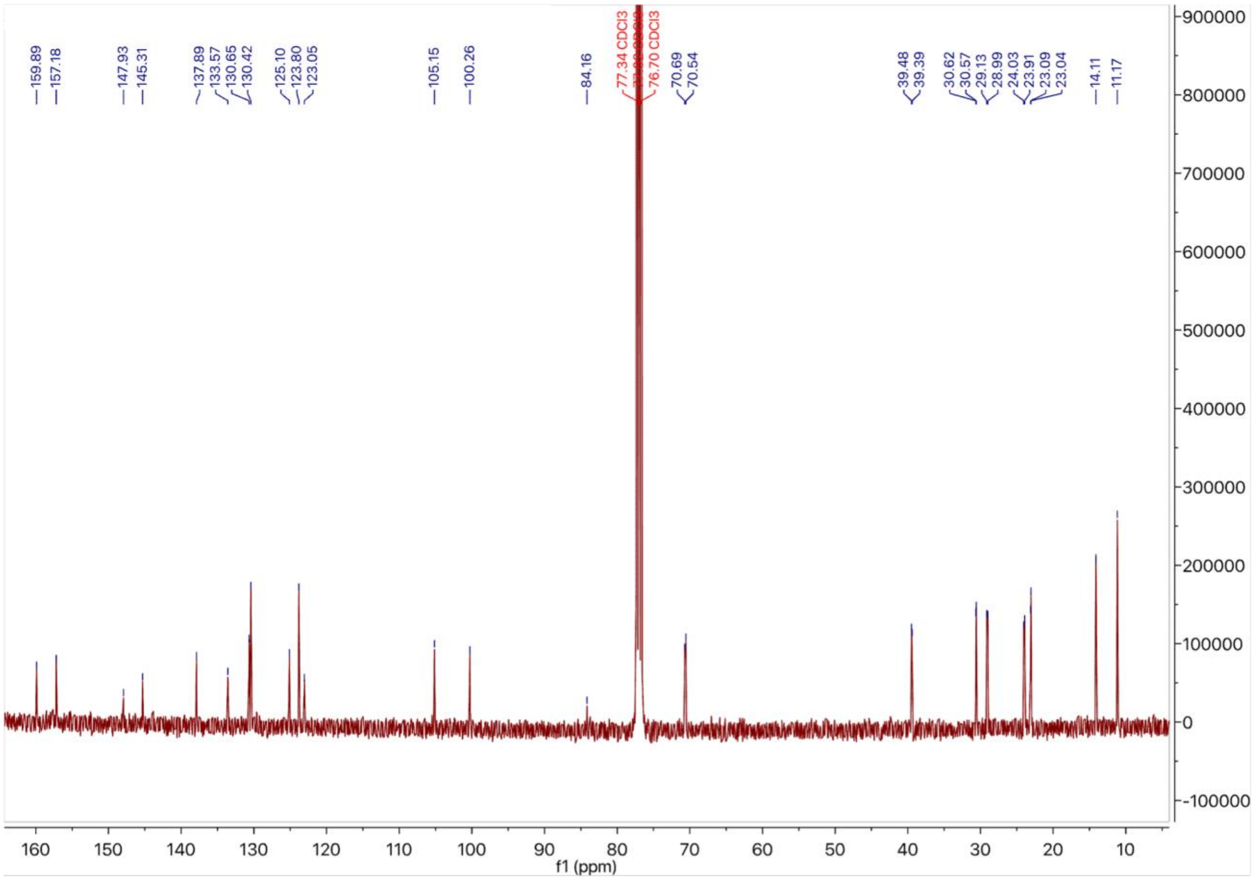

Figure 53. Carbon NMR of compound **21** for 100 MHz in $CDCl_3$ at room temp.

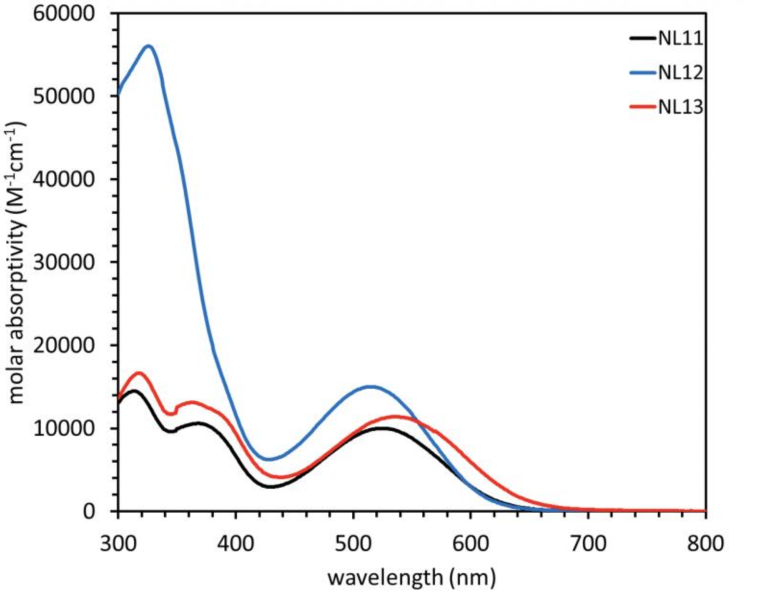

Figure 54: UV-Vis absorption spectra collected for **NL11-NL13** dyes in 0.01 M Bu_4NOH in DMF.

Table 20: Absorption and dye loading data for **NL11-NL13**

Dye	λ_{max}(nm)	ε($M^{-1}cm^{-1}$)	$^{b}\lambda_{onset}$(nm)	^{c}Dye loading (mmol/cm^2)
NL11	525	10000	630	5.00×10^{-5}
NL12	515	15000	620	9.74×10^{-6}
NL13	540	11000	650	2.54×10^{-5}

[b] The absorption onset was taken by drawing a tangent line for the λ_{max} absorption curve (from the long wavelength region), and extrapolating it to cross with the x-axis of the of the absorption curve. [c] Dye loading was calculated from completely desorbed solution (18 h) from 0.50 cm^2 surface.

Table 21: Device parameters for **D35** and the structure of **D35.**

entry	Li+ (M)	electrolyte	V_{oc} (mV)	J_{sc} (mA/cm^2)	FF	PCE (%)
1	1.00	I^-/I_3^-	679	12.5	0.75	6.6
2	0.05	Co^{2+}/Co^{3+}	846	10.7	0.70	6.6
3	0.05[a]	Co^{2+}/Co^{3+}	855	10.3	0.72	6.5

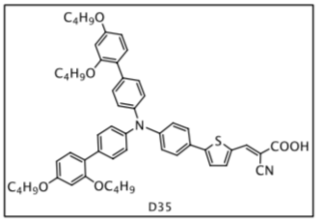

See experimental section for TiO_2 film thicknesses and compositions. Dyes were deposited from a THF:EtOH (1:4) solution with a dye concentration of 0.3 mM and a 40:1 CDCA:dye ratio overnight in the dark at room temperature unless otherwise noted. *I^-/I_3^- electrolyte:* 1.0 M DMII, 30 mM I_2, 0.5 M TBP, 0.1 M GNCS in acetonitrile:valeronitrile (v/v 85/15) with LiI concentration varied. *Co^{2+}/Co^{3+} electrolyte:* 0.25 M $Co(bpy)_3(PF_6)_2$, 0.05 M $Co(bpy)_3(PF_6)_3$, 0.05 M LiTFSI, 0.5 M TBP in acetonitrile. [a]Dye was loaded onto TiO_2 with acetonitrile:*tert*-butanol (1:1) with 10:1 CDCA:dye concentration.

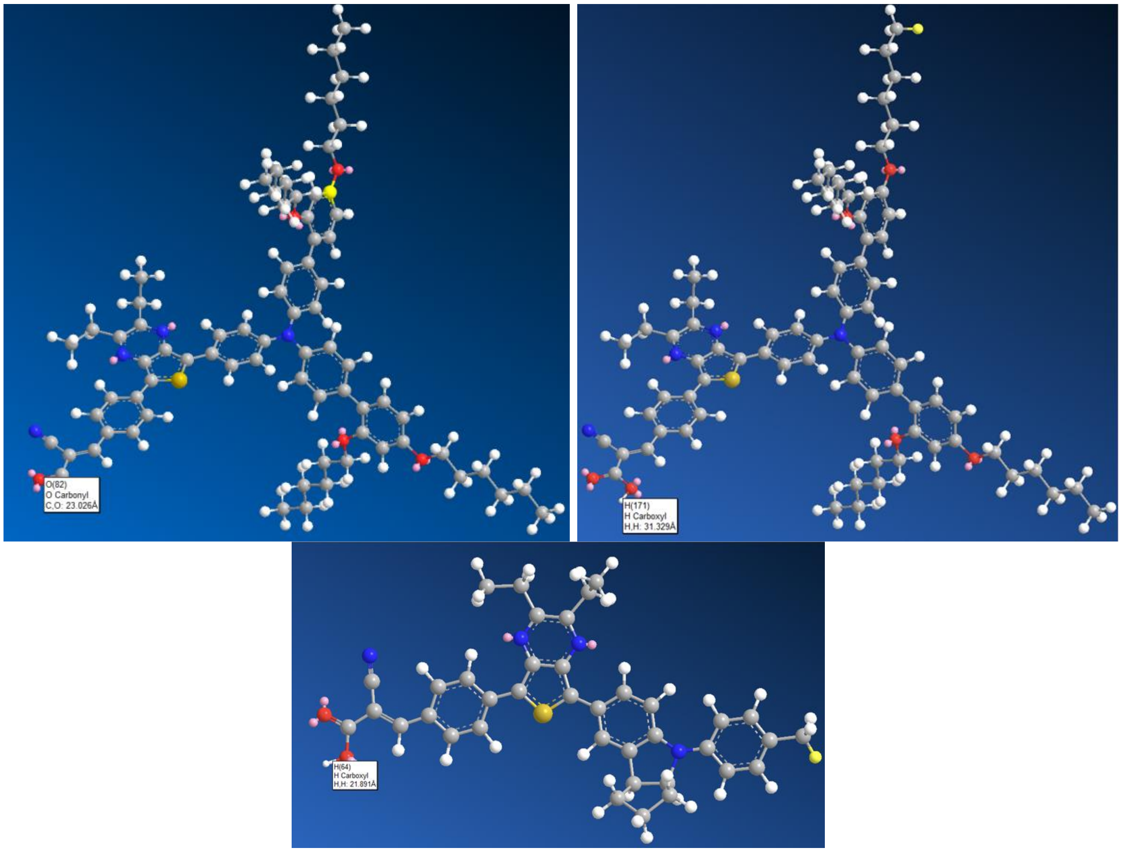

Figure 55: Illustration of dye donor sizes based on (a) only the conjugated groups for **NL12** (maximum length 23.026 Å), (b) the maximum size based on variable alkane conformations of **NL12** (maximum length 31.329 Å) and (c) of the donor group for **NL13** (maximum length 19.992 Å) based on MM2 optimized models.

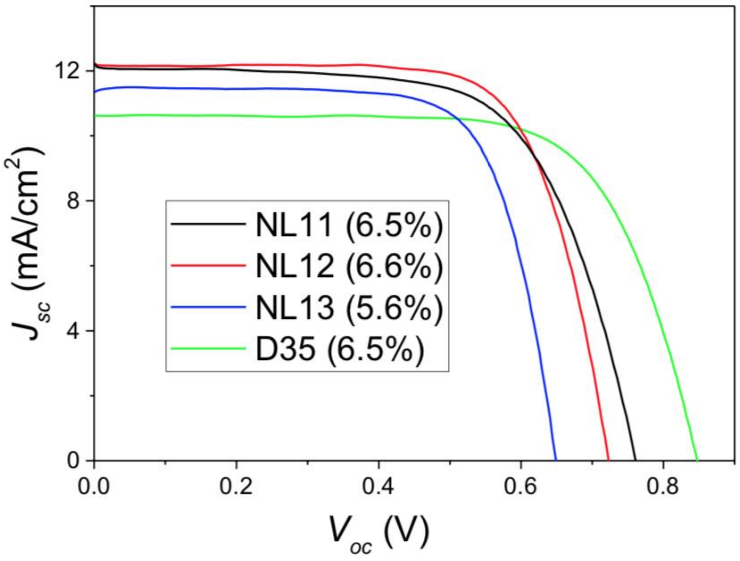

Figure 56: J-V curves for the best Co devices reported in **Table 3**.

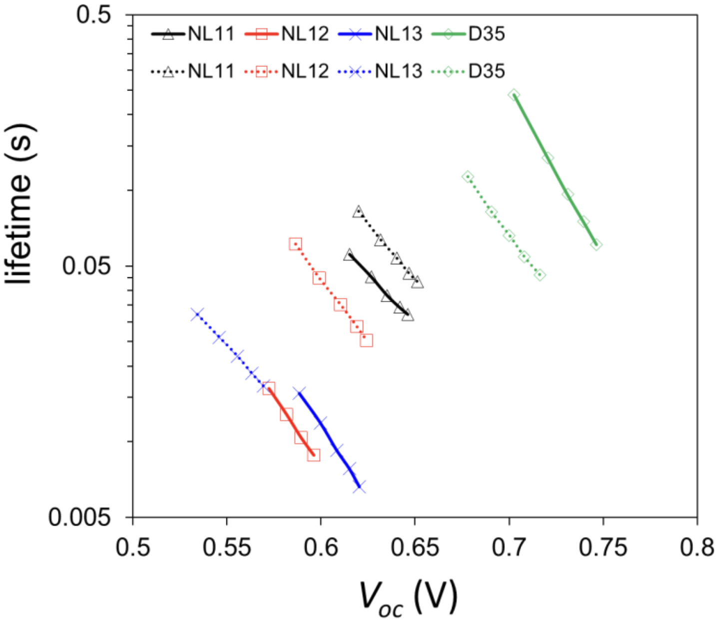

Figure 57: Electron lifetime data measured for devices with iodine based electrolyte based on **NL11- NL13** and **D35** with 0.05 M LiI (solid) and 1.00 M LiI (dotted) electrolyte.

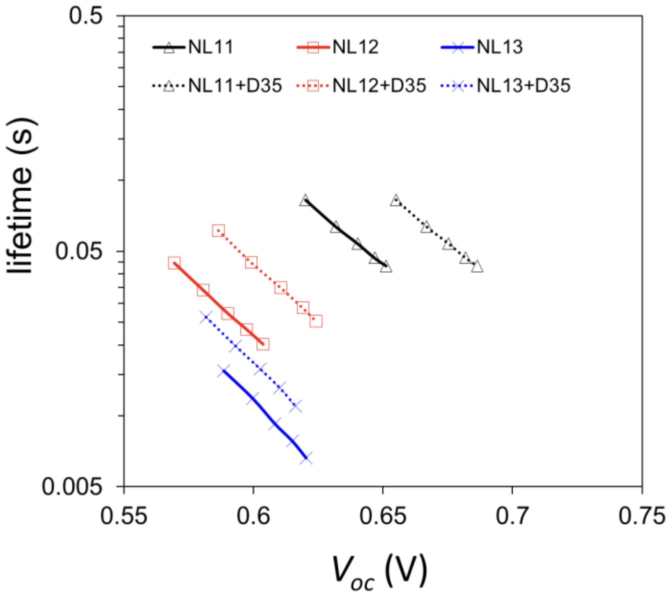

Figure 58. Electron lifetime data measured for devices with iodine based electrolyte without (solid) and with co-sensitization (dotted) with 1.00 M LiI for **NL11** versus **NL11** + **D35**, 1.00 M LiI for **NL12** versus **NL12** + **D35** and with 0.05 M LiI for **NL13** versus **NL13** + **D35**.

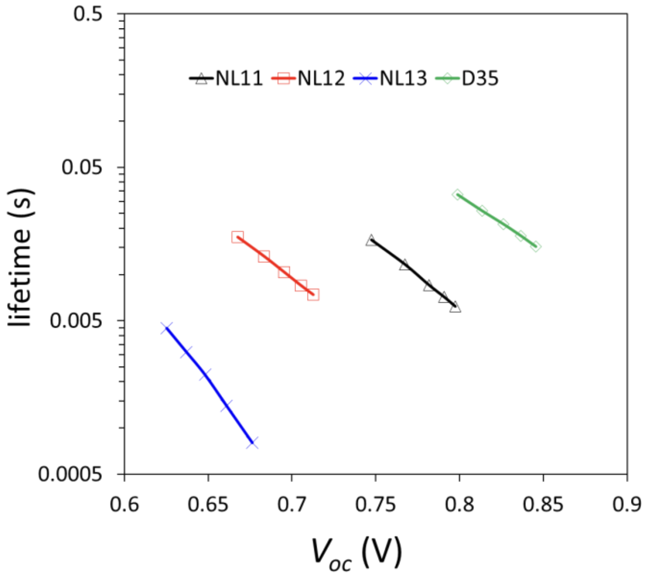

Figure 59. Electron lifetime for devices made with cobalt electrolyte and dyes deposited from acetonitrile:*tert*-butanol solutions.

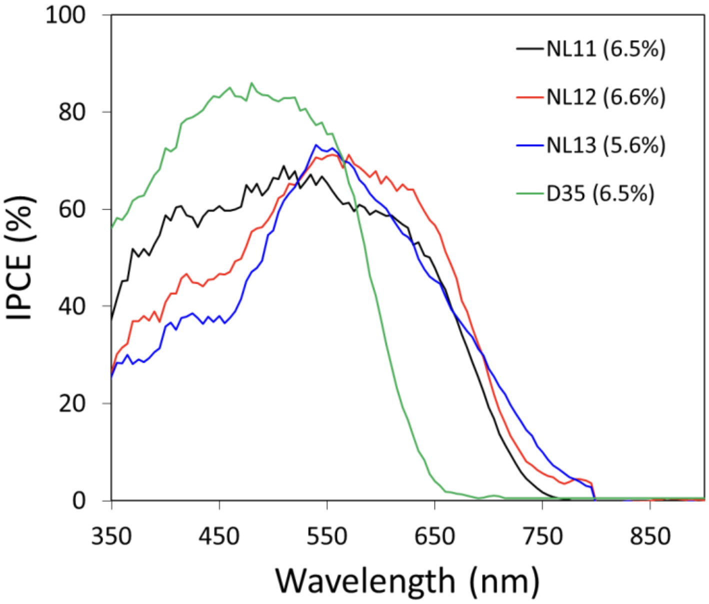

Figure 60. IPCE spectrums for devices made based on **NL11-NL13** dyes with cobalt electrolyte.

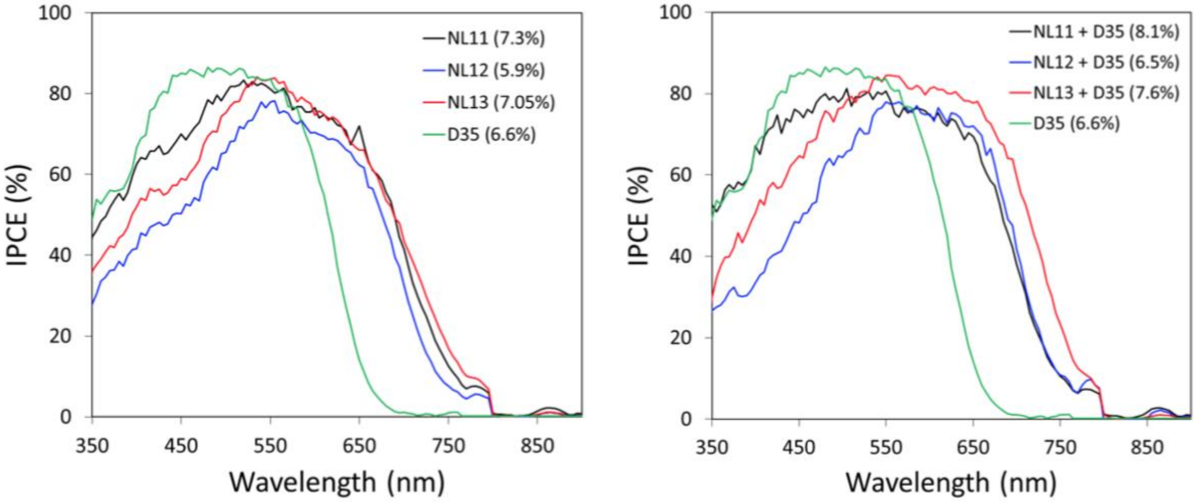

Figure 61. IPCE spectrum for **NL11-NL13** based devices without co-sensitization (right) and with co-sensitized with **D35** (left).

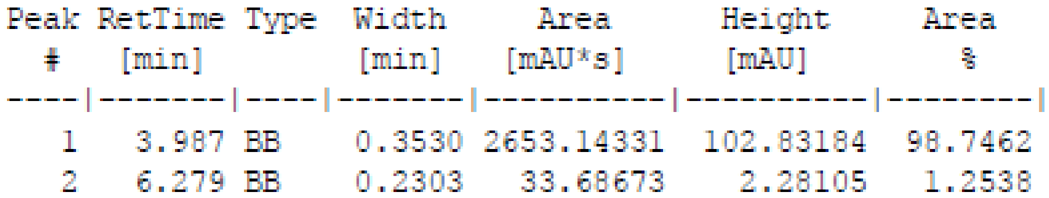

```
Peak RetTime Type  Width     Area      Height     Area  
  #   [min]        [min]   [mAU*s]     [mAU]        %   
----|-------|----|-------|----------|----------|--------|
   1   3.987 BB    0.3530 2653.14331  102.83184  98.7462
   2   6.279 BB    0.2303   33.68673    2.28105   1.2538
```

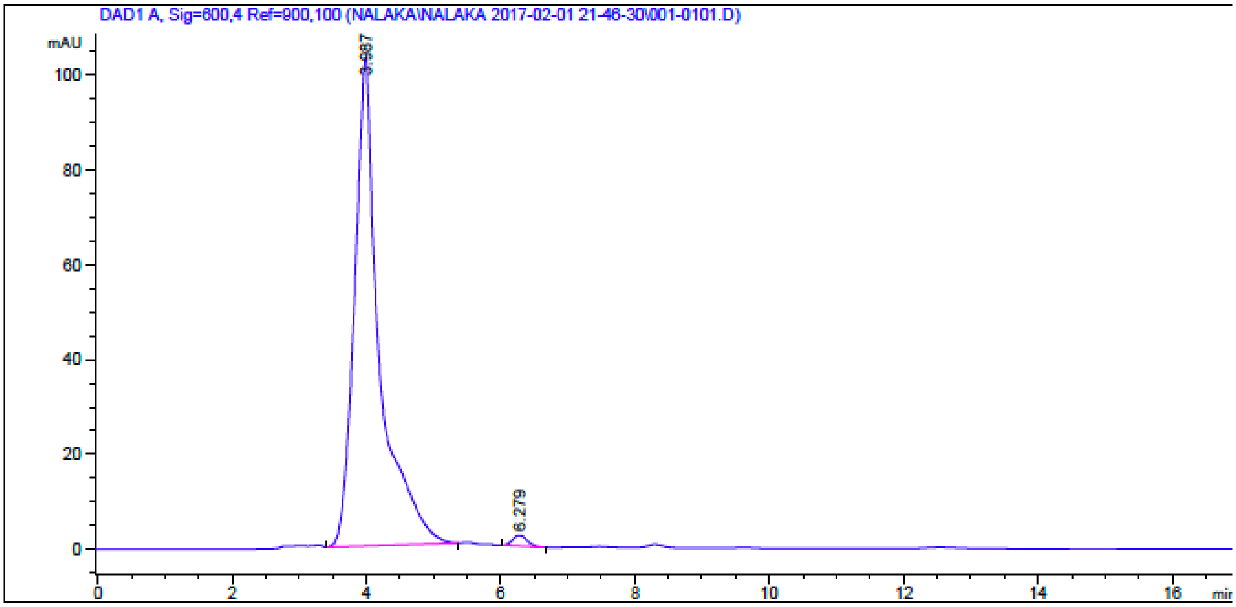

Figure 62. HPLC data for **NL11** (98.7 % purity).

```
Peak RetTime Sig Type    Area      Height     Area
  #   [min]             [mAU*s]     [mAU]       %
----|-------|---|----|----------|----------|--------|
   1   3.332  1  MM T   47.41194    2.55462   1.8959
   2   4.158  1  MB R 2453.36328   60.16072  98.1041
```

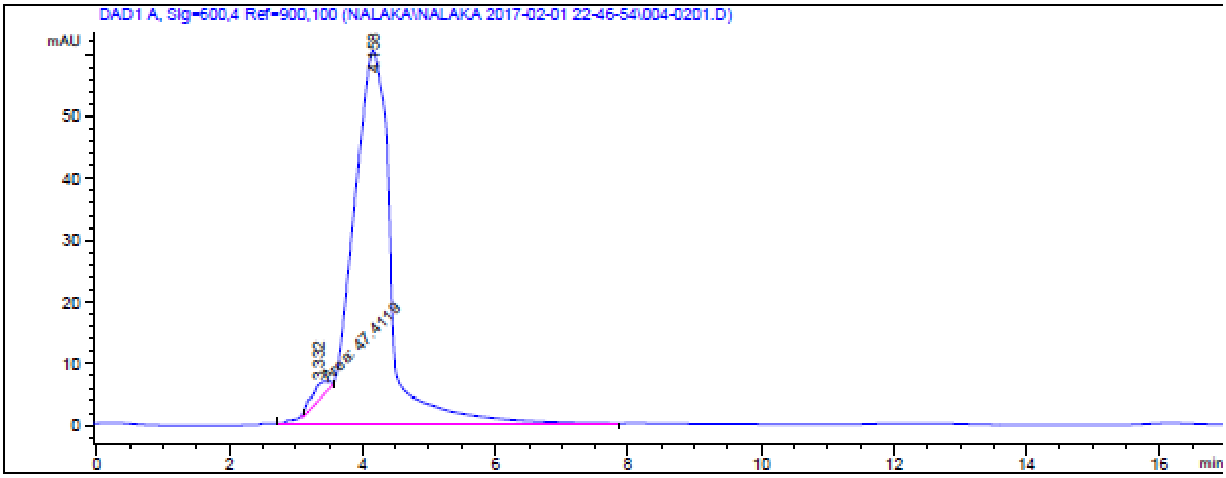

Figure 63. HPLC data for **NL12** (98.1 % purity).

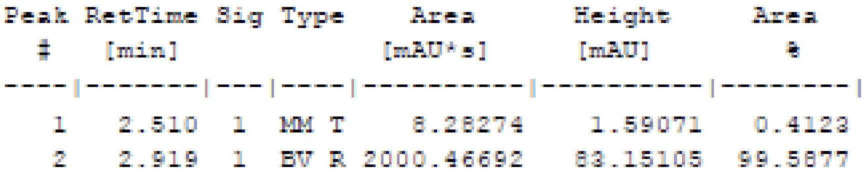

```
Peak RetTime Sig Type    Area      Height     Area
  #   [min]              [mAU*s]   [mAU]        %
----|-------|---|----|----------|----------|--------|
   1   2.510   1  MM T    8.28274   1.59071   0.4123
   2   2.919   1  BV R 2000.46692  83.15105  99.5877
```

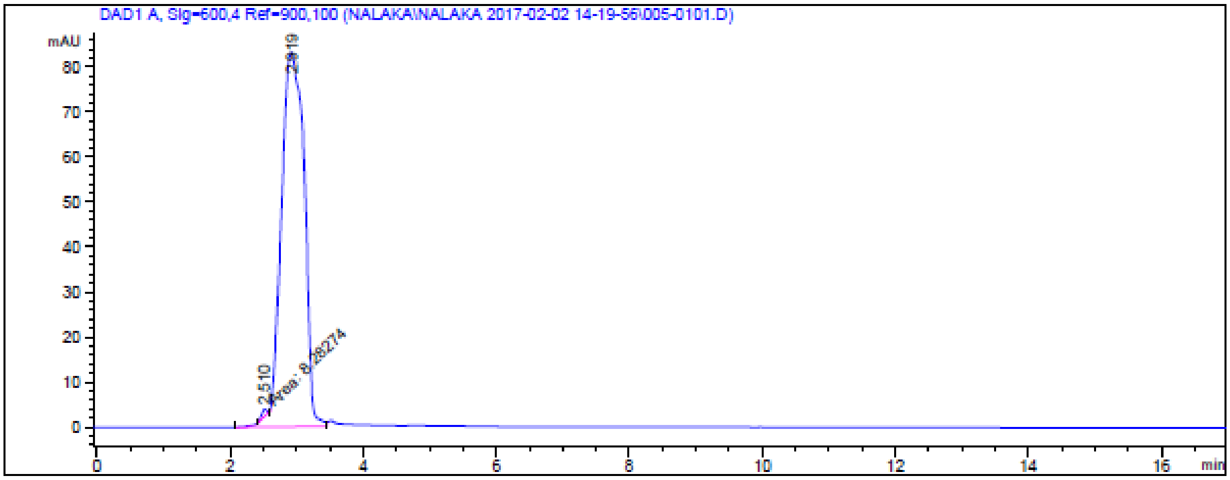

Figure 64. HPLC data for **NL13** (99.6 % purity).

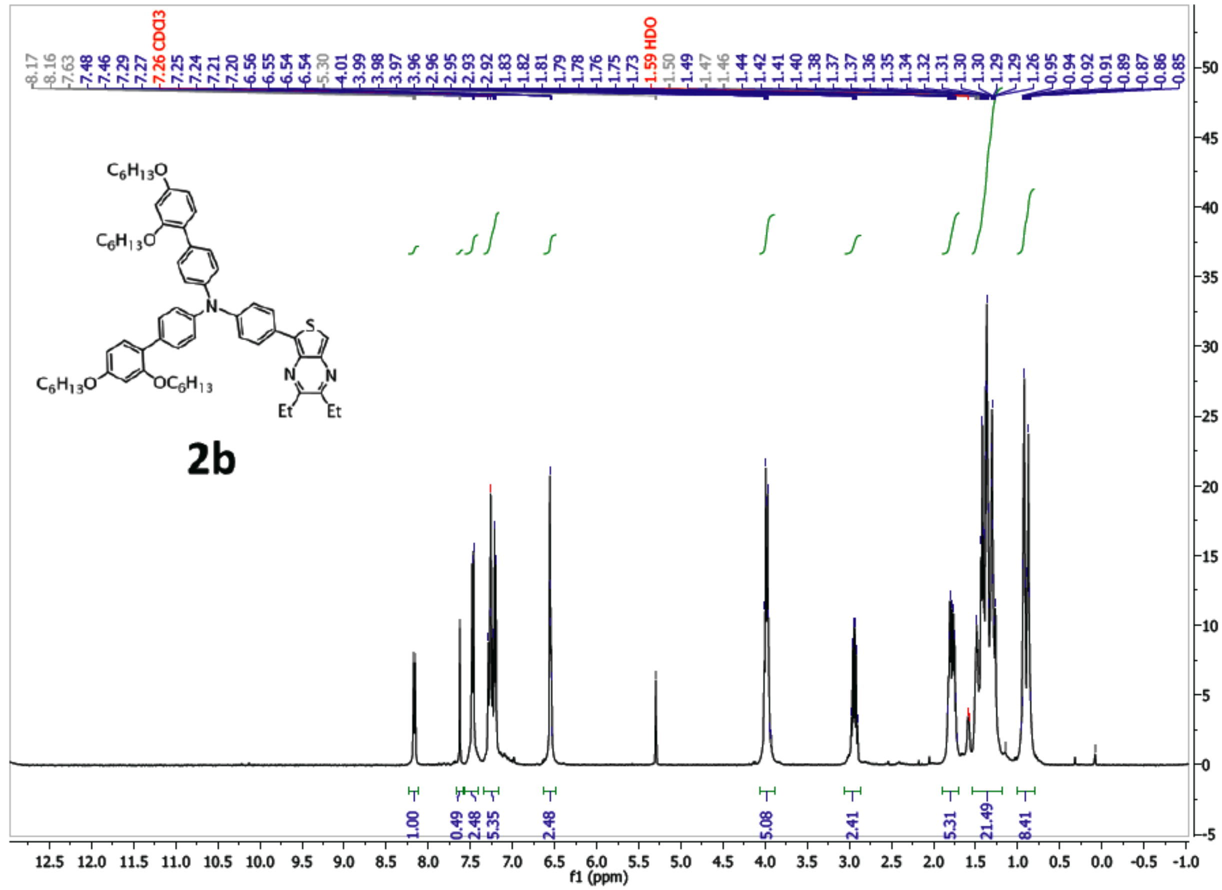

Figure 65. ^{1}H NMR spectrum of thienopyrazine-HF.

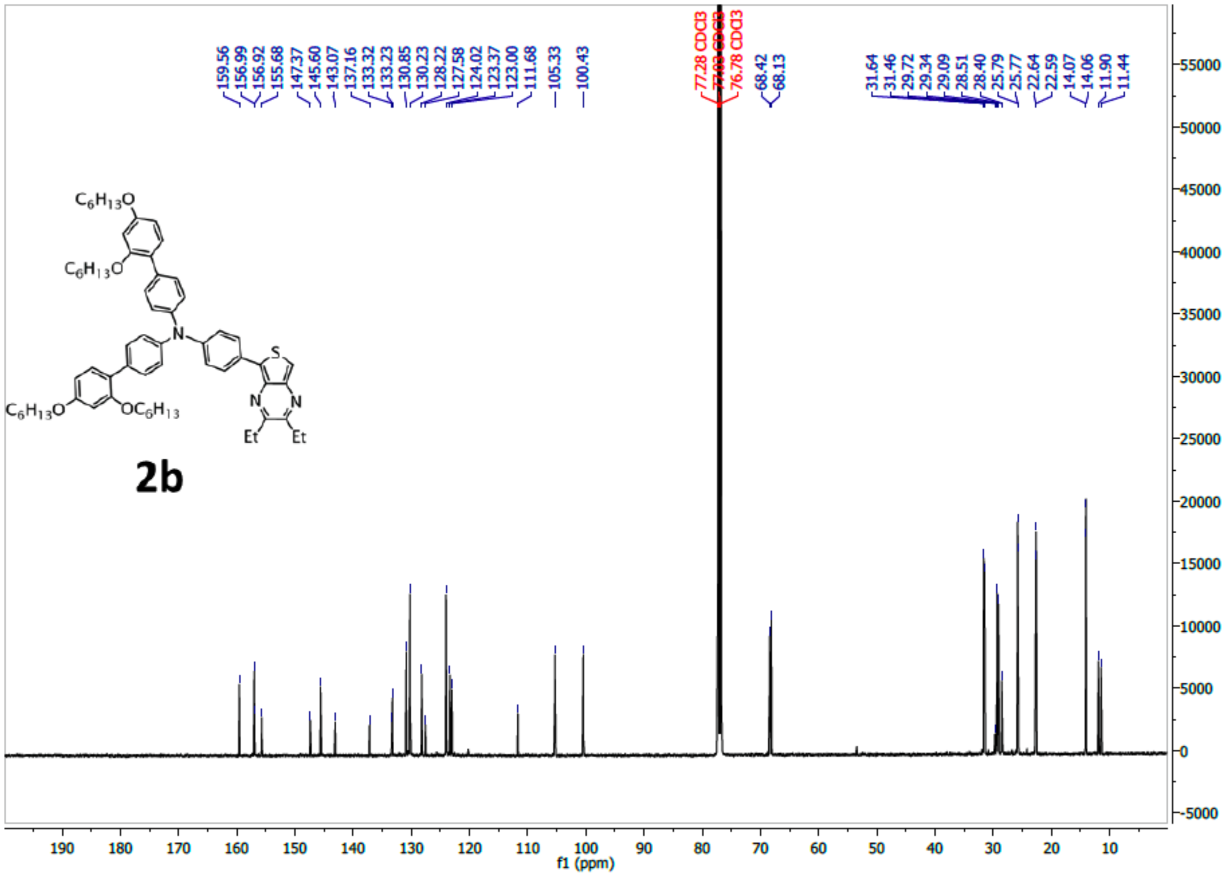

Figure 66. ^{13}C NMR spectrum of thienopyrazine-HF.

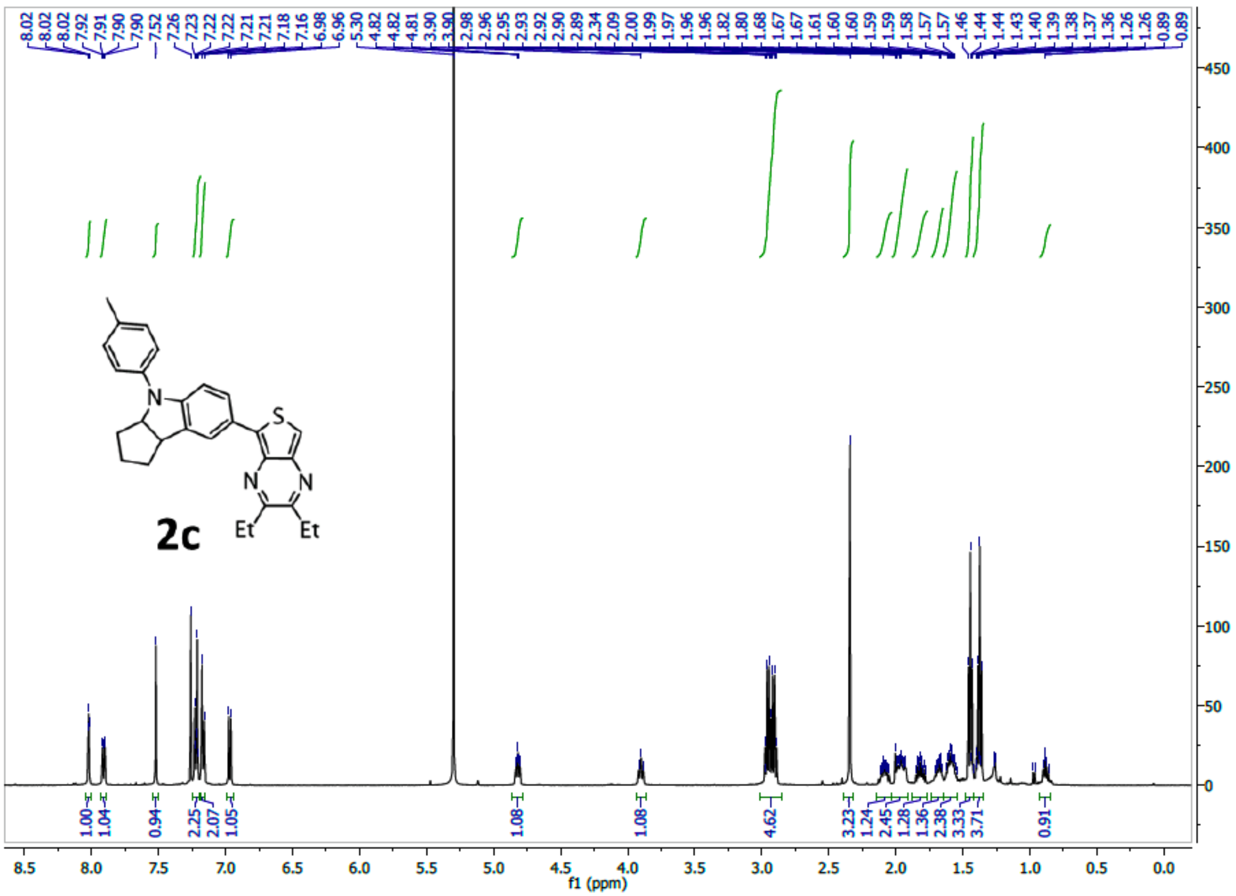

Figure 67. ^{1}H NMR spectrum of thienopyrazine-Ind.

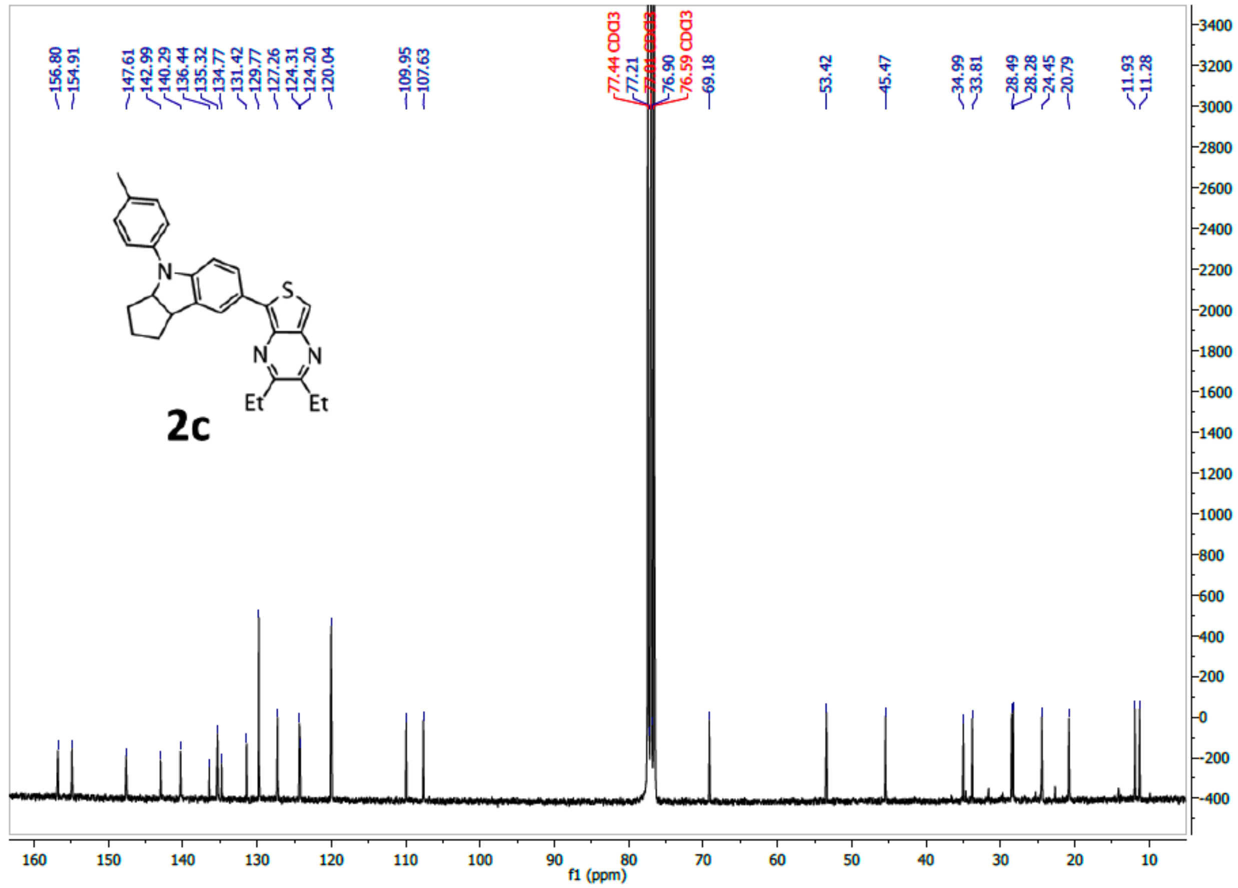

Figure 68. ^{13}C NMR spectrum of thienopyrazine-Ind.

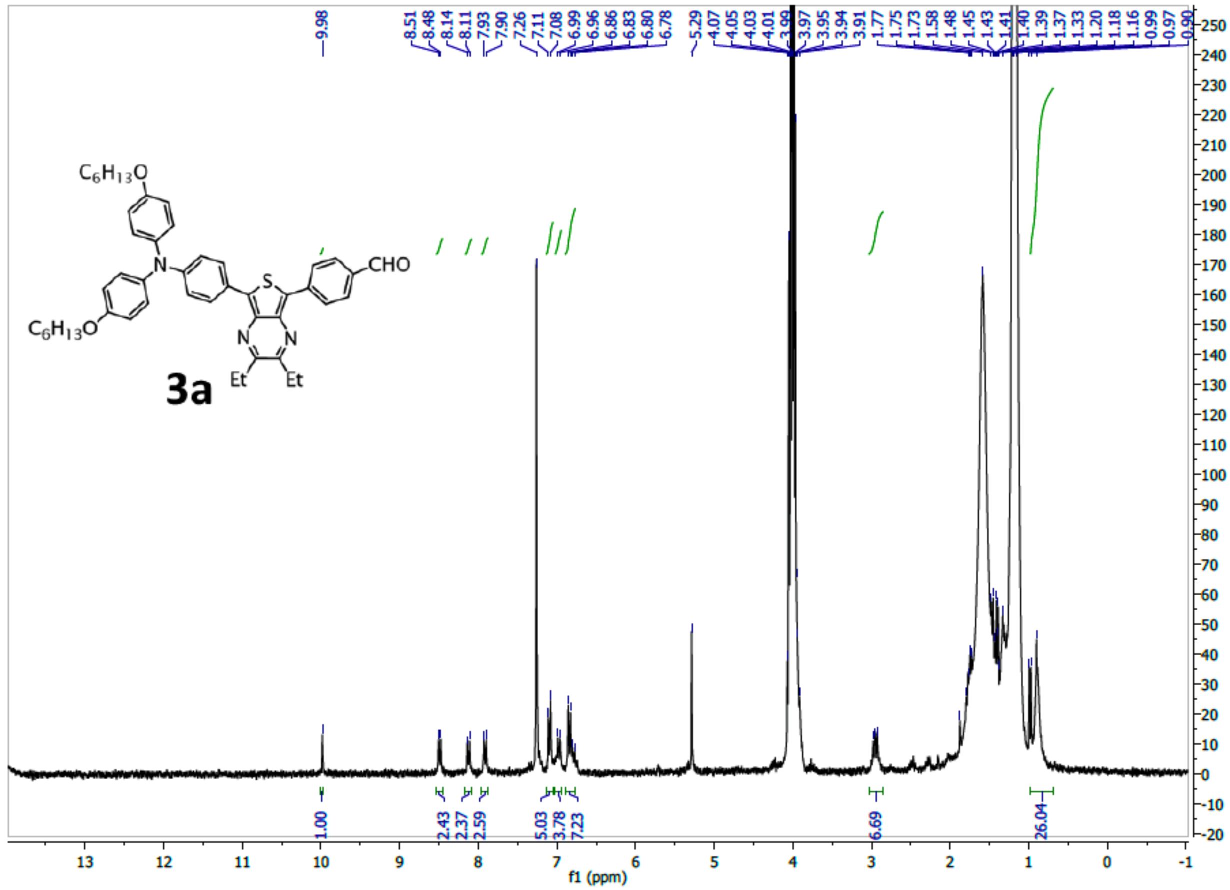

Figure 69. ^{1}H NMR spectrum of thienopyrazine-TPA-aldehyde.

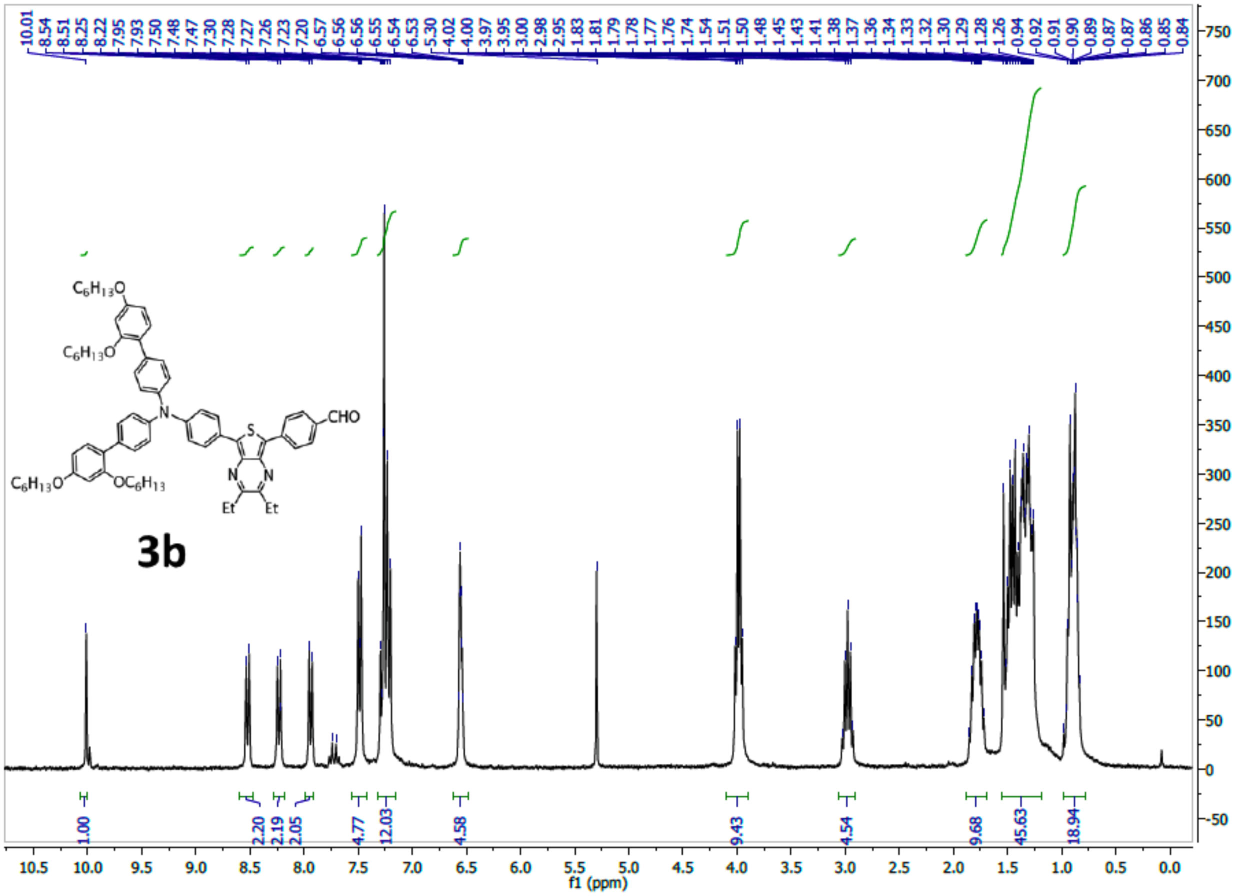

Figure 70. ^{1}H NMR spectrum of thienopyrazine-HF-aldehyde.

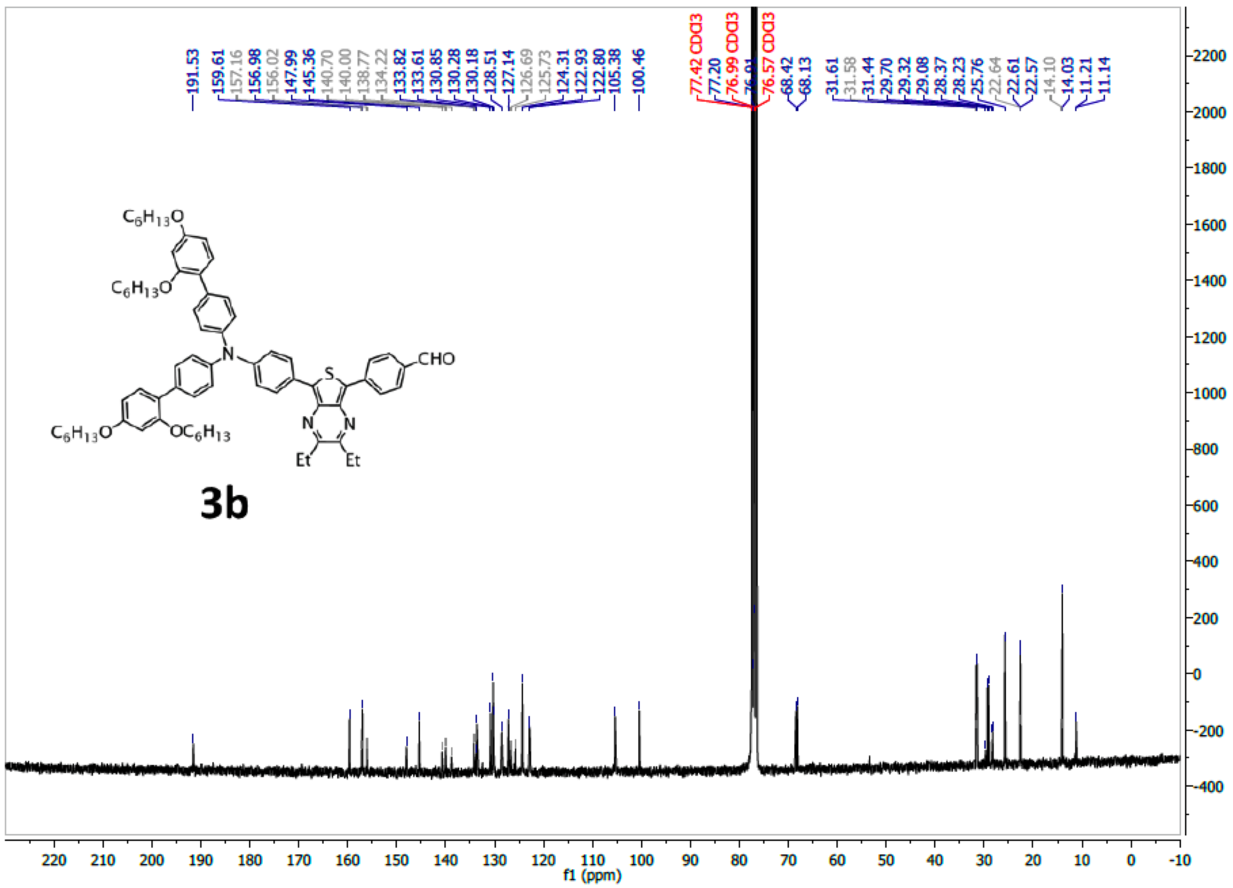

Figure 71. ^{13}C NMR spectrum of thienopyrazine-HF-aldehyde.

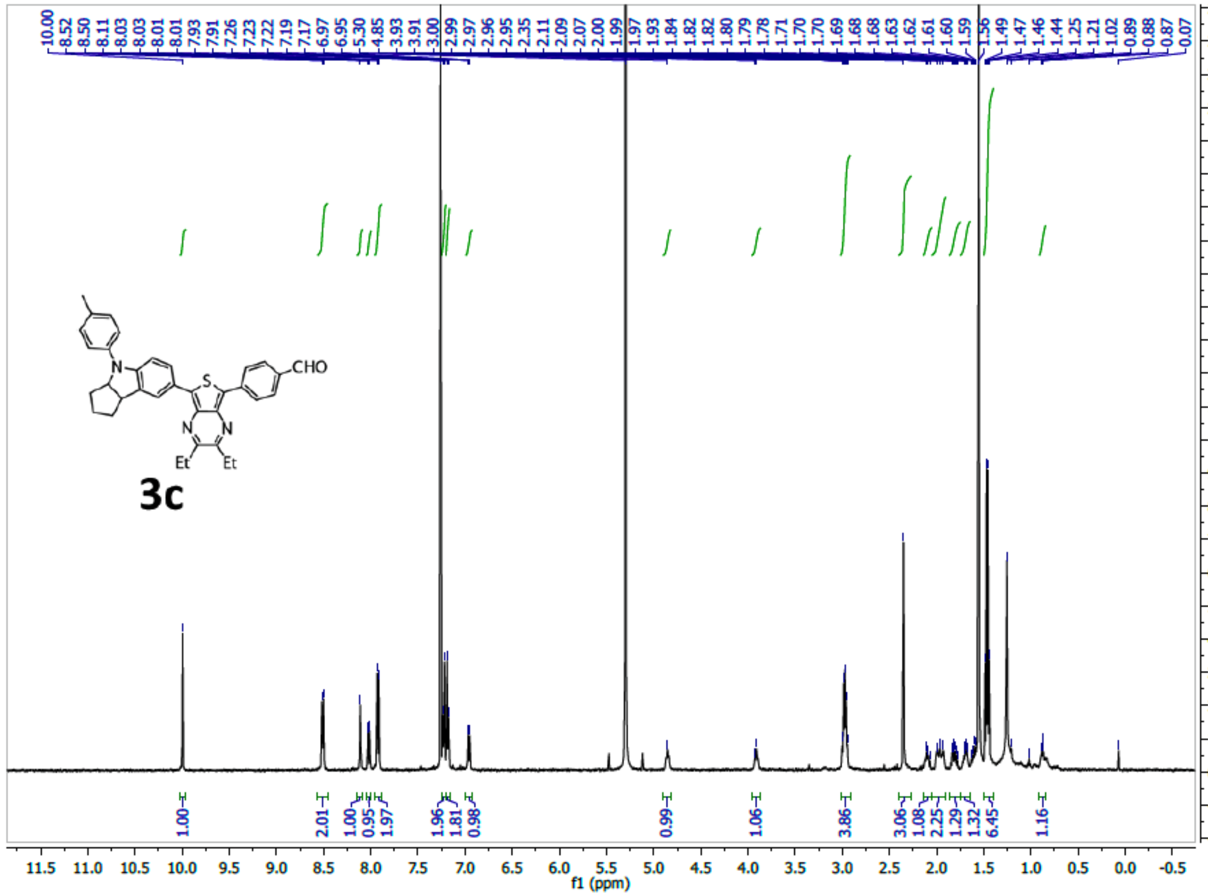

Figure 72. ^{1}H NMR spectrum of thienopyrazine-Ind-aldehyde.

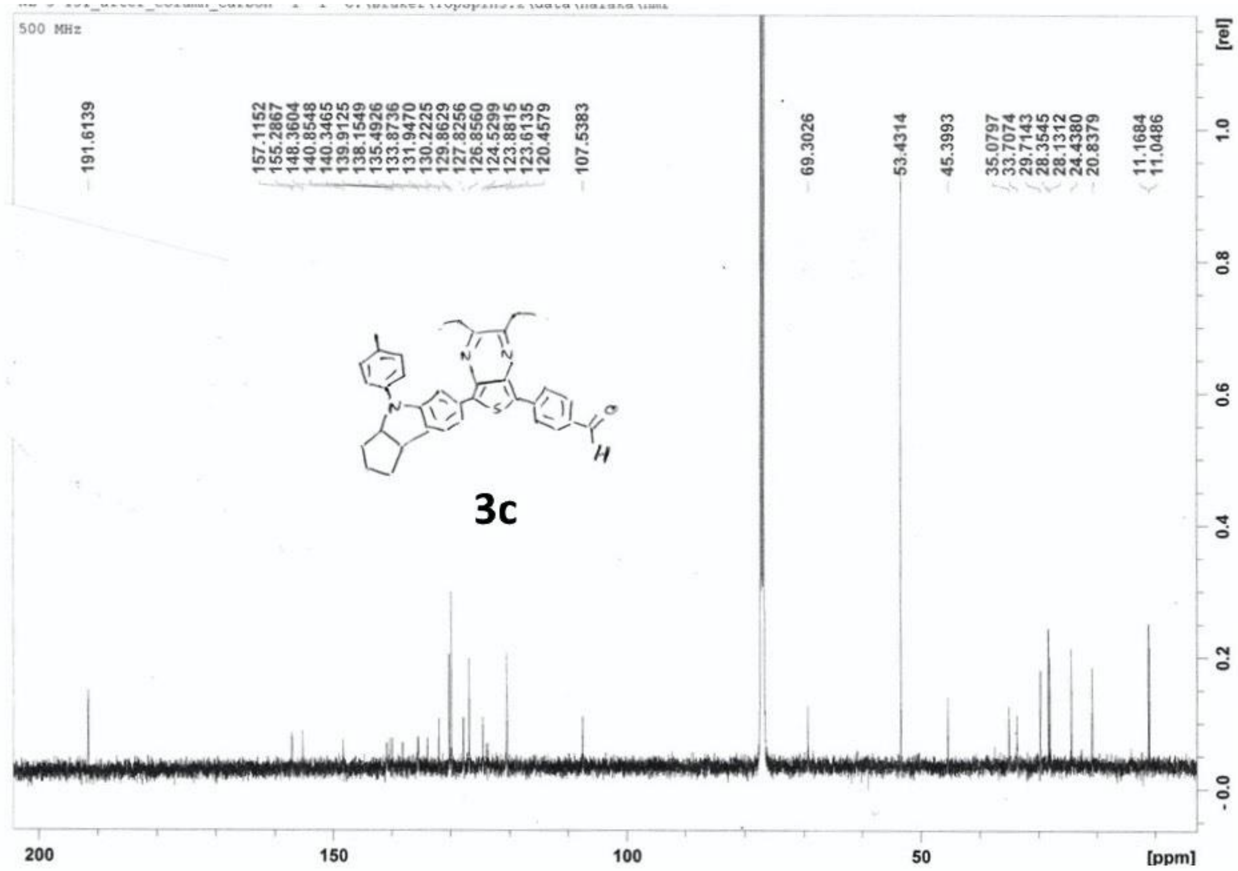

Figure 73. ^{13}C NMR spectrum of thienopyrazine-Ind-aldehyde.

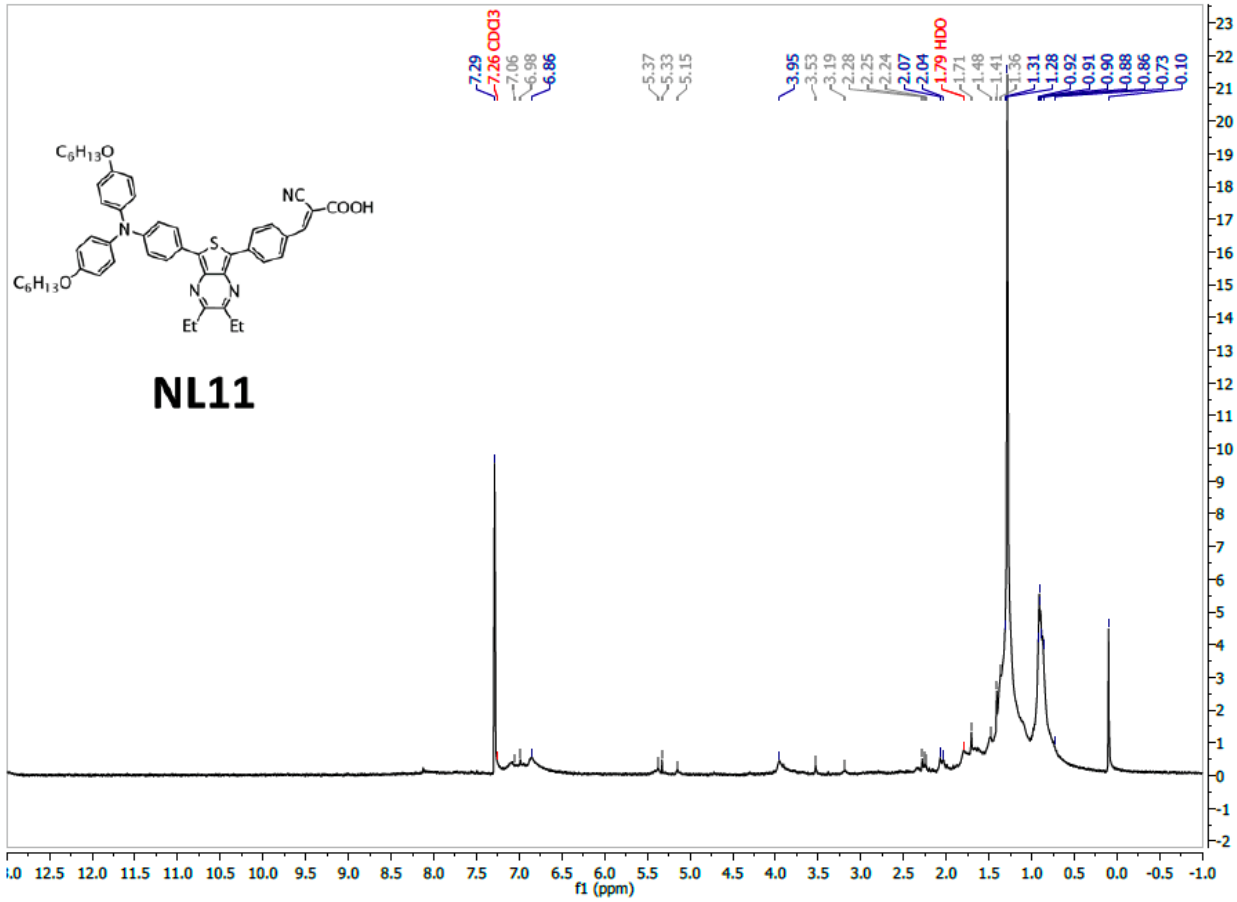

Figure 74. ^{1}H NMR spectrum of **NL11**.

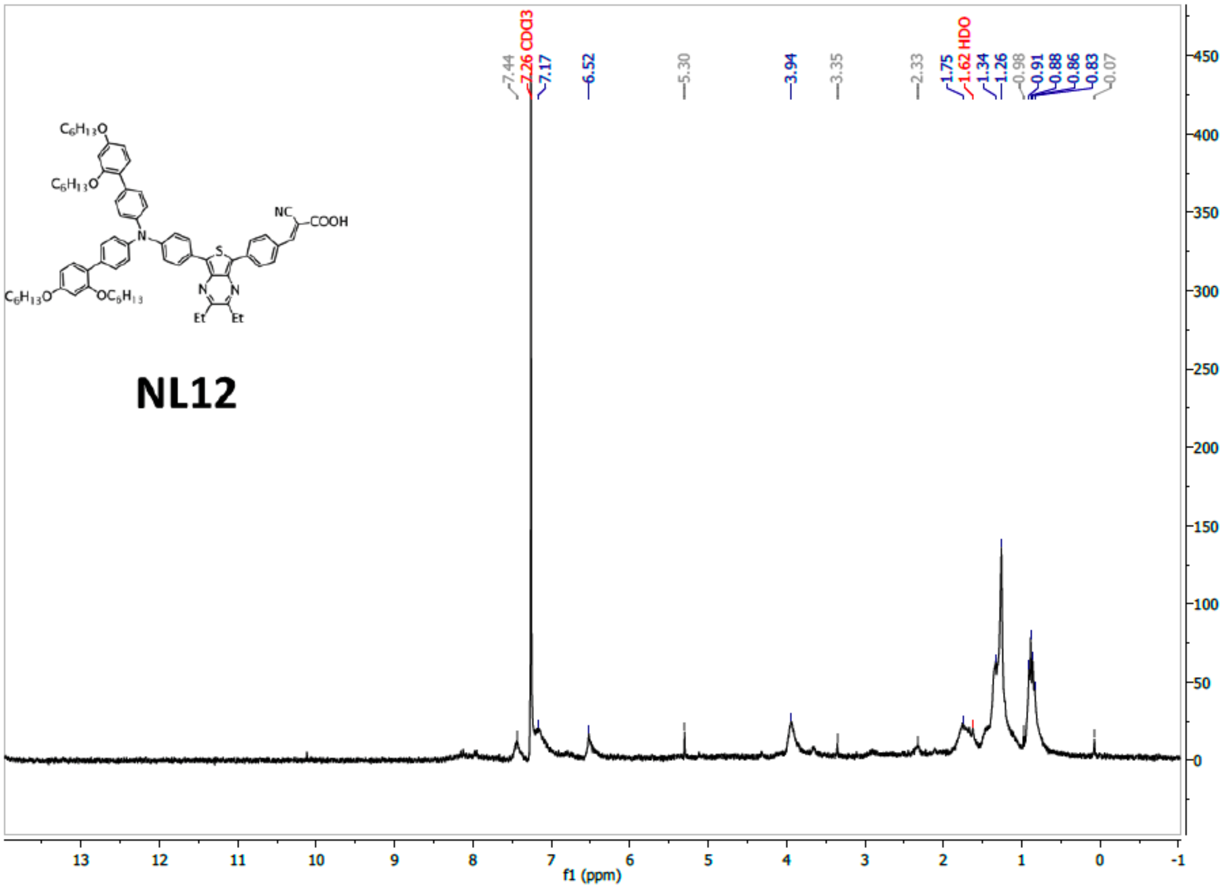

Figure 75. ^{1}H NMR spectrum of **NL12**.

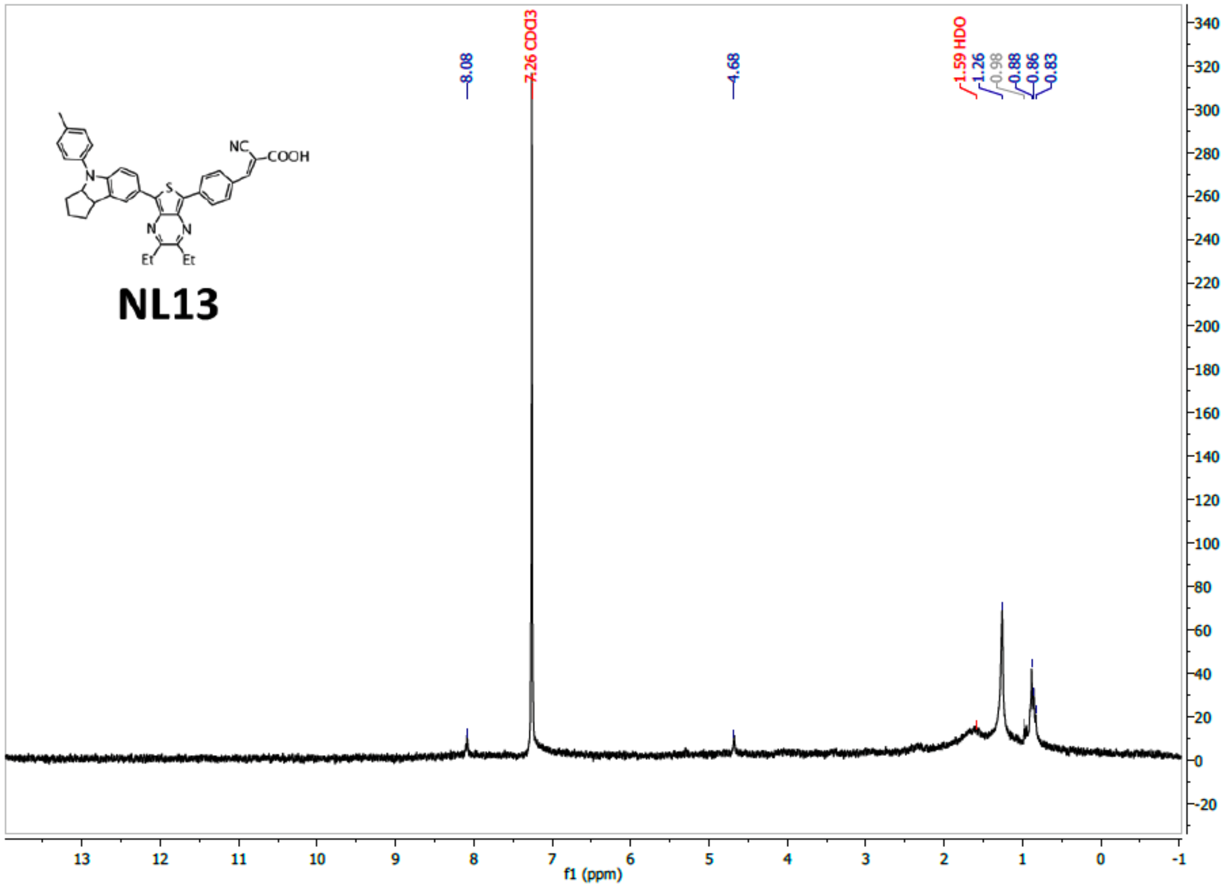

Figure 76. ^{1}H NMR spectrum of **NL13**.

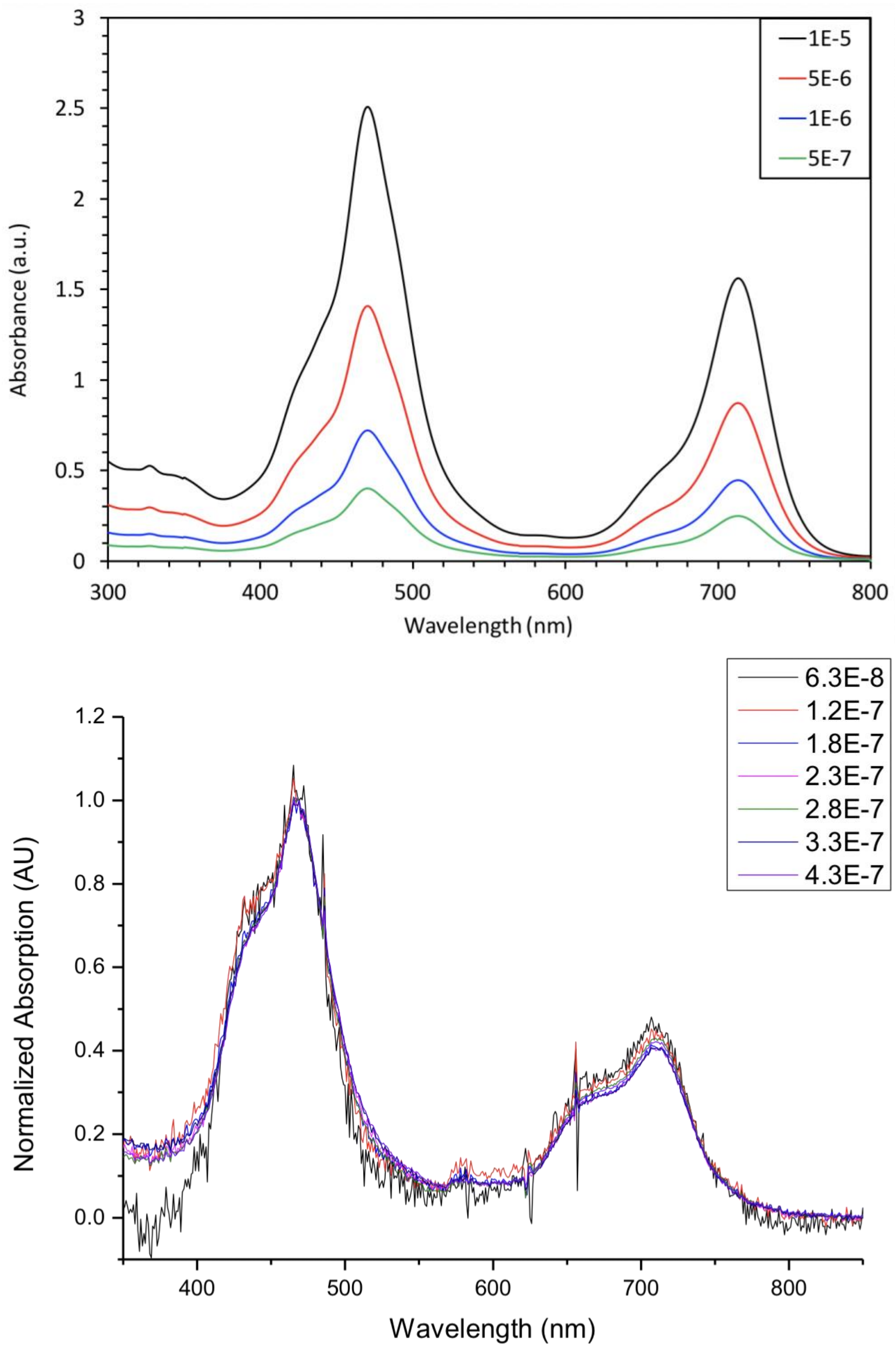

Figure 77. Absorption spectrum of **SM85** in THF at varying concentration ranging from approximately 1 × 10^{-5} M to 5 × 10^{-7} M (left) and 4.3 × 10^{-7} M to near the spectrometer detection limit at 6.3 × 10^{-8} M (right), demonstrating the persistence of J-aggregation (l_{max} = 710 nm), even at the spectrometer detection limit.

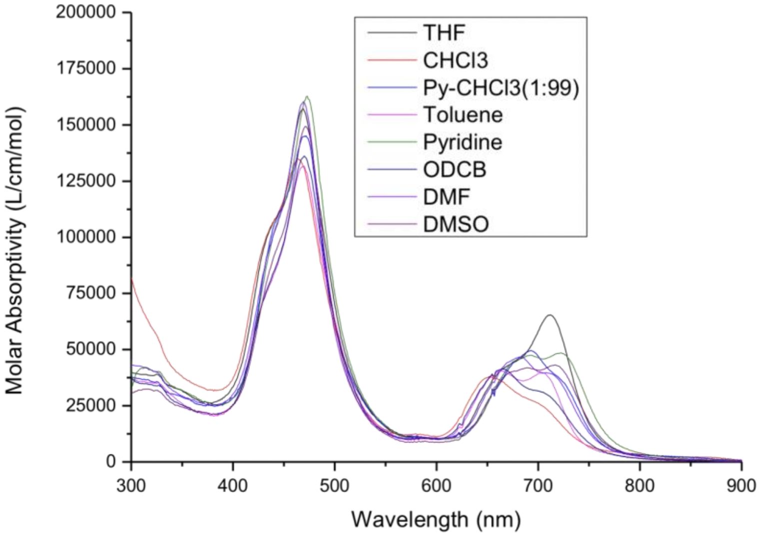

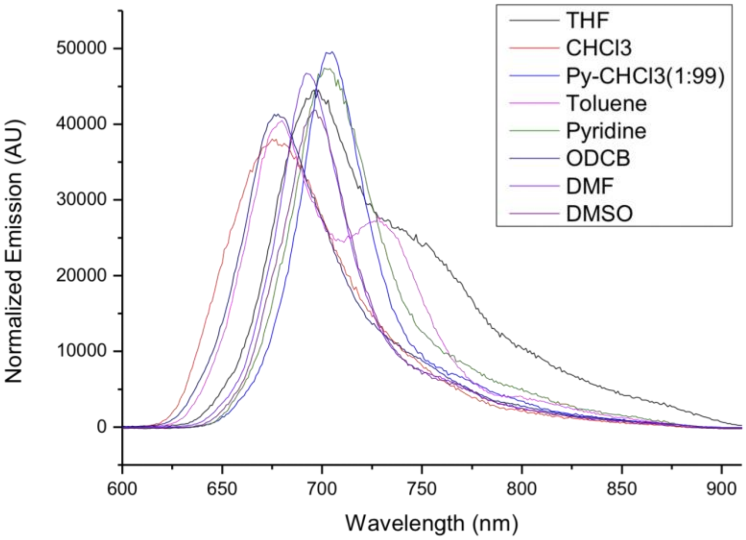

Figure 78. Absorption (left) and emission (right) spectra of **SM85** in various solvents with a full scan window for the absorption curves.

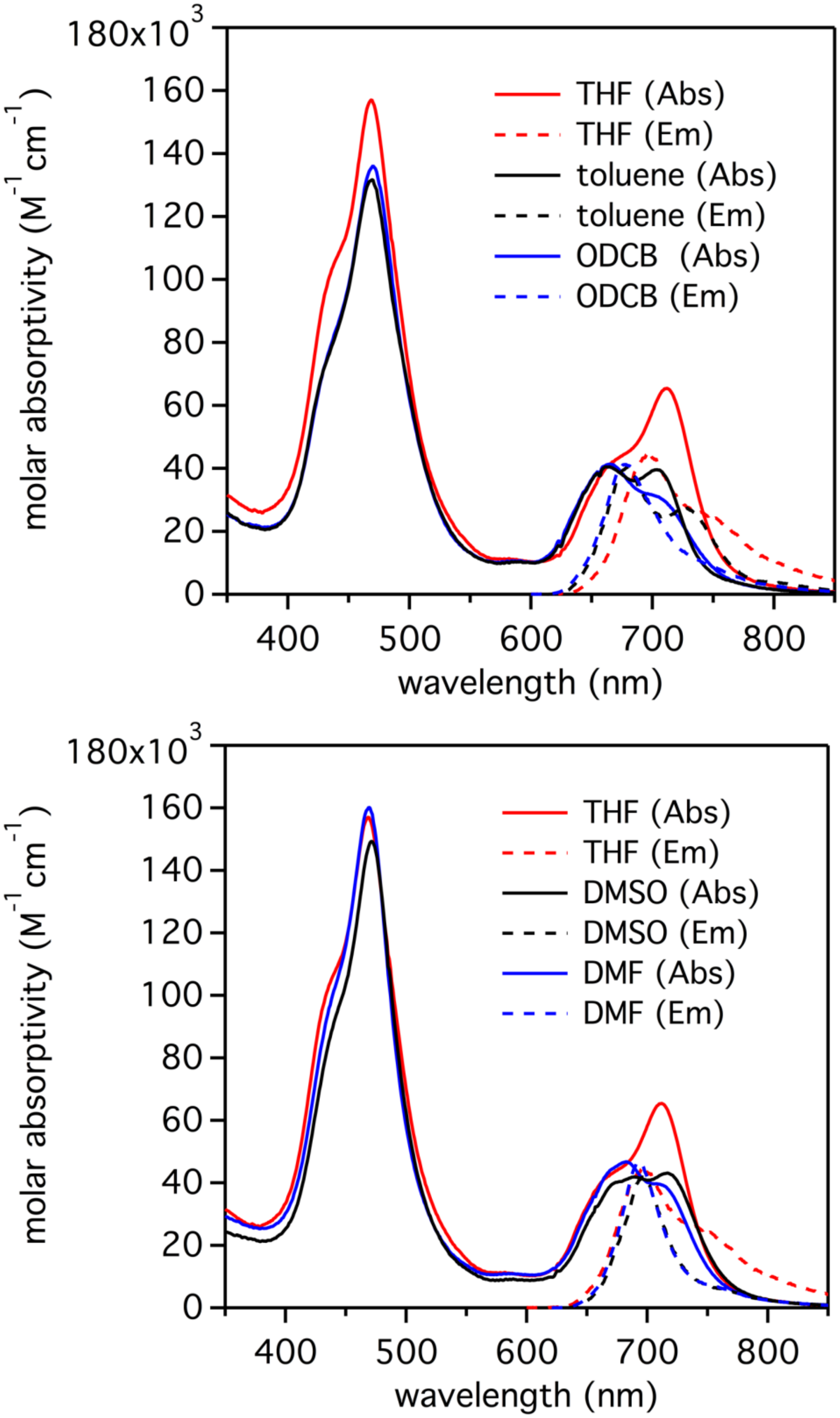

Figure 79. Comparison of absorption and emission curves of **SM85** in THF, toluene, and *ortho*-dichlorobenzene (left) and in THF, DMF and DMSO (right).

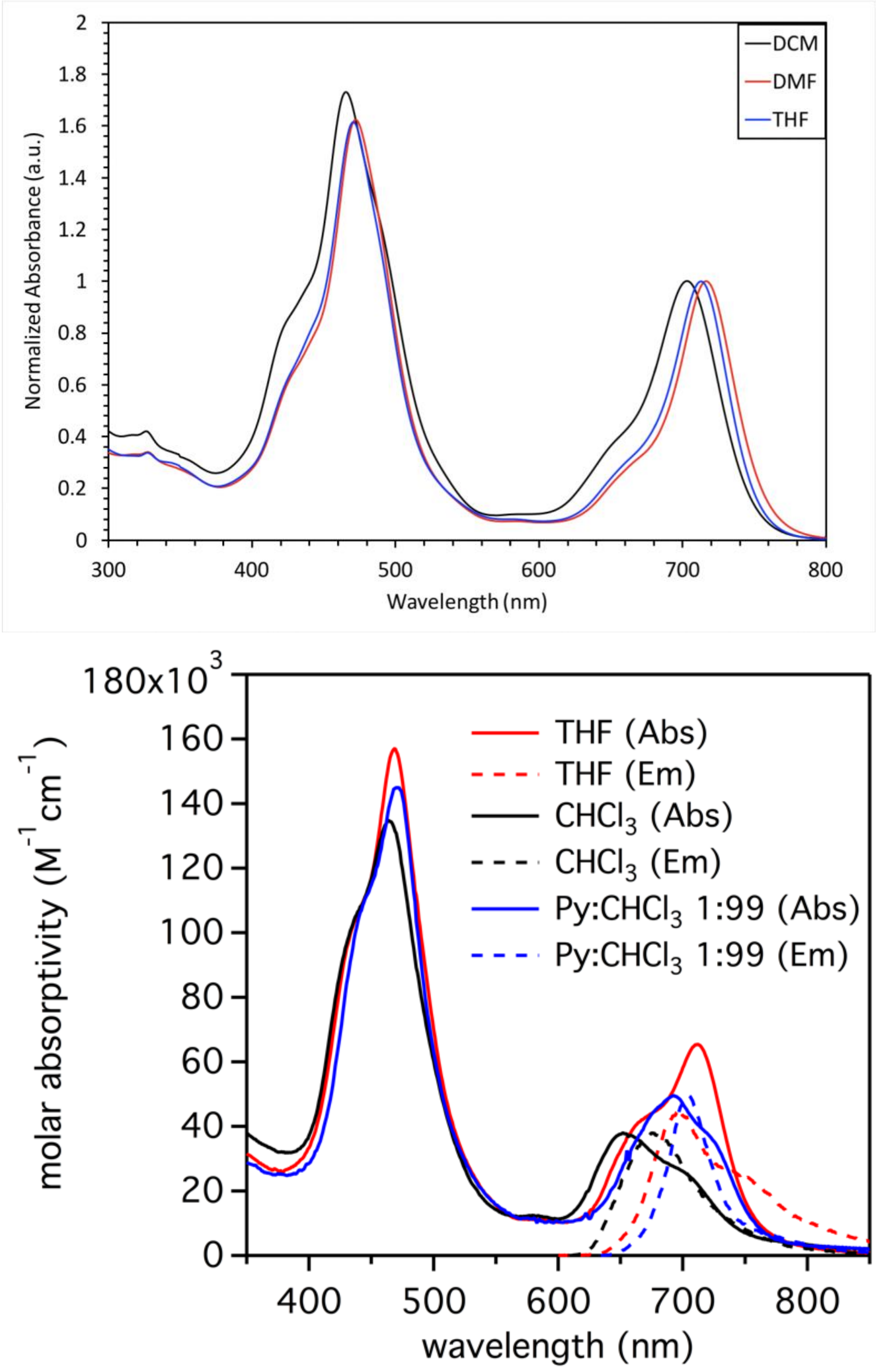

Figure 80. Comparison of dramatically different polarity solvents to evaluate solvatochromic effects on the absorption spectrum of **SM85** (left) and a comparison of absorption and emission of **SM85** in THF, $CHCl_3$ and pyridine:$CHCl_3$ (1:99) (right).

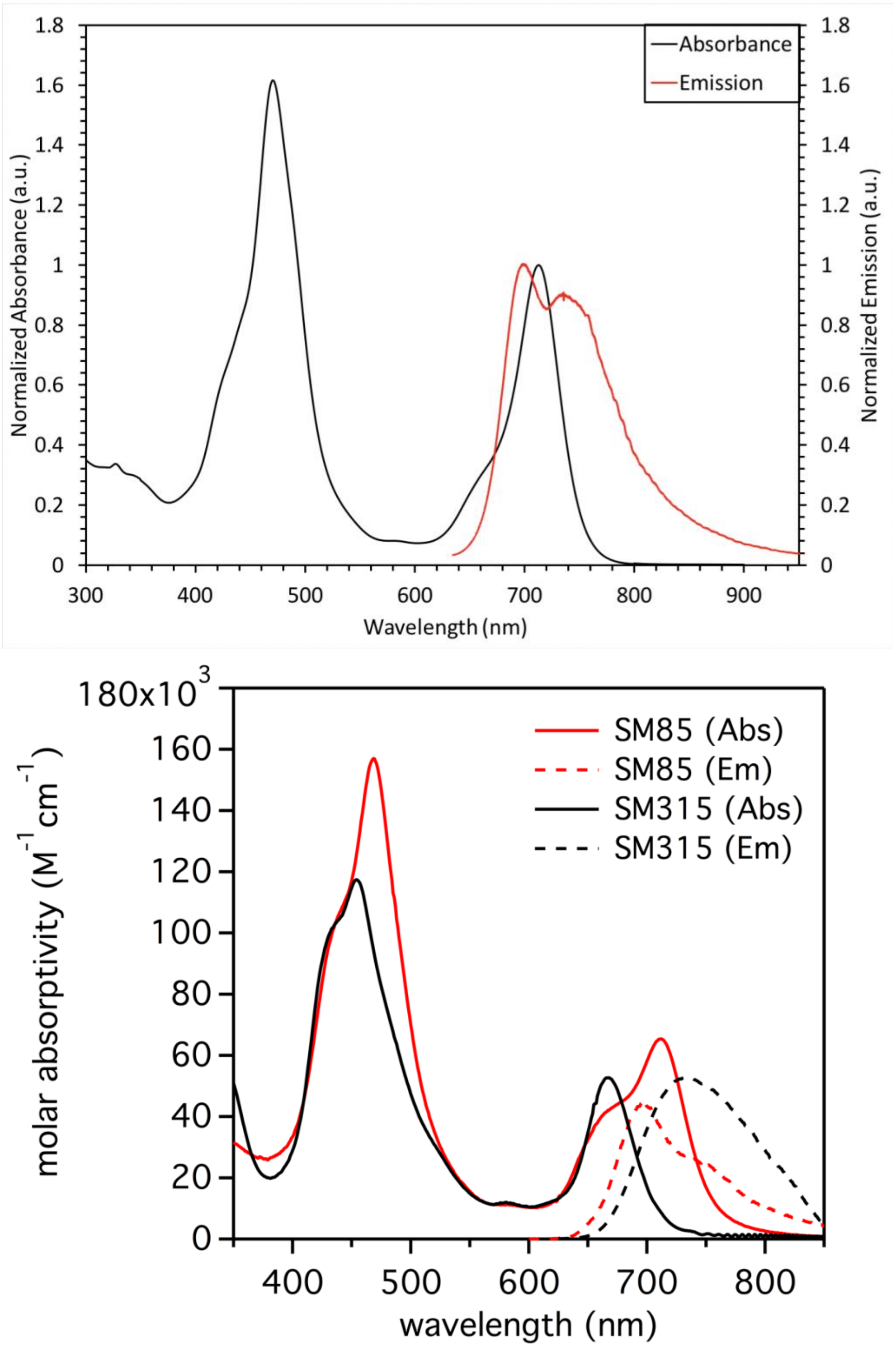

Figure 81. Absorption and emission of **SM85** in THF (left) and data compared to **SM315** (right).

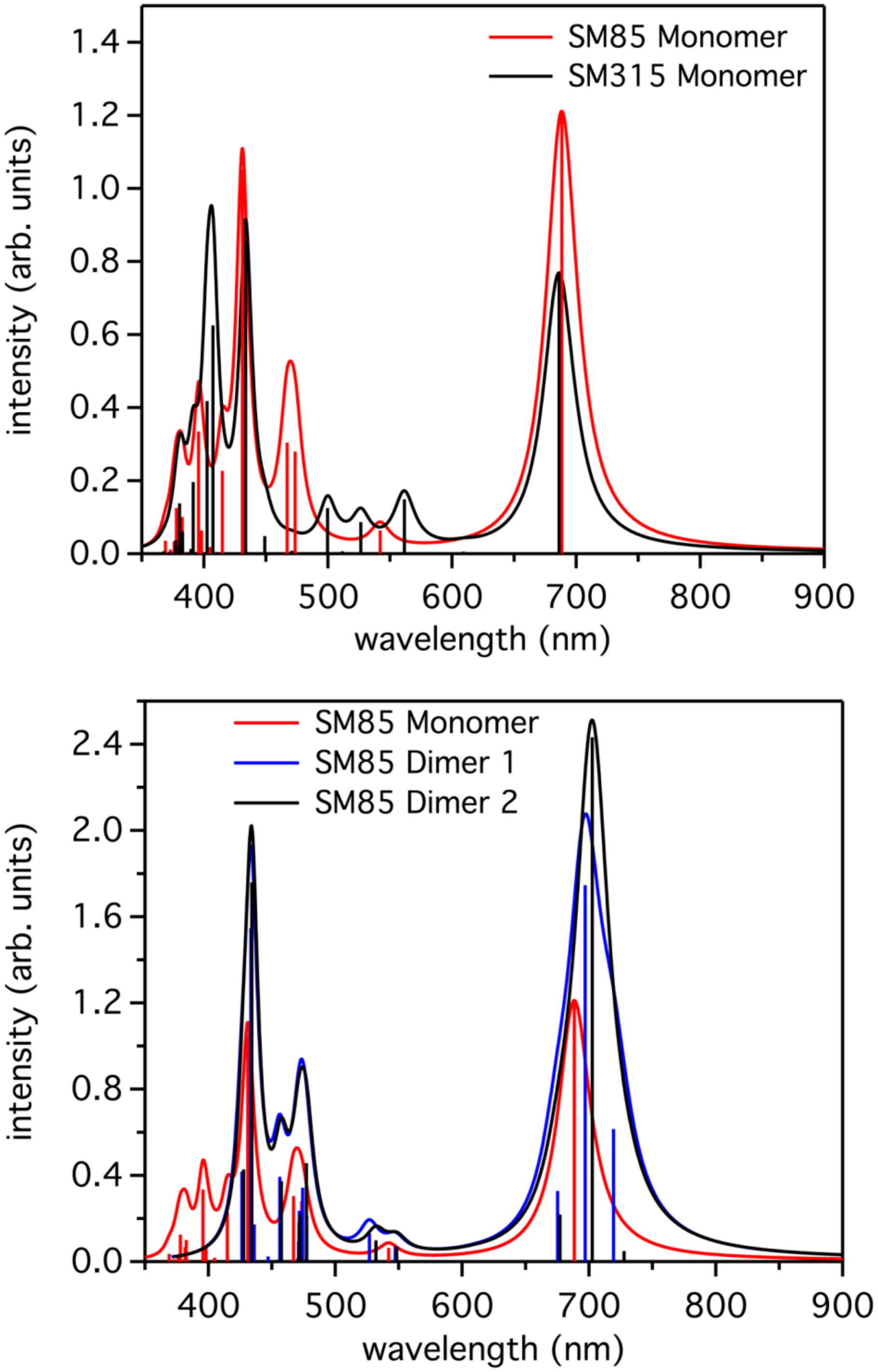

Figure 82. Simulated absorption spectra as determined via TD-DFT calculations at the OT-LC-ωPBE/6-31G(d,p) level of theory.

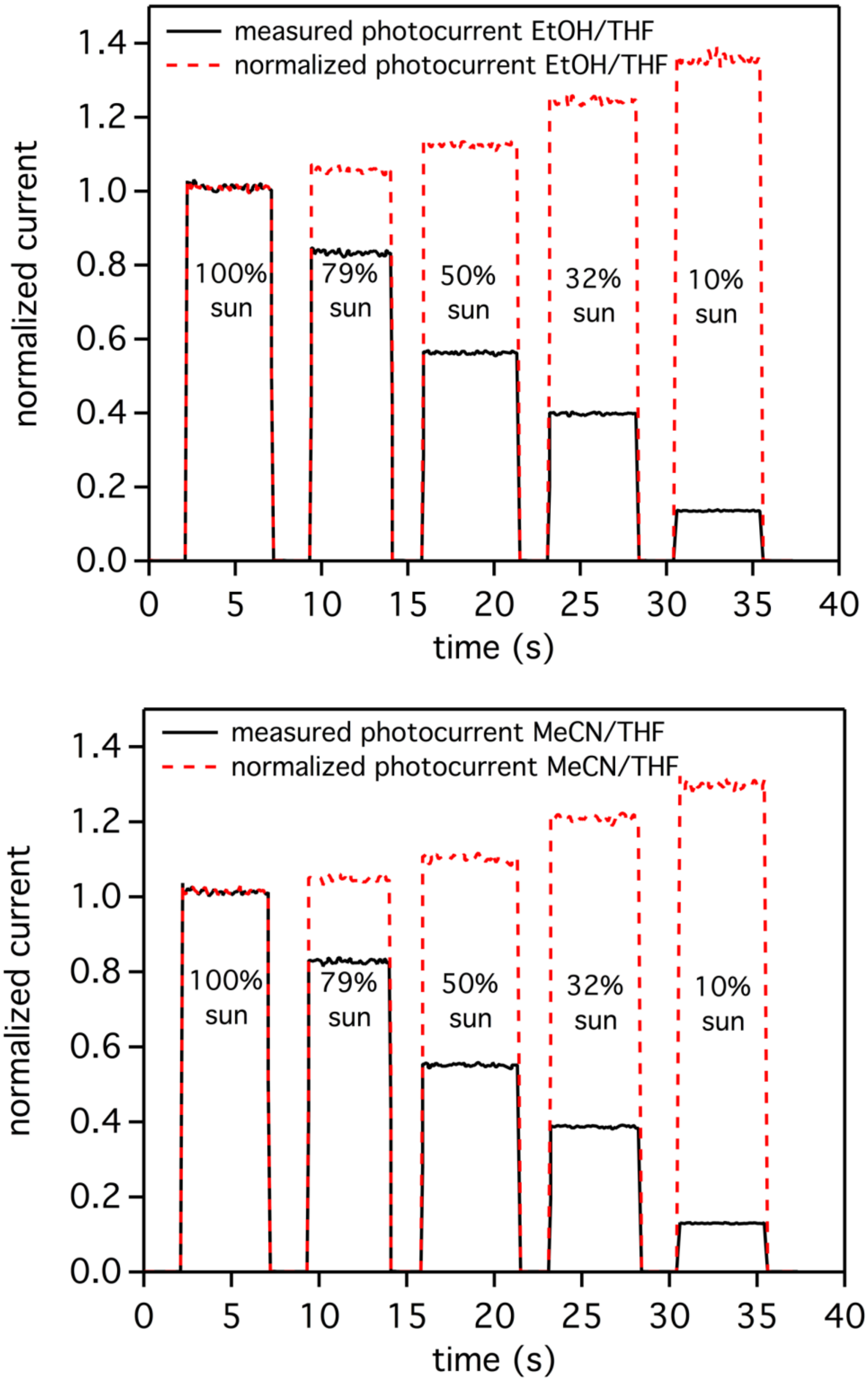

Figure 83. Current dynamics comparing effect of loading solvent on device performance for EtOH:THF (4:1, left) and MeCN:THF (1:1, right).

Table 22. Dye loadings measured by dye desorption.

Entry	Electrode	Moles cm^{-2}	dielectric constant
1	EtOH:THF (4:1)	7.1×10^{-6}	20
2	MeCN:*t*BuOH (1:1)	1.2×10^{-5}	26
3	MeCN:THF (1:1)	7.1×10^{-6}	23
4	toluene:MeCN (9:1)	2.0×10^{-6}	6
5	toluene:EtOH (1:1)	3.3×10^{-6}	14

For dye loading, dye sensitized 3 μm TiO_2 films were dipped in the dye solution for 3 hours until electrodes were completely white. Dye desorption studies were performed in 0.1 M TBAOH in DMF. A molar absorptivity of 14,000 $M^{-1}cm^{-1}$ at 662 nm was measured in 0.1 M TBAOH in DMF. Dielectric constants were approximated from the equation: $e_{mix} = X(e_{sol1}) + Y(e_{sol2})$, where e_{mix} is the approximated dielectric constant, e_{sol1} is the dielectric constant of pure solvent 1, e_{sol2} is the dielectric constant of pure solvent 2, X is the volume fraction for solvent 1, and Y is the volume fraction for solvent 2.[200] Dielectrics of the pure solvents were taken as follows: EtOH (25), THF (8), MeCN (38), *t*BuOH (13), toluene (2).

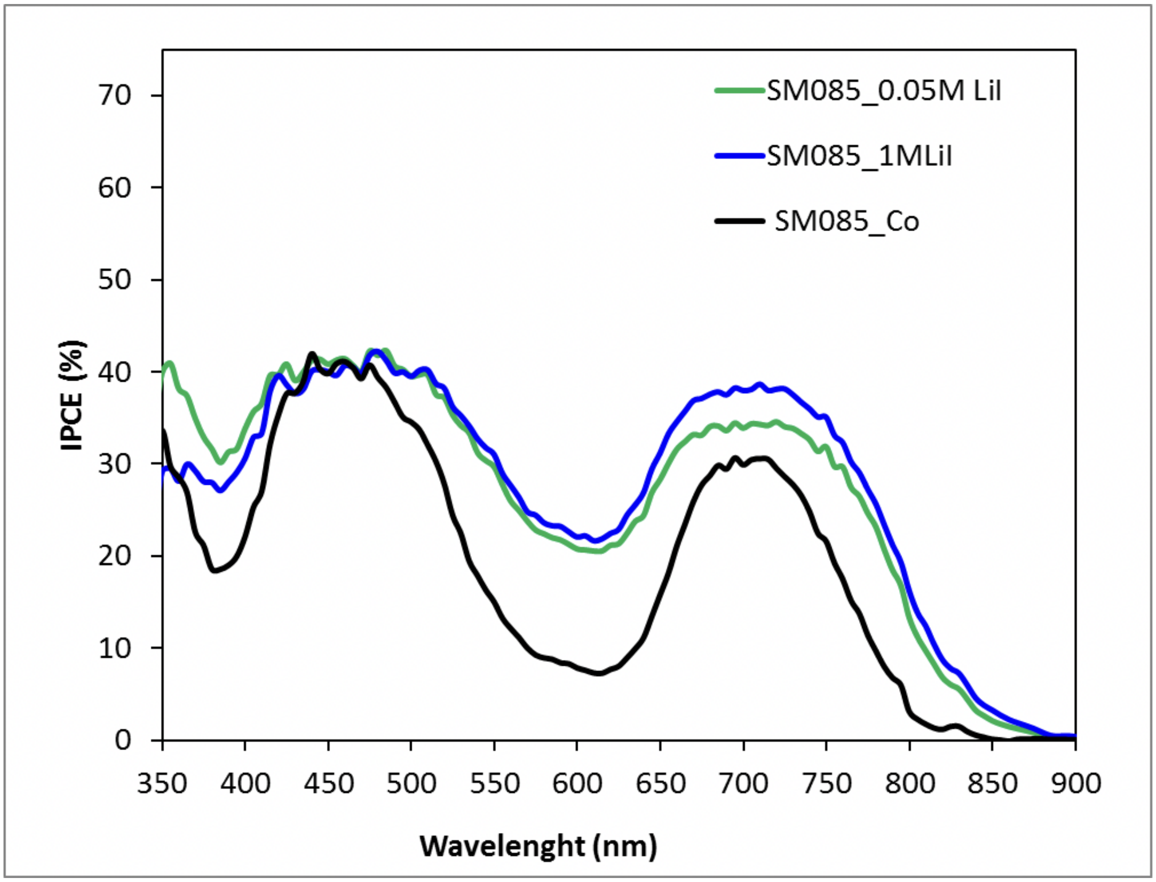

Figure 84. Comparison of **SM85** device IPCEs with Co(bpy)3$^{3+/2+}$ based electrolyte and with two concentration of LiI (see Table 19 for conditions).

Table 23. Summary of photovoltaic parameters for DSC devices prepared with **SM85**.

entry	electrolyte	V_{oc} (mV)	J_{sc} (mA cm^{-2})	FF (%)	PCE (%)
1	0.05 M LiI	582	9.1	70	3.8
2	1.0 M LiI	537	9.2	63	3.1
3	$Co(bpy)_3^{3+/2+}$	636	6.5	56	2.4

Device performances under AM 1.5G irradiation. TiO_2 electrodes are comprised of a 10 μm film active layer of 20 nm TiO_2 nanoparticles with a 5 μm film scattering layer of >100 nm TiO_2 nanoparticles on top for LiI based devices. TiO_2 electrodes are comprised of a 5 μm film active layer of 30 nm TiO_2 nanoparticles with a 5 μm film scattering layer of >100 nm TiO_2 nanoparticles on top for Co based devices. Films were sensitized with EtOH:THF mixtures at 0.3 mM dye concentration and 2x CDCA. For the LiI based electrolytes the concentration of LiI listed was used along with: 1.0 M DMII (1,3-dimethylimidazolium iodide), 0.03 M I_2, 0.5 M TBP (4-*tert*-butylpyridine), 0.1 M GuNCS (guanidinium thiocyanide) in acetonitrile (MeCN):valeronitrile (85:15,v/v) solvent. For the $Co(bpy)_3^{3+/2+}$ electrolyte the following was used: 0.25 M $Co(bpy)_3[PF_6]_2$, 0.05 M $Co(bpy)_3[PF_6]_3$, 0.25 M TBP, and 0.1 MLiTFSI. Active area was masked at 0.15 cm^2 with black tape.

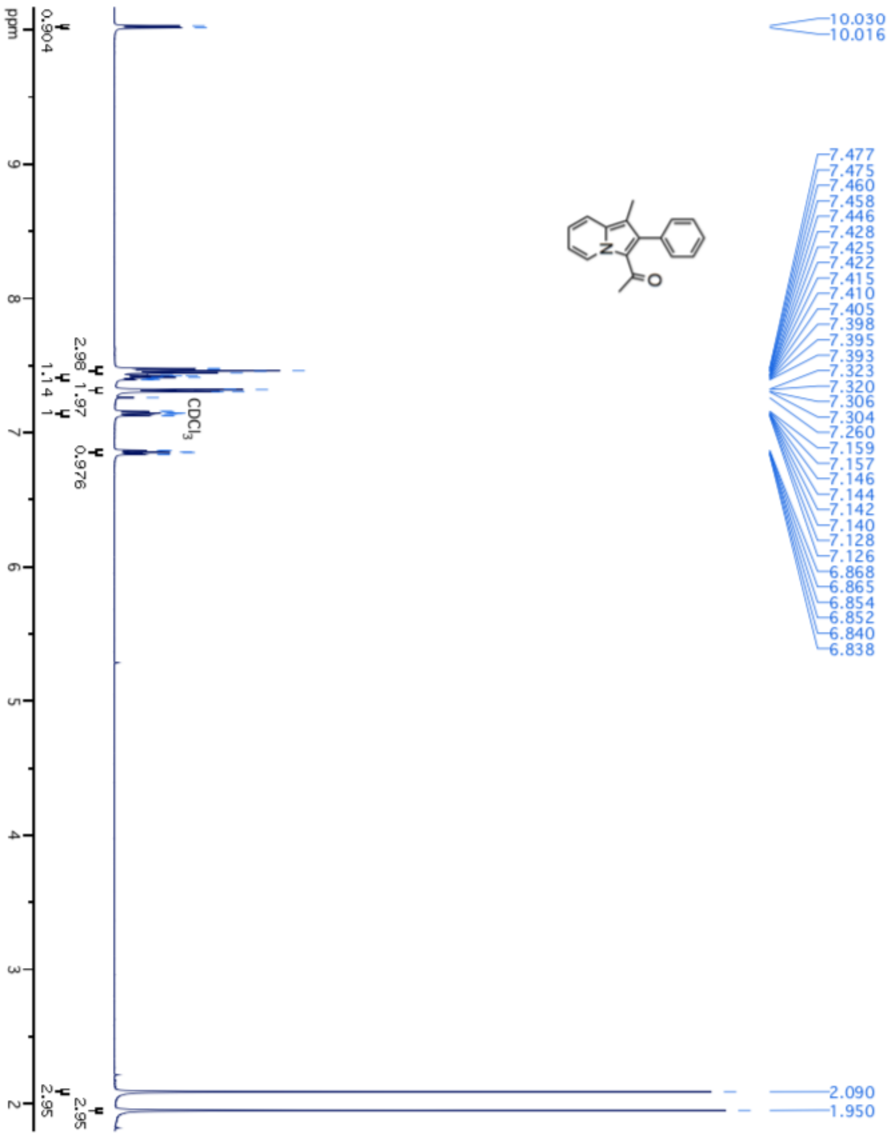

Figure 85. ^{1}H NMR of **2**, 500 MHz, CDCl$_3$, room temperature

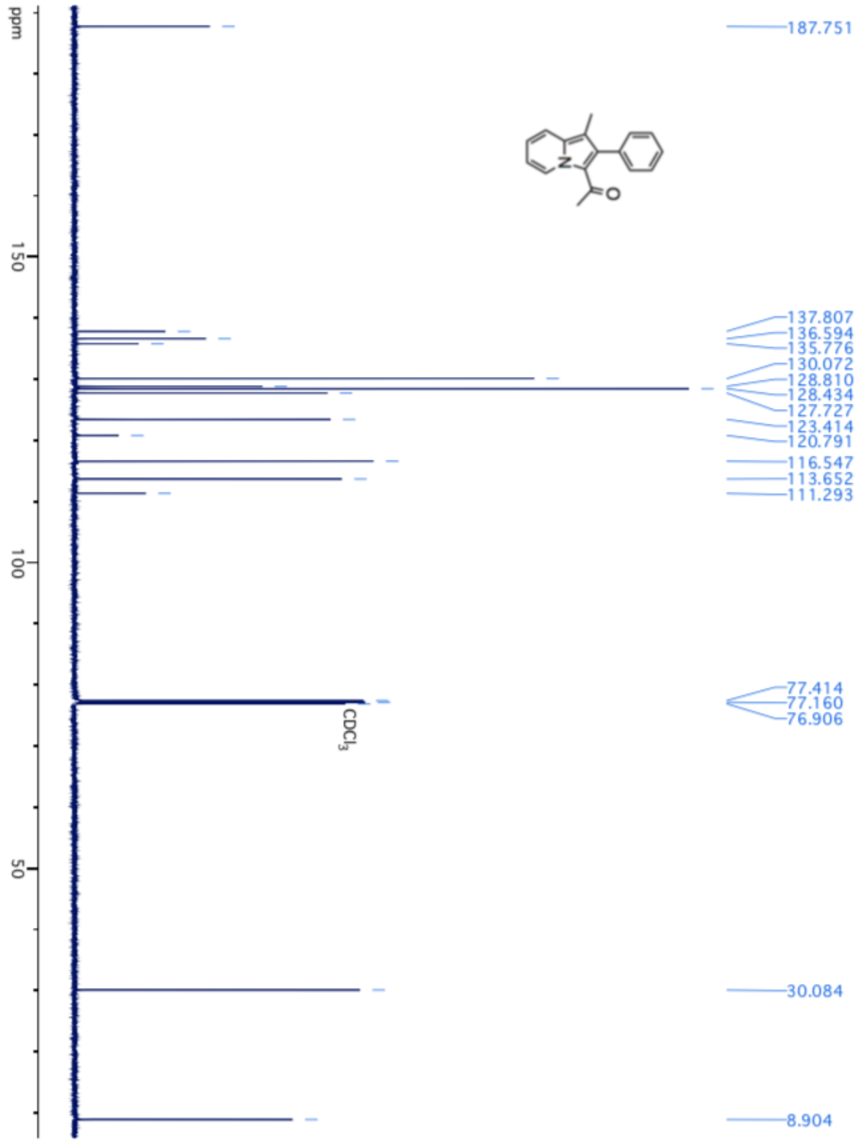

Figure 86. ^{13}C NMR of **2**, 125 MHz, CDCl$_3$, room temperature

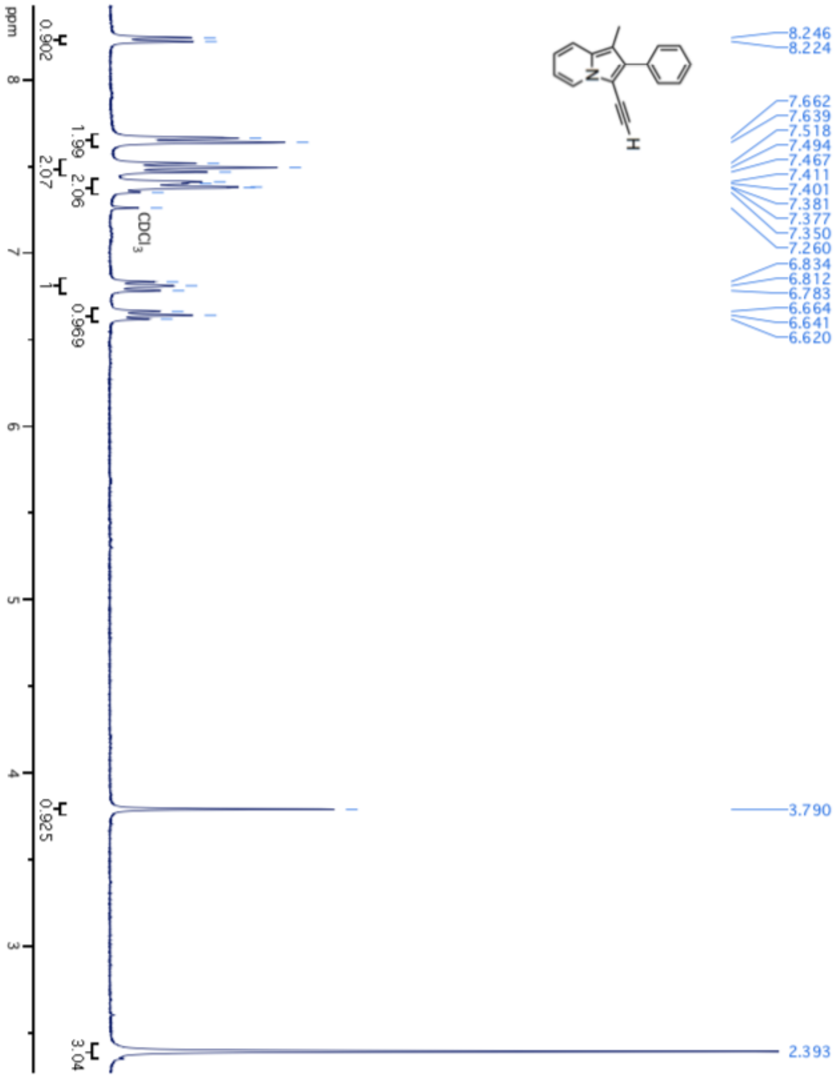

Figure87. ^{1}H NMR of **3**, 300 MHz, $CDCl_3$, room temperature

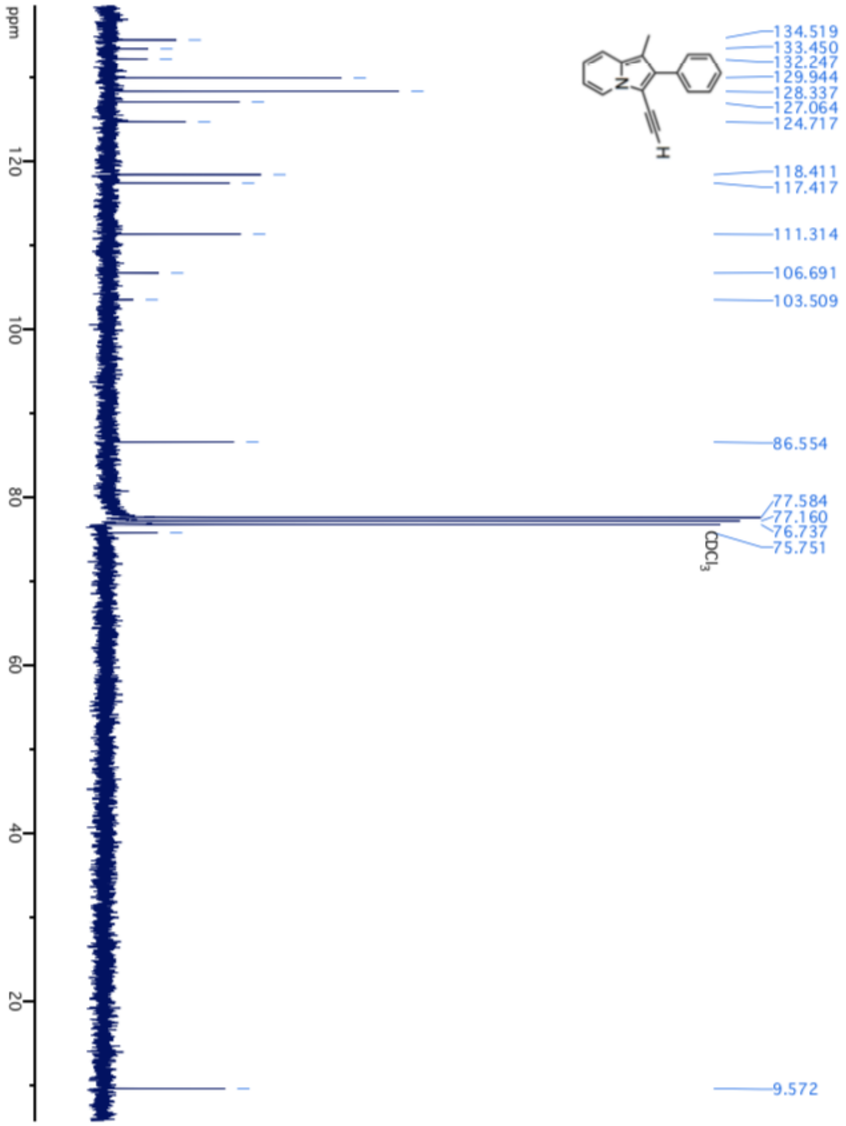

Figure 88. ^{13}C NMR of **3**, 125 MHz, $CDCl_3$, room temperature

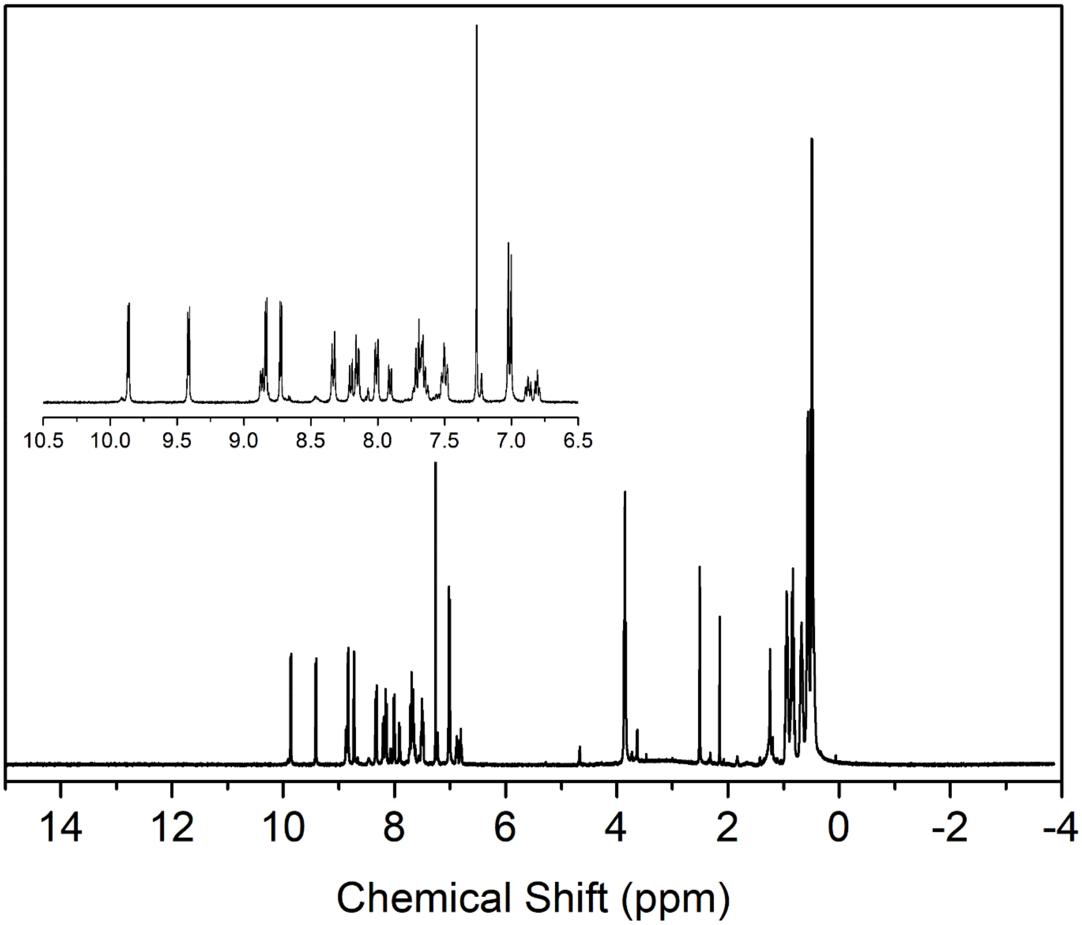

Figure 89. ^{1}H NMR (400 MHz, $CDCl_3$+C_5D_5N) of **SM85**.

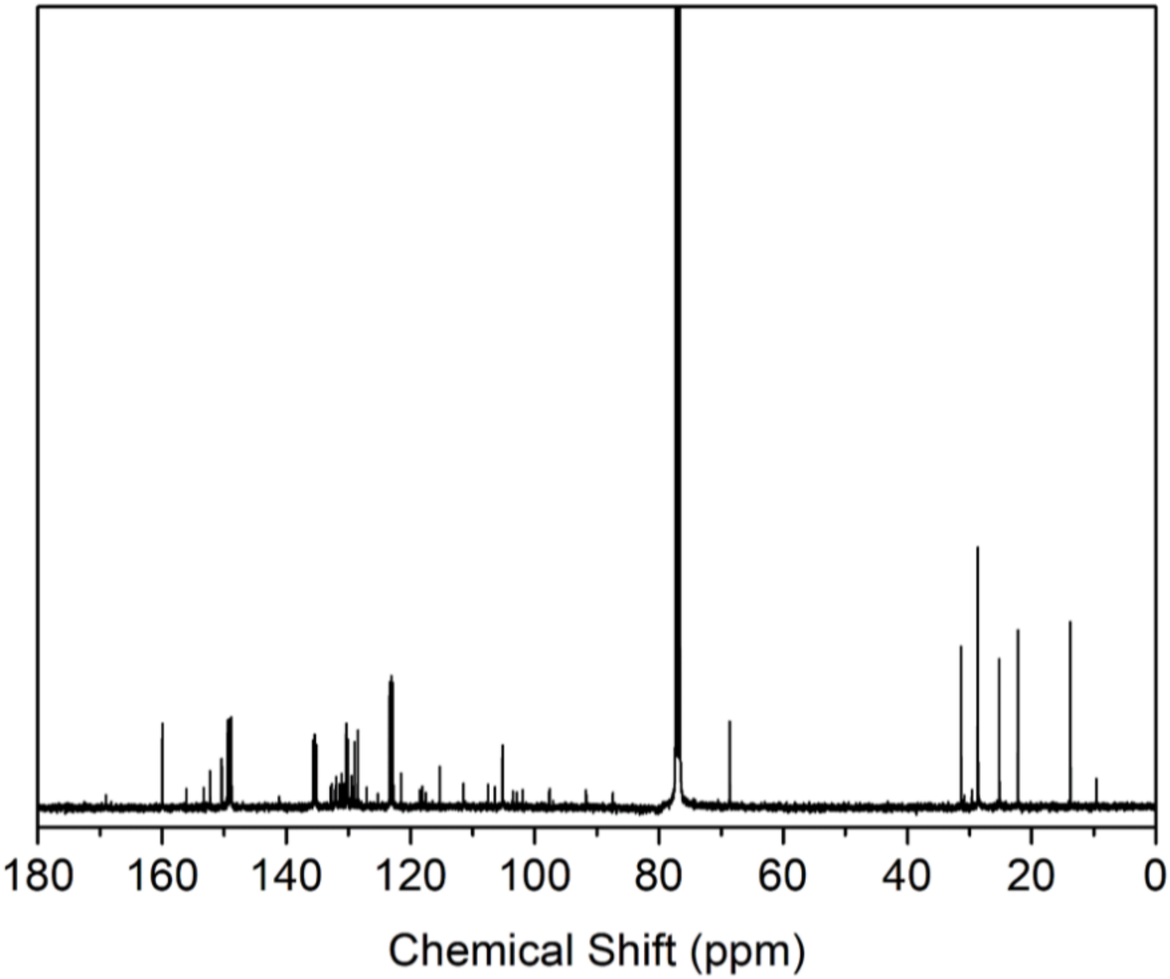

Figure 90. ^{13}C NMR (100 MHz, $CDCl_3$+C_5D_5N) of **SM85**.

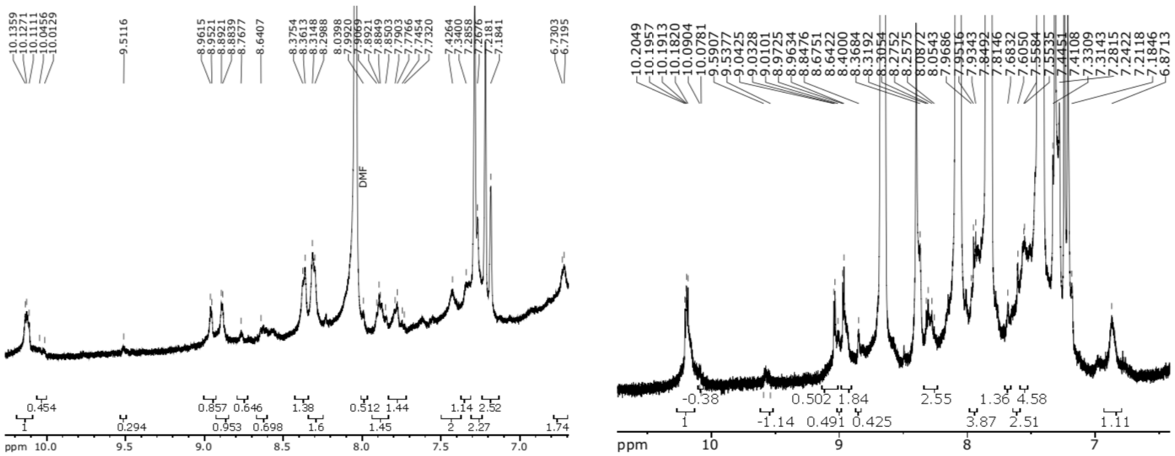

Figure 91. ^{1}H NMR (500 MHz, *d*$_6$-DMF) of **SM85** without (left) and with (right) C_5D_5N.

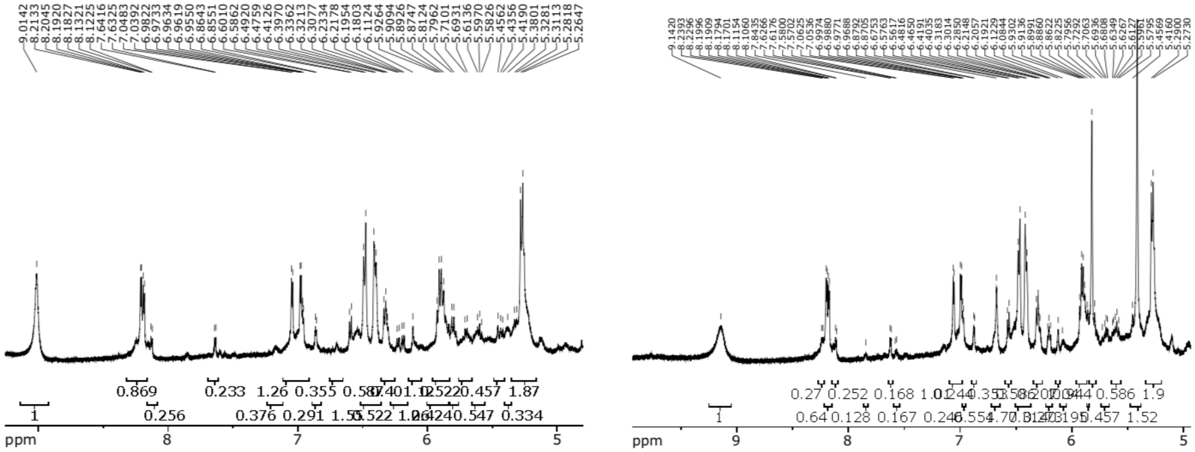

Figure 92. ^{1}H NMR (500 MHz, *d*$_8$-THF) of **SM85** without (left) and with (right) C_5D_5N.

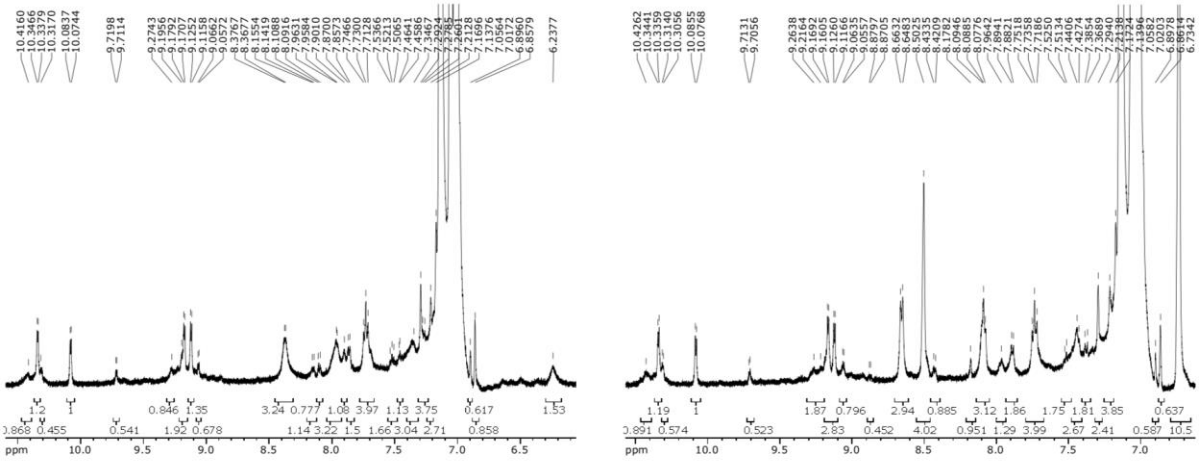

Figure 93. ^{1}H NMR (500 MHz, *d*$_8$-toluene) of **SM85** without (left) and with (right) C_5D_5N.

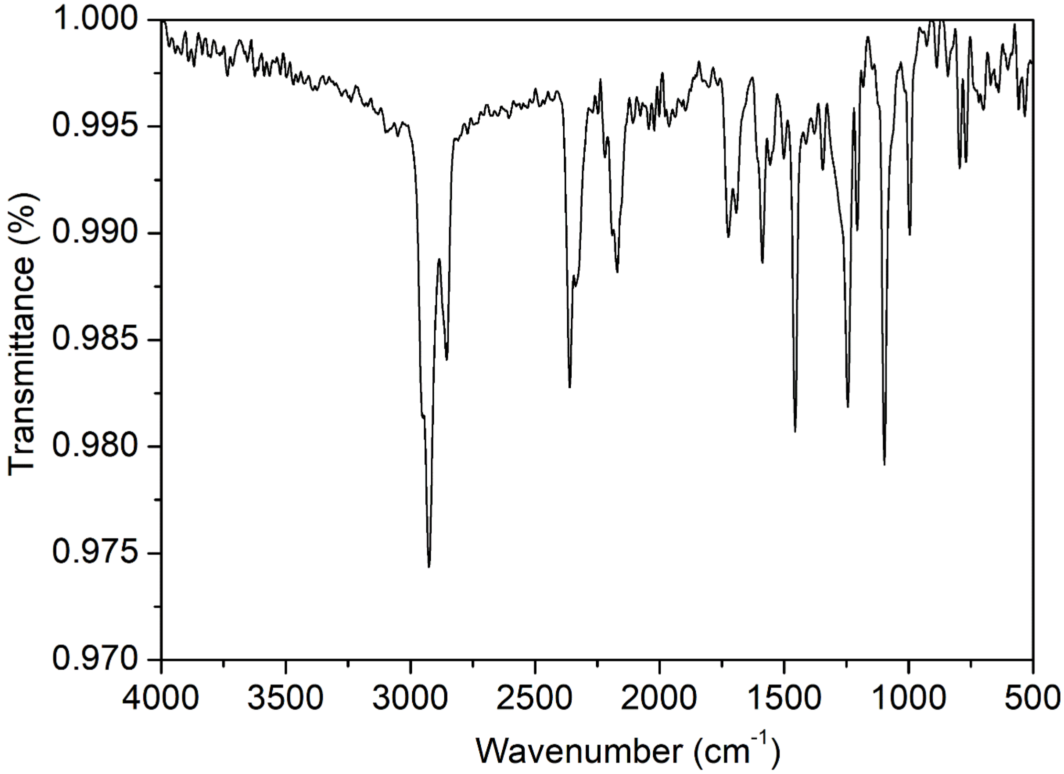

Figure 94. FT–IR (ATR, neat film) of **SM85**.

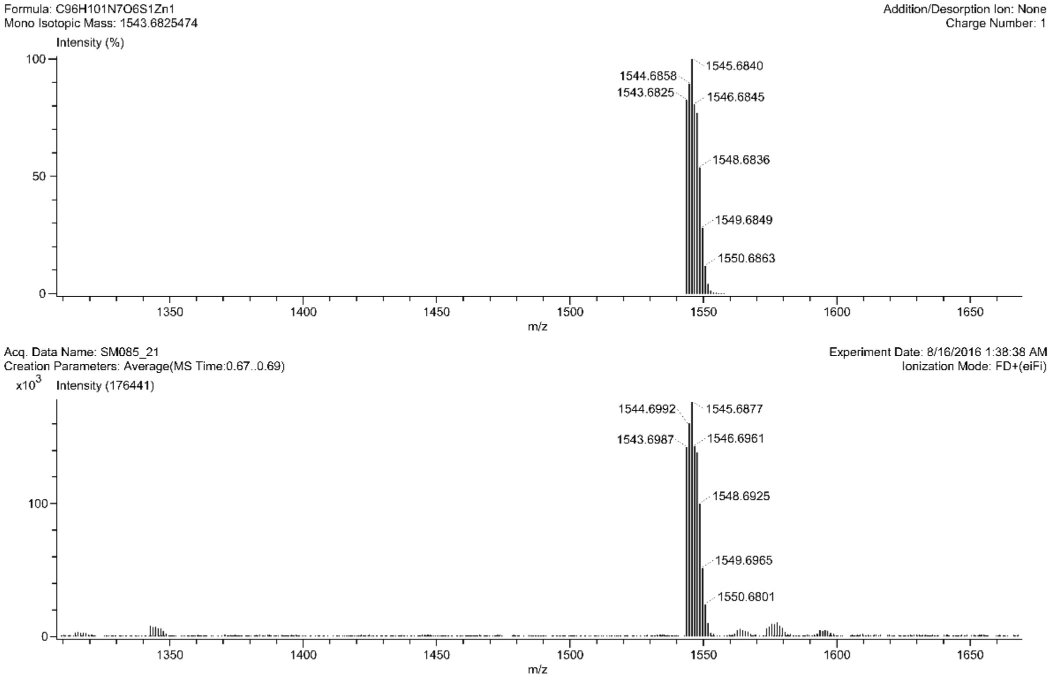

Figure 95. HRMS of **SM85** (FD–MS).

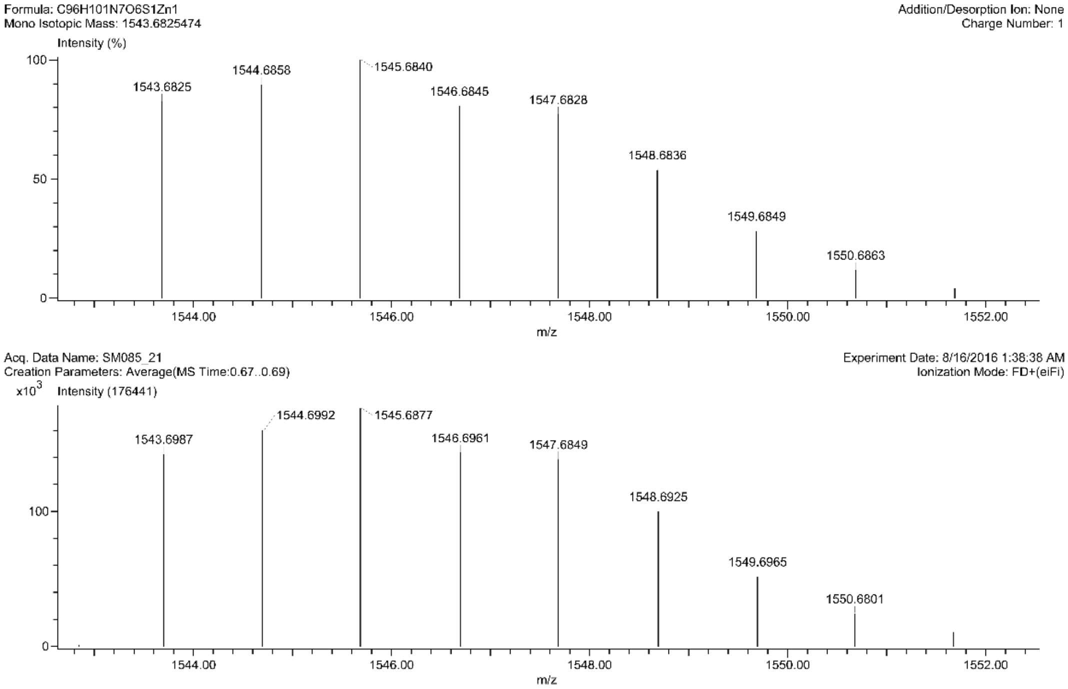

Figure 96. HRMS (zoom) of **SM85** (FD–MS).

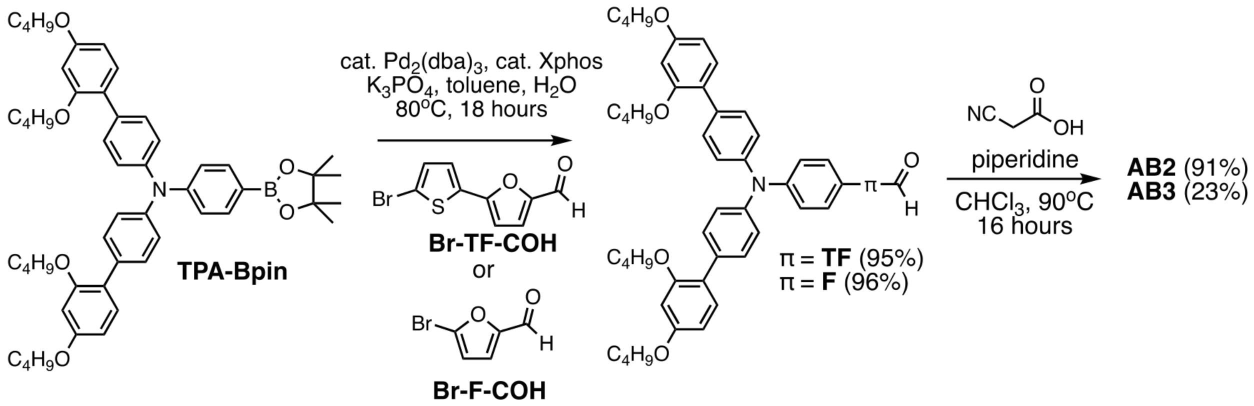

Scheme 4. Synthetic route to **AB2** and **AB3**.

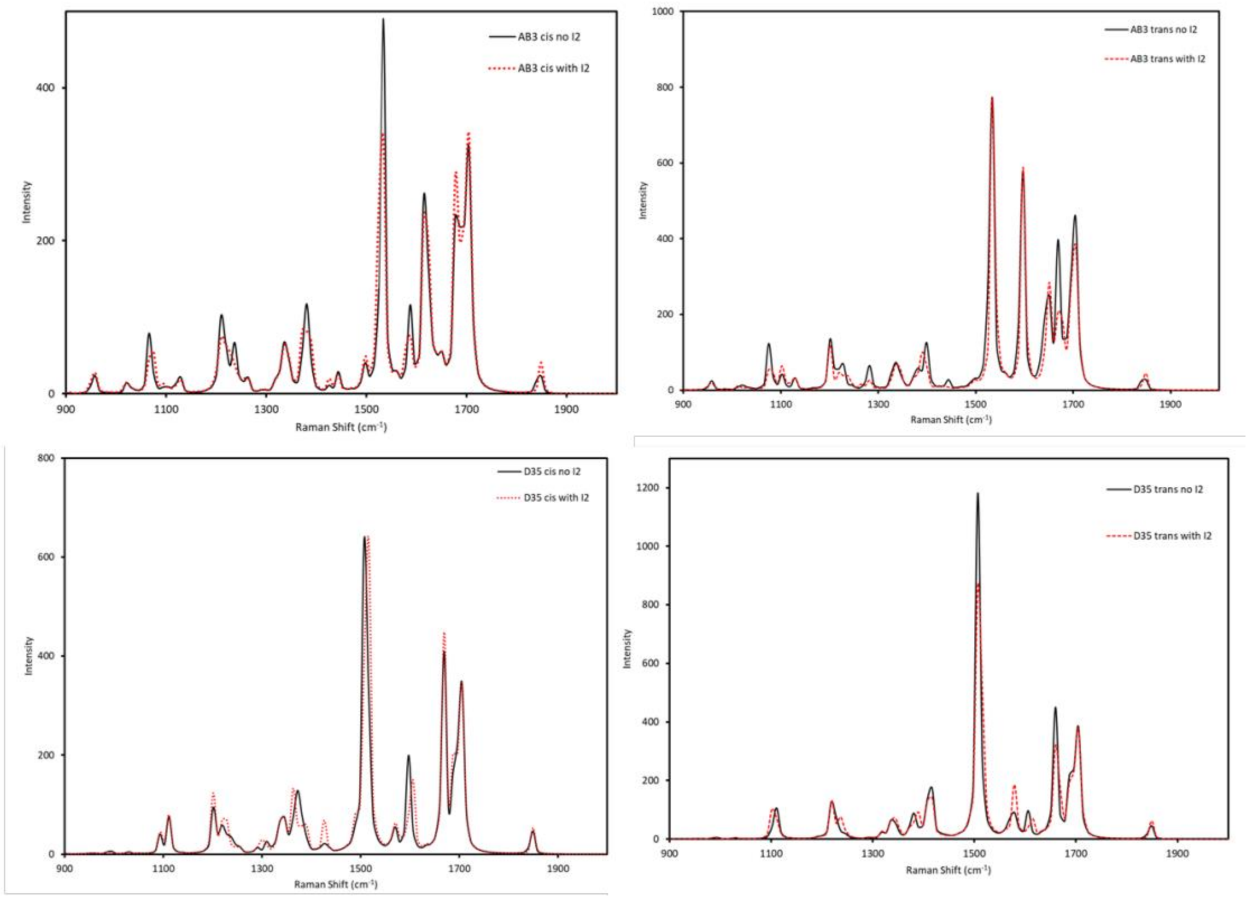

Figure 97: Predicted Raman spectrum for *cis* and *trans* isomers of **AB1, AB2, D35** and **AB3**

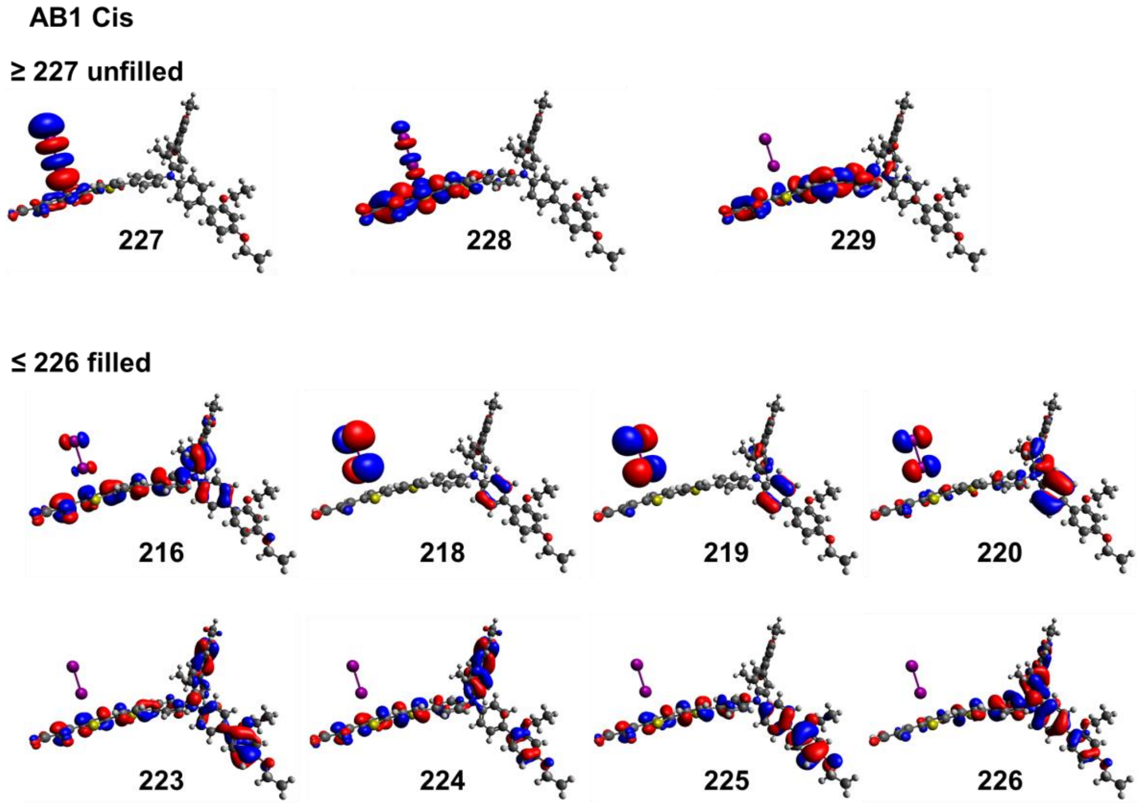

Figure 98. Orbitals contributing to TD-DFT predicted transitions for **AB1**. Calculations were done at wB97XD/6-31+g* level of theory and basis set.

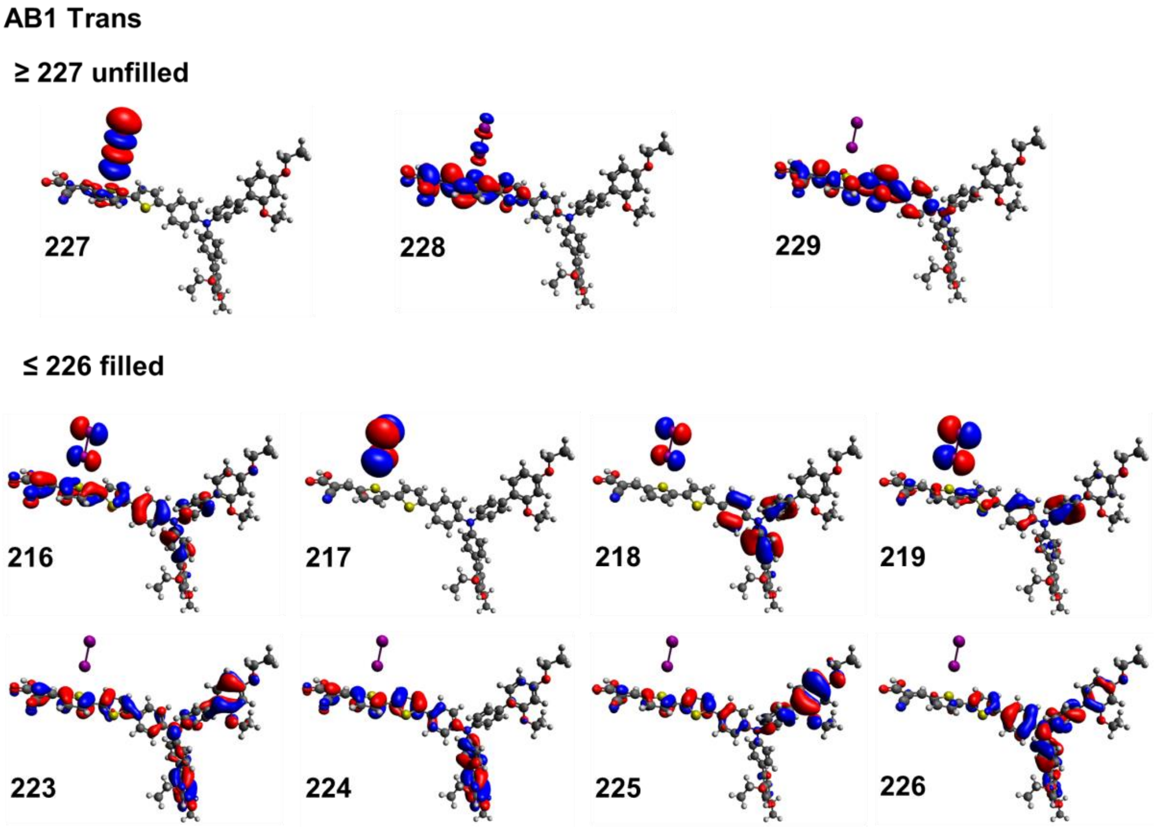

Figure 99. Orbitals contributing to TD-DFT predicted transitions for trans **AB1**. Calculations were done at wB97XD/6-31+g* level of theory and basis set.

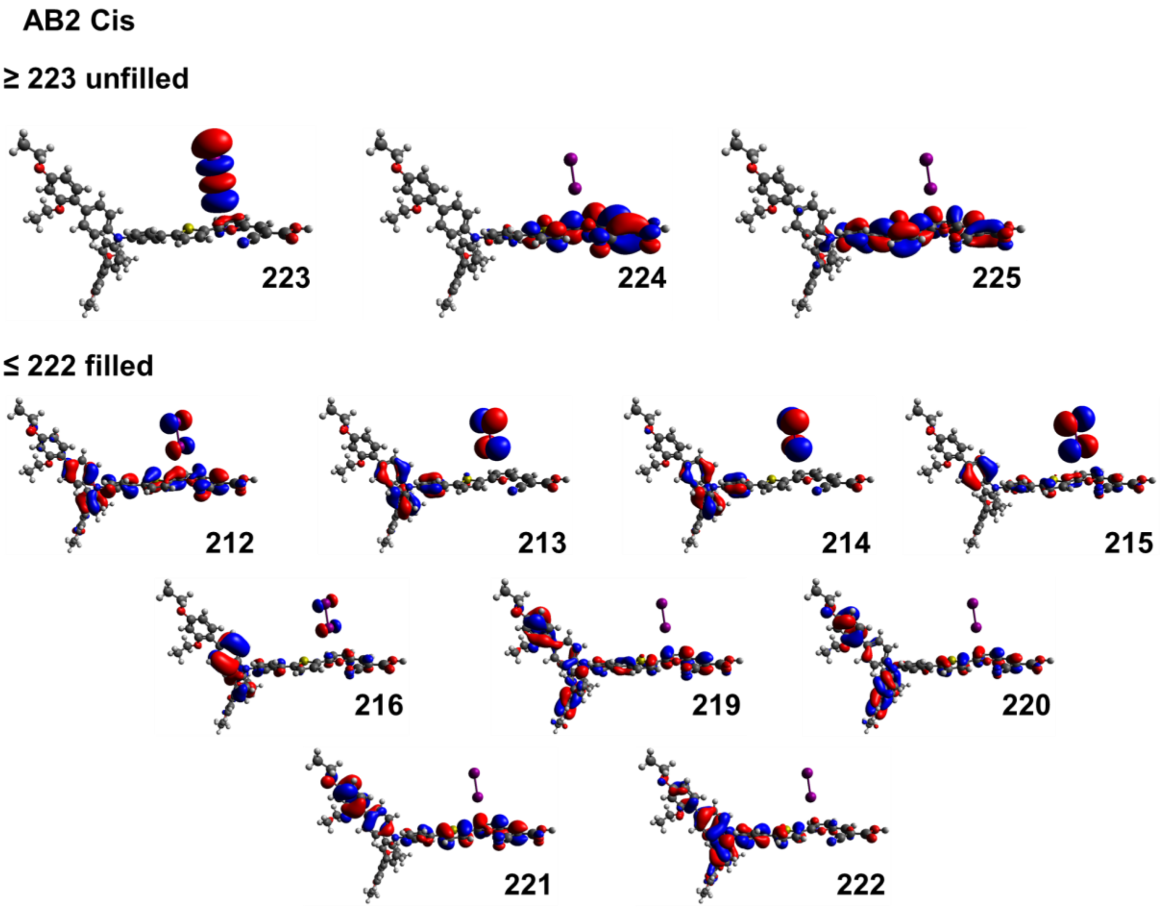

Figure 100. Orbitals contributing to TD-DFT predicted transitions for cis **AB2**. Calculations were done at wB97XD/6-31+g* level of theory and basis set.

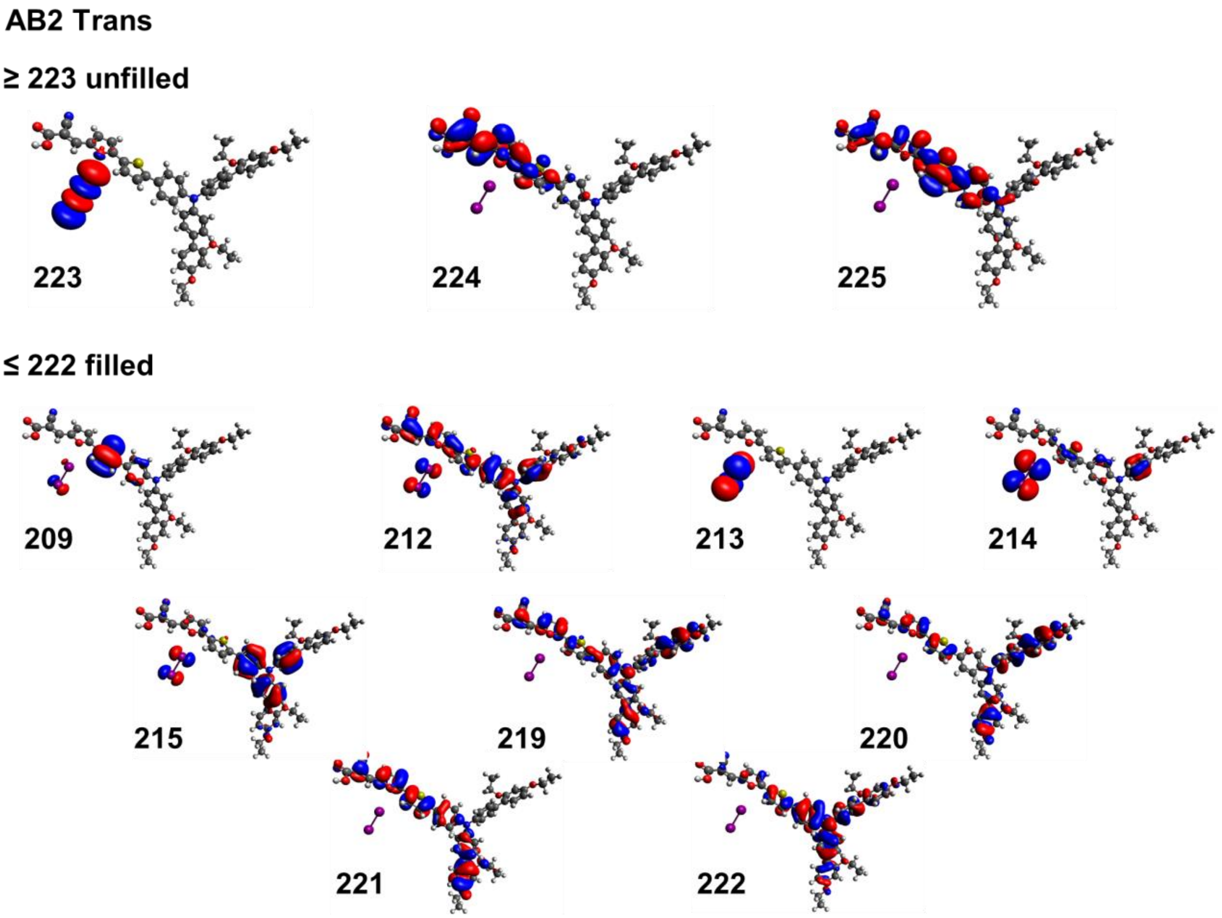

Figure 101. Orbitals contributing to TD-DFT predicted transitions for *trans* **AB2**. Calculations were done at wB97XD/6-31+g* level of theory and basis set.

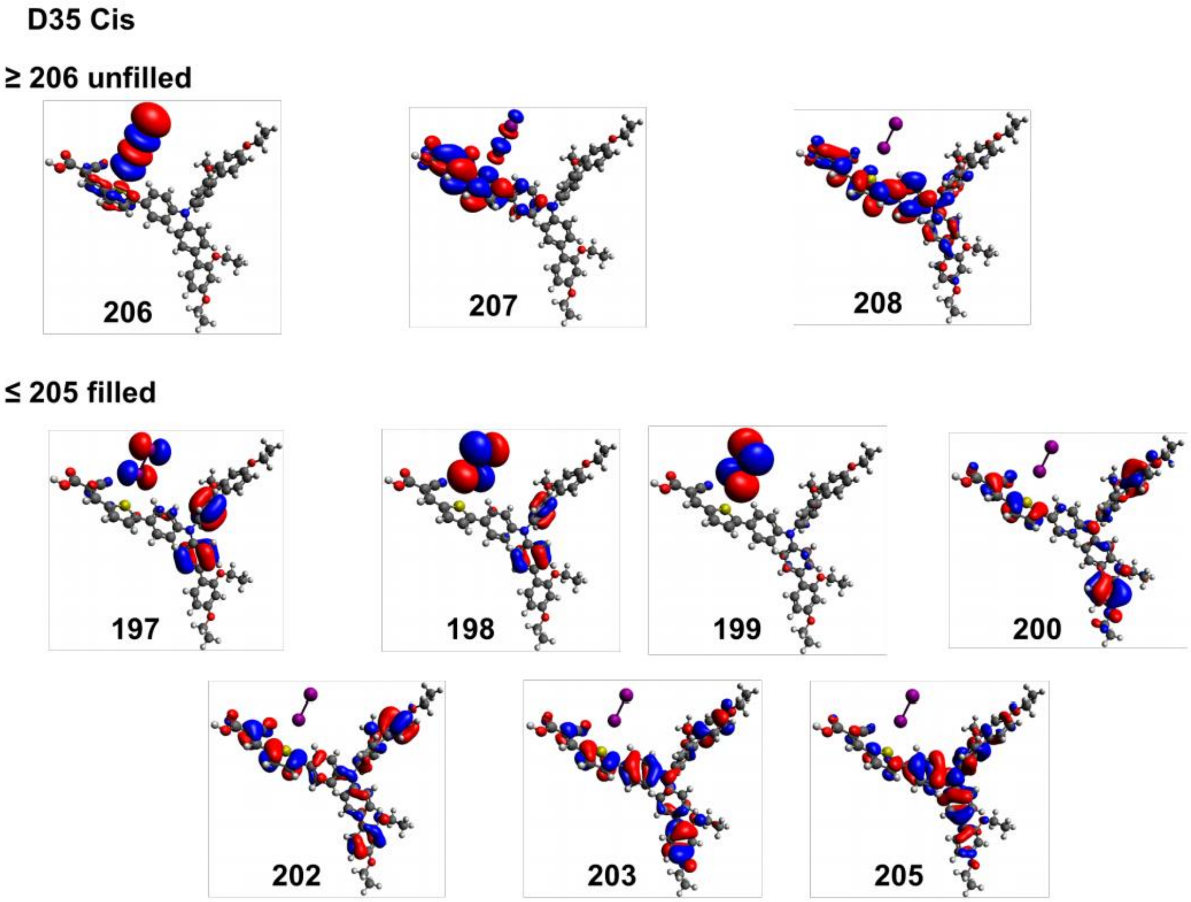

Figure 102. Orbitals contributing to TD-DFT predicted transitions for *cis* **D35**. Calculations were done at wB97XD/6-31+g* level of theory and basis set.

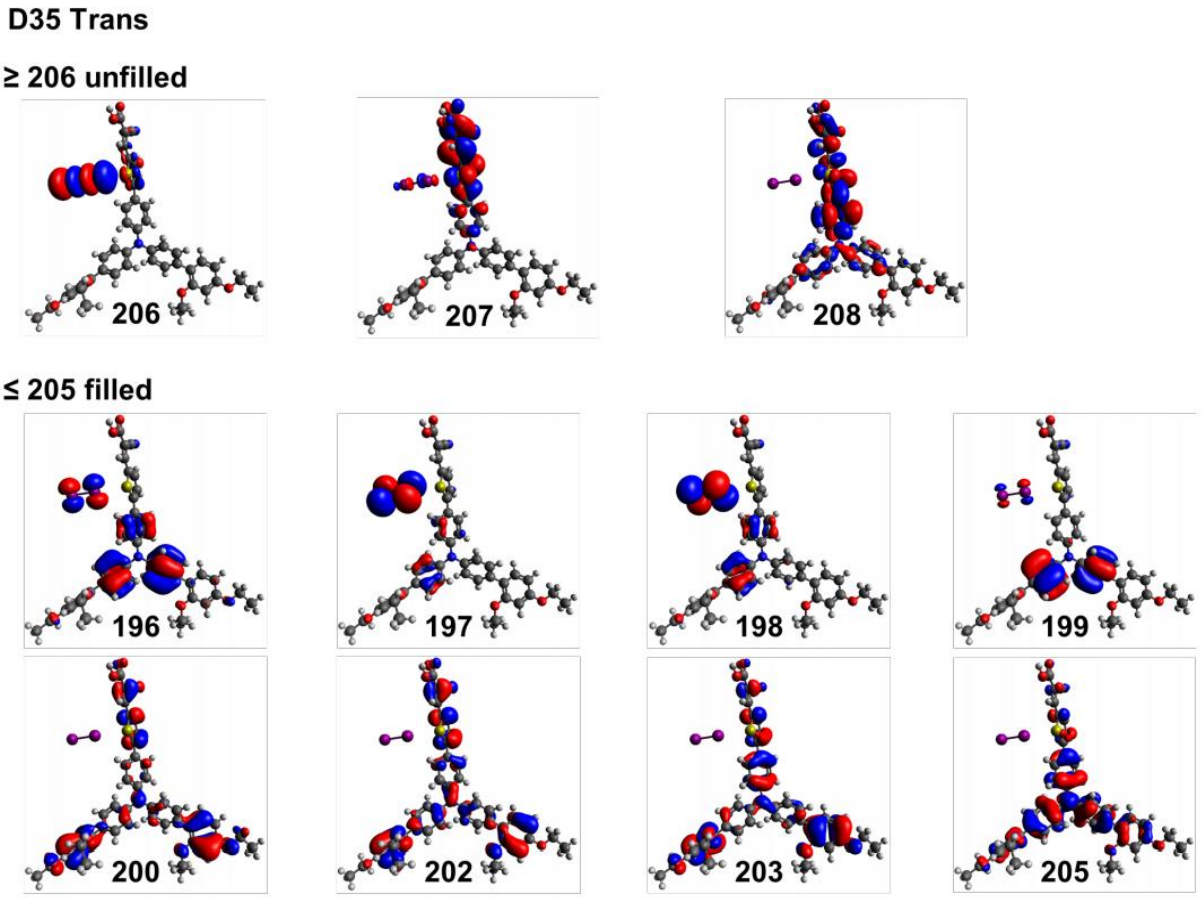

Figure 103. Orbitals contributing to TD-DFT predicted transitions for *trans* **D35**. Calculations were done at wB97XD/6-31+g* level of theory and basis set.

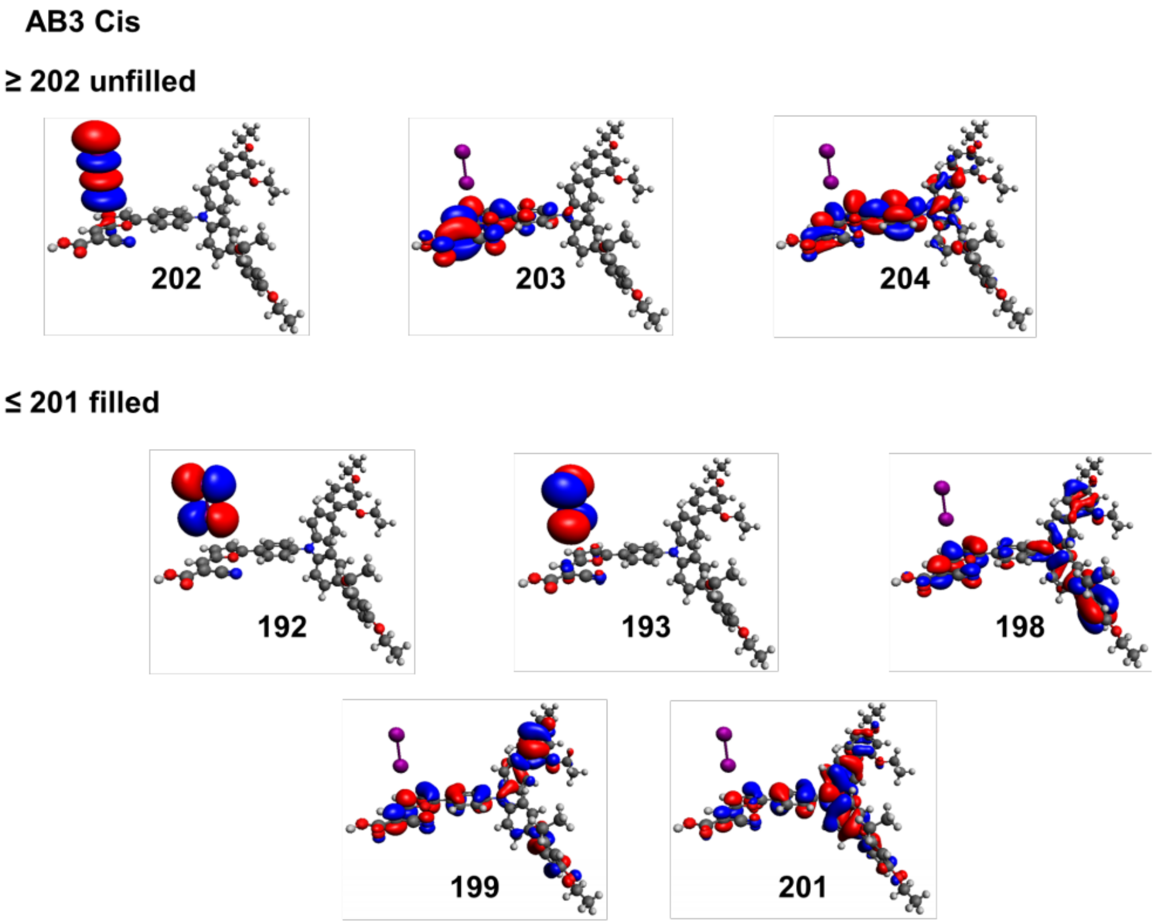

Figure 104. Orbitals contributing to TD-DFT predicted transitions for *cis* **AB3**. Calculations were done at wB97XD/6-31+g* level of theory and basis set.

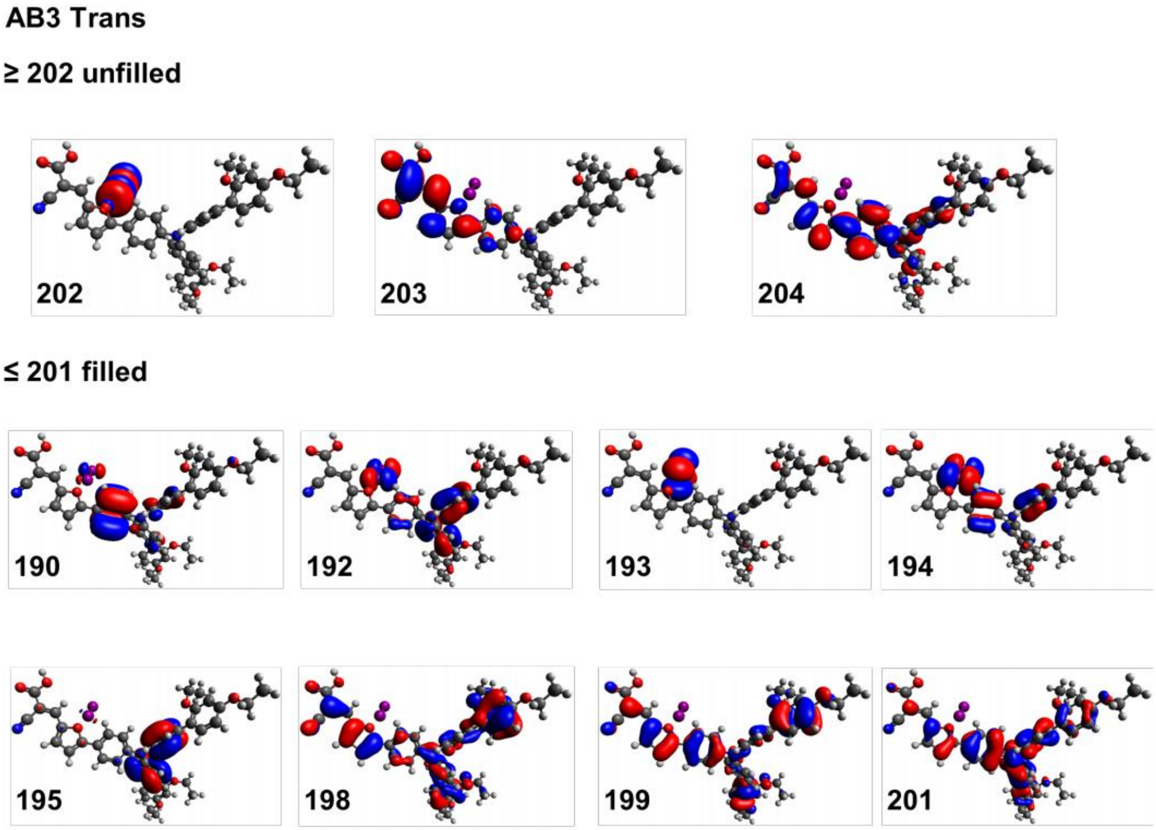

Figure 105. Orbitals contributing to TD-DFT predicted transitions for *trans* **AB3**. Calculations were done at wB97XD/6-31+g* level of theory and basis set.

Table 24. Excited state orbital transitions for cis **AB1**. Calculations were done at wB97XD/6-31+g* level of theory and basis set.

dye	State	transition orbitals	contribution (%)	vert. trans. (nm | eV)	oscillator strength	energy (Hatrees)
AB1 cis	1	219 (I_2) → 227 (I_2) 219 (I_2) → 228 (dye/I_2) 220 (dye/I_2) → 227 (I_2)	66 4 27	523 | 2.37	0.0004	-3310.9
AB1 cis	2	216 (dye/I_2) → 227 (I_2) 218 (I_2) → 227 (I_2) 218 (I_2) → 228 (dye/I_2) 219 (I_2) → 227 (I_2) 220 (dye/I_2) → 227 (I_2)	2 77 4 2 12	518 | 2.39	0.0004	-3310.9
AB1 cis	3	223 (dye) → 227 (I_2) 223 (dye) → 228 (dye/I_2) 224 (dye) → 227 (I_2) 224 (dye) → 228 (dye/I_2) 225 (dye) → 227 (I_2) 225 (dye) → 228 (dye/I_2) 226 (dye) → 227 (I_2) 226 (dye) → 228 (dye/I_2) 226 (dye) → 229 (dye)	6 3 14 7 15 7 27 12 4	423 | 2.93	0.9905	-3310.9

AB1 cis (no I_2)	1	216 (dye) → 220 (dye) 217 (dye) → 220 (dye) 218 (dye) → 220 (dye) 219 (dye) → 220 (dye) 219 (dye) → 221 (dye)	6 9 36 35 7	404 | 3.07	1.6582	-3288.1

Table 25. Excited state orbital transitions for trans **AB1**. Calculations were done at wB97XD/6-31+g* level of theory and basis set.

dye	**State**	**transition orbitals**	**contribution (%)**	**vert. trans. (nm | eV)**	**oscillator strength**	**energy (Hatrees)**
AB1 trans	1	216 (dye/I_2) → 227 (I_2) 217 (I_2) → 227 (I_2) 218 (I_2) → 227 (dye/I_2) 219 (dye/I_2) → 227 (I_2)	11 19 11 53	522 | 2.37	0.0005	-3310.9
AB1 trans	2	216 (dye/I_2) → 227 (I_2) 217 (I_2) → 227 (I_2) 217 (I_2) → 228 (dye/I_2) 219 (dye/I_2) → 227 (I_2)	4 77 3 14	520 | 2.38	0.0003	-3310.9

AB1 trans	3	223 (dye) → 227 (I_2) 223 (dye) → 228 (dye/I_2) 224 (dye) → 227 (I_2) 224 (dye) → 228 (dye/I_2) 225 (dye) → 227 (I_2) 225 (dye) → 228 (dye/I_2) 226 (dye) → 227 (I_2) 226 (dye) → 228 (dye/I_2) 226 (dye) → 229 (dye)	8 2 20 6 13 4 32 7 3	426 | 2.91	0.7251	-3310.9
AB1 trans (no I_2)	1	216 (dye) → 220 (dye) 217 (dye) → 220 (dye) 218 (dye) → 220 (dye) 219 (dye) → 220 (dye) 219 (dye) → 221 (dye)	8 13 31 34 8	401 | 3.09	1.7475	-3288.1

Table 26. Excited state orbital transitions for cis **AB2**. Calculations were done at wB97XD/6-31+g* level of theory and basis set.

dye	**State**	**transition orbitals**	**contribution (%)**	**vert. trans. (nm | eV)**	**oscillator strength**	**energy (Hatrees)**
AB2 cis	1	212 (dye/I_2) → 223 (I_2) 213 (I_2) → 223 (I_2) 215 (dye/I_2) → 223 (I_2) 216 (dye/I_2) → 223 (I_2)	12 5 72 8	522 | 2.37	0.0003	-2987.9

AB2 cis	2	214 (I_2) → 223 (I_2)	98	519 | 2.39	0.0007	-2987.9
AB2 cis	3	219 (dye) → 223 (I_2) 220 (dye) → 223 (I_2) 221 (dye) → 223 (I_2) 222 (dye) → 223 (I_2) 222 (dye) → 224 (dye)	5 10 32 44 2	429 | 2.89	0.1524	-2987.9
AB2 cis (no I_2)	1	212 (dye) → 216 (dye) 213 (dye) → 216 (dye) 214 (dye) → 216 (dye) 215 (dye) → 216 (dye) 215 (dye) → 217 (dye)	4 3 45 35 7	407 | 3.07	1.4447	-2965.1

Table 27. Excited state orbital transitions for trans **AB2**. Calculations were done at wB97XD/6-31+g* level of theory and basis set.

dye	State	transition orbitals	contribution (%)	vert. trans. (nm | eV)	oscillator strength	energy (Hatrees)
AB2 trans	1	209 (dye/I_2) → 223 (I_2) 212 (dye/I_2) → 223 (I_2) 214 (I_2) → 223 (I_2) 215 (I_2) → 223 (I_2)	3 7 57 33	522 | 2.38	0.0001	-2987.9
AB2 trans	2	213 (I_2) → 223 (I_2)	98	517 | 2.40	0.0003	-2987.9

AB2 trans	3	219 (dye) → 223 (I_2) 220 (dye) → 223 (I_2) 221 (dye) → 223 (I_2) 222 (dye) → 223 (I_2)	6 11 35 43	430 | 2.88	0.0248	-2987.9
AB2 trans (no I_2)	1	212 (dye) → 216 (dye) 213 (dye) → 216 (dye) 214 (dye) → 216 (dye) 215 (dye) → 216 (dye) 215 (dye) → 217 (dye)	5 4 43 34 8	400 | 3.10	1.8967	-2965.1

Table 28. Excited state orbital transitions for cis **D35**. Calculations were done at wB97XD/6-31+g* level of theory and basis set.

dye	**State**	**transition orbitals**	**contribution (%)**	**vert. trans. (nm | eV)**	**oscillator strength**	**energy (Hatrees)**
D35 cis	1	199 (I_2) → 206 (I_2) 199 (I_2) → 207 (dye/I_2)	94 3	523 | 2.37	0.0004	-2759.2
D35 cis	2	197 (I_2) → 206 (I_2) 198 (I_2) → 206 (I_2) 198 (I_2) → 207 (dye/I_2)	9 83 3	519 | 2.39	0.0007	-2759.2

D35 cis	3	202 (dye) → 206 (I_2) 203 (dye) → 206 (I_2) 203 (dye) → 207 (dye/I_2) 205 (dye) → 206 (I_2) 205 (dye) → 207 (dye/I_2) 205 (dye) → 208 (dye)	4 12 2 66 8 2	431 | 2.88	0.4107	-2759.2
D35 cis (no I_2)	1	195 (dye) → 199 (dye) 196 (dye) → 199 (dye) 198 (dye) → 199 (dye) 198 (dye) → 200 (dye)	8 18 61 7	393 | 3.16	1.2567	-2736.3

Table 29. Excited state orbital transitions for trans **D35**. Calculations were done at wB97XD/6-31+g* level of theory and basis set.

dye	**State**	**transition orbitals**	**contribution (%)**	**vert. trans. (nm | eV)**	**oscillator strength**	**energy (Hatrees)**
D35 trans	1	196 (I_2) → 206 (I_2) 197 (I_2) → 206 (I_2) 198 (I_2) → 206 (dye/I_2) 199 (dye/I_2) → 206 (I_2)	13 46 30 5	521 | 2.38	0.0009	-2759.2
D35 trans	2	197 (I_2) → 206 (I_2) 198 (I_2) → 206 (I_2)	32 64	520 | 2.38	0.0004	-2759.2

D35 trans	3	202 (dye) → 206 (I_2) 203 (dye) → 206 (I_2) 205 (dye) → 206 (I_2) 205 (dye) → 207 (dye/I_2)	4 12 74 4	437 | 2.84	0.2797	-2759.2
D35 trans (no I_2)	1	195 (dye) → 199 (dye) 196 (dye) → 199 (dye) 198 (dye) → 199 (dye) 198 (dye) → 200 (dye)	9 19 59 8	390 | 3.18	1.4418	-2736.3

Table 30. Excited state orbital transitions for cis **AB3**. Calculations were done at wB97XD/6-31+g* level of theory and basis set.

dye	**State**	**transition orbitals**	**contribution (%)**	**vert. trans. (nm | eV)**	**oscillator strength**	**energy (Hatrees)**
AB3 cis	1	192 (I_2) → 202 (I_2) 193 (I_2) → 202 (I_2)	2 93	528 | 2.35	0.0021	-2436.2
AB3 cis	2	192 (I_2) → 202 (I_2) 193 (I_2) → 202 (I_2)	97 3	523 | 2.37	0.0003	-2436.2
AB3 cis	3	193 (I_2) → 202 (I_2) 198 (dye) → 202 (I_2) 199 (dye) → 202 (I_2) 201 (dye) → 202 (I_2) 201 (dye) → 203 (dye)	3 5 14 67 4	447 | 2.77	0.1710	-2436.2

AB3 cis (no I_2)	1	191 (dye) → 195 (dye) 192 (dye) → 195 (dye) 193 (dye) → 195 (dye) 194 (dye) → 195 (dye) 194 (dye) → 196 (dye)	5 15 3 66 6	407 | 3.04	1.0472	-2413.4

Table 31. Excited state orbital transitions for trans **AB3**. Calculations were done at wB97XD/6-31+g* level of theory and basis set.

dye	**State**	**transition orbitals**	**contribution (%)**	**vert. trans. (nm | eV)**	**oscillator strength**	**energy (Hatrees)**
AB3 trans	1	190 (dye/I_2) → 202 (I_2) 192 (I_2) → 202 (I_2) 193 (I_2) → 202 (I_2) 194 (I_2) → 202 (I_2) 195 (dye) → 202 (I_2)	3 18 3 72 4	521 | 2.38	0.0004	-2436.2
AB3 trans	2	192 (I_2) → 202 (I_2) 193 (I_2) → 202 (I_2)	3 96	516 | 2.40	0.0003	-2436.2
AB3 trans	3	198 (dye) → 202 (I_2) 199 (dye) → 202 (I_2) 201 (dye) → 202 (I_2)	6 11 35	458 | 2.71	0.0042	-2436.2

AB3 trans (no I_2)	1	191 (dye) → 195 (dye) 192 (dye) → 195 (dye) 194 (dye) → 195 (dye) 194 (dye) → 196 (dye)	6 19 64 7	397 | 3.12	1.5510	-2413.4

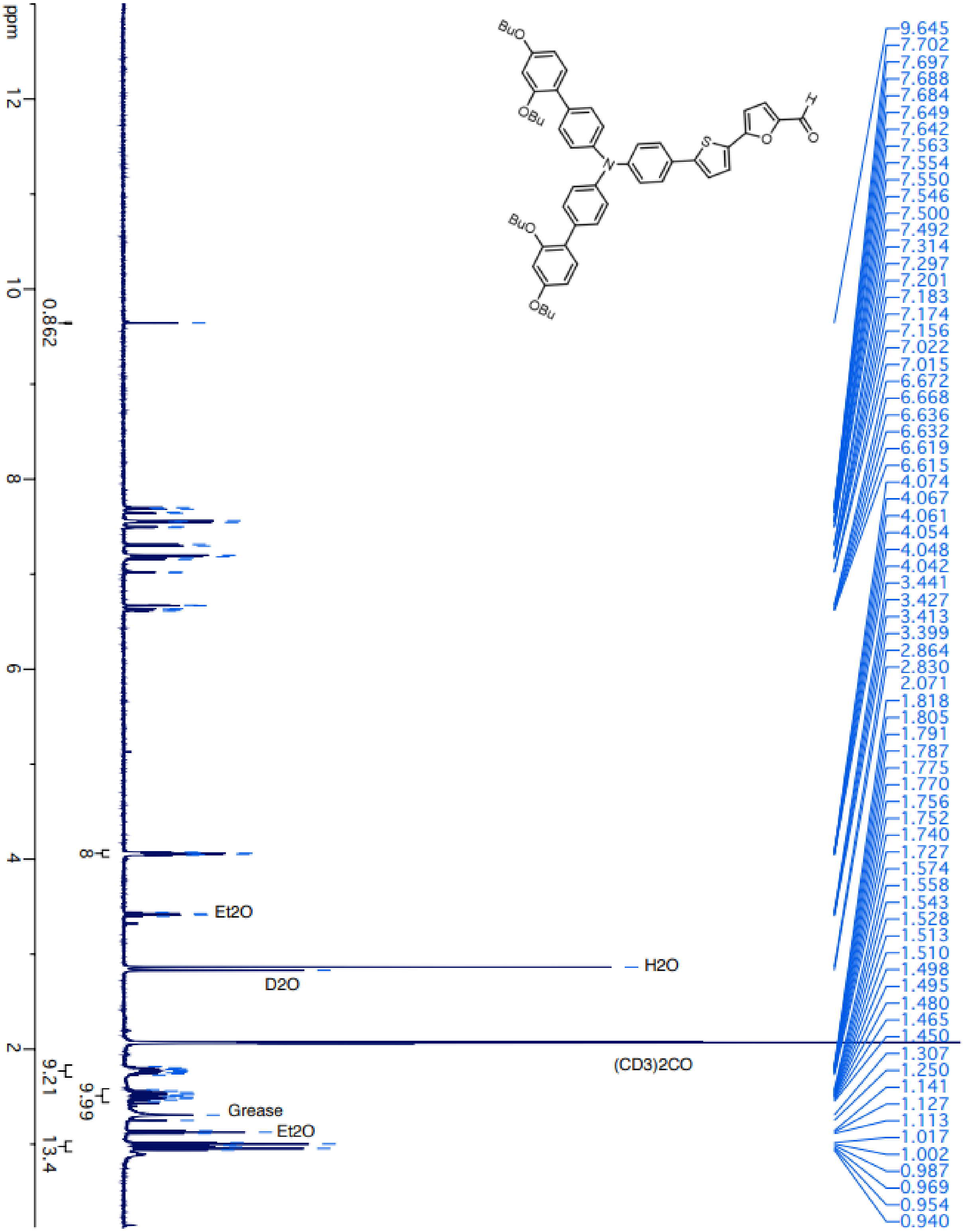

Figure 106. ^{1}H NMR spectrum of compound **TF** in $(CD_3)_2CO$ at room temperature and 500 MHz

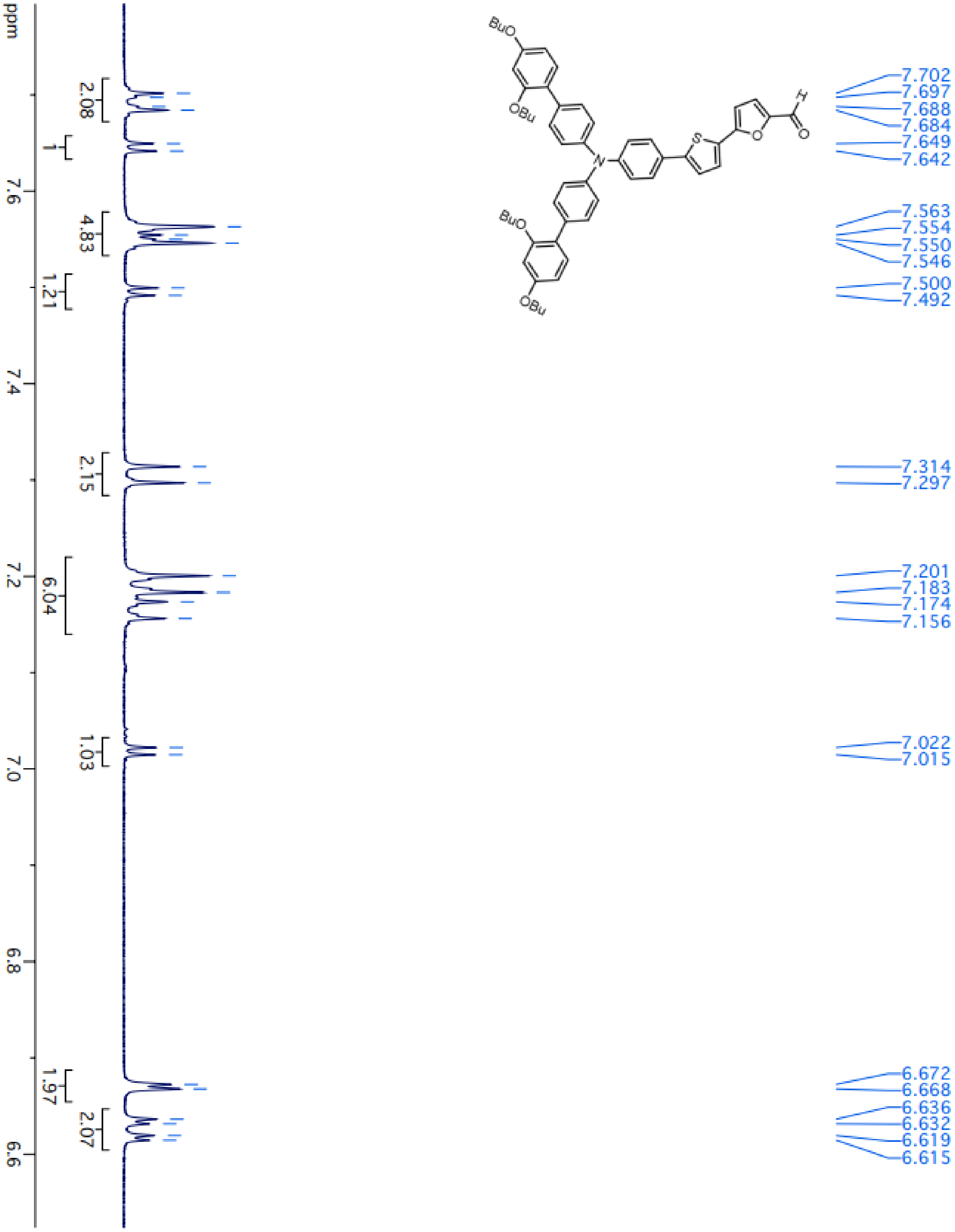

Figure 107. ^{13}C NMR spectrum of compound **TF** in CDCl$_3$ at room temperature and 125 MHz

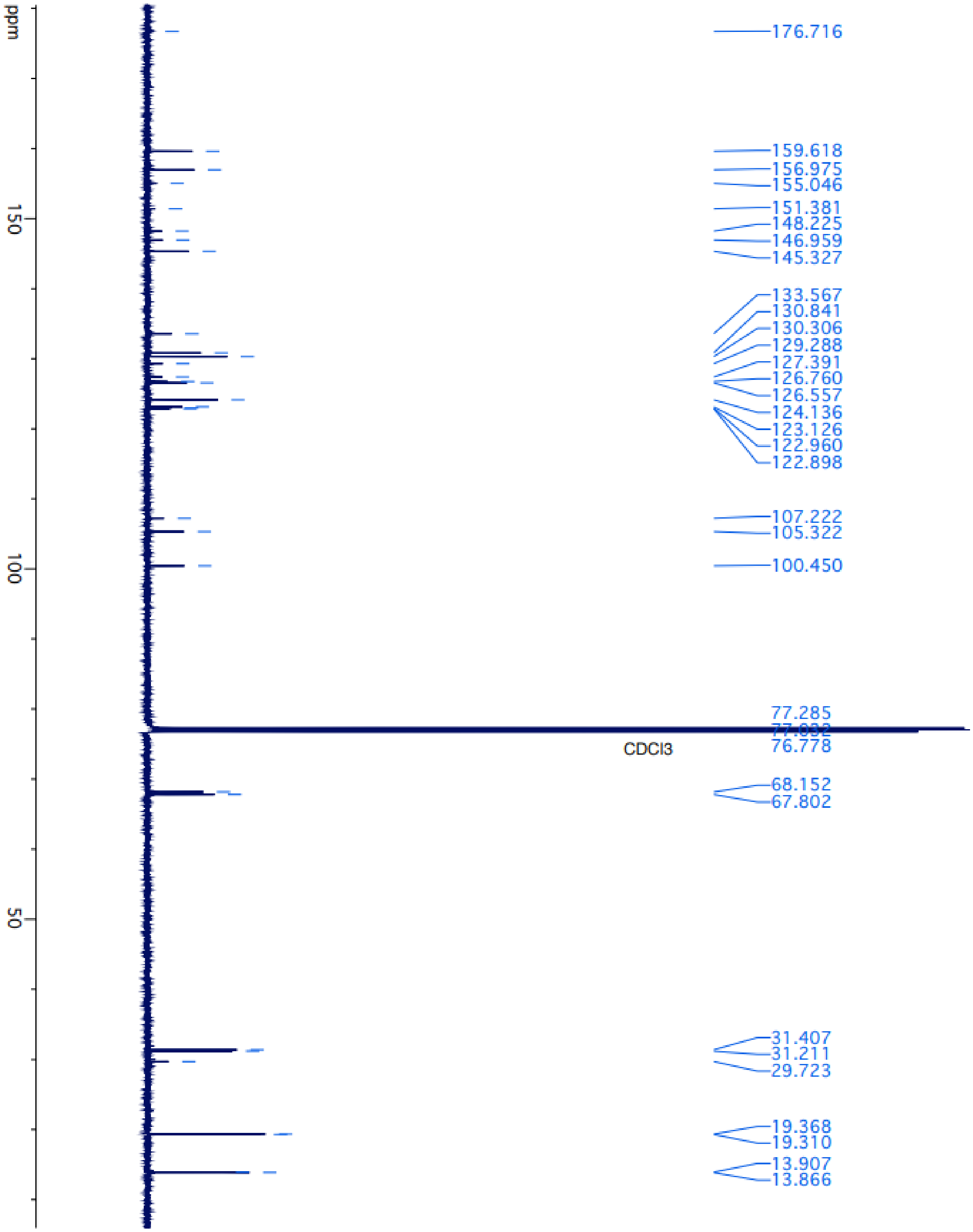

Figure 108. ^{1}H NMR spectrum of compound **AB2** in $(CD_3)_2CO$ at room temperature and 500 MHz

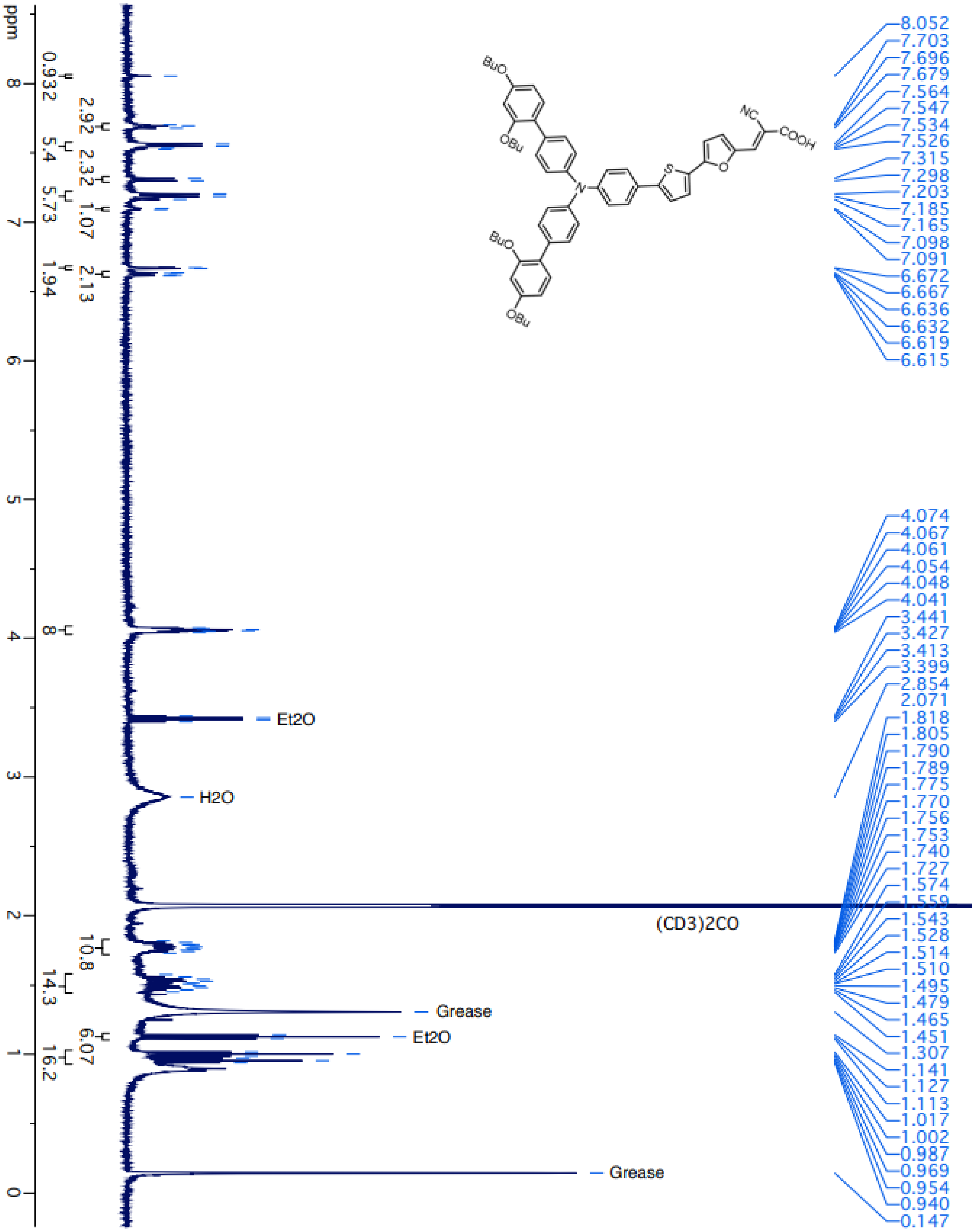

Figure 109. ^{1}H NMR spectrum of compound **F** in $CDCl_3$ at room temperature and 500 MHz

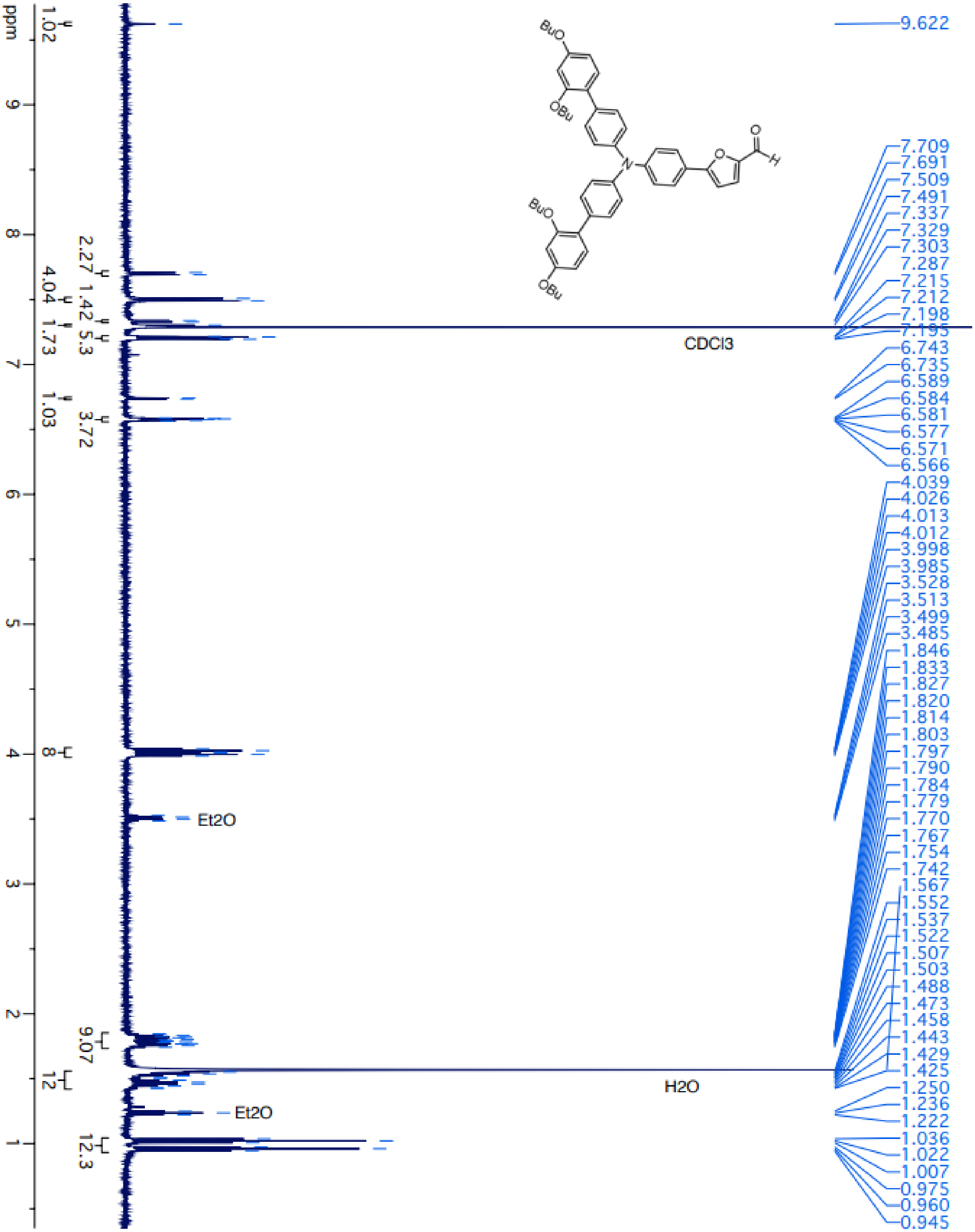

Figure 110. ^{13}C NMR spectrum of compound **F** in $CDCl_3$ at room temperature and 125 MHz

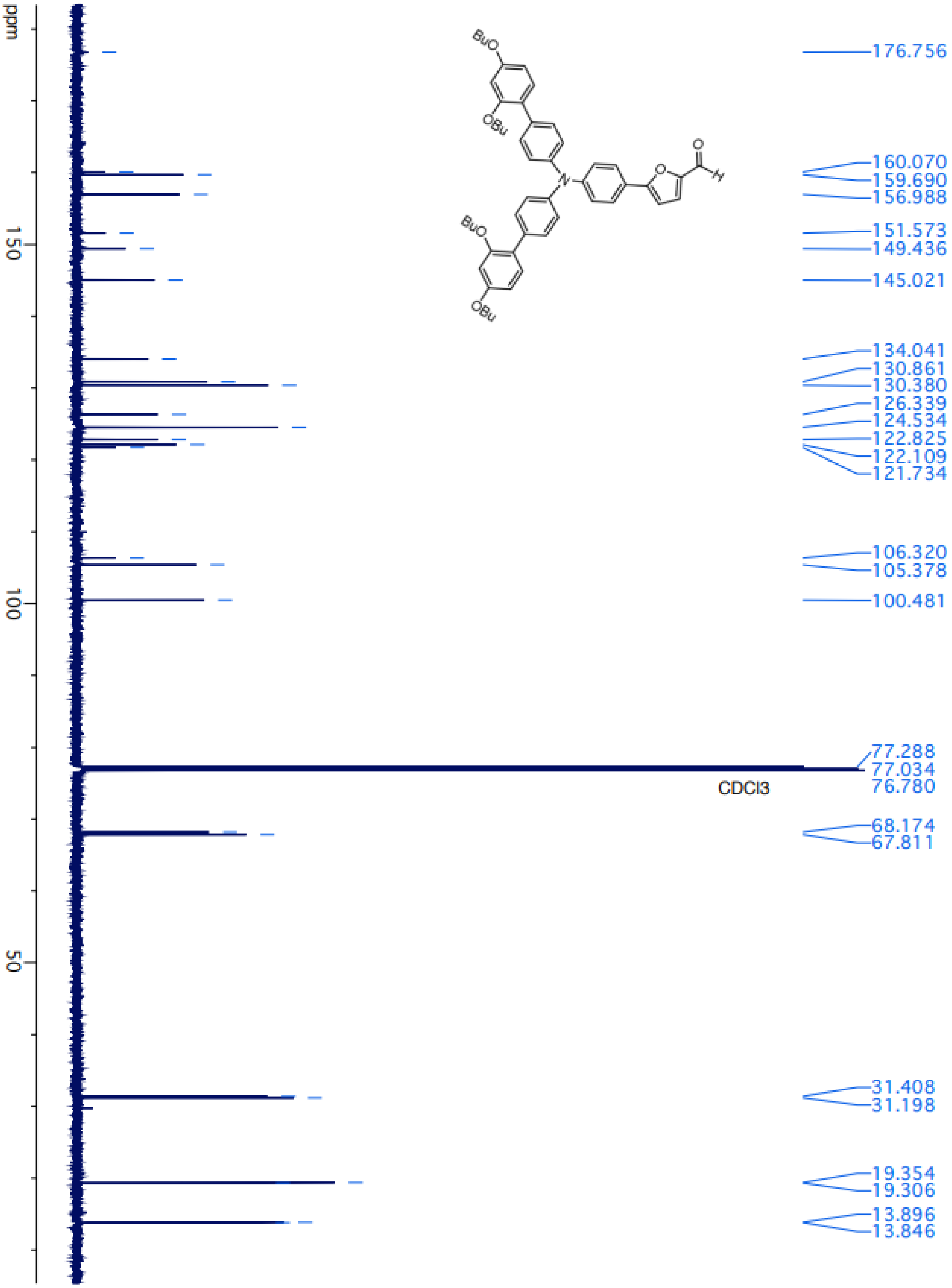

Figure 111. ^{1}H NMR spectrum of compound **AB3** in $CDCl_3$ at room temperature and 500 MHz

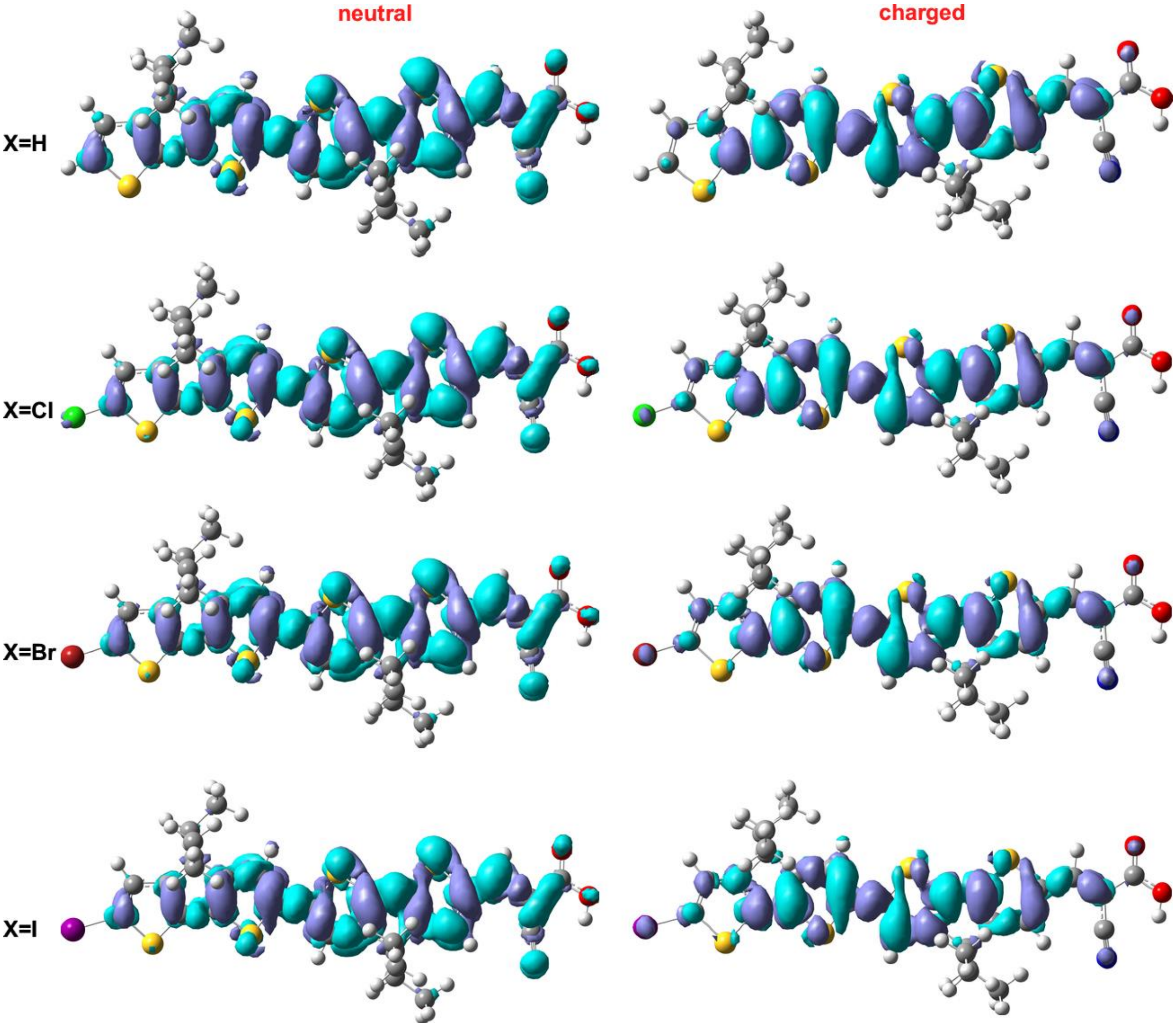

Figure 112: The total density difference (Δρ) between the ground and first singlet excited state (S_0-S_1) of the neutral and positively charged dyes. The purple and blue-green surface represents the depletion (where electrons came from) and increment (where electrons went) of density due to excitation at Isovalue=0.0005, respectively.

Table 32: Calculated binding energy between the redox-shuttles and different dyes, the distance between the dye substituents (*X*) and redox-shuttles and the dihedral angle connecting the substituents with the redox-shuttles.

Redox-shuttle	Substituents (*X*)	Binding Energy (kcal/mole)		Distance (Å)		N-N-X-C dihedral (^{0})	
		Neutral	Charged	Neutral	Charged	Neutral	Charged
Co(N-tpy)$_3$	H	-7.17	-7.27	2.34	2.28	-5.41	-1.20
	Cl	-6.37	-6.22	3.14	3.07	4.29	5.05
	Br	-7.69	-7.39	3.07	3.00	34.91	19.24
	I	-9.44	-9.30	3.07	3.00	29.58	16.27
Co(tpy)$_3$	H	-	-4.62	-	3.08	-	93.95
	Cl	-	-4.81	-	3.63	-	-30.86
	Br	-	-4.86	-	3.76	-	84.40
	I	-	-5.01	-	3.96	-	128.24
I$^-$	H	-1.43	-2.99	3.16	2.99	-	-
	Cl	-0.67	-1.84	4.05	3.89	-	-
	Br	-1.74	-3.21	3.91	3.75	-	-
	I	-3.22	-5.08	3.83	3.71	-	-

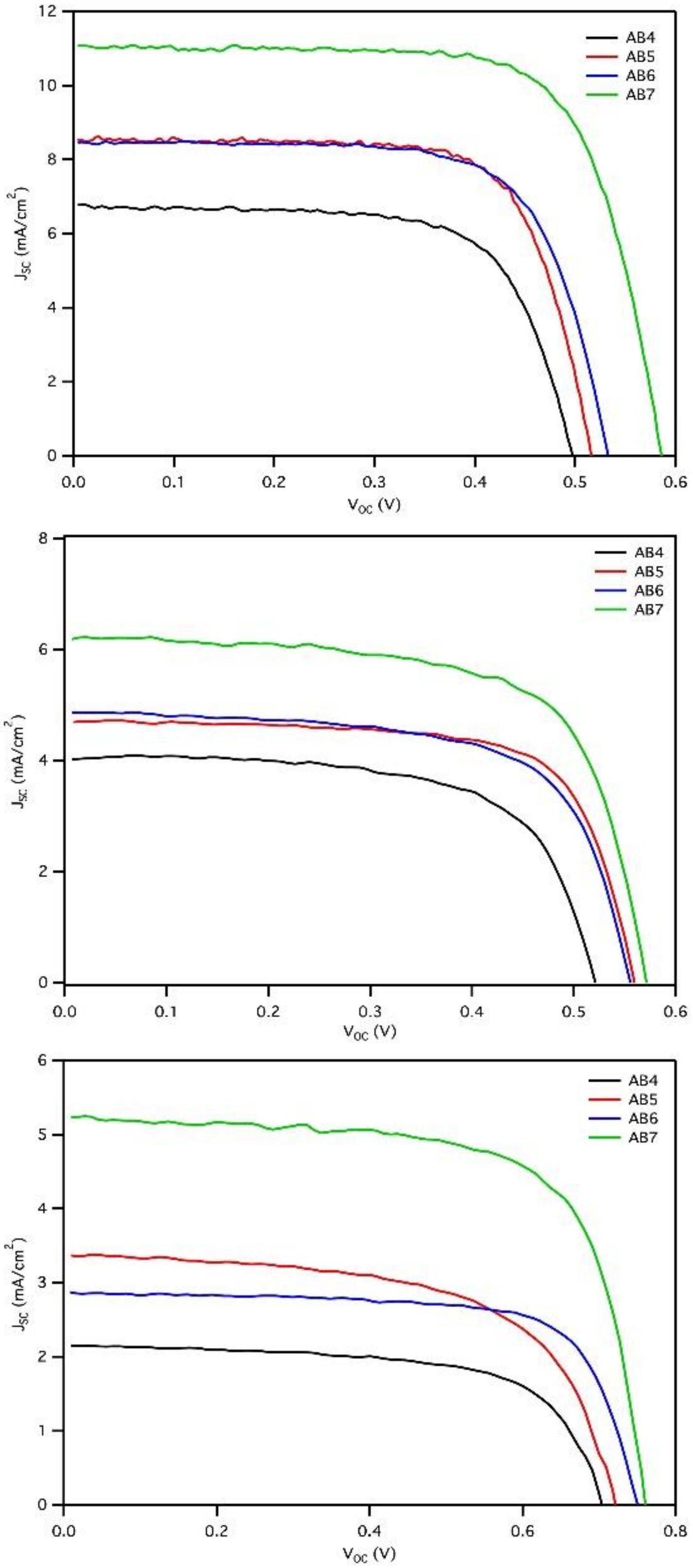

Figure 113. *J*-*V* curves of **AB4**, **AB5**, **AB6** and **AB7** dyes with top) I_3^-/I^-, middle) Co(tpy)$_2^{3+/2+}$, and bottom) Co(*N*-tpy)$_2^{3+/2+}$ redox shuttles.

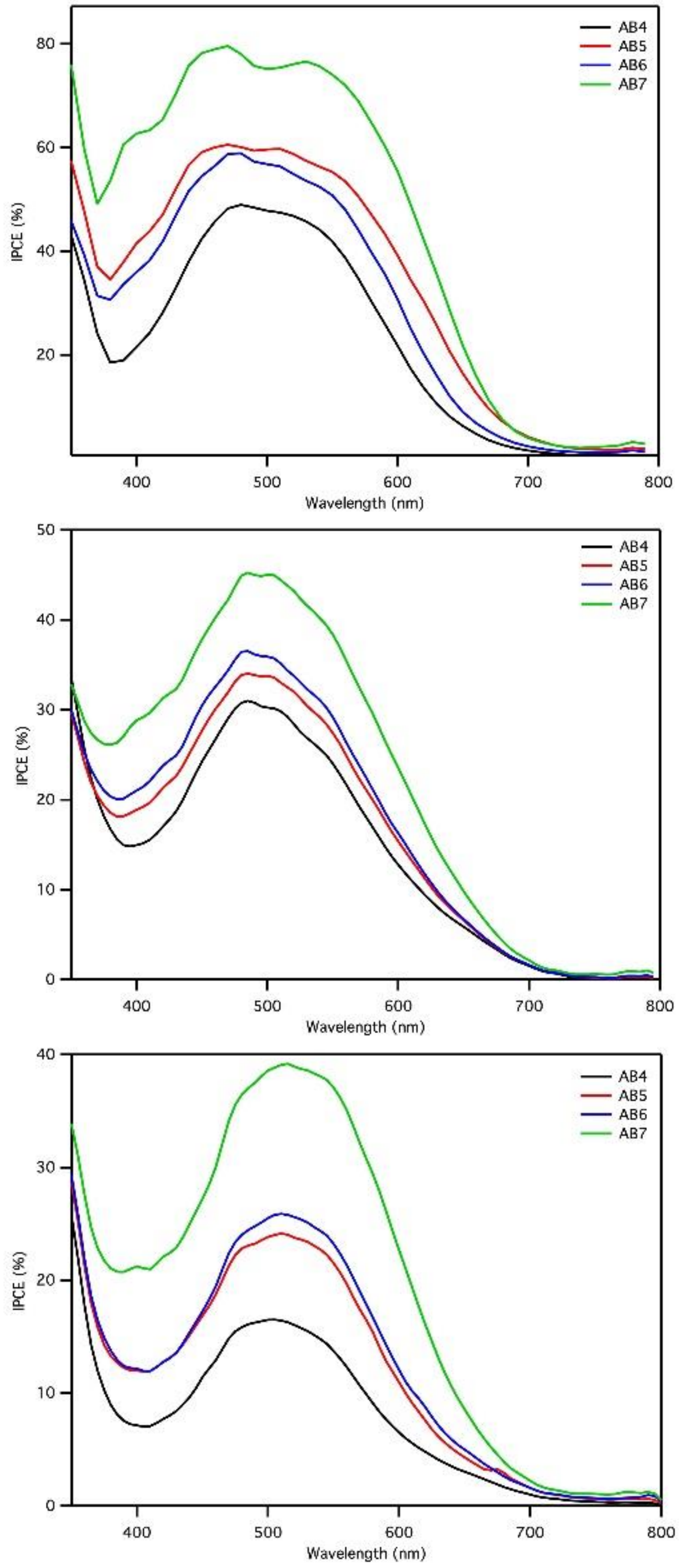

Figure 114. IPCE spectrum of **AB4**, **AB5**, **AB6** and **AB7** dyes with top) I_3^-/I^-, middle) $Co(tpy)_2^{3+/2+}$, and bottom) $Co(N\text{-}tpy)_2^{3+/2+}$ redox shuttles.

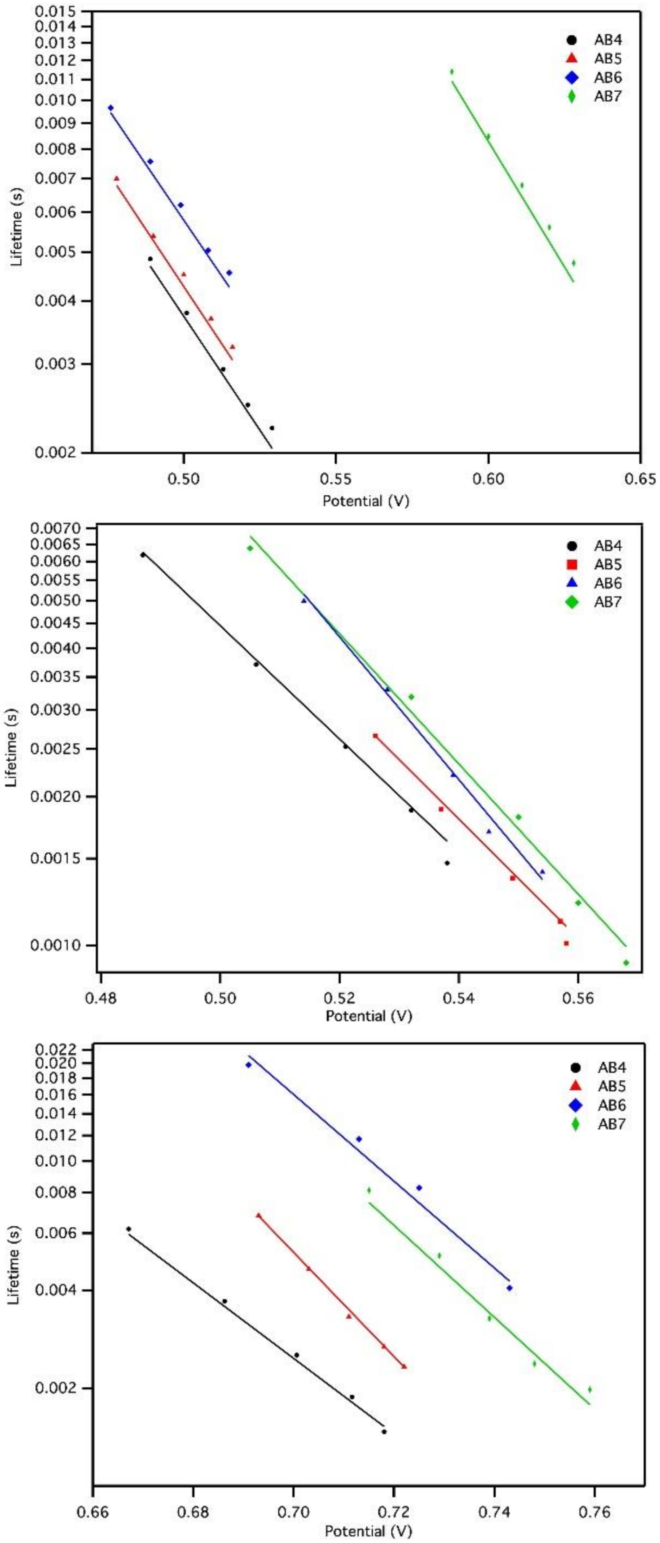

Figure 115. Small modulated photovoltage transient data of **AB4**, **AB5**, **AB6** and **AB7** dyes with top) I_3^-/I^-, middle) Co(tpy)$_2^{3+/2+}$, and bottom) Co(*N*-tpy)$_2^{3+/2+}$ redox shuttles.

Table 33: Electrochemical impedance spectroscopy data.

Dye	R_s (Ω)	R_{rec} (Ω)	C_μ (mF)	R_{CE} (Ω)	C_{CE} (mF)	η_{cc} (%)	τ_{TiO2} (ms)
Iodine							
AB4	13.38	73.15	2.91 x 10^{-5}	13.99	8.54 x 10^{-6}	84	0.99
AB5	12.76	61.60	1.71 x 10^{-5}	12.71	1.49 x 10^{-4}	83	4.82
AB6	15.68	43.38	1.21 x 10^{-5}	11.30	8.63 x 10^{-5}	79	2.34
AB7	12.40	40.72	1.46 x 10^{-5}	8.86	2.89 x 10^{-4}	82	6.63
$Co(terpy)_2^{2+/3+}$							
AB4	17.85	77.16	2.00 x 10^{-2}	18.13	7.00 x 10^{-3}	81	0.51
AB5	17.90	77.20	2.00 x 10^{-2}	18.10	7.00 x 10^{-3}	81	0.51
AB6	13.60	73.6	2.00 x 10^{-2}	13.70	1.00 x 10^{-3}	84	0.63
AB7	16.18	50.5	2.30 x 10^{-2}	12.0	9.00 x 10^{-3}	81	0.50
$Co(N\text{-}terpy)_2^{2+/3+}$							
AB4	11.20	132.80	1.00 x 10^{-2}	12.10	1.70 x 10^{-2}	92	2.00
AB5	10.70	193.00	1.00 x 10^{-2}	19.90	1.00 x 10^{-2}	91	1.00
AB6	9.70	159.30	1.00 x 10^{-2}	43.60	4.00 x 10^{-3}	79	1.26
AB7	12.50	76.85	2.00 x 10^{-2}	14.50	9.00 x 10^{-3}	84	0.50

Table 34: Summary of transient absorption spectroscopy data for target dyes **AB4**, **AB5**, **AB6** and **AB7** with the I^-/I_3^- redox shuttle.

Dye	k_{reg} (s^{-1})	k_{rec} (s^{-1})	Φ (%)
AB4	3400	270	92
AB5	4600	280	94
AB6	3700	180	95
AB7	3000	130	96

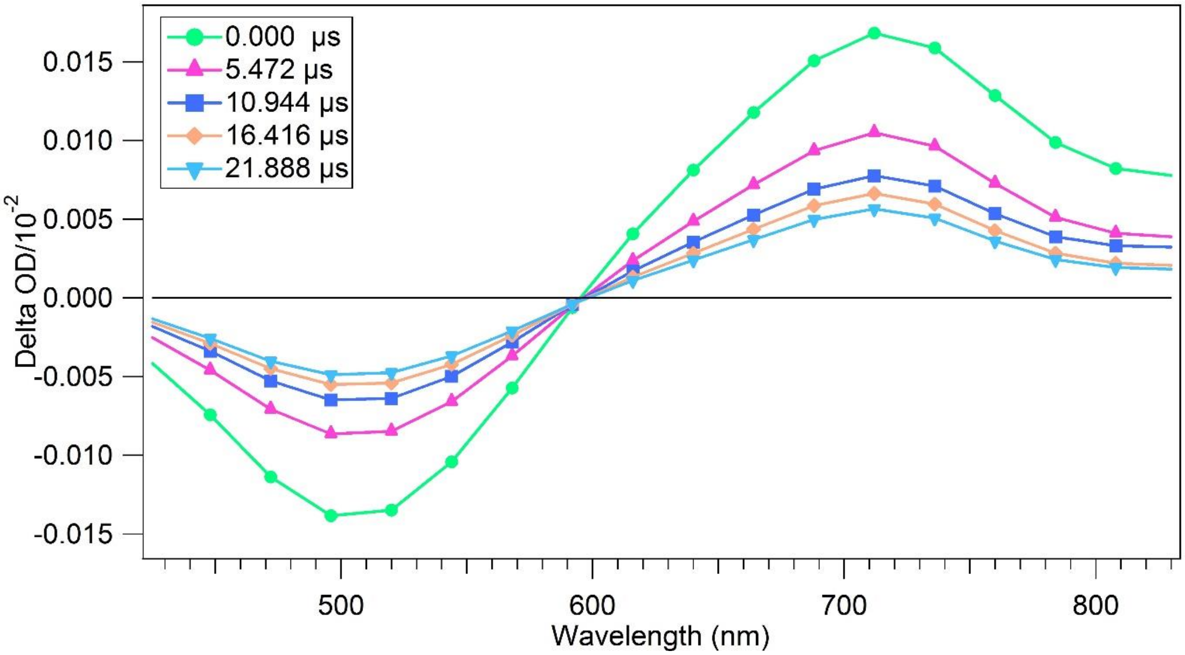

Figure 116: Spectral data for **AB4** in mock iodine solution.

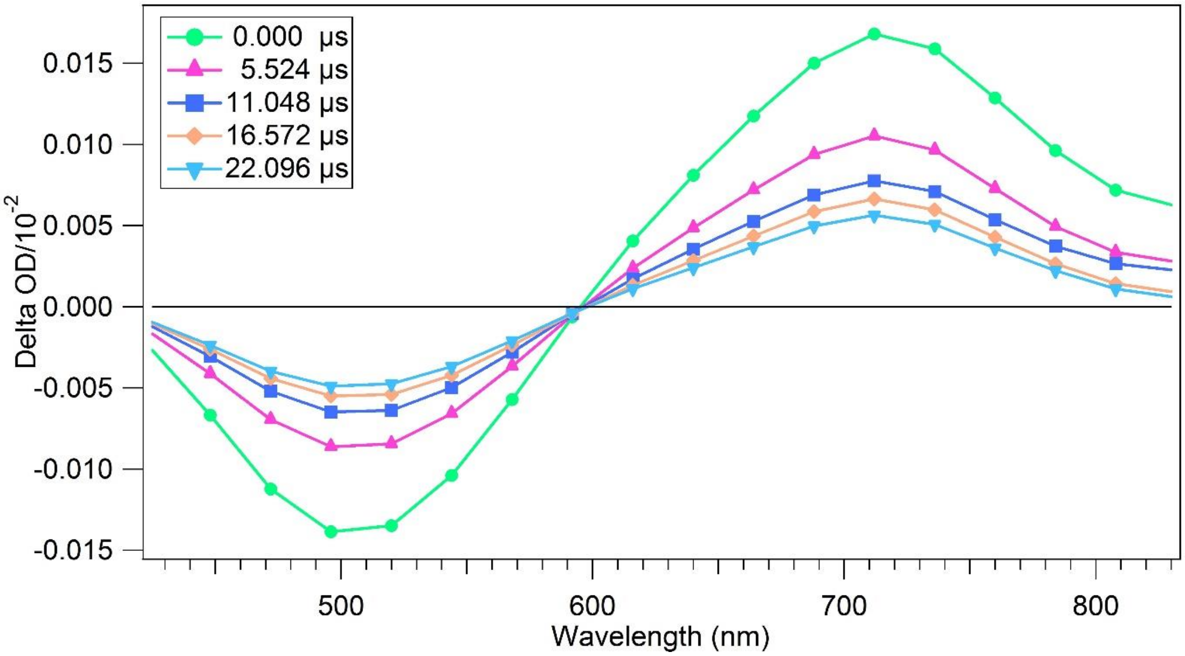

Figure 117: Spectral data for **AB4** in iodine solution.

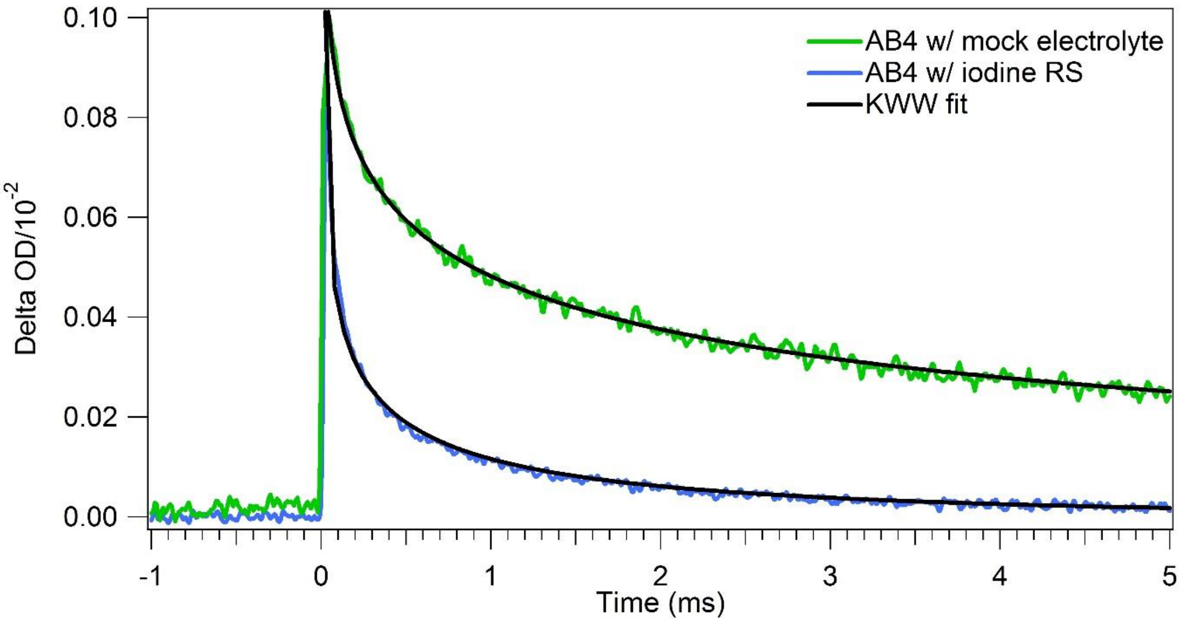

Figure 118: Spectral decay data for **AB4** devices with iodine electrolytes.

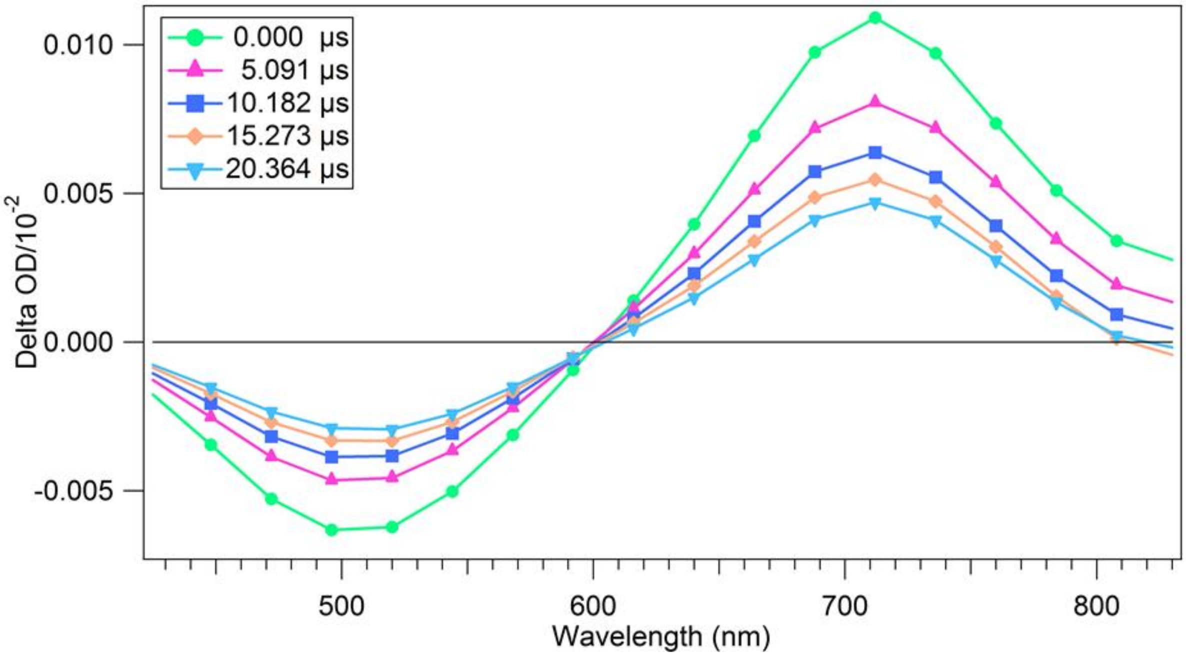

Figure 119: Spectral data for **AB4** in mock cobalt solution.

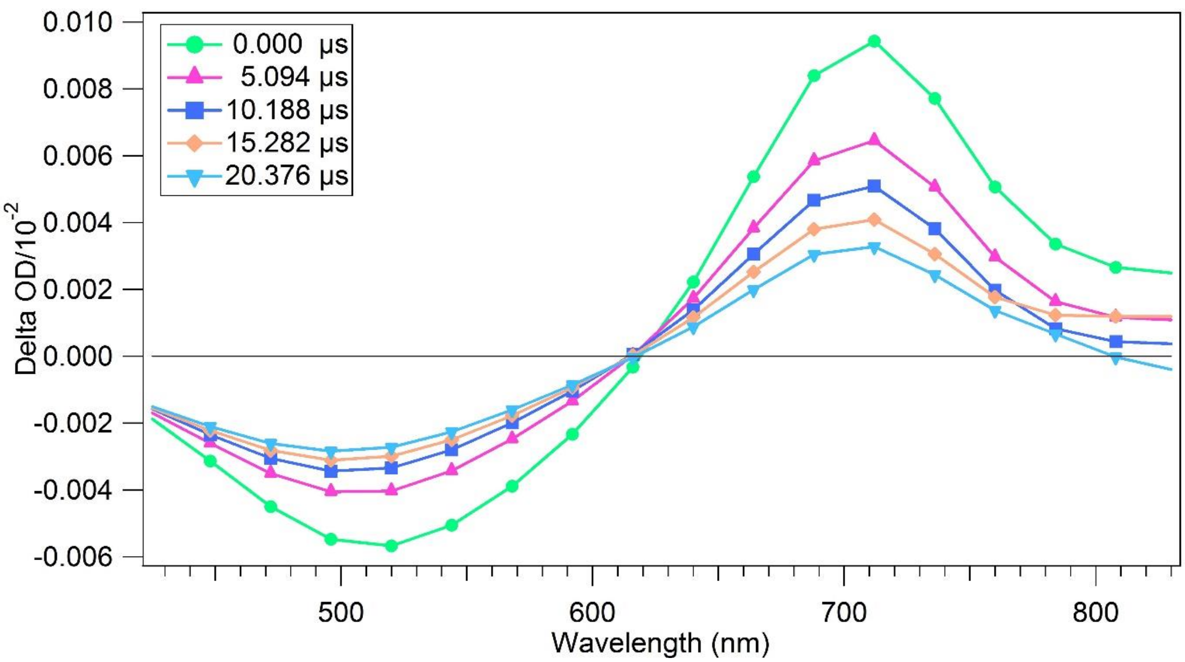

Figure 120: Spectral data for **AB4** in N-terpy cobalt solution.

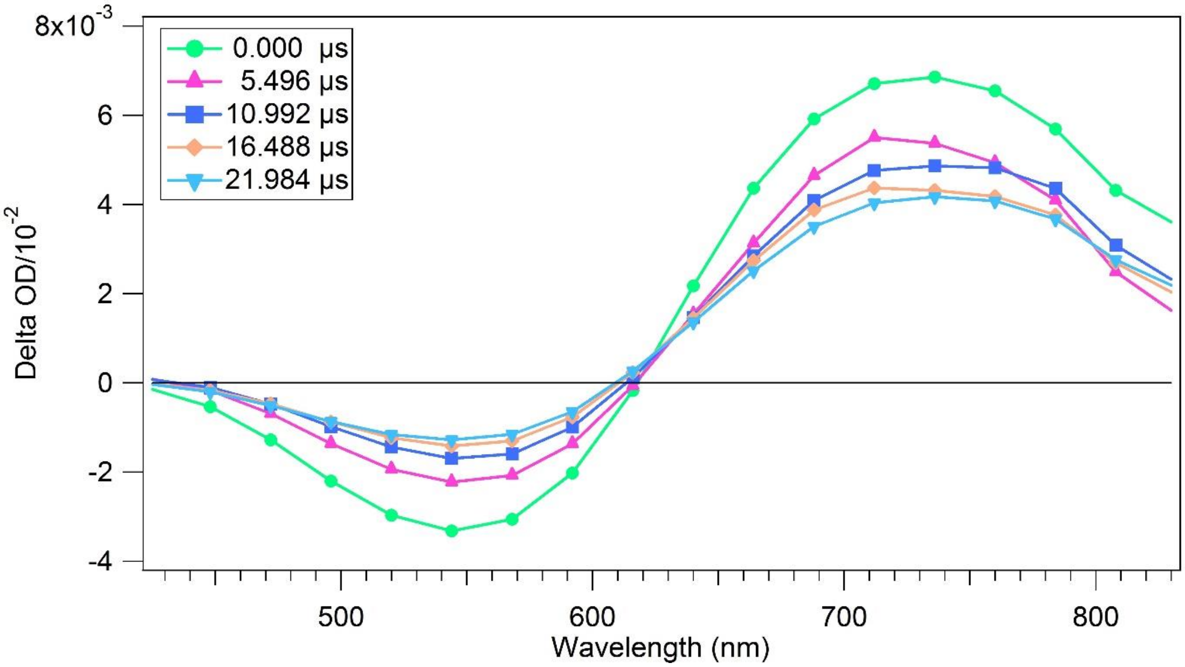

Figure 121: Spectral data for **AB4** in Terpy cobalt solution.

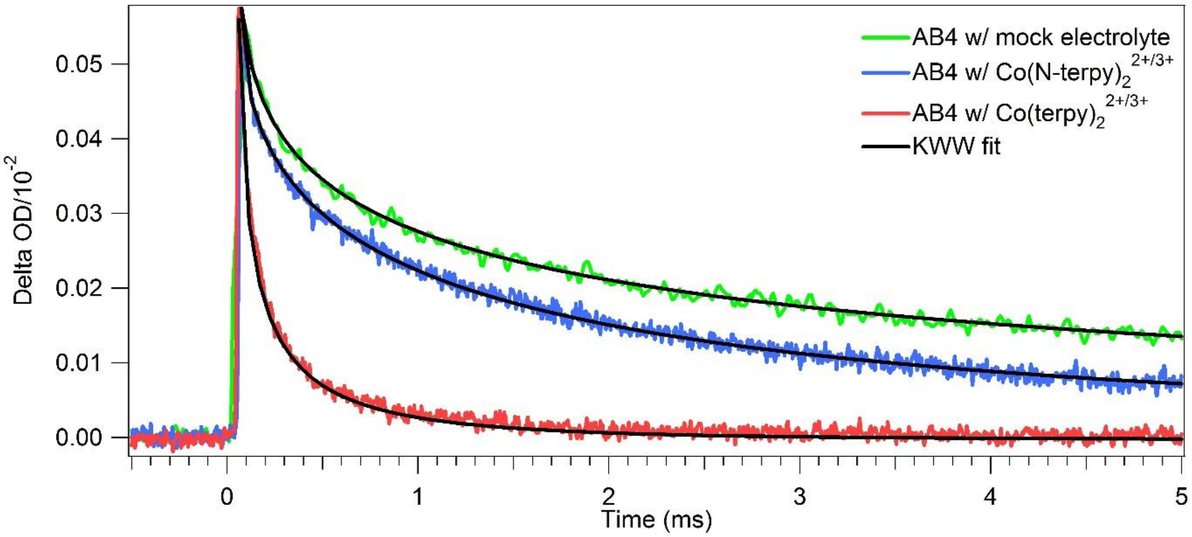

Figure 122: Spectral decay data for **AB4** devices with cobalt electrolytes.

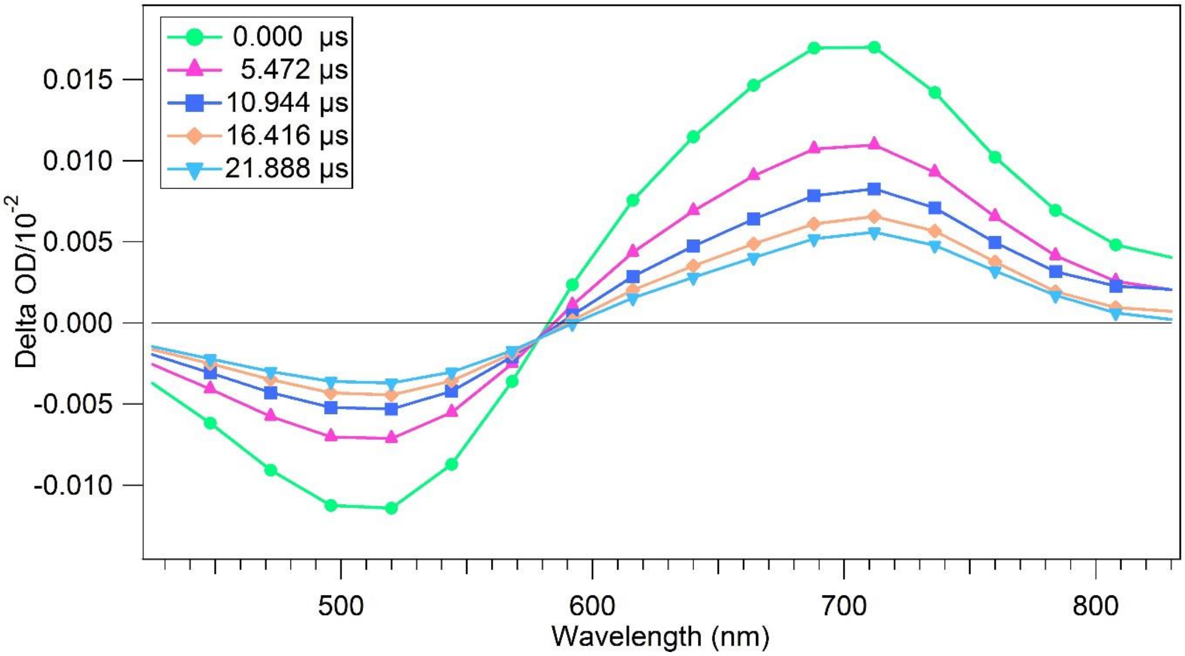

Figure 123: Spectral data for **AB5** in mock iodine solution.

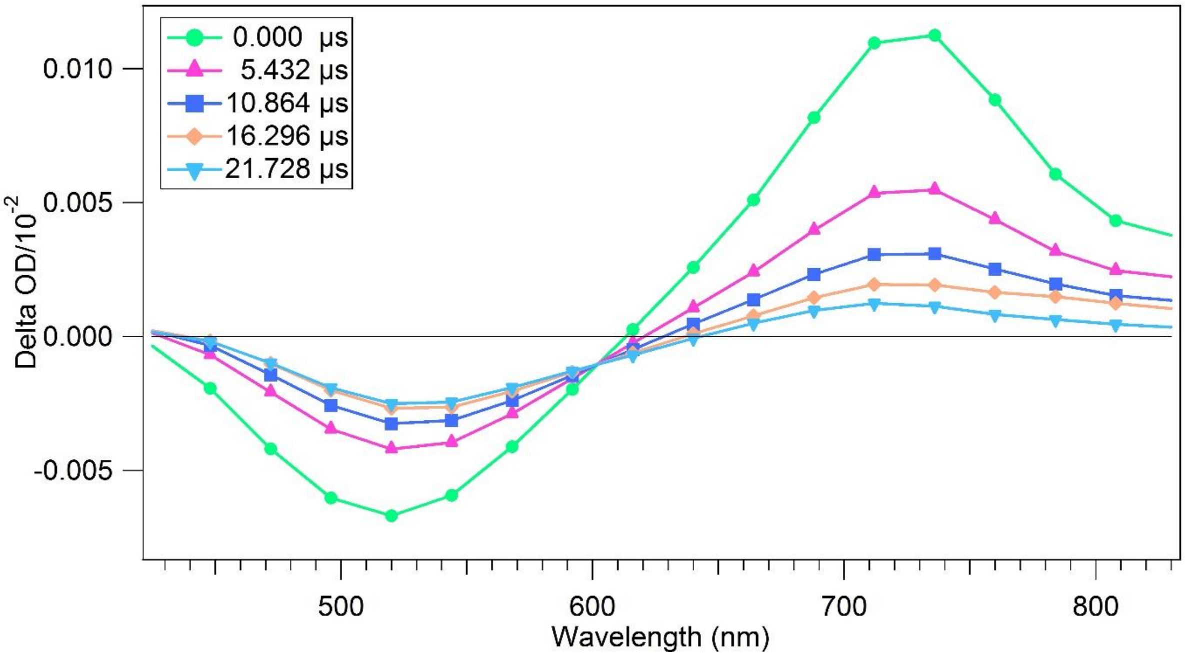

Figure 124: Spectral data for **AB5** in iodine solution.

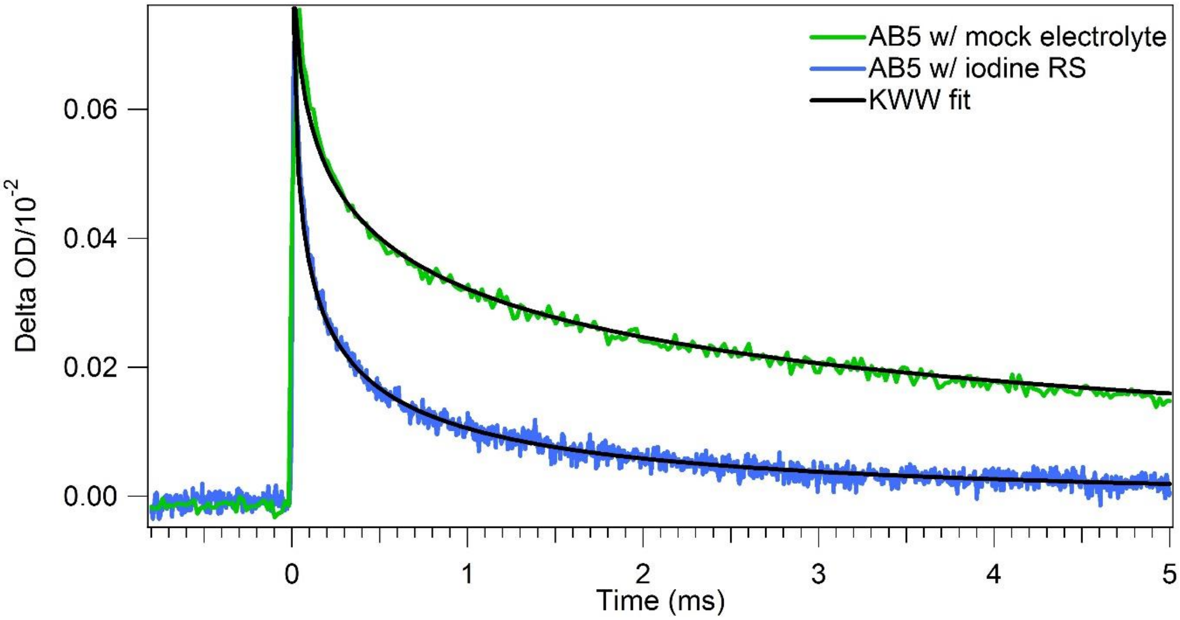

Figure 125: Spectral decay data for **AB5** devices with iodine electrolytes.

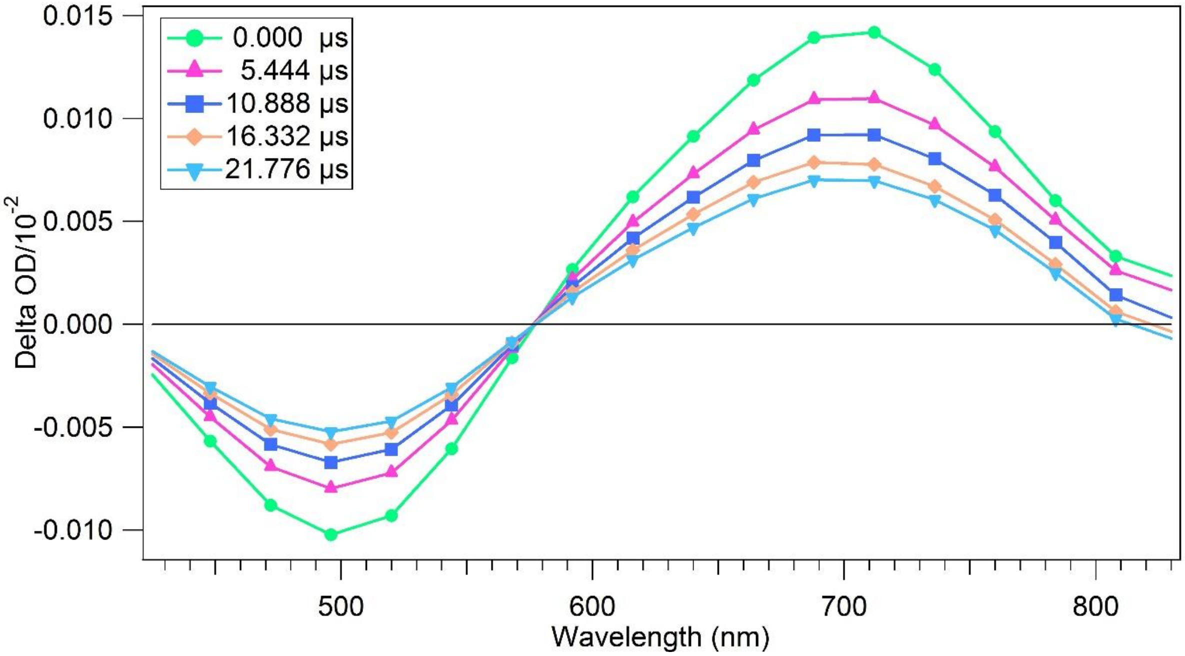

Figure 126: Spectral data for **AB5** in mock cobalt solution.

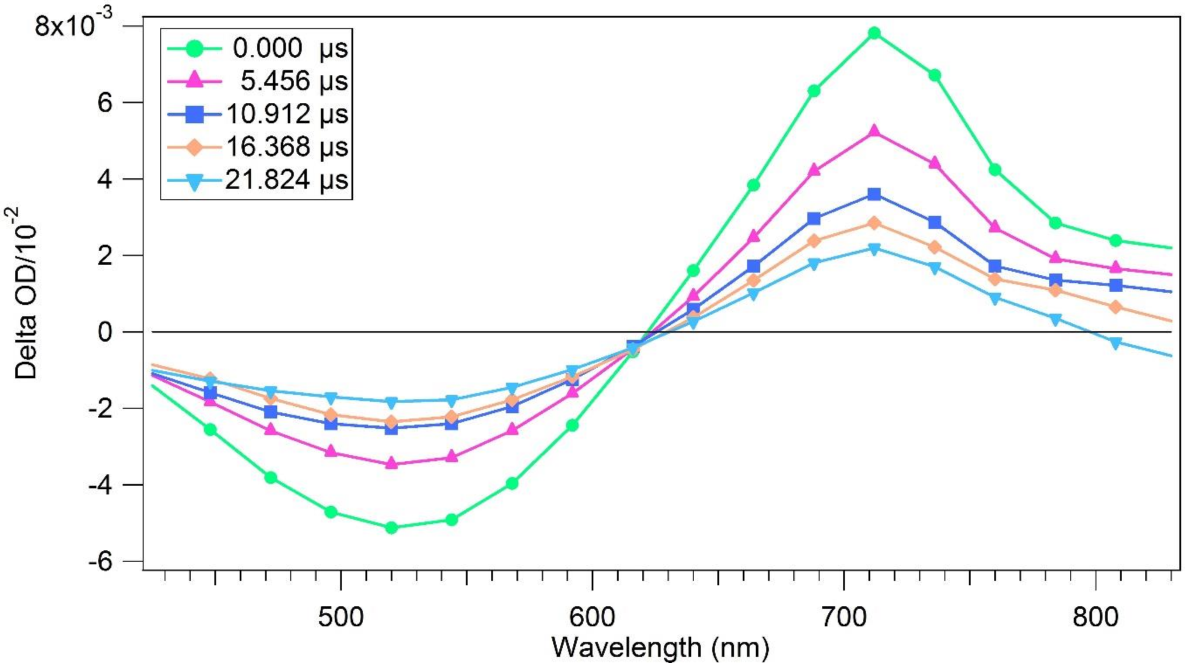

Figure 127: Spectral data for **AB5** in N-terpy cobalt solution.

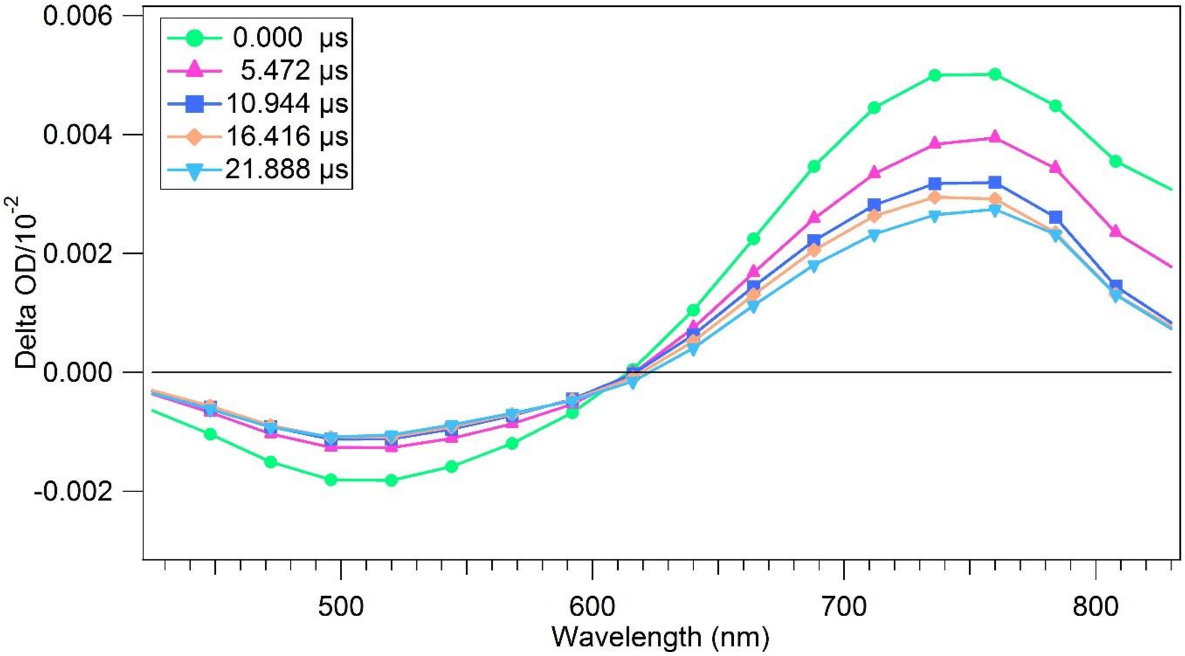

Figure 128: Spectral data for **AB5** in Terpy cobalt solution.

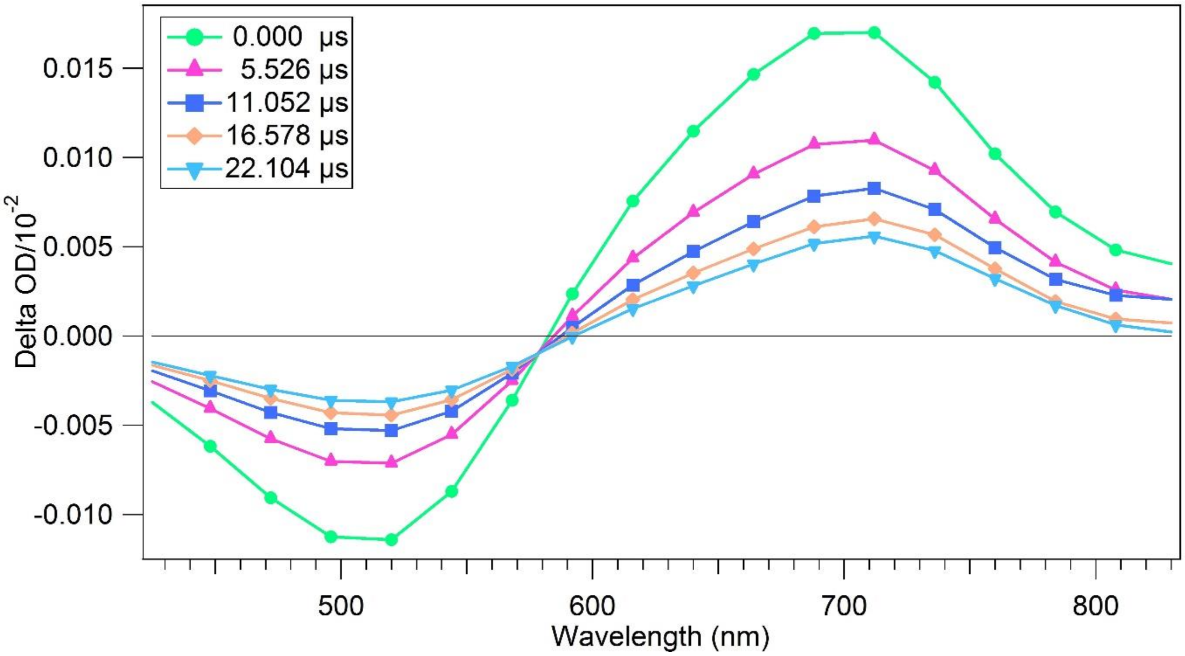

Figure 129: Spectral data for **AB6** in mock iodine solution.

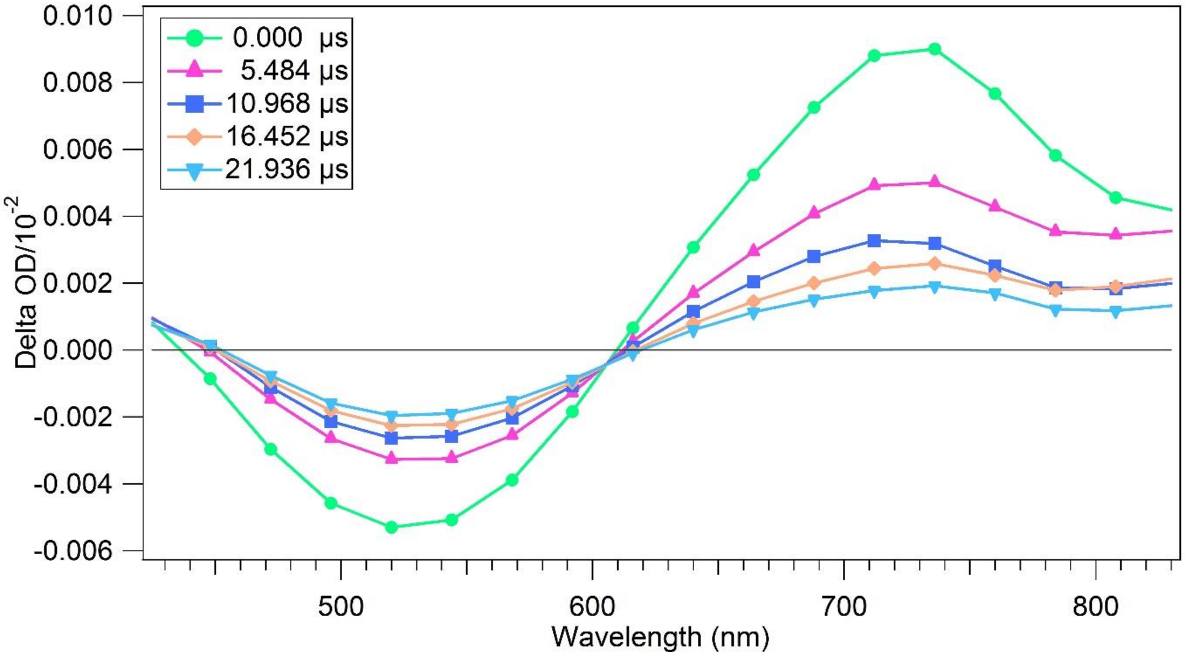

Figure 130: Spectral data for **AB6** in iodine solution.

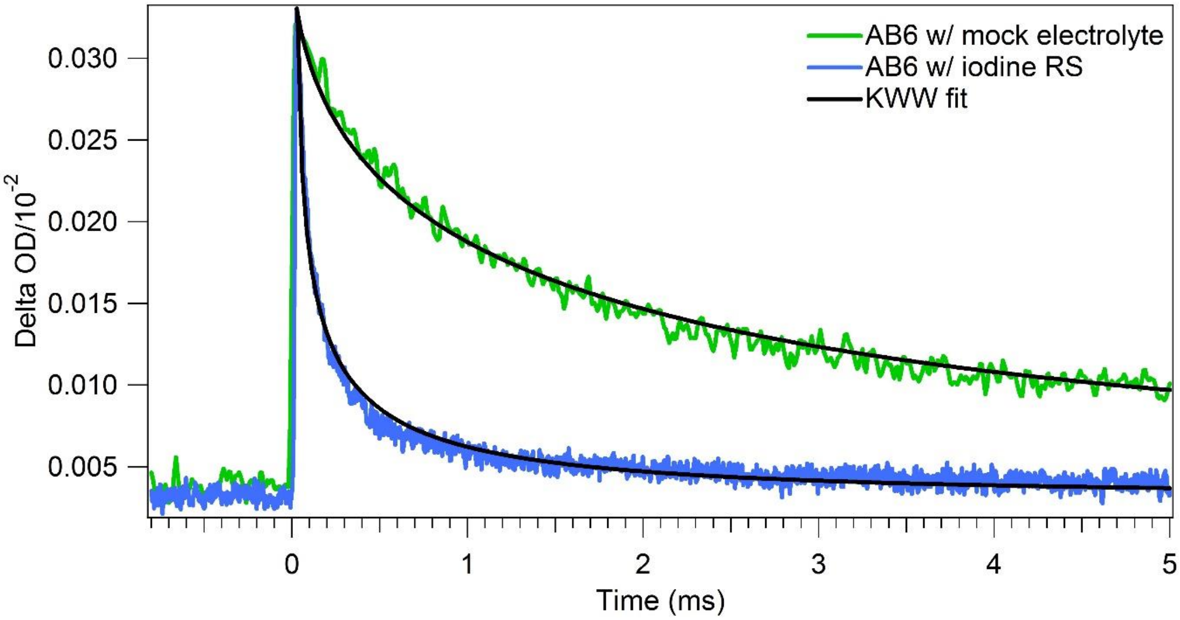

Figure 131: Spectral decay data for **AB6** devices with iodine electrolytes.

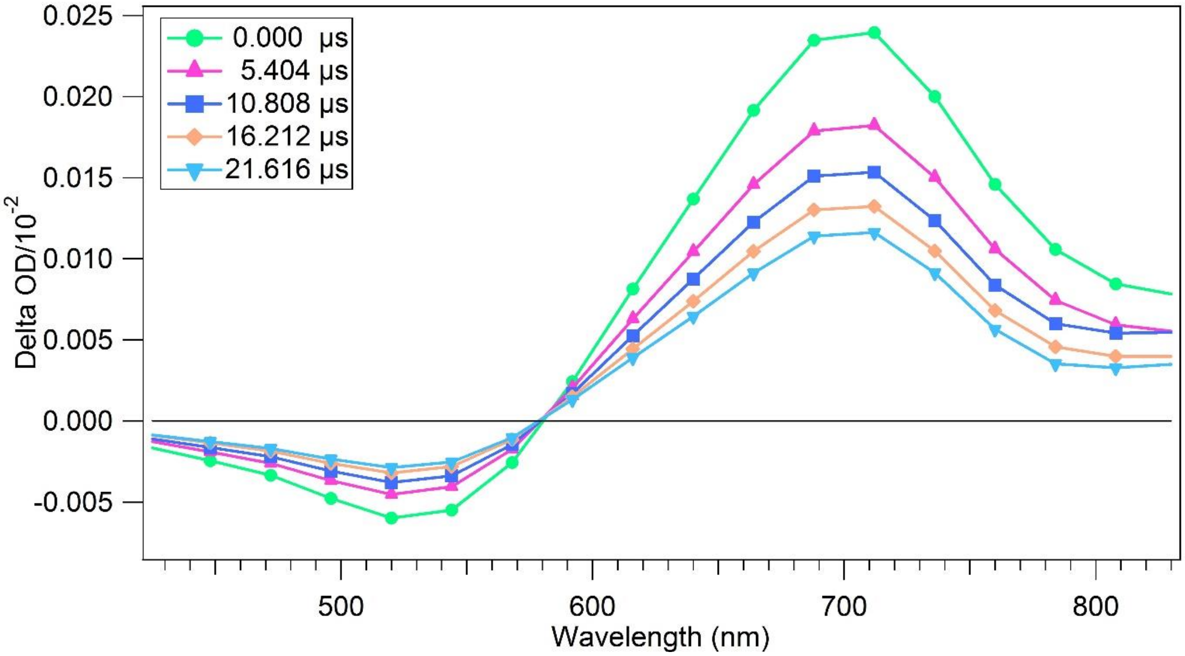

Figure 132: Spectral data for **AB6** in mock cobalt solution.

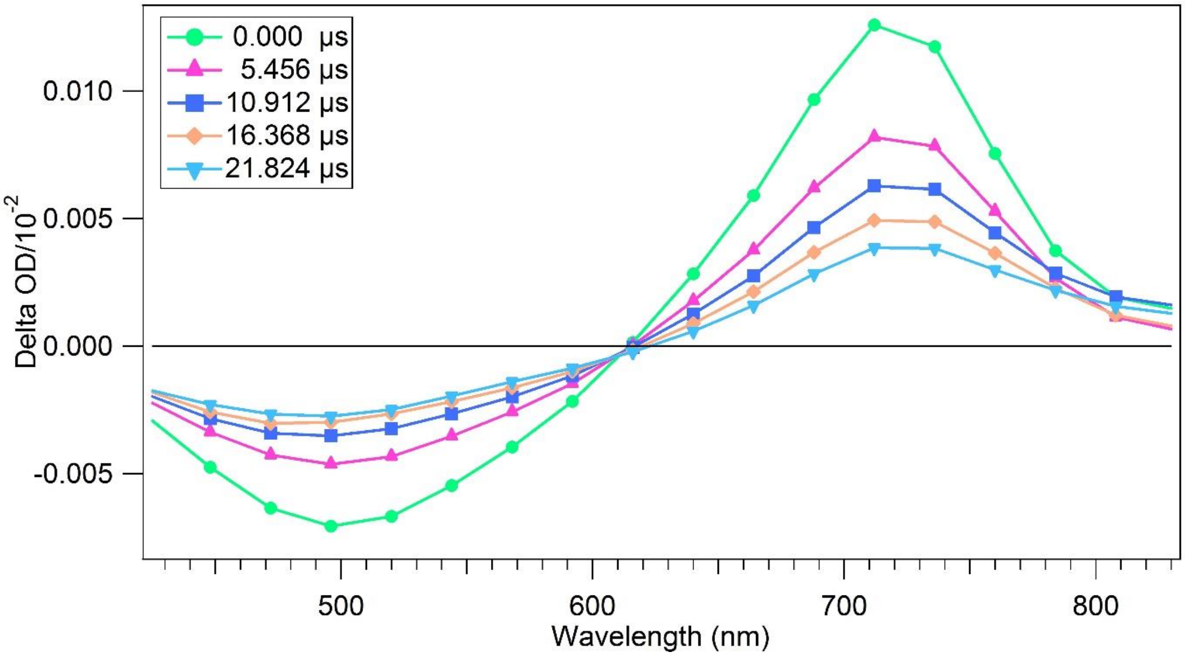

Figure 133: Spectral data for **AB6** in N-terpy cobalt solution.

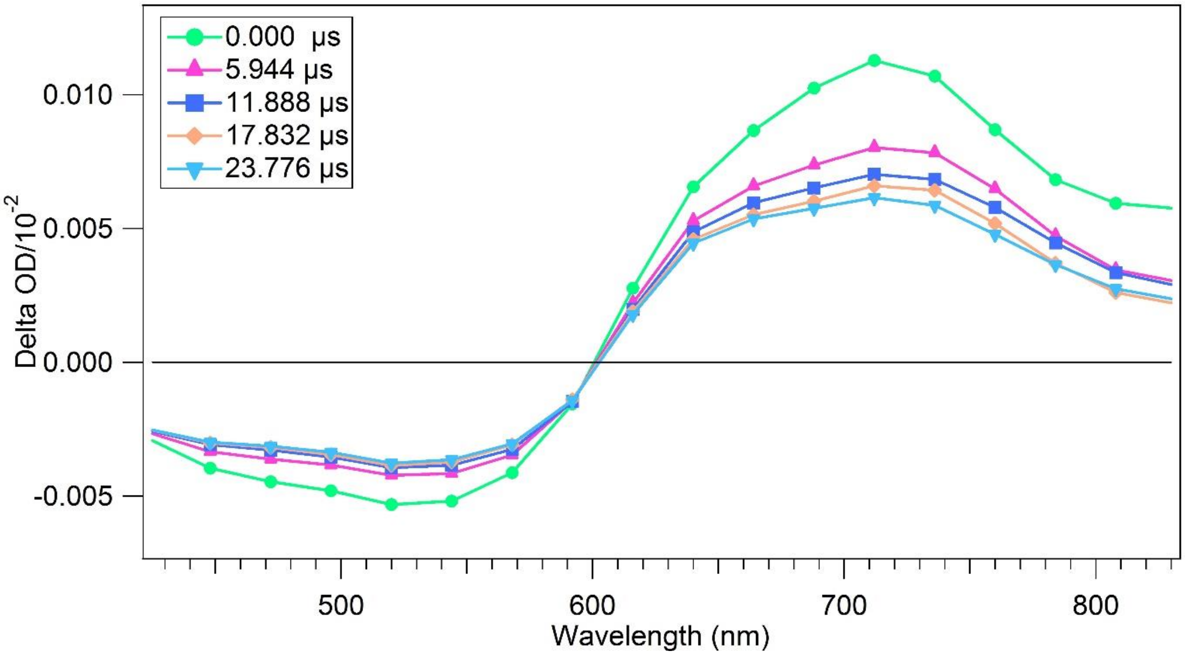

Figure 134: Spectral data for **AB6** in Terpy cobalt solution.

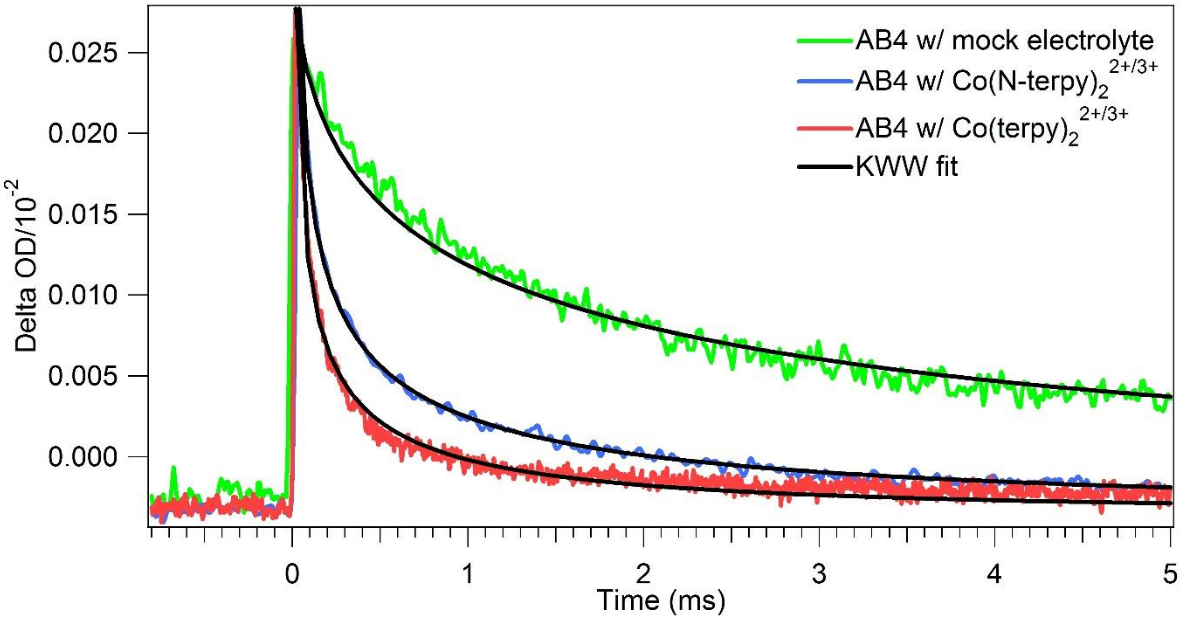

Figure 135: Spectral decay data for **AB6** devices with cobalt electrolytes.

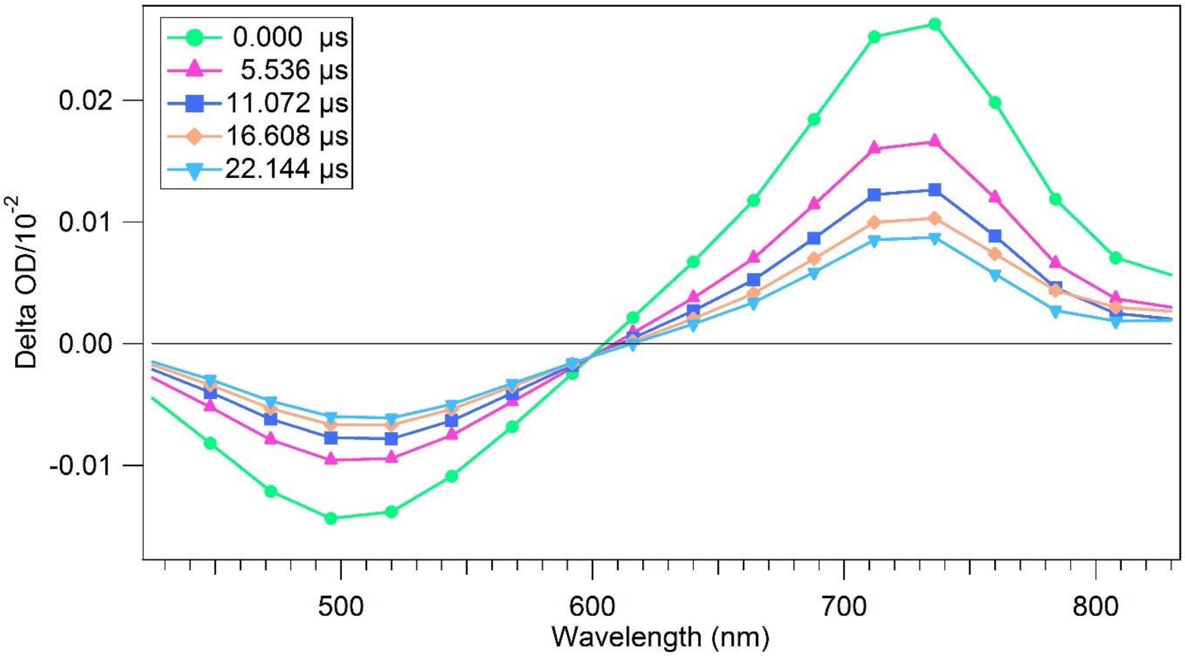

Figure 136: Spectral data for **AB7** in mock iodine solution.

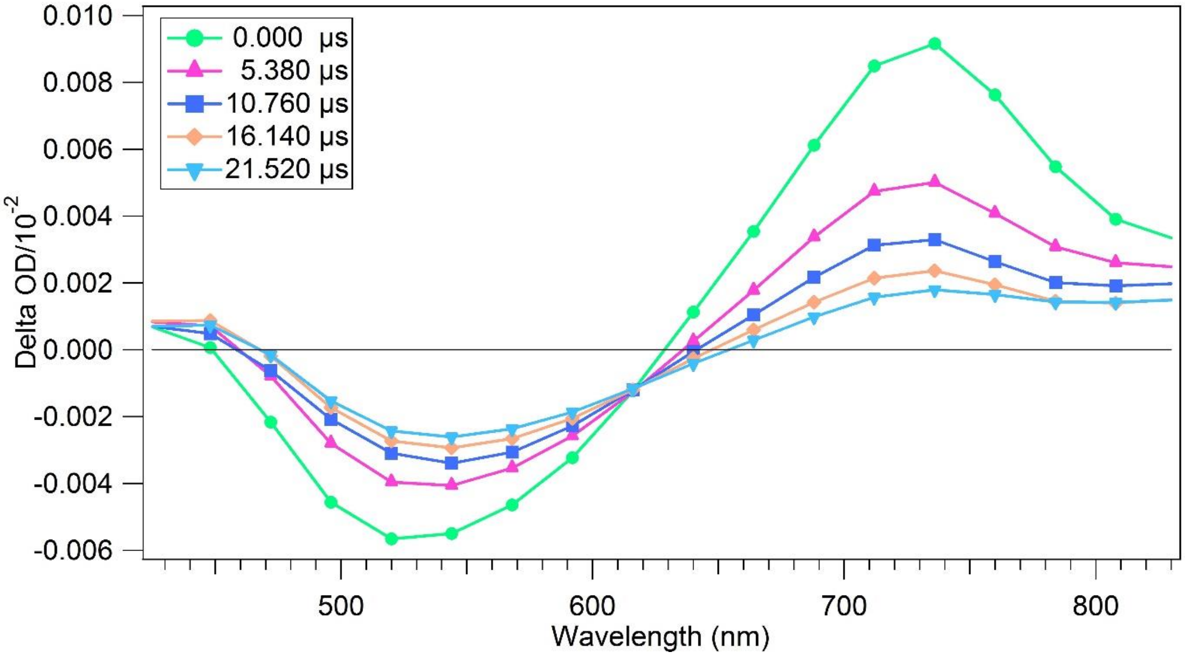

Figure 137: Spectral data for **AB7** in iodine solution.

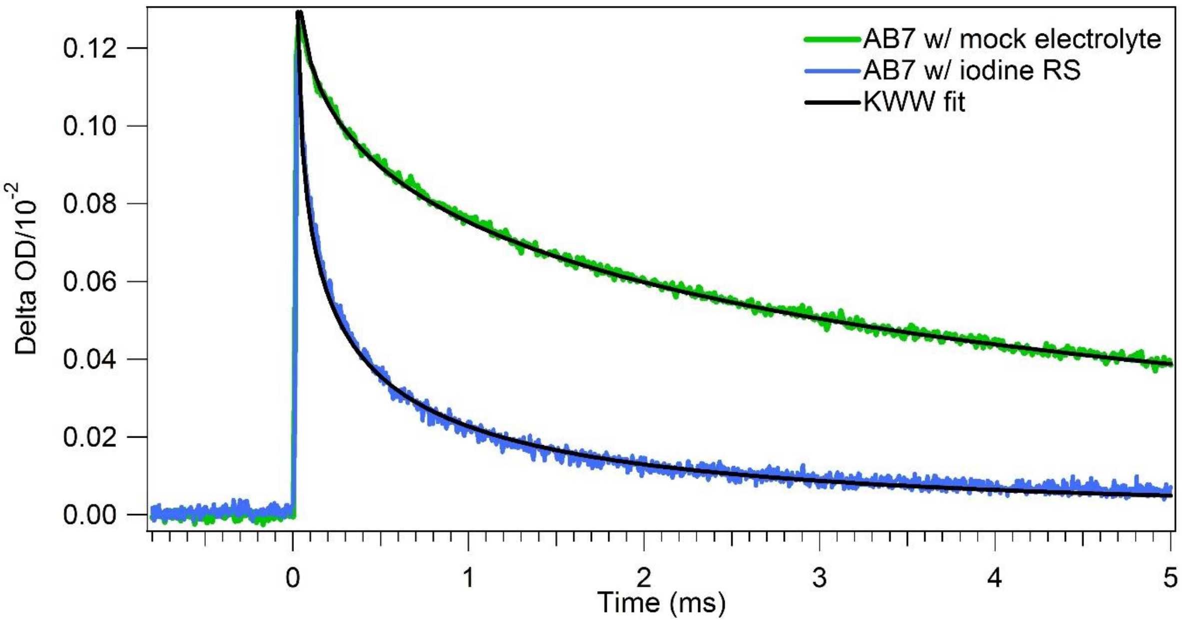

Figure 138: Spectral decay data for **AB7** devices with iodine electrolytes.

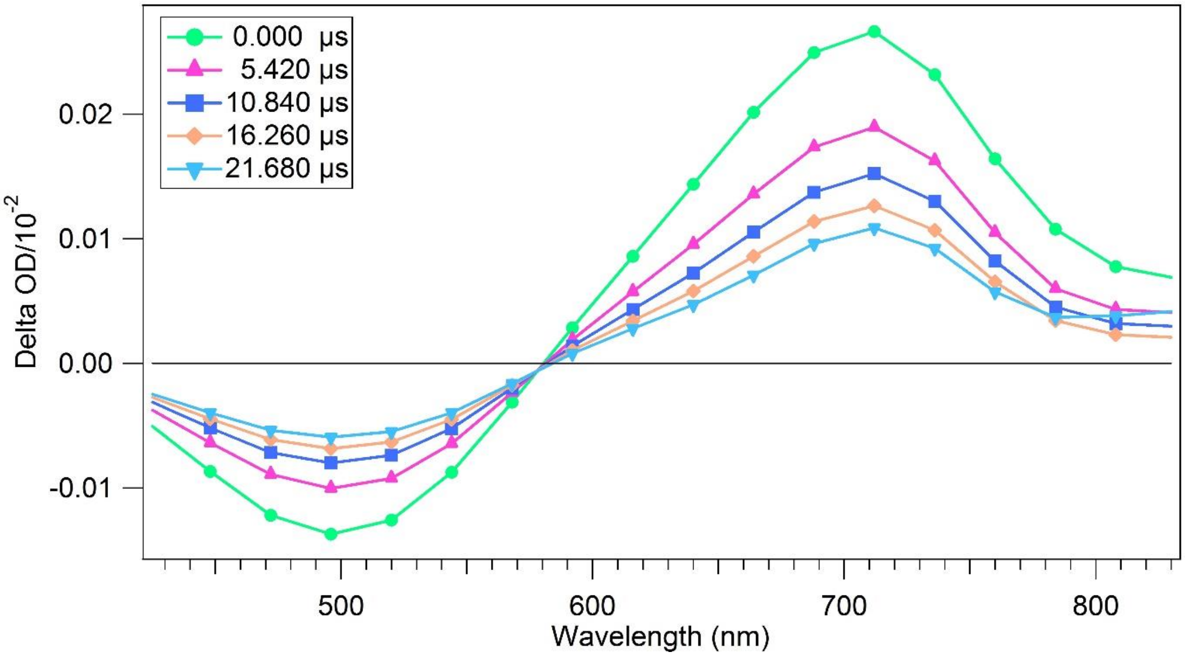

Figure 139: Spectral data for **AB7** in mock cobalt solution.

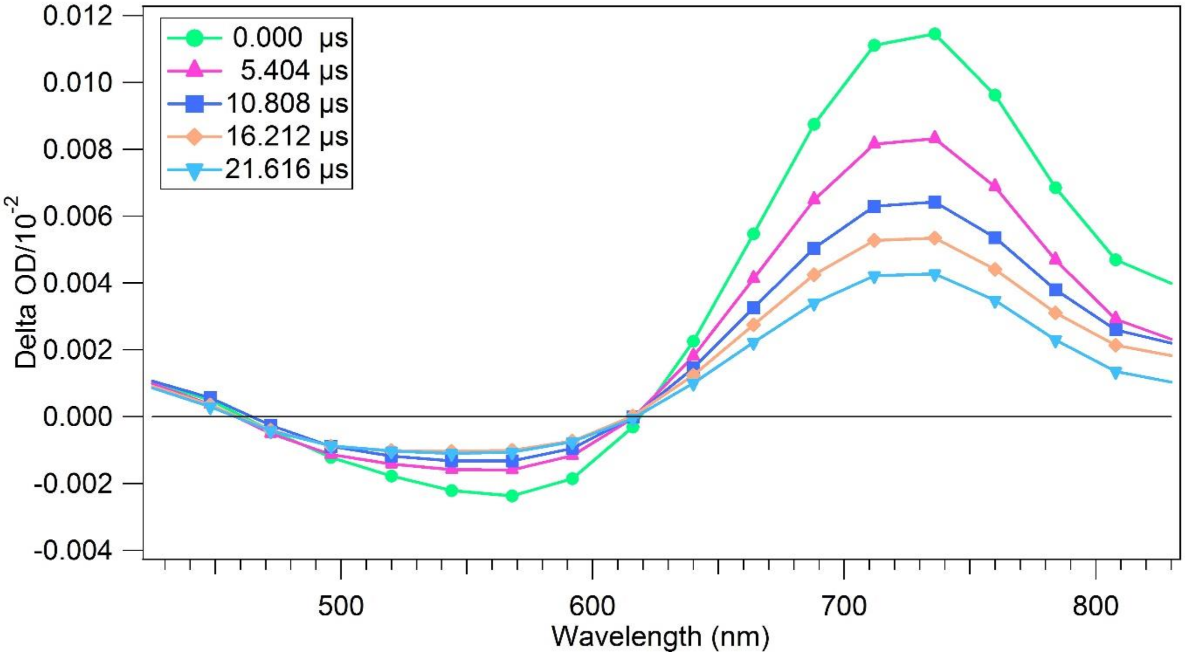

Figure 140: Spectral data for **AB7** in N-terpy cobalt solution.

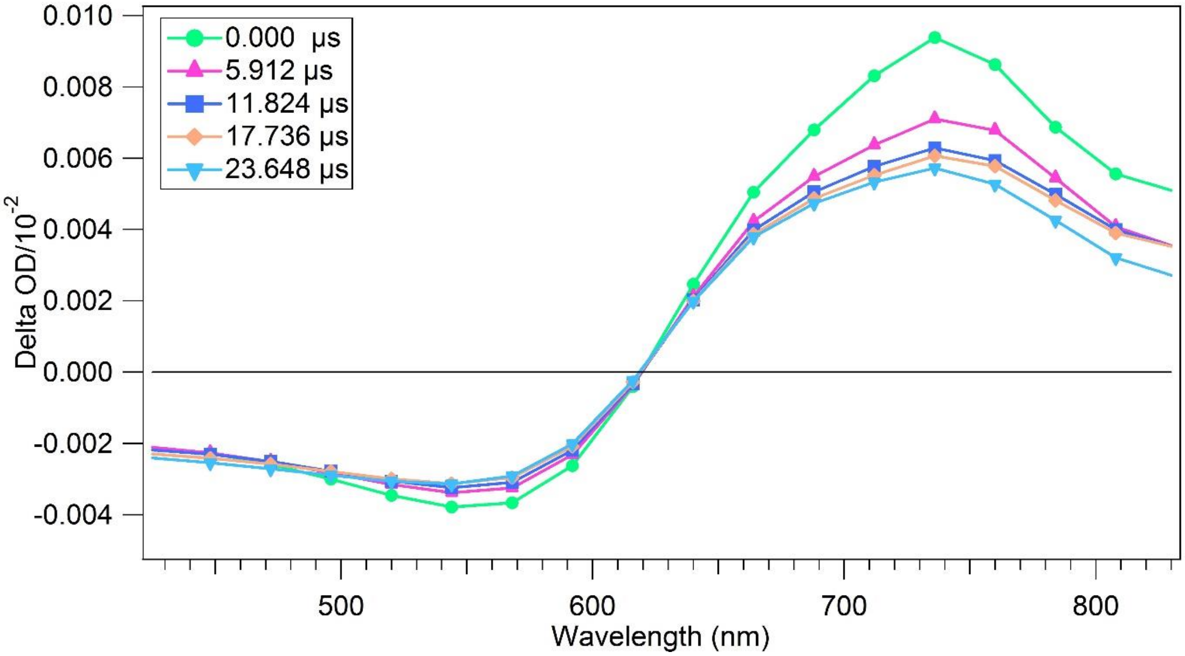

Figure 141: Spectral data for **AB7** in Terpy cobalt solution.

APPENDIX B: PHOTOVOLTAIC MEASUREMENTS AND DEVICE FABRICATION

DSC Device Fabrication: For the photoanode, TEC 10 glass was purchased from Hartford Glass. Once cut into 2x2 cm squares, the substrate was submerged in a 0.2% Deconex 21 aqueous solution and sonicated for 15 minutes at room temperature. The electrodes were rinsed with water and sonicated in acetone for 10 minutes followed by sonication in ethanol for 10 minutes. Finally, the electrodes were placed under UV/ozone for 15 minutes (UV-Ozone Cleaning System, Model ProCleaner by UVFAB Systems). A compact TiO_2 underlayer is then applied by pretreatment of the substrate submerged in a 40 mM $TiCl_4$ solution in water (prepared from 99.9% $TiCl_4$ between 0-5 ^oC). The submerged substrates (conductive side up) were heated for 30 minutes at 70 ^oC. After heating, the substrates were rinsed first with water then with ethanol. The photoanode consists of thin TiO_2 electrodes comprised of a 10 μm mesoporous TiO_2 layer (particle size, 20 nm, Dyesol, DSL 18NR-T) for iodine cells and 5 μm mesoporous TiO_2 layer (particle size, 30 nm, Dyenamo, DN-GPS-30TS) for cobalt cells. All the photoanodes had 5.0 μm TiO_2 scattering layer (particle size, 100 nm, Solaronix R/SP). All the layers were screen printed from a Sefar screen (54/137–64W). Between each print, the substrate was heated for 7 minutes at 125 ^oC and the thickness was measured with a profilometer (Alpha-Step D-500 KLA Tencor). After all layers were deposited, the substrate was then sintered with progressive heating from 125^oC (5-minute ramp from r.t., 5 minute hold) to 325 ^oC (15 minute ramp from 125^oC, 5 minute hold) to 375 ^oC (5 minute ramp from 325 ^oC, 5 minute hold) to 450 ^oC (5 minute ramp from 375 ^oC, 15 minute hold) to 500 ^oC (5 minute ramp from 450 ^oC, 15 minute hold) using a programmable furnace (Vulcan® 3-Series Model 3-550). The cooled sintered photoanode was soaked 30 min at 70 ^oC in a 40 mM $TiCl_4$ water solution and heated again at 500

^{o}C for 30 minutes prior to sensitization. The complete working electrode was prepared by immersing the TiO_2 film into the dye solution overnight. The solution is 0.3 mM of dye in MeCN:t-BuOH:THF mixture (1:1:1) with a 20:1 CDCA:dye ratio unless otherwise indicated. For preparing counter electrodes, 2x2 cm squares TEC 7 FTO glasses were drilled using Dremel-4000 with Dremel 7134 Diamond Taper Point Bit from the conductive and taped FTO side. The electrodes were washed with water followed by 0.1 M HCl in EtOH rinse and sonication in acetone bath for 10 minutes. The washed FTO electrodes were then dried at 400 ^{o}C for 15 minutes. A thin layer of Pt-paste (Solaronix, Platisol T/SP) was slot printed on the FTO and the printed electrodes were then cured at 450 ^{o}C for 10 minutes. After allowing them to cool to room temperature, the working electrodes were then sealed with a 25 μm thick hot melt film (Surlyn, Solaronix, “Meltonix 1170-25”) by heating the system at 130 ^{o}C under 0.2 psi pressure for 1 minute. Devices were completed by filling the electrolyte by pre-drilled holes in the counter electrodes and finally the holes were sealed with a Surlyn pre-cut circle and a thin glass cover by heating at 130 ^{o}C under pressure 0.1 psi for 25 seconds. Finally, soldered contacts were added with a MBR Ultrasonic soldering machine (model USS-9210) with solder alloy (Cerasolzer wire dia 1.6 mm item # CS186-150). A circular black mask (active area 0.15 cm^2) punched from black tape was used in the subsequent photovoltaic studies.

Photovoltaic Measurements: Current-Voltage Curves: Photovoltaic characteristics were measured using a 150 W Xenon lamp (Model SF150B, SCIENCETECH Inc. Class ABA) solar simulator equipped with an AM 1.5 G filter for a less than 2% spectral mismatch. Prior to each measurement, the solar simulator output was calibrated with a KG5 filtered mono-crystalline silicon NREL calibrated reference cell from ABET Technologies (Model 15150-KG5). The current density-voltage characteristic of each cell was obtained with Keithley digital source meter (Model 2400). Device performances under AM 1.5G irradiation were analyzed based on the equation PCE = (J_{sc}*V_{oc}*FF)/I_0. The incident photon-to-current conversion efficiency was measured with an IPCE instrument manufactured by Dyenamo comprised of a 175 W Xenon lamp (CERMAX, Model LX175F), monochromator (Spectral Products, Model CM110, Czerny-Turner, dual-grating), filter wheel (Spectral Products, Model AB301T, fitted with filter AB3044 [440 nm high pass] and filter AB3051 [510 nm high pass]), a calibrated UV-enhanced silicon photodiode reference and Dyenamo issued software.

Electron lifetime measurements: Also known as small modulation photovoltage transient measurements, were carried out with a Dyenamo Toolbox (DN-AE01) instrument and software. The intensity of the LED light source (Seoul Semiconductors, Natural White, S42182H, 450 nm to 750 nm emission) is varied to modulate the device open-circuit voltage. The base light intensity was modulated by applied voltages of 2.80, 2.85, 2.90, 2.95 and 3.00 V applied to the LED with the 3.0 V bias approaching 1 sun intensity (97%). The direction of illumination was from the photoanode to the counter electrode, and the device was positioned 5 cm from the LED light source. The voltage rise and decay times are fitted with a Levenberg-Marquardt fitting algorithm via LabView, and the electron lifetime was obtained from the averaging of rise and decay times.

TAS device fabrication: TEC 10 glass was purchased from Hartford Glass. Once cut into 2x2 cm squares, the substrate was rinsed with water and acetone. The electrodes were comprised of a single 10 µm or 5 µm mesoporous TiO_2 layer (particle size, 30 nm, Dyenamo, DN-GPS-30TS) for iodine and cobalt cells, respectively. All the layers were screen printed from a Sefar screen (54/137–64W). Following the print, the substrate was heated for 7 minutes at 125 ^{o}C and the thickness was measured with a profilometer (Alpha-Step D-500 KLA Tencor). Once the layer was deposited, the substrate was then sintered with progressive heating from 125^{o}C (5-minute ramp from r.t., 5 minute hold) to 325 ^{o}C (15 minute ramp from 125^{o}C, 5 minute hold) to 375 ^{o}C (5 minute ramp from 325 ^{o}C, 5 minute hold) to 450 ^{o}C (5 minute ramp from 375 ^{o}C, 15 minute hold) to 500 ^{o}C (5 minute ramp from 450 ^{o}C, 15 minute hold) using a programmable furnace (Vulcan® 3-Series Model 3-550). The cooled electrode was prepared by immersing the TiO_2 film into the dye solution for 3 hours. The solution is 0.3 mM of dye in MeCN:t-BuOH:THF mixture (1:1:1) with a 20:1 CDCA:dye ratio unless otherwise indicated. The electrodes were washed with acetonitrile and the dried substrates were then partially sealed with a pre-cut semicircle of 25 μm thick hot melt film (Surlyn, Solaronix, “Meltonix 1170-25”) and a thin glass cover slip by heating the system at 130 ^{o}C under 0.1 psi pressure for 30 seconds. Devices were completed by filling the cells with electrolyte solution by injecting it into the open portion of the coverslip with a micro syringe. The device is then sealed with a light-cured adhesive (Permabond UV6231) and curing under 450 nm light for 45 seconds. Iodine cells were light-soaked for 24 hours before measurements were taken.

APPENDIX C: JOURNAL PERMISSION FOR REPRODUCED MANUSCRIPTS

1.Journal permission for Chapter 3.1

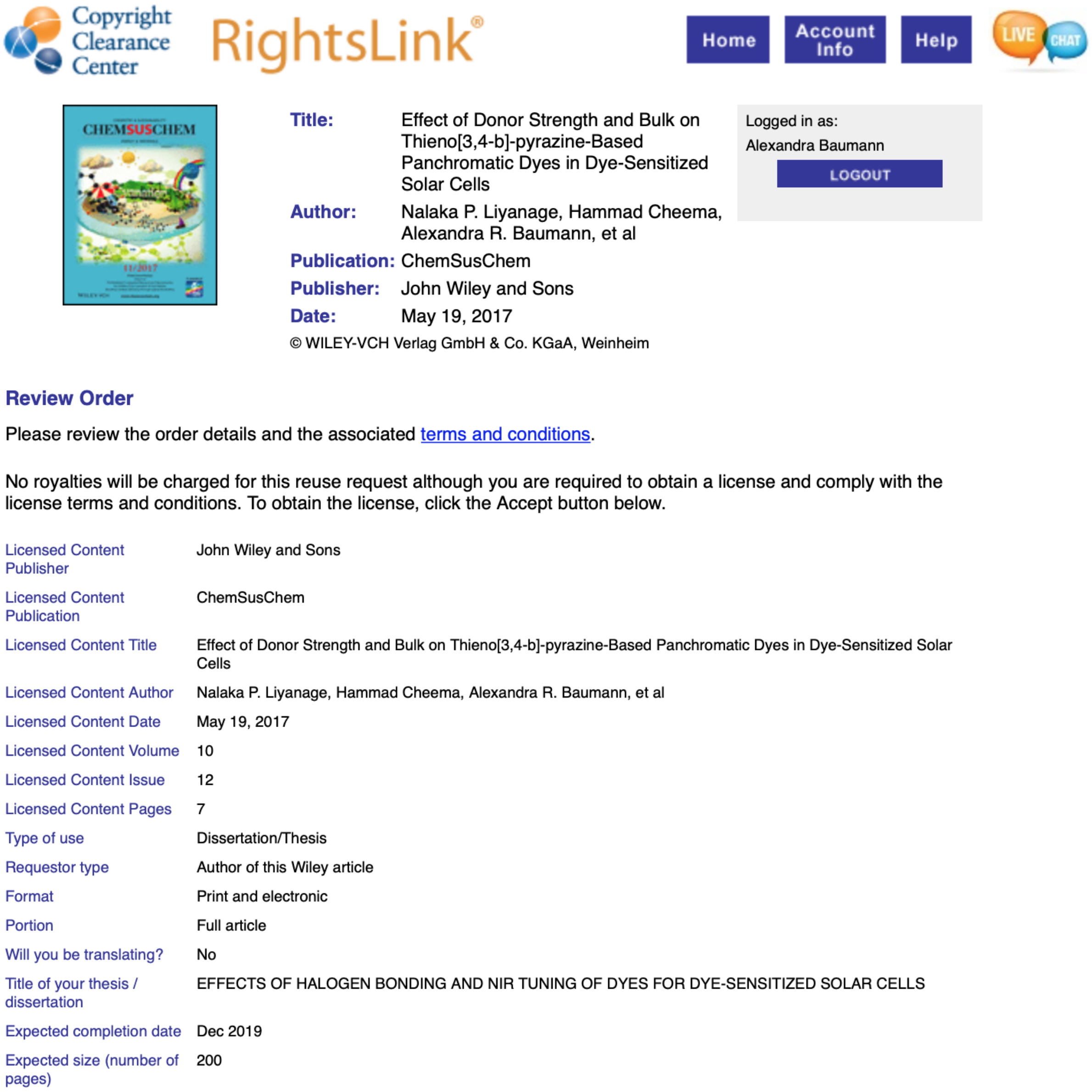

Title:	Effect of Donor Strength and Bulk on Thieno[3,4-b]-pyrazine-Based Panchromatic Dyes in Dye-Sensitized Solar Cells
Author:	Nalaka P. Liyanage, Hammad Cheema, Alexandra R. Baumann, et al
Publication:	ChemSusChem
Publisher:	John Wiley and Sons
Date:	May 19, 2017

© WILEY-VCH Verlag GmbH & Co. KGaA, Weinheim

Logged in as:
Alexandra Baumann

Review Order

Please review the order details and the associated terms and conditions.

No royalties will be charged for this reuse request although you are required to obtain a license and comply with the license terms and conditions. To obtain the license, click the Accept button below.

Licensed Content Publisher	John Wiley and Sons
Licensed Content Publication	ChemSusChem
Licensed Content Title	Effect of Donor Strength and Bulk on Thieno[3,4-b]-pyrazine-Based Panchromatic Dyes in Dye-Sensitized Solar Cells
Licensed Content Author	Nalaka P. Liyanage, Hammad Cheema, Alexandra R. Baumann, et al
Licensed Content Date	May 19, 2017
Licensed Content Volume	10
Licensed Content Issue	12
Licensed Content Pages	7
Type of use	Dissertation/Thesis
Requestor type	Author of this Wiley article
Format	Print and electronic
Portion	Full article
Will you be translating?	No
Title of your thesis / dissertation	EFFECTS OF HALOGEN BONDING AND NIR TUNING OF DYES FOR DYE-SENSITIZED SOLAR CELLS
Expected completion date	Dec 2019
Expected size (number of pages)	200

2.Journal permission for Chapter 4.1

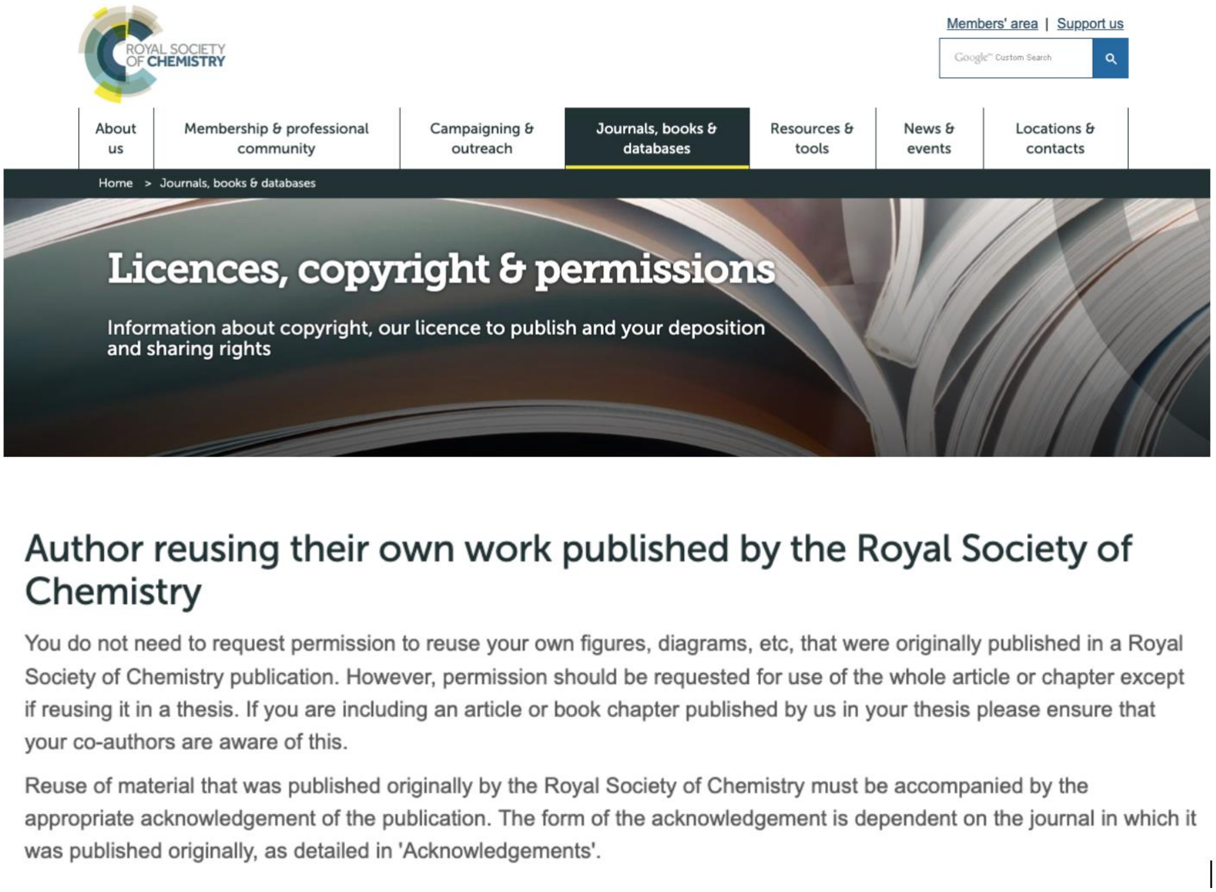

Licences, copyright & permissions

Information about copyright, our licence to publish and your deposition and sharing rights

Author reusing their own work published by the Royal Society of Chemistry

You do not need to request permission to reuse your own figures, diagrams, etc, that were originally published in a Royal Society of Chemistry publication. However, permission should be requested for use of the whole article or chapter except if reusing it in a thesis. If you are including an article or book chapter published by us in your thesis please ensure that your co-authors are aware of this.

Reuse of material that was published originally by the Royal Society of Chemistry must be accompanied by the appropriate acknowledgement of the publication. The form of the acknowledgement is dependent on the journal in which it was published originally, as detailed in 'Acknowledgements'.

3.Journal permission for Chapter 5.1

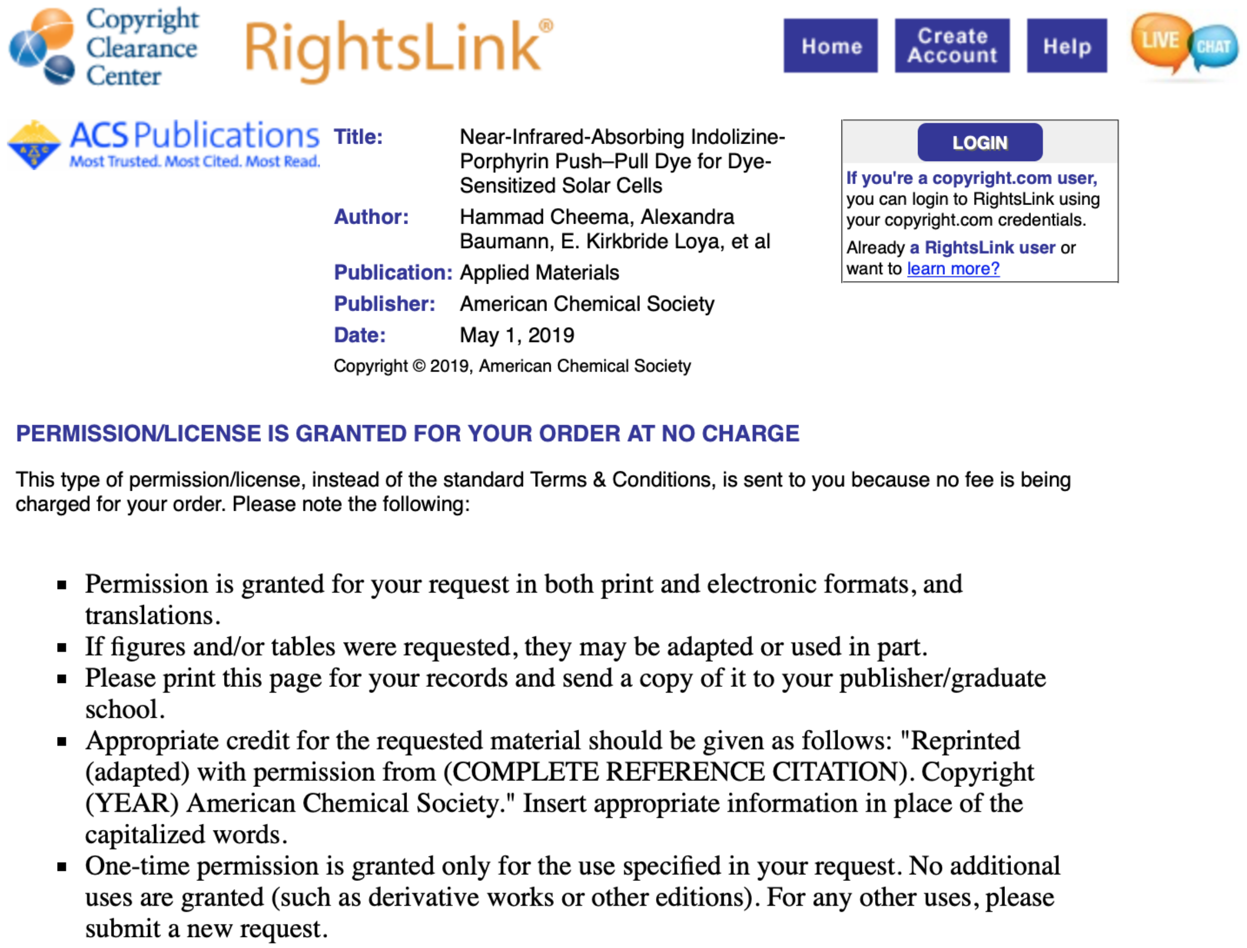

Title: Near-Infrared-Absorbing Indolizine-Porphyrin Push–Pull Dye for Dye-Sensitized Solar Cells

Author: Hammad Cheema, Alexandra Baumann, E. Kirkbride Loya, et al

Publication: Applied Materials

Publisher: American Chemical Society

Date: May 1, 2019

Copyright © 2019, American Chemical Society

If you're a copyright.com user, you can login to RightsLink using your copyright.com credentials.

Already **a RightsLink user** or want to learn more?

PERMISSION/LICENSE IS GRANTED FOR YOUR ORDER AT NO CHARGE

This type of permission/license, instead of the standard Terms & Conditions, is sent to you because no fee is being charged for your order. Please note the following:

- Permission is granted for your request in both print and electronic formats, and translations.
- If figures and/or tables were requested, they may be adapted or used in part.
- Please print this page for your records and send a copy of it to your publisher/graduate school.
- Appropriate credit for the requested material should be given as follows: "Reprinted (adapted) with permission from (COMPLETE REFERENCE CITATION). Copyright (YEAR) American Chemical Society." Insert appropriate information in place of the capitalized words.
- One-time permission is granted only for the use specified in your request. No additional uses are granted (such as derivative works or other editions). For any other uses, please submit a new request.

VITA

ALEXANDRA BAUMANN

University of Mississippi, Department of Chemistry and Biochemistry, 478 Coulter Hall, University, MS 38677 ; Email: abaumann@go.olemiss.edu, alexandra.r.baumann@gmail.com

EDUCATION

University of Mississippi: Department of Chemistry and Biochemistry, University, MS, 2013-2019

Advisor: Prof. Jared H. Delcamp; Degree: Chemistry, Ph.D.

Marist College: Department of Chemistry and Biochemistry, Poughkeepsie, NY, 2009-2013

Advisors: Prof. Richard Kepner and Prof. Elisa Woolridge; Degree: B.S. Biomedical Sciences and B.A. Biochemistry

WORK HISTORY

Research and Teaching Assistant: University of Mississippi, University, MS, 2013-2019

RESEARCH EXPERIENCE

- High efficiency organic dye design, synthesis, and characterization.
- Solar cells devices manufacturing and data analysis

PUBLICATIONS

1) Liyanage, N. P.; Cheema, H.; **Baumann, A.**; Zylstra, A. R.; Delcamp, J. H. "Effect of Donor Strength and Bulk on Thieno[3,4-b]pyrazine-Based Panchromatic Dyes in Dye-Sensitized Solar Cells" *ChemSusChem* **2017**, *10*, 2635.

2) **Baumann, A.**; Cheema, H.; Sabuj, M. A.; McNamara, L. E.; Peddapuram, A.; Zhang, Y.; Nguyen, S. T.; Watkins, D. L.; Hammer, N. I.; Delcamp, J. H. "Iodine Binding with Thiophene Versus Furan Based Dyes for DSCs" *Phys. Chem. Chem. Phys*. **2018**, *20*, 17859.

3) Cheema, H.; **Baumann, A.**; Loya, E. K.; Brogdon, P.; McNamara, L. E.; Carpenter, C. A.; Hammer, N. I.; Mathew, S.; Risko, C.; Delcamp, J. H. "Near-Infrared-Absorbing Indolizine-Porphyrin Push-Pull Dye for Dye-Sensitized Solar Cells" *ACS Appl. Mater. Interfaces* **2019**, *11*, 16474.

ORAL PRESENTATIONS

1) July 2016. "Synthetic Pathways to the Hagfeldt Donor: A Critical DSC Building Block", Feeding and Powering the World, University of Mississippi, University, MS.

POSTER PRESENTATIONS

3) March 2018. "Iodine Binding with Thiophene versus Furan Based Dyes for DSCs" National Meeting of the American Chemical Society, New Orleans, LA.

2) July 2017. “Evidence of Iodine Binding with Thiophene Based Dyes in DSCs” Feeding and Powering the World, University of Mississippi, University, MS.

1) November 2015. “MP2 and CCSD(T) Energetics for Proton Transfer in $(HCl)_m(H_2O)_n$ clusters where $m+n\geq 6$”, Southeastern Regional Meeting of the American Chemical Society, Memphis, TN